Semiconductors, Vol. 35, No. 11, 2001, pp. 1223–1230. Translated from Fizika i Tekhnika Poluprovodnikov, Vol. 35, No. 11, 2001, pp. 1281–1288.

ATOMIC STRUCTURE AND NONELECTRONIC PROPERTIES OF SEMICONDUCTORS

Physical Foundations of Metastable Impurity Center Reconstruction in Semiconductors

D. E. Onopko and A. I. Ryskin

"Vavilov State Optical Institute" All-Russia Scientific Center, St. Petersburg, 199034 Russia

Submitted January 24, 2001; accepted for publication April 19, 2001

Abstract—The manner in which the electronic structure and chemical bonding of a perfect crystal change upon doping and vary with the charge state of a defect is analyzed. The obtained results serve as a basis for proposing a general pattern of reconstruction of metastable impurity centers, of both donor and acceptor types, in various semiconductors: "classical" III–V and II–VI semiconductor compounds, mostly ionic CdF_2 crystal, and narrow-gap IV–VI compounds. Reasons are revealed for center reconstruction; general tendencies of the process and the specificity of their manifestation in some classes of crystals and types of impurity centers are established. © *2001 MAIK "Nauka/Interperiodica".*

1. INTRODUCTION

Metastable impurity centers have long attracted the attention of researchers not only in connection with the complex physical phenomena accompanying the formation of these centers, but also owing to the influence exerted by them on a semiconductor and its properties. In particular, the most important types of such centers (*DX* centers and acceptor analogues of these) make it impossible to obtain the necessary type and level of conduction in semiconductors, being one of the main reasons for their self-compensation. However, crystals with *DX* centers have found practical application recently, serving as a basis for the development of effective holographic recording media (see, e.g., [1–3]).

Modern methods for the calculation of impurity centers, based on the extended-cell approximation, are widely employed for studying metastable centers [4–7]. Essential specific features of the centers have been revealed and an understanding of basic experimental results has been gained with the use of these methods. Nevertheless, a number of fundamental questions concerning the formation and structure of metastable centers remain unanswered. In particular, it is not clear why the *DX* center undergoes a fundamental reconstruction and why this reconstruction has a trigonal nature in some cases and an orthorhombic one in others. Why are such centers more readily formed in II–VI compounds, compared with III–V compounds in which some "external" (with respect to a center) influence is necessary for center formation (passing to solid solutions, uniform compression, etc.)? Why do the basically similar trigonally reconstructed *DX* centers in III–V and II–VI compounds, nevertheless, differ significantly in structure? Why do some impurities form metastable centers, whereas others of nearly the same chemical nature, do not? There may be many more questions of this kind.

Our recent investigations have shown that of key importance for the formation of metastable centers is how the electronic structure and chemical bonding of a crystal change upon doping and vary with the charge state of a defect [7–10]. It has been demonstrated that the main body of data on how these parameters change can be obtained even in terms of the minimum cluster, without considering an extended crystal fragment including tens of atoms. Naturally, such an approach gives no way of describing the center quantitatively, but it furnishes a clear notion of the reasons for, and also the type and probability of, the center reconstruction, i.e., this approach provides answers to the questions remaining open within the crystal approach.

The present study establishes for the first time, on the basis of the cluster approach, a general pattern of reconstruction of metastable donor and acceptor centers in "classical" III–V and II–VI semiconductors; in an unusual, ionic semiconductor CdF_2 (with only donor centers possible); and narrow-gap IV–VI compounds (the metastable centers in these crystals being amphoteric). This study reveals both the fundamental aspects of this reconstruction and its specific features for concrete classes of compounds and types of impurity centers.

2. CATIONIC DONOR CENTERS IN III–V CRYSTALS

According to calculations based on the extended-cell method [4, 5], the neutral tetrahedrally symmetrical state of a shallow donor center in GaAs:Si is unstable with respect to a change in the charge state and formation of a *DX* center under the above-mentioned conditions (hydrostatic pressure, passing to an $Al_xGa_{1-x}As$ solid solution, etc.). The capture of an additional electron causes a trigonal C_{3v} reconstruction of the defect, with the doping atom shifted along the threefold axis

1063-7826/01/3511-1223$21.00 © 2001 MAIK "Nauka/Interperiodica"

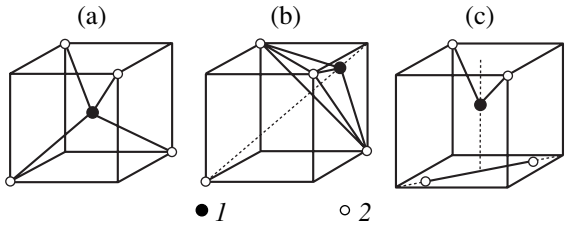

Fig. 1. Structure of (a) tetrahedral substitutional center and reconstructed (b) trigonal C_{3v} and (c) orthorhombic C_{2v} *DX* centers in III–V and II–VI crystals. (*1*) Impurity atom and (*2*) lattice atom.

into the immediate vicinity of the nearest interstitial site (Figs. 1a and 1b). The arising distortion of the crystal lattice compensates for the increase in energy that results from the addition of this electron. On the other hand, loss of a donor electron, which is in excess for chemical bonding, favors preservation of the tetrahedral symmetry of the defect. The total energy of the charged, either positively or negatively, impurity center exceeds in absolute value its energy in the neutral state. These three states of the center are separated by potential barriers, with the result that the neutral state is metastable. A system of this kind is characterized by negative correlation energy U^- [11].

Analysis of the impurity center in GaAs:Si in terms of the cluster approximation (the $GaAs_4^{3q-}$ cluster was calculated using the scattered-wave technique, q is the ion charge) reveals essential details of this reconstruction [8]. Comparison of the electronic structures of the perfect GaAs crystal and an impurity center in GaAs:Si (Table 1) shows that structural change upon doping is relatively slight: the charge distribution among main bonding orbitals $1a_1$, $2a_1$, and $2t_2$ is slightly modified and an electron appears in the antibonding state $3a_1$. Such a change in the electronic structure cannot give rise to any significant reconstruction of the impurity center [9].

However, capture of an additional electron by the antibonding level $3a_1$ changes the situation fundamentally. The three a_1 states are mainly formed on the basis of three atomic orbitals: 3*s* Si and 4*s*, 4*p* As (the valence *s* functions of the four ligands decompose in the field of tetrahedral symmetry into irreducible representations a_1 and t_2, and the *p* functions, into a_1, e, t_1, and two t_2). As a result, the complete filling of the antibonding state $3a_1$ dramatically reduces the overall contribution from the orbitals with a_1 symmetry to the binding energy of the impurity center. The insignificant binding effect of these orbitals may be due to admixture of the corresponding excited states of the central atom and the ligands (4*s* Si and 4*d*, 5*s*, 5*p* As). Thus, as a result of the capture of an additional electron, $2t_2$ becomes the main, and virtually the only, bonding orbital of the defect.

Two variants of further development are possible: the center either remains a tetrahedrally symmetrical defect under conditions of markedly weakened sp^3 hybridization or it is reconstructed in accordance with a symmetry that is optimal for a bonding six-electron t_2 state (in other words, a *DX* center is formed). Let us consider the nature of this reconstruction.

The t_2 state is characterized by three equivalent directions of the strongest localization of the electron density, and, consequently, three bonds between the central atom and the ligands can be formed on its base. Therefore, the reconstructed center has, in the general case, the trigonal symmetry C_{3v}. In the process of this reconstruction, one of the four tetrahedral bonds of an Si impurity atom is ruptured (substantially weakened) as a result of the localization of the four remaining valence electrons at the bonding and antibonding orbitals of this bond (the negatively charged GaAs:Si^- center has ten valence electrons); i.e., the electrons are localized at the central atom and the corresponding ligand.

For the Si atom, the mentioned lone pair will be constituted by its 3*s* electrons, which are not involved, as noted above, in the chemical bonding of the defect. This means that, as a result of reconstruction, the Si impurity atom passes into a divalent state—the state with lower valence (Si valence in the initial tetrahedral center is four). In III–V crystals, the cation donates $0.75e$ per bond, and the anion, $1.25e$; therefore, the transition of the impurity atom upon formation of three bonds into the divalent state also seems to be quite natural from this standpoint. Repulsion between lone pairs of electrons on the impurity atom and on the mentioned ligand leads to a shift of the smaller positive Si ion along the threefold axis toward the nearest interstitial site. The important role of such repulsion was also revealed in terms of the crystalline approach [4, 5].

Of fundamental importance for the partially symmetrical reconstruction of the GaAs:Si center is that the chemical bonds are directional, i.e., they have a covalent constituent. In an ionic crystal, having no directional bonds of the above kind, the reconstruction of this kind cannot occur. The reconstruction is ensured by the presence in the lattice of an interstitial site toward which the impurity atom is shifted.

In this way, the reconstruction and formation of *DX* centers in most of the metastable donor defects in III–V:IV crystals occurs.

3. CATIONIC DONOR CENTERS IN II–VI CRYSTALS

The considered mechanism of formation of *DX* centers in III–V:IV crystals is also valid for II–VI:III impurity centers. Only a single remark should be made concerning the mechanism of trigonal reconstruction [10]. In accordance with the aforesaid, the dopant atom passes in the course of reconstruction into a state with lower valence. For a Group-III atom (specifically, an Al atom), this means that the impurity becomes univalent. If it is taken into account that the cation and anion

in II–VI crystals donate, respectively, 0.5*e* and 1.5*e* per bond, it may be assumed that Al forms bonds with two ligands by means of its single valence electron, whereas its lone pair occupies the third tetrahedral orbital, with the fourth orbital remaining free (in the initial II–VI:III center, Al is in the sp^3-hybridized state). The additional electron of the II–VI:III$^-$ defect fills the dangling bond orbital of each of the remaining pair of ligands (similarly to III–V:IV$^-$, the II–VI:III$^-$ center possesses 10 valence electrons). As a result, one of these saturated bonds, interacting with the unoccupied orbital of Al, forms a third bond with this atom, in no way different from the two already existing bonds. The repulsion between the lone electron pairs of Al and the fourth ligand leads to a trigonal C_{3v} reconstruction of the defect (Fig. 1b).

The results of crystal calculations also indicate a trigonal structure of the II–VI:III centers [12, 13]. According to these calculations, the shift of the impurity atom in the formation of *DX* centers in II–VI:III crystals corresponds with good precision to its reflection in the plane of three ligands (Fig. 1b) [13], whereas in III–V:IV, this distance decreases by approximately 25% [5].

At the level of interatomic interactions, this situation can be understood as follows. Group-IV atoms tend to form multiple bonds, with the result that the *DX* center in GaAs is formed with an admixture of states corresponding to higher multiplicity of bonding of the Si atom with the three aforementioned ligands. At the same time, the formation of multiple bonds is uncharacteristic of Group-III atoms. It is this fact that determines the above-mentioned difference between the shifts of the impurity atom in the formation of *DX* centers in III–V:IV and II–VI:III crystals. This difference results in a more profound disruption of the bond with the fourth ligand in III–V:IV. In other words, the *DX* state—the state of the lone pair of electrons of the impurity atom—loses its antibonding character to a greater extent in II–VI:III and lies deeper in the energy gap, compared with III–V:IV. This accounts for the spontaneous formation of *DX* centers in II–VI:III crystals, in contrast to III–V:IV compounds in which such a reconstruction, as a rule, requires some additional external influence (see above).

Table 1. Electronic charge distribution among valence orbitals of GaAs, GaAs:Si, and GaAs:As crystals (AB_4^{3q-} clusters, $q = 0.4e$) [8]

Crystal	Γ	–*E*, Ry	q_A	q_B	q_{II}
GaAs	$4a_1$	0.129			
	$1t_1$	0.303	0.1	55	38
	$3t_2$	0.323	6.1	59	32
	$1e$	0.364	0.6	46	47
	$2t_2$	0.438	13	40	40
	$2a_1$	0.716	40	35	22
	$1t_2$	1.011	2.4	75	21
	$1a_1$	1.094	16	56	26
GaAs:Si	$4a_1$	0.122			
	$3a_1$	0.156	13	20	48
	$1t_1$	0.319	0.2	59	36
	$3t_2$	0.363	4.8	54	35
	$1e$	0.389	1.2	49	45
	$2t_2$	0.488	19	39	37
	$2a_1$	0.795	36	40	19
	$1t_2$	1.031	3.4	72	23
	$1a_1$	1.136	23	48	28
GaAs:As	$4a_1$	0.124			
	$3a_1$	0.202	13	45	32
	$1t_1$	0.298	0.2	58	37
	$3t_2$	0.349	4.1	52	39
	$1e$	0.369	1.2	48	45
	$2t_2$	0.519	30	34	32
	$2a_1$	0.881	26	54	17
	$1t_2$	1.015	4.9	70	23
	$1a_1$	1.212	48	28	24

Note: Γ is irreducible representation; *E* the single-electron energy; q_A, q_B, and q_{II} the fractions of the orbital charge (%) localized inside the central atom's sphere, inside the ligand atomic spheres, and in the interatomic region, respectively. The fraction of charge in the outer region $q_{III} = 1 - q_A - q_B - q_{II}$.

The noticeable presence of the orbital charge within the atomic spheres of different atoms (q_A, q_B) and in the interatomic region (q_{II}) indicates a covalent bonding between these atoms, effected by the given molecular orbital; in the case when one of the above conditions is not satisfied, the orbital has atomic (ionic) nature.

For the GaAs crystal, orbital $4a_1$ corresponds to the bottom of the conduction band, and orbital $1t_1$, to the top of the valence band.

4. CATIONIC DONOR CENTERS IN CdF_2 CRYSTAL

The described mechanism of formation of cationic *DX* centers is largely preserved in the ionic semiconductor CdF_2 doped with gallium and indium, which belong to a Subgroup of Group III (the boron Subgroup). This crystal possesses a fluorite structure in which the cation has an eightfold cubic coordination, and the anion, a fourfold tetrahedral coordination. Doping of CdF_2 with the mentioned atoms markedly enhances the covalent component of the chemical bond (Table 2, orbitals $1a_{1g}$, $1t_{1u}$) [14].

The capture of an additional electron by the CdF_2:M defect (M = Ga, In) into the $2a_{1g}$ state (comparatively deep a_{1g} state of valence *s* electrons of ligands is not given in Table 2) leads, as it also does in the III–V:IV and II–VI:III crystals considered above, to formation of the *DX* center. The stability of the CdF_2:M$^-$ defect is

Table 2. Electronic charge distribution among valence orbitals of CdF_2 and CdF_2:Ga crystals (AB_4^{3q-} clusters) [14]

Crystal	Γ	$-E$, Ry	q_A	q_B	q_{II}
CdF_2	$2a_{1g}$	0.056			
	$3t_{2g}$	0.372	9.4	80	6.0
	$1e_u$	0.379	0.0	90	9.7
	$1a_{2u}$	0.391	1.1	87	6.2
	$1t_{1g}$	0.391	0.3	88	11
	$2t_{1u}$	0.414	0.8	83	12
	$2t_{2g}$	0.436	3.3	81	15
	$1t_{2u}$	0.468	0.2	79	18
	$2e_g$	0.478	6.6	71	19
	$1t_{1u}$	0.482	3.4	78	16
	$1a_{1g}$	0.536	11.5	70	16
	$1e_g$ (4*d* Cd)	0.707	90.9	3.7	5.3
	$1t_{2g}$ (4*d* Cd)	0.717	86.8	9.3	3.7
CdF_2:Ga	$3a_{1g}$	0.028			
	$2a_{1g}$	0.138	36	30	13
	$1e_u$	0.400	0.0	90	9.6
	$1a_{2u}$	0.410	1.0	88	6.1
	$1t_{1g}$	0.412	0.4	88	11
	$3t_{2g}$	0.420	0.9	86	8.4
	$2t_{1u}$	0.436	0.8	83	12
	$2t_{2g}$	0.472	1.0	84	15
	$1t_{2u}$	0.487	0.2	80	18
	$2e_g$	0.513	0.6	75	22
	$1t_{1u}$	0.516	6.0	76	16
	$1a_{1g}$	0.630	30	52	17
	$1t_{2g}$ (3*d* Ga)	1.315	99.1	0.6	0.3
	$1e_g$ (3*d* Ga)	1.316	99.5	0.0	0.5

Note: Designations are the same as in Table 1. Orbital $2a_{1g}$ in the CdF_2 crystal corresponds to the bottom of the conduction band, and orbital $3t_{2g}$, to the top of the valence band.

also disrupted by the filling of the donor $2a_{1g}$ level and the loss of the bonding character of three states with a_{1g} symmetry. As a result, the impurity atom passes into the univalent state.

The specificity of the CdF_2:M centers is manifested in the character of their reconstruction. Localization of an excess pair of electrons—the lone pair of the impurity atom—on a single bond is impossible in the fluorite crystal: the cubic coordination of the central atom rules out any possibility of it being shifted along the threefold axis, and the alternative shift of the ligand, F^- ion, toward the center of a cube composed of the same ions is clearly unfavorable energetically. If account is taken of the poorly pronounced directional nature of bonds in CdF_2:M (relatively low level of covalence), the possibility that the cation is shifted along the fourfold axis, and the fact that a single electron of the central atom is involved in bonding with four ligands, then it is natural to assume that formation of a lone pair on the cation leads to the rupture of its bonds with the ligands lying on a face of the cube and to a shift of the cation along the mentioned axis toward the nearest interstitial site (Fig. 2) [14]. The thus reconstructed center will have a tetragonal symmetry C_{4v}.

It is this structure of the *DX* center that was yielded by the first-principles calculation [15]. This calculation also indicates the importance of *d–d* interactions between the impurity and cations in the formation of *DX* centers in CdF_2. It is for this reason that the *DX* centers are formed in this crystal from boron-subgroup atoms, beginning with Ga. The formation of these centers is also confirmed experimentally by positron spectroscopy, which revealed an open-volume defect in CdF_2:Ga and CdF_2:In crystals [16].

Doping of CdF_2 with Group-III transition metals (Sc, Y, La) enhances the ionic character of the chemical bond and thereby makes impossible any essential distortion of the crystal lattice, which invariably accompanies the formation of *DX* centers [14].

5. ANTISITE DEFECTS IN III–V CRYSTALS

The considered features of how the reconstruction of cationic donor defects occurs give insight into the specificity of the reconstruction of antisite defects in III–V crystals. Anionic antisite defects, a typical example of which is $GaAs:As_{Ga}$, are deep double-donor centers. When such a defect is formed, the electronic structure of the perfect GaAs crystals is modified rather strongly (Table 1) [7]. Here, particular emphasis should be placed on the virtually nonbonding overall character of the three states with a_1 symmetry. For the *DX* centers in III–V:IV and II–VI:III crystals this effect appears upon capture of an additional electron, whereas for the antisite defect, it occurs even in the neutral state. Similarly to the case of the *DX* centers considered above, two variants of relaxation are, in principle, possible for the antisite defect, yielding a relatively weakly bound tetrahedral structure or reconstructed trigonal structure of C_{3v} symmetry. The latter is determined by the nature of virtually the only bonding orbital $2t_2$ and also by the possibility of transition of the As atom into a trivalent state (with two 4*s* electrons of As forming its lone pair). This structure seems to be preferable for the ground state from the standpoint of interatomic interactions.

The results obtained in the crystal approach are not the same for different antisite defects: a trigonal symmetry of the ground state has been obtained for $GaAs:As_{Ga}$ [4, 17] and a trigonal C_{3v} symmetry for antisite defects in nitrides BN, AlN, and GaN [18–20]. A specific feature of how the latter appears in the reconstruction of $AlN:N_{Al}$ and $GaN:N_{Ga}$ centers is the increased multiplicity of bonding of an impurity atom

N with one of its ligands (N), in contrast to the commonly occurring rupture of this bond in $BN:N_B$. The appearance of such a structure (in $BN:N_B$ this is hindered by the exceedingly small interatomic distance) is due to the marked energy gain in formation of multiple bonds between two N atoms and does not contradict the approach to reconstruction of metastable centers, which is developed here.

The above-mentioned discrepancies between the calculated structures of antisite defects are presumably due to the small difference between the total energies of the tetrahedral and trigonal defects, which, on the one hand, makes the defect structure sensitive to the nature of a crystal, and, on the other, hinders a researcher from obtaining unambiguous theoretical results. Unfortunately, experimental investigations give no way of solving the problem of the structure of the antisite defect either. For example, for the best studied defect $GaAs:As_{Ga}$, early results [21] indicate a tetrahedral symmetry of the ground state, whereas a recent study [22] points to a trigonal structure of this defect.

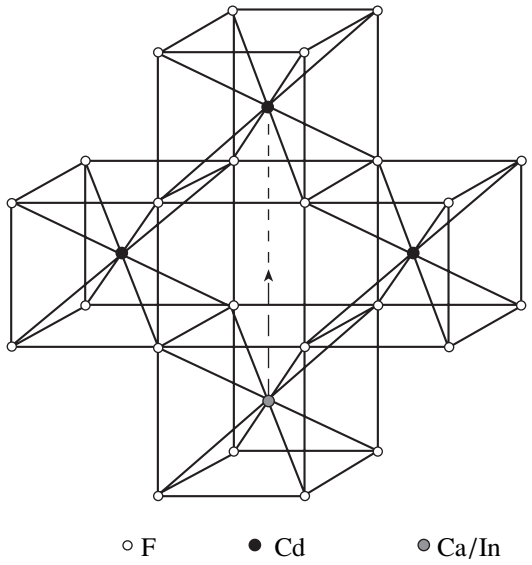

Fig. 2. Reconstruction of CdF_2:M (M = Ga, In) impurity center.

6. ANIONIC DONOR CENTERS IN II–VI AND III–V CRYSTALS

The process of formation of *DX* centers on the basis of anionic donor defects II–VI:VII is largely similar to that considered above for cationic centers: the capture of an additional electron disrupts the stability of the defect because of the loss of the overall bonding nature by the three states with a_1 symmetry; in this, as in the preceding case, an orbital with t_2 symmetry is the main bonding orbital of the negatively charged tetrahedral center $II–VI:VII^-$ [10]. The only difference consists in the somewhat broader range of possibilities for reconstruction of this defect.

The excess pair of valence electrons of the impurity center (for the sake of definiteness, only the ZnSe:Cl crystal will be considered further, possessing 10 valence electrons similarly to other metastable defects in II–VI and III–V crystals) cannot be localized on the doping Cl atom, which is negatively charged even without this pair. As a result, the mentioned pair will reside on one or two ligands (Zn ions), forming in the latter case a covalent bond between the ligands. The conventional trigonal reconstruction C_{3v} occurs in the first case (Fig. 1b) and the orthorhombic C_{2v}, in the second (Fig. 1c). In the latter case, the Cl atom forms bonds with two ligands, having captured a valence electron belonging to them, and the four remaining valence electrons of the Cl atom form two unshared pairs on this atom.

Thus, the possibility of localization of the excess pair of electrons on one or two ligands gives rise to two variants of reconstruction of the anionic donor center II–VI:VII, in contrast to the only possible trigonal variant for cationic centers.

Results of crystal calculations [23] confirm the existence of two variants of reconstruction of the II–VI:VII center. In addition, the possibility is noted of the existence of one more kind of trigonal transformation (C_{3v}) in which all four bonds of the impurity atom with ligands are preserved, one of these bonds being, however, strongly modified. From the cluster standpoint, such a structure may be formed if the excess pair of electrons is localized in a state constituted by three antibonding orbitals of the impurity atom or one of its ligands [10].

Anionic *DX* centers are formed this way also in III–V:VI crystals [7, 24]. As for the way in which a separate bond in a crystal is filled with electrons of the cation and anion (see above), trigonal reconstruction seems to be more probable for III–V:VI centers, and orthorhombic, for II–VI:VII defects [7].

It should be noted that for neutral Si:VI centers, whose reconstruction mechanism is identical with that considered above for negatively charged $II–VI:VII^-$ and $III–V:VI^-$ defects, the probability of orthorhombic transformation is predominant [9].

7. ACCEPTOR CENTERS IN II–VI AND III–V CRYSTALS

The mechanism of reconstruction of anionic acceptor centers II–VI:V markedly differs from that for donor defects. For the significant reconstruction of II–VI:V centers to occur, the following condition must be satisfied: the electronegativity of the impurity atom must not noticeably exceed the electronegativity of the anion [25]. In this case, the reconstruction of acceptor centers will be determined by the extent to which the electronic structure of the crystal is modified by doping and will occur, in most cases, with the number of electrons of the defect remaining unchanged [25, 26]. The

Table 3. Electronic charge distribution among valence orbitals of PbTe and PbTe:Ga crystals (AB_6^{5q-} clusters, $q = 0.05e$) [29]

Crystal	Γ	$-E$, Ry	q_A	q_B	q_{II}
PbTe	$4t_{1u}$	0.133			
	$3a_{1g}$	0.359	18	65	16
	$3e_g$	0.431	3.1	77	16
	$1t_{1g}$	0.432	0.4	75	24
	$3t_{1u}$	0.446	2.3	70	25
	$1t_{2u}$	0.449	0.2	71	27
	$2t_{2g}$	0.485	0.5	64	34
	$2t_{1u}$	0.541	19	52	26
	$2a_{1g}$	0.827	61	24	14
	$2e_g$ (5*s* Te)	1.050	0.5	88	10
	$1t_{1u}$ (5*s* Te)	1.061	1.3	86	11
	$1a_{1g}$ (5*s* Te)	1.095	10	74.5	15
	$1t_{2g}$ (5*d* Pb)	1.912	99.5	0.0	0.5
	$1e_g$ (5*d* Pb)	1.913	99.5	0.1	0.4
PbTe:Ga	$4a_{1g}$	0.094			
	$3a_{1g}$	0.358	19	64	15
	$1t_{1g}$	0.413	0.3	76	24
	$3e_g$	0.414	3.0	77	16
	$3t_{1u}$	0.425	2.8	71	24
	$1t_{2u}$	0.430	0.1	71	27
	$2t_{2g}$	0.466	0.5	64	33
	$2t_{1u}$	0.501	14	57	26
	$2a_{1g}$	0.764	68	19	13
	$2e_g$ (5*s* Te)	1.035	0.5	89	10
	$1t_{1u}$ (5*s* Te)	1.043	1.0	87	11
	$1a_{1g}$ (5*s* Te)	1.067	6.1	80	13
	$1t_{2g}$ (3*d* Ga)	1.553	99.9	0.0	0.1
	$1e_g$ (3*d* Ga)	1.554	99.8	0.1	0.1

Note: Designations are the same as in Tables 1, 2. Orbital $4t_{1u}$ in the PbTe crystal corresponds to the bottom of the conduction band, and orbital $3a_{1g}$, to the top of the valence band.

trivalence of the Group-V atom and the localization of the vacancy on the bond of the impurity atom with one of the ligands lead to a trigonal C_{3v} structure of the reconstructed center. Such a reconstruction occurs, in particular, in ZnSe:P.

If the electronegativity of the impurity atom greatly exceeds that of the anion, then the vacancy on the acceptor level is occupied by an electron from the second coordination shell, with the level related to this center remaining shallow [25]. In particular, such a situation is observed in ZnTe:N and ZnSe:N crystals. In some cases (ZnSe:N), more complex centers, leading, in turn, to self-compensation of a sample, are formed on the basis of acceptor centers, interstitial N atoms, and intrinsic defects of the crystal [27, 28].

A similar situation is observed for acceptor III–V:IV centers [7]. The only difference from the preceding case of II–VI:V consists in the stability of the tetrahedral structure of the defect (this structure is characteristic of a negatively charged Group-IV atom) even for impurity atoms less electronegative than the anion. Under these conditions, the effect of the anion consists only in the modification of the chemical bonding of the center and the possible appearance, depending on the extent of this change, of a relatively deep acceptor state.

In the reconstruction of cationic acceptor centers III–V:II and II–VI:I, the electron vacancy is, in most cases, localized on a single bond and the defects are reconstructed in accordance with the trigonal symmetry C_{3v}.

8. CATIONIC CENTERS IN IV–VI CRYSTALS

Up to this point we considered donor and acceptor impurity centers in crystals whose interatomic bonds are two-center. The reconstruction of metastable centers in crystals with triple-center bonds—IV–VI:III defects (PbTe:Ga)—occurs in quite a different way.

The chemical bonding in narrow-gap IV–VI crystals with the NaCl structure is characterized by a substantial covalent component (Table 3, orbital $2t_{1u}$).

The contribution from three states with a_{1g} symmetry to the binding energy of the center is rather limited: the states are completely filled and the contribution may be different from zero only because of an admixture of excited states of the interacting atoms.

In doping a IV–VI crystal with Group-III atoms, the $3a_{1g}$ level is occupied by only a single electron (Table 3). This level largely depends on the doping atom and may lie in the band gap or in an allowed band in its vicinity. This level is capable of not only readily accepting, but also readily donating an electron, i.e., it is amphoteric. If this level is regarded as the donor level, then the appearance on it of an additional, second antibonding electron impairs the stability of the impurity center. On the other hand, capture of an electron by the acceptor state makes the electronic structure of the impurity center closer to that of the perfect crystal and improves the stability of the defect. A similar situation takes place when this level loses an electron.

The above contradiction can be resolved by the triple-center nature of the chemical bond in IV–VI (high lattice polarizability) [29]. This circumstance determines the possibility of a pronounced, fully symmetric deformation of the IV–VI:III charged center: in the presence of a negative charge, the distance between the central atom and the ligands increases and that between the ligands and the next-nearest neighbors decreases, with the changes being the opposite for a positively charged center (Fig. 3). A deformation of this kind is also favored by the absence of interstitial sites in the

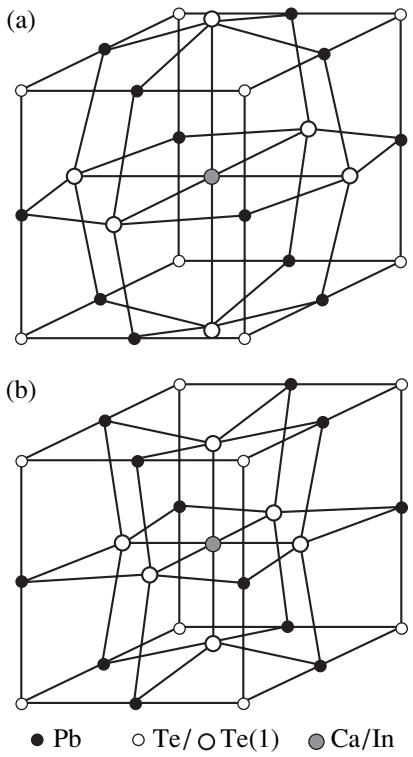

Fig. 3. Reconstruction of PbTe:III impurity center charged (a) negatively and (b) positively. Te(1) are atoms of the first coordination octahedron (first coordination sphere). Atoms of the second coordination octahedron (fourth coordination shell) are not shown.

NaCl structure. Disturbances of the symmetry of the defect may occur in its neutral state. Indeed, if it is assumed, on the basis of the distribution of two electrons of the negatively charged center among the six bonds with the ligands (see above), that a single donor electron is distributed among three bonds, then it is conceivable that the impurity atom is shifted away from the inversion center. Experimental studies confirm both this assumption and the absence of noncentrosymmetric distortions in the negatively charged center [30].

9. CONCLUSION

In crystals with two-center interatomic bonds, the relative stability of donor centers, both cationic and anionic, is disturbed by the capture of an additional electron: the system of three levels corresponding to a fully symmetric representation of the point group of the defect ceases to be a bonding one. A concrete structure of the appearing *DX* center is defined by the localization of an excess (with respect to chemical bonding) pair of electrons (donor and additional ones).

In the cationic *DX* centers, this pair is localized on the impurity atom, lowering its valence. In the process of such a reconstruction, the minimum possible (from the standpoint of structural features of the perfect crystal) number of bonds of the impurity atom with the ligands is ruptured: one in III–V and II–VI crystals and four in CdF_2. In accordance with this circumstance, the symmetry of the *DX* center is trigonal (C_{3v}) in the first case and tetragonal (C_{4v}) in the second.

In the anionic *DX* centers, the impurity atom captures the number of electrons it needs to form a closed structure, whereas the excess electron pair of the defect is localized on one or two ligands, yielding, respectively, a trigonal (C_{3v}) or orthorhombic (C_{2v}) symmetry of the reconstructed center. Presumably, the localization of this pair on an orbital constructed from three antibonding orbitals of the impurity atom or one of its ligands (center symmetry C_{3v}) is also possible.

Reconstruction of anionic acceptor centers (occurring in the case when the electronegativity of the impurity atom does not greatly exceed that of the anion) is determined by changes in the electronic structure of the perfect crystal upon doping. Localization of the electron vacancy on a single bond is responsible for the trigonal C_{3v} structure of such a center.

Of fundamental importance in all cases of reconstruction of donor and acceptor centers is the covalent component of the chemical bonding of the defect; reconstruction is also greatly promoted by the presence of interstitial sites in the crystal lattice.

In crystals with triple-center bonds (IV–VI:III), reconstruction of metastable centers occurs in a different way: a negatively or positively charged defect undergoes a fully symmetric reconstruction because of the amphoteric nature of the impurity state and the mentioned specificity of the bond characteristic of a perfect crystal, whereas in the neutral state, the symmetry is lowered.

REFERENCES

1. R. A. Linke, I. Redmond, T. Thio, and D. J. Chadi, J. Appl. Phys. **83**, 661 (1998).
2. A. I. Ryskin, A. S. Shcheulin, E. V. Miloglyadov, *et al.*, J. Appl. Phys. **83**, 2215 (1998).
3. R. A. Linke, A. S. Shcheulin, A. I. Ryskin, *et al.*, Appl. Phys. B: Lasers Opt. **B72** (6), 677 (2001).
4. J. Dabrowski and M. Scheffler, Mater. Sci. Forum **83–87**, 735 (1992).
5. D. J. Chadi and K. J. Chang, Phys. Rev. B **39**, 10063 (1989).
6. P. M. Mooney, J. Appl. Phys. **67**, R1 (1990).
7. D. E. Onopko and A. I. Ryskin, Zh. Strukt. Khim. **41**, 813 (2000).
8. D. E. Onopko, N. T. Bagraev, and A. I. Ryskin, Fiz. Tekh. Poluprovodn. (St. Petersburg) **31**, 1310 (1997) [Semiconductors **31**, 1128 (1997)].
9. D. E. Onopko, N. T. Bagraev, and A. I. Ryskin, Fiz. Tekh. Poluprovodn. (St. Petersburg) **30**, 142 (1996) [Semiconductors **30**, 82 (1996)].
10. D. E. Onopko and A. I. Ryskin, Fiz. Tverd. Tela (St. Petersburg) **38**, 689 (1996) [Phys. Solid State **38**, 382 (1996)].

11. P. W. Anderson, Phys. Rev. Lett. **34**, 953 (1975).
12. D. J. Chadi, Phys. Rev. Lett. **72**, 534 (1994).
13. C. H. Park and D. J. Chadi, Phys. Rev. B **52**, 11884 (1995).
14. D. E. Onopko and A. I. Ryskin, Phys. Rev. B **61**, 12952 (2000).
15. C. H. Park and D. J. Chadi, Phys. Rev. Lett. **82**, 113 (1999).
16. J. Nissila, K. Saarinen, P. Hautojarvi, *et al.*, Phys. Rev. Lett. **82**, 3276 (1999).
17. D. J. Chadi and K. J. Chang, Phys. Rev. Lett. **60**, 2187 (1988).
18. J. L. P. Castineira, J. R. Leite, L. M. R. Scolfaro, *et al.*, in *Proceedings of the 23rd International Conference on Physics of Semiconductors*, Ed. by M. Scheffler and R. Zimmermann (World Scientific, Singapore, 1996), Vol. 4, p. 2901.
19. T. Mattila, A. P. Seitsonen, and R. M. Nieminen, Phys. Rev. B **54**, 1474 (1996).
20. I. Gorczyca, A. Svane, and N. E. Christensen, Solid State Commun. **101**, 747 (1997).
21. M. Kaminska, M. Skowronski, and W. Kuszko, Phys. Rev. Lett. **55**, 2204 (1985).
22. N. T. Bagraev, J. Phys. I **1**, 1511 (1991).
23. D. J. Chadi and C. H. Park, Mater. Sci. Forum **196–201**, 285 (1995).
24. C. H. Park and D. J. Chadi, Phys. Rev. B **54**, R14246 (1996).
25. D. E. Onopko and A. I. Ryskin, Opt. Spektrosk. **84**, 56 (1998) [Opt. Spectrosc. **84**, 49 (1998)].
26. D. J. Chadi, Appl. Phys. Lett. **59**, 3589 (1991).
27. C. H. Park and D. J. Chadi, Phys. Rev. Lett. **75**, 1134 (1995).
28. S. Pöykkö, M. J. Puska, and R. M. Nieminen, Phys. Rev. B **57**, 12174 (1998).
29. D. E. Onopko and A. I. Ryskin, Fiz. Tekh. Poluprovodn. (St. Petersburg) **34**, 270 (2000) [Semiconductors **34**, 264 (2000)].
30. D. R. Khokhlov and B. A. Volkov, in *Proceedings of the 23rd International Conference on Physics of Semiconductors*, Ed. by M. Scheffler and R. Zimmermann (World Scientific, Singapore, 1996), Vol. 4, p. 294.

Translated by M. Tagirdzhanov

Semiconductors, Vol. 35, No. 11, 2001, pp. 1231–1241. Translated from Fizika i Tekhnika Poluprovodnikov, Vol. 35, No. 11, 2001, pp. 1289–1298.

ATOMIC STRUCTURE AND NONELECTRONIC PROPERTIES OF SEMICONDUCTORS

A Model of High- and Low-Temperature Phosphorus Diffusion in Silicon by a Dual Pair Mechanism

O. V. Aleksandrov

St. Petersburg State Electrotechnical University, St. Petersburg, 197376 Russia

e-mail: aleks_ov@mailbox.alkor.ru

Submitted March 19, 2001; accepted for publication April 23, 2001

Abstract—A model of phosphorus diffusion in silicon was developed on the basis of a dual pair mechanism; according to this model, the contribution of the impurity–vacancy (P*V*) and impurity–self-interstitial (P*I*) pairs to diffusion is accounted for directly in terms of the phosphorus diffusion coefficient. A violation of thermodynamic equilibrium in relation to native point defects occurs as a result of diffusion of the P*I* neutral pairs. At the high-temperature diffusion stage, the phosphorus diffusion is described by a single diffusion equation with the diffusion coefficient dependent on both the local and surface phosphorus concentrations; whereas at the next (occurring at lower temperatures) stage, the phosphorus diffusion is described by two diffusion equations for the total concentrations of the components containing phosphorus and self-interstitials. An anomalously high rate of the low-temperature diffusion is ensured by excess self-interstitials accumulated in the doped layer during the preceding high-temperature diffusion. The model makes it possible to quantitatively account for the special features of the phosphorus diffusion in a wide range of the surface concentrations at both the high (900–1100°C) and lower (500–700°C) temperatures. © *2001 MAIK "Nauka/Interperiodica".*

1. INTRODUCTION

Phosphorus diffusion in silicon, if the P surface concentration is high and exceeds the intrinsic charge-carrier concentration, has certain special features [1, 2]; in order to account for the latter, a number of models based on various diffusion mechanisms have been suggested (see reviews [3, 4]). It has been assumed in earlier models [5–9] that phosphorus diffuses solely as phosphorus–vacancy (P*V*) pairs in various charge states. A model for phosphorus diffusion via two channels has also been suggested [3, 10, 11]: slow diffusion proceeds over vacancies (the *E*-center mechanism), whereas fast diffusion occurs via interstices. According to the concepts based on more recent studies (see review [12]), diffusion of substitutional impurities in silicon occurs with the involvement of native point defects of both types; the latter include not only vacancies but also self-interstitials. As a result, the mobile impurity–vacancy (P*V*) and impurity–interstitial (P*I*) pairs are formed. A number of models for phosphorus diffusion in silicon have been suggested on the basis of the above dual pair mechanism [13–23]. In the quasi-equilibrium models [13–17], additional simplifying assumptions have been used, in addition to the assumption that there is a local equilibrium between the diffusing components. In other models [13, 14], the concentration of the P*I* pairs has been assumed to be much lower than that of self-interstitials. The models suggested in [15–17] relied on the condition that the concentrations of the native point defects and pairs are quasi-steady, which limits the applicability of these models. In nonequilibrium pair models [18–23], the rates of the direct and reverse reactions of the recharging of native point defects, of the formation and dissociation of pairs composed of ionized phosphorus atoms and native point defects in various charge states, and of the recombination of vacancies and self-interstitials either directly with each other or in different pairs were taken into account. The problem of determining the phosphorus concentration profile is reduced to the simultaneous solution of several diffusion–kinetics equations with a large number of parameters; various attempts to reduce this number have failed (the number of the parameters remained as large 134 [23]). Furthermore, the similarly denoted parameters differ from each other in dissimilar models, and they also differ often from the well-known experimental data (this is true, for example, for the diffusion coefficients and binding energies of the P*V* pairs). As a rule, the results of the calculations [13–23] are restricted to obtaining the characteristic special features in the phosphorus profiles for certain fixed conditions of performing the diffusion, which gives no way of assessing the adequacy of the models in a wide range of varying the conditions of diffusion.

A special feature of phosphorus diffusion consists in the emergence of an additional inflection and tail in the P concentration profile at low P concentrations after heat treatment of the diffusion layer at comparatively low temperatures of 500–700°C [24–26]. In bipolar transistors, this leads to a decrease in the punch-through voltage owing to a decrease in the base thickness [27]. The displacement of the *p–n* junction depth during this low-temperature diffusion (LTD) stage is

much higher than that expected on the basis of the extrapolation of the high-temperature values of the phosphorus diffusion coefficient and depends not only on the LTD temperature but also on the temperature of the preceding high-temperature diffusion (HTD) stage [26]. As the LTD duration increases, a deviation of the *p–n*-junction displacement kinetics from the square-root law is observed; this deviation is caused by a decrease in the diffusion rate [26]. In a heavily doped region of the concentration distribution, a decrease in the charge-carrier concentration related to the decomposition of the phosphorus solid solution in silicon is observed [24, 26, 28]. Shwettman and Kendall [24, 25] related the origin of the inflection and tail in the P concentration profile to the fast *E*-center diffusion. Panteleev [10] related the formation of the profile tail to the two-channel phosphorus diffusion: the slow diffusion via the *E* centers and the fast diffusion over the interstices; the concentration corresponding to the inflection point was related to the substitutional phosphorus solubility. Prokhorov *et al*. [29] believe that the tail is caused by enhanced phosphorus diffusion via vacancies that migrate from the crystal bulk to the SiP precipitates that grow during the LTD. However, the data, showing that the concentrations corresponding to the inflection points for LTD and HTD feature the same temperature dependences [25], apparently indicate that these inflection points have the same origin. An attempt to extrapolate the implications of the Fair–Tsai model [5, 6] to the low-temperature region [30] yields results that deviate significantly from experimental data—this deviation increasing with decreasing LTD temperature. The authors of other quantitative models of phosphorus diffusion in silicon [13–23] restricted themselves to the consideration of only the high-temperature stage.

The objective of this study was to use the dual pair mechanism as the basis for the development of a fairly simple quantitative model that describes the special features of phosphorus diffusion in silicon at both high and comparatively low temperatures. In contrast to other pair models, the contribution of the P*V* and P*I* pairs in various charge states to the diffusion is accounted for directly in terms of the phosphorus diffusion coefficient; it is also assumed that the diffusion of neutral P*I* pairs alone causes the violation of thermodynamic equilibrium with respect to the native point defects.

2. STATEMENTS AND EQUATIONS OF THE MODEL

We assume that phosphorus diffuses in silicon according to the dual pair mechanism with the participation of vacancies V^r and self-interstitials I^s in the possible charge states r and s (both r and s can be equal to 0, –1, and –2); the ionized phosphorus atoms and the above native defects form the mobile impurity–vacancy (P^+V^r) and impurity–self-interstitial (P^+I^s) pairs in the charge states of $r + 1$ and $s + 1$, respectively. If there is a gradient of phosphorus concentration, concentration gradients of the impurity–defect pairs form in the layer where the diffusion occurs; as a result, these pairs can diffuse independently. It can be easily shown that, if the condition for local equilibrium between the charged and neutral pairs and the condition for local electroneutrality are satisfied, the diffusion fluxes of negatively charged pairs are completely compensated by the corresponding drift fluxes; i.e., the negatively charged pairs are kept within the doped layer by an internal electric field. The binding energy of positively charged pairs is lower than those of the negatively charged and neutral pairs; therefore, the positively charged pairs dissociate relatively fast. In contrast to the impurity–vacancy pairs, the migration of which in a diamond-like structure involves their partial dissociation, the impurity–interstitial pairs can migrate without dissociation [1, 3]. Hence, it follows that, among all the impurity–defect pairs, only the neutral PI^0 (P^+I^-) pairs can diffuse into the silicon bulk. The subsequent dissociation of the neutral pairs results in the deviation of concentrations of native point defects from the thermodynamically equilibrium values.

A variation in the concentrations of native point defects results in a change in the phosphorus diffusion coefficient D_P, which, for the dual pair mechanism, is the sum of the diffusion coefficients via the P*V* and P*I* pairs; i.e.,

$$D_\mathrm{P} = D_{\mathrm{P}V} + D_{\mathrm{P}I}.$$

If the concentrations of native point defects deviate from the thermodynamically equilibrium values, the expression for the phosphorus diffusion coefficient, with allowance made for an internal electric field, can be written as

$$D_\mathrm{P} = (D^*_{\mathrm{P}V}a_V + D^*_{\mathrm{P}I}a_I)h. \quad (1)$$

Here, $D^*_{\mathrm{P}V}$ and $D^*_{\mathrm{P}I}$ are the phosphorus diffusion coefficients with the involvement of the P*V* and P*I* pairs, respectively (under the equilibrium conditions with respect to the native point defects); and a_V and a_I are the degrees of supersaturation (or undersaturation) with respect to vacancies and self-interstitials, respectively. We have

$$a_V = [V]/[V_\mathrm{eq}], \quad a_I = [I]/[I_\mathrm{eq}],$$

where $[V_\mathrm{eq}]$ and $[I_\mathrm{eq}]$ are the thermodynamically equilibrium concentrations of vacancies and self-interstitials, and h is a factor of the enhancement of ionized phosphorus diffusion by an internal electric field. Using the local-electroneutrality approximation (see, for example, [31]), we obtain

$$h = 1 + \frac{[\mathrm{P}^+]}{\sqrt{[\mathrm{P}^+]^2 + 4n_i^2}} = \frac{2n}{2n - [\mathrm{P}^+]},$$

where $[P^+]$ is the concentration of ionized phosphorus atoms, n is the electron concentration, and n_i is the intrinsic concentration of the charge carriers. If the condition for local equilibrium between the vacancies and self-interstitials is satisfied, we have $[I][V] = [I_{eq}][V_{eq}]$, so that $a_V = 1/a_I$.

The contribution of various charge states and pairs to the diffusion can be taken into account by introducing the partial diffusion coefficients for phosphorus and the fractions of the vacancy- and interstitial-related diffusion components; i.e.,

$$D^*_{PV} = f^0_V D^0 + f^-_V D^- + f^{2-}_V D^{2-}, \quad (2)$$

$$D^*_{PI} = f^0_I D^0 + f^-_I D^- + f^{2-}_I D^{2-}, \quad (3)$$

where D^0, D^-, and D^{2-} are the partial coefficients for phosphorus diffusion with involvement of the native point defects in the corresponding charge states; f^0_V, f^-_V, and f^{2-}_V are the fractions of diffusion components with vacancies in the corresponding involved charge states (or for diffusion as the PV^+, PV^0, and PV^- pairs); and f^0_I, f^-_I, and f^{2-}_I are the fractions of the diffusion components with the self-interstitials in the corresponding involved charge states (or for diffusion as the PI^+, PI^0, and PI^- pairs). Obviously,

$$f^0_V + f^0_I = 1, \quad f^-_V + f^-_I = 1 \quad \text{and} \quad f^{2-}_V + f^{2-}_I = 1.$$

The concentration of electrically active phosphorus $[P^+]$ in the high-concentration profile region is controlled by the equilibrium process of the cluster formation and is related to the total phosphorus concentration [P] by the expression [32]

$$[P] = [P^+]\left[1 + \sum_m \left(\frac{[P^+]}{N_m}\right)^{m-1}\right], \quad (4)$$

where m is the number of atoms in the clusters ($m \geq 2$), and N_m are the coefficients related to the equilibrium constants for the formation–decomposition reactions of the clusters. According to [32], the atoms of electrically inactive phosphorus occupying the crystal-lattice sites [33] are weakly linked to each other; therefore, we assume that these atoms are also involved in diffusion.

For the diffusion components under consideration (i.e., for the atoms of electrically active and inactive phosphorus, the neutral PI pairs, the negatively charged self-interstitials incorporated into these pairs, and the neutral self-interstitials related to them), a system of diffusion–kinetics equations is written as

$$\frac{\partial [P]}{\partial t} = \frac{\partial}{\partial x}\left(D_P \frac{\partial [P]}{\partial x}\right) - k_{1F}[P^+][I^-] + k_{2F}F, \quad (5)$$

$$\frac{\partial F}{\partial t} = D_F \frac{\partial^2 F}{\partial x^2} + k_{1F}[P^+][I^-] - k_{2F}F, \quad (6)$$

$$\frac{\partial [I^-]}{\partial t} = -k_{1F}[P^+][I^-] + k_{2F}F + k_{1I}[I^0]n - k_{2I}[I^-], \quad (7)$$

$$\frac{\partial [I^0]}{\partial t} = D_I \frac{\partial^2 [I^0]}{\partial x^2} - k_{1I}[I^0]n + k_{2I}[I^-], \quad (8)$$

where t is the diffusion duration; F is the concentration of neutral pairs PI; D_F and D_I are the diffusion coefficients for the neutral PI pairs and neutral self-interstitials, respectively; k_{1F} and k_{2F} are the rate constants for the direct and reverse reactions of formation of neutral pairs PI, respectively; and k_{1I} and k_{2I} are the rate constants for the direct and reverse reaction of recharging of self-interstitials, respectively. It is noteworthy that the diffusion- and drift-related terms are omitted in Eq. (7). The reason for this is that, if the conditions for local equilibrium and for local electroneutrality are satisfied, these terms completely compensate each other. Combining the left- and right-hand sides of Eqs. (5) and (6) and doing the same for Eqs. (6)–(8), we obtain

$$\frac{\partial ([P] + F)}{\partial t} = \frac{\partial}{\partial x}\left(D_P \frac{\partial [P]}{\partial x}\right) + D_F \frac{\partial^2 F}{\partial x^2}, \quad (9)$$

$$\frac{\partial (F + [I^-] + [I^0])}{\partial t} = D_F \frac{\partial^2 F}{\partial x^2} + D_I \frac{\partial^2 [I^0]}{\partial x^2}. \quad (10)$$

The time needed for establishing the quasi-equilibrium distribution of negatively charged defects I^- is controlled by fast electronic processes and is, thus, much shorter than the diffusion time of neutral I^0 defects and PI pairs; therefore, we assume that $\partial[I^-]/\partial t = 0$ in Eq. (10). If the conditions for local equilibrium between the diffusion components are satisfied, we obtain $[I^-] = k_I[I^0]n$, where k_I is the equilibrium constant for the recharging reaction of the self-interstitials. In addition, we have $F = k_F[P^+][I^-]$, where k_F is the equilibrium constant for the formation–dissociation reaction of the neutral PI pairs. In this situation, Eqs. (9) and (10) can be reduced to the typical form of diffusion equations with nonconstant coefficients; i.e.,

$$\frac{\partial [P_F]}{\partial t} = \frac{\partial}{\partial x}\left(D_{PF} \frac{\partial [P_F]}{\partial x}\right), \quad (11)$$

$$\frac{\partial F_I}{\partial t} = \frac{\partial}{\partial x}\left(D_{FI} \frac{\partial F_I}{\partial x}\right), \quad (12)$$

where $[P_F]$ is the total concentration of the components that incorporate phosphorus atoms, $[P_F] = [P] + F$; D_{PF} is the diffusion coefficient of these components,

$$D_{PF} = \frac{D_P[P] + D_F F}{[P_F]}, \quad (13)$$

F_I is the total concentration of the neutral components that incorporate the self-interstitials, $F_I = F + [I^0]$; and D_{FI} is the diffusion coefficient of these components and is given by

$$D_{FI} = \frac{D_F F + D_I[I^0]}{F_I}. \quad (14)$$

Thus, the problem of determining the phosphorus concentration profile is reduced, in the general case, to the simultaneous solution of two diffusion equations (11) and (12) with the diffusion coefficients defined by (13) and (14) and dependent on the concentrations of the components [P], F, and $[I^0]$.

3. THE HIGH-TEMPERATURE DIFFUSION STAGE

3.1. Analysis

If the diffusion process includes only the high-temperature stage (the HTD), the problem can be simplified. For large diffusion coefficients of the neutral PI pairs and self-interstitials ($D_F \gg D_P$ and $D_I \gg D_P$), we have $D_{FI} \gg D_{PF}$, and, in accordance with diffusion equation (12), the distribution of the total concentration of neutral components incorporating self-interstitials may be assumed uniform along the entire phosphorus profile; i.e., we have

$$F_I(x) = F(x) + [I^0](x) \cong F_{IS}, \quad (15)$$

where F_{IS} is the total concentration of the components incorporating the self-interstitials for the highest phosphorus concentration (in the case under consideration, this corresponds to the phosphorus concentration at the surface). We assume that the concentration of neutral self-interstitials at the surface is equal to the thermodynamically equilibrium concentration; i.e., $[I_S^0] = [I_{eq}^0]$. Using the relation for local equilibrium and expression (15), we obtain

$$F_{IS} = (1 + k_{IF}[P_S^+]n_S)[I_{eq}^0], \quad (16)$$

where $[P_S^+]$ and n_S are the surface concentrations of ionized phosphorus and electrons, respectively; and $k_{IF} = k_I k_F$. Using expressions (15) and (16), we obtain the concentration profile of neutral self-interstitials and of the PI pairs as

$$[I^0](x) = \frac{1 + k_{IF}[P_S^+]n_S}{1 + k_{IF}[P^+]n}[I_{eq}^0], \quad (17)$$

$$F(x) = \frac{k_{IF}(1 + k_{IF}[P_S^+]n_S)[P^+]n}{1 + k_{IF}[P^+]n}[I_{eq}^0]. \quad (18)$$

As can be deduced from formulas (17) and (18), the concentrations $[I^0](x)$ and $F(x)$ depend on the coordinate x only in terms of local concentrations of ionized phosphorus and electrons. The same is true for the degree of supersaturation a_I with respect to self-interstitials. Using expression (17), the a_I profile can be given by

$$a_I(x) = \frac{1 + k_{IF}[P_S^+]n_S}{1 + k_{IF}[P^+]n}. \quad (19)$$

For the lightly doped region of the concentration profile (for $[P^+] \ll n_i$), we use formula (19) to determine the degree of supersaturation for self-interstitials as

$$a_{It} = 1 + k_{IF}[P_S^+]n_S. \quad (20)$$

This supersaturation governs the enhancement of phosphorus diffusion in the low-concentration region of the profile tail and, as can be deduced from formula (20), is independent of the local phosphorus concentration.

Thus, if only the high-temperature stage is used in the diffusion process, the problem of calculating the phosphorus concentration profile is reduced to solving diffusion equation (11) with the diffusion coefficient defined by (13). For the low concentration of neutral pairs PI ($F \ll [P]$ and $D_F F \ll D_P[P]$), we have $[P_F] \approx [P]$ and $D_{PF} \approx D_P$ in formula (13); i.e., Eq. (11) transforms into the diffusion equation for phosphorus with the diffusion coefficient defined by expressions (1)–(3), in which $a_I(x)$ is defined by expression (19), and $a_V = 1/a_I$. In this situation, the phosphorus diffusion coefficient depends solely on the local and surface concentrations of electrically active phosphorus.

3.2. Parameters

The parameters of the model for the high-temperature diffusion stage include the following quantities: the partial coefficients of phosphorus diffusion with the involvement of native point defects in different charge states (D^0, D^-, and D^{2-}), the equilibrium constant for the formation reaction of negatively charged self-interstitials (k_I), and the equilibrium constant for the formation reaction of neutral pairs PI (k_F). The partial diffusion coefficients are determined from the well-known expression for the isoconcentration diffusion coefficient of phosphorus in silicon [2, 6, 34]; i.e.,

$$D = D^0 + D^- + D^{2-} = D_i^0 + D_i^-\left(\frac{n}{n_i}\right) + D_i^{2-}\left(\frac{n}{n_i}\right)^2, \quad (21)$$

where D_i^0, D_i^-, and D_i^{2-} are partial inherent coefficients of diffusion with involvement of the native point defects in the neutral state and in the singly and doubly negatively charged states, respectively. For low phosphorus concentrations ($n < n_i$), the first term is prevalent in the right-hand side of (21); this term is related to the diffusion in which neutral native point defects are involved. The proportion of the interstitial component

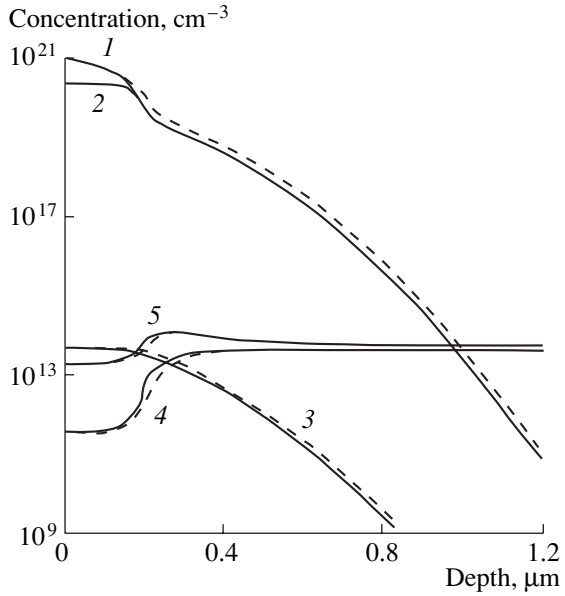

Fig. 1. Variations of the diffusion-component concentrations with depth at T = 900°C for t = 30 min and $[P_S]$ = 10^{21} cm^{-3}: (*1*) is for [P]; (*2*), for $[P^+]$; (*3*), for F; (*4*), for $[I^0]$; and (*5*), for $[I^-]$. The solid lines represent the results of calculations for $a_V = 1/a_I$, and the dashed lines correspond to calculations with $a_V = 1$.

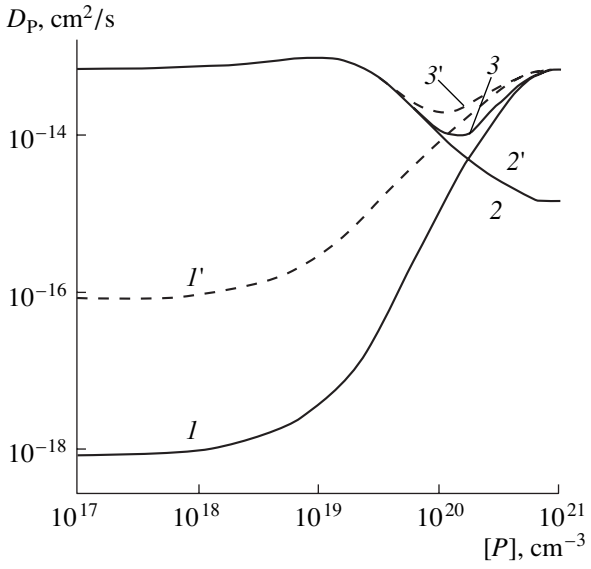

Fig. 2. Concentration dependences of the phosphorus diffusion coefficient at T = 900°C and $[P_S]$ = 10^{21} cm^{-3}: curves *1* and *1*' are for D_{PV}; curves *2* and *2*', for D_{PI}; and curves *3* and *3*', for $D_{PV} + D_{PI}$. The solid lines (*1–3*) represent the results of calculations for $a_V = 1/a_I$, and the dashed lines (*1*'–*3*') correspond to calculations with $a_V = 1$.

in the phosphorus diffusion in the case of low concentration amounts to f_I^0 = 0.93–0.96 [12, 35]; therefore, we assume that f_I^0 = 0.95 and f_V^0 = 0.05. For high phosphorus concentrations ($n > n_i$), the second and third terms in the right-hand side of (21) are dominant; these terms are related to the phosphorus diffusion with the involvement of singly and doubly negatively charged native point defects. There are no direct data available on the quantities f_I and f_V for the case under consideration; however, there are indirect data indicating that the pair–vacancy diffusion mechanism is prevalent in silicon layers doped heavily with phosphorus. These data include, first, the suppression of the oxidation-enhanced diffusion (i.e., diffusion caused by the excess of self-interstitials) as the phosphorus concentration increases [36]. Second, a high substitutional solubility (up to 10^{19} cm^{-3}) of rapidly diffusing metallic impurities (Au, Cu, and Co) has been observed at both high (900–1100°C) [37] and comparatively low (400–700°C) [38] temperatures in the silicon layers doped heavily with phosphorus. Third, the data of Mössbauer spectroscopy indicate that there is a high concentration of vacancies (up to 10^{19} cm^{-3}) related to phosphorus in heavily doped silicon layers [39]. All the above data suggest that $f_V^- \approx f_V^{2-} \approx 1$ and, correspondingly, $f_I^- \approx f_I^{2-} \approx 0$.

The constant k_I depends on the level of the negatively charged self-interstitials in the band gap; i.e.,

$$(k_I)^{-1} = n_I = N_C \exp[-(E_c - E_I)/kT],$$

where N_C is the effective density of states in the conduction band, k is the Boltzmann constant, T is absolute temperature, and $E_c - E_I$ is the position of the level of a negatively charged self-interstitial in reference to the conduction-band bottom ($E_I \approx E_c - 0.4$ eV according to estimates reported by Frank [40]).

There are no available experimental data on the complex-formation constant k_F for the neutral P*I* pairs. We determined this constant by comparing the calculated phosphorus profiles with experimental profiles at various temperatures and phosphorus surface concentrations; thus, $k_F = k_{F0}\exp(E_B/kT)$, where $k_{F0} = 8.2 \times 10^{-28}$ cm^3 and E_B is the binding energy (E_B = 1.65 eV).

3.3. Results of Calculations and Discussion

Diffusion equation (11), with the diffusion coefficients defined by (1)–(3) and the boundary condition for the constancy of the surface concentration $[P_F](0, t) \approx [P_S]$ = const, was solved numerically by the finite-difference method using an implicit scheme. Variations in the concentrations of components ([P], $[P^+]$, F, $[I^-]$, and $[I^0]$) with the depth at a diffusion temperature of 900°C are illustrated in Fig. 1. The concentration $[I^0]$ increases

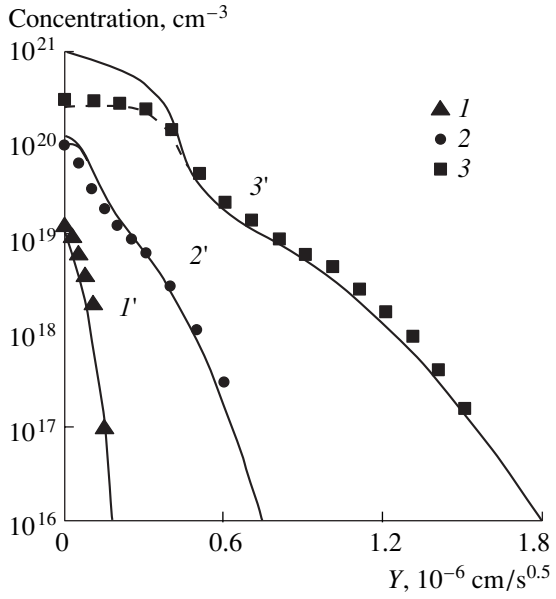

Fig. 3. The concentration profiles for phosphorus and charge carriers for the diffusion temperature of T = 900°C and the surface phosphorus concentrations $[P_S]$ = (*1'*) 1.4×10^{19}, (*2'*) 1.3×10^{20}, and (*3'*) 10^{21} cm^{-3}. The solid lines represent the results of calculations of [P](x), the dashed line corresponds to the calculation of $[P^+](x)$, and symbols *1–3* represent experimental data [7].

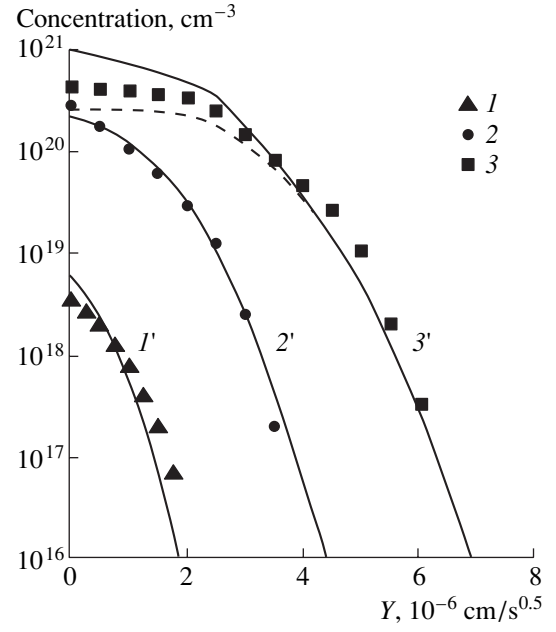

Fig. 4. The concentration profiles for phosphorus and charge carriers for the diffusion temperature of T = 1100°C and the surface phosphorus concentrations $[P_S]$ = (*1'*) 6×10^{18}, (*2'*) 2.3×10^{20}, and (*3'*) 10^{21} cm^{-3}. The solid lines represent the results of calculations of [P](x), the dashed line corresponds to the calculation of $[P^+](x)$, and symbols *1–3* represent the experimental data [7].

at first with depth and then attains a constant level; as a result, the phosphorus diffusion is enhanced in the tail region of the concentration profile owing to the positively charged pairs PI^+. The shape of phosphorus distribution is controlled by the concentration dependence of the coefficient of diffusion via the PV and PI pairs in accordance with expression (1); this dependence is shown in Fig. 2. The plateau in concentration profiles for high surface concentrations is due to a heavy concentration dependence of the pair–vacancy diffusion-coefficient component $D_{PV} \propto n$ or $D_{PV} \propto n^2$ [see (21)]. The transitional inflection region is related to an increase in the role of the pair–interstitial component as the phosphorus and electron concentrations decrease: $D_{PI} \propto [I^0] \propto (n[P^+])^{-1}$ [see (19)]. In the distribution-tail region, $D_{PI} \propto n_S[P_S^+]$ according to expression (21); thus, D_{PI} is independent of both depth and local phosphorus concentration. It is noteworthy that, if the local concentrations of self-interstitials and vacancies are assumed to be unrelated to each other [the dashed lines in Figs. 1 and 2 for $a_V = 1$ in formula (2)], the profiles of the diffusion components, including phosphorus itself, change insignificantly. This result is inconsistent with inferences made in [19, 20], according to which the plateau and inflection in the phosphorus profiles are caused by the active bimolecular recombination of nonequilibrium vacancies and self-interstitials. As the surface phosphorus concentration becomes higher than 5×10^{20} cm^{-3}, the diffusion coefficient ceases to increase with total phosphorus concentration owing to the leveling off of the dependence $[P^+] = f([P])$ as a result of the intensification of the cluster formation in accordance with formula (4). It is noteworthy that $D_F F \ll D_P[P]$ in formula (13); i.e., the direct contribution of the neutral PI pairs to phosphorus diffusion is small, whereas the indirect contribution (due to the emergence of supersaturation of self-interstitials in the low-concentration portion of the profile) is fairly large.

For diffusion with constant surface phosphorus concentration $[P_S]$ = const and for the diffusion coefficient dependent only on the local and surface concentrations, the phosphorus concentration distribution becomes a function of the reduced depth $Y = x/\sqrt{t}$ according to experimental data reported by Yoshida [7]. The role of the surface phosphorus concentration is illustrated in Figs. 3 and 4 for different diffusion temperatures; the solid lines represent the calculated phosphorus concentration profiles, whereas the symbols correspond to experimental data. At the diffusion temperature of 900°C (Fig. 3), an inflection and a tail become distinct in the distributions in the medium-doped and lightly doped regions as the surface phosphorus concentration increases above the intrinsic concentration of charge carriers $[P_S] > n_i \approx 10^{19}$ cm^{-3}; if $[P_S] \gtrsim 10^{20}$ cm^{-3}, a plateau emerges in the heavily doped region, and the total and electrically active phosphorus concentrations

diverge from each other. As the diffusion temperature increases, the inflection and tail become less pronounced and almost cease to exist at 1100°C (Fig. 4). In all the cases, there is satisfactory agreement between the results of calculations and experimental phosphorus profiles measured in [5, 7].

4. THE LOW-TEMPERATURE DIFFUSION STAGE

4.1. Analysis

If diffusion is performed at lower temperatures [the low-temperature diffusion (LTD)] subsequent to high-temperature diffusion (the HTD), the thermodynamically equilibrium concentration of self-interstitials decreases, which is bound to lead to a corresponding decrease in the P*I* pair concentration at the surface. In this situation, the P*I* pairs and the self-interstitials accumulated in the diffusion layer during the previous HTD act as the sources of excess self-interstitials. The problem of calculating the combined diffusion of the components considered in the model (phosphorus atoms, neutral P*I* pairs, and the negatively charged and neutral self-interstitials) is reduced in the case of LTD to solving the two diffusion equations (11) and (12), for the total concentrations of the phosphorus-incorporating and neutral interstitial-incorporating components, with the diffusion coefficients that are defined by (13) and (14) and which depend on the component concentrations. The initial conditions for the LTD are represented by the distributions for the total concentrations of the phosphorus- and interstitial-incorporating components immediately after the HTD completion; i.e.,

$$\begin{aligned}[P_F](x, 0) &= [P_{FH}](x),\\ F_I(x, 0) &= F_{IH}(x) \approx F_{IHS},\end{aligned} \tag{22}$$

where the subscript H indicates the high-temperature diffusion stage. For the boundary conditions we use the condition for reflection for the total concentration of the phosphorus-incorporating components at both boundaries of the solution interval (for $x = 0$ and $x = L$); we also impose the condition for reflection at the far boundary ($x = L$) for the total concentration of the neutral interstitial-incorporating components and assume that the self-interstitial concentration at the surface is equal to the equilibrium concentration ($[I_S^0] = [I_{\text{eq}}^0]$); thus, we have

$$\frac{\partial[P_F](0, t)}{\partial x} = \frac{\partial[P_F](L, t)}{\partial x} = 0, \tag{23}$$

$$F_I(0, t) = F_{I\text{eq}}, \quad \frac{\partial F_I(L, t)}{\partial x} = 0. \tag{24}$$

For $F \ll [P]$, we have $[P] \approx [P_F]$; as a result, Eq. (11) transforms into the diffusion equation for phosphorus. The concentrations of the other components are determined by solving Eq. (12) using the relations for local equilibrium between the diffusing components.

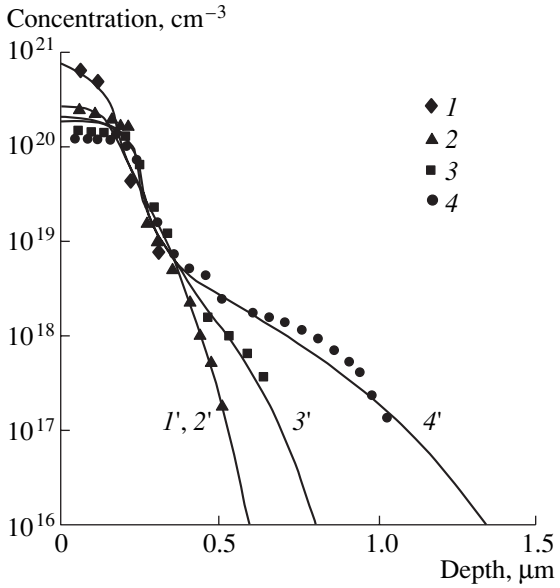

Fig. 5. The concentration profiles for (*1*') [P] and (*2*'–*4*') [P^+] (*1*', *2*') before and (*3*', *4*') after the low-temperature diffusion at T = 700°C (T_H = 1000°C and t_H = 5 min). The duration of the low-temperature diffusion was (*3*') 0.5 and (*4*') 16 h. The solid lines represent the results of calculations, and symbols *1*–*4* represent the experimental data [26].

At the very beginning of LTD, self-interstitials are redistributed between the interstitial-incorporating components in accordance with the conditions for local equilibrium at a new (lower) temperature. As a result, the following initial distribution of neutral self-interstitials over depth is established:

$$[I^0](x, 0) = \frac{F_{IH}(x)}{1 + k_{IF}[P^+]n}. \tag{25}$$

We use (25) to obtain the dependence of the initial degree of supersaturation for self-interstitials on depth

$$a_I(x, 0) = \frac{(1 + k_{IFH}[P_S^+]n_S)[I_{\text{eq}H}^0]}{(1 + k_{IF}[P^+]n)[I_{\text{eq}}^0]} \tag{26}$$

and the degree of initial supersaturation for self-interstitials at the tail of the concentration profile for $[P^+] \ll n_i$:

$$a_{It}(0) = (1 + k_{IFH}[P_S^+]n_S)\frac{[I_{\text{eq}H}^0]}{[I_{\text{eq}}^0]}. \tag{27}$$

As can be seen from formulas (26) and (27), the initial degree of supersaturation for self-interstitials depends not only on the LTD temperature but also on the HTD temperature, in agreement with experimental data [26]. As the LTD duration increases, the reserve of self-interstitials formed during HTD is reduced, owing to drain of the excess self-interstitials and P*I* pairs to the surface

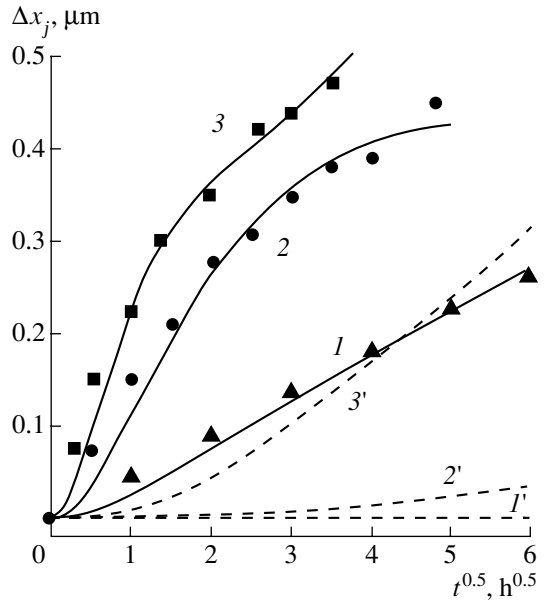

Fig. 6. Dependences of the *p–n*-junction displacement on the duration of the low-temperature diffusion (T_H = 1000°C and t_H = 5 min). The low-temperature diffusion was performed at T = (*1*, *1*') 500, (*2*, *2*') 600, and (*3*, *3*') 700°C. The solid lines represent the results of calculations based on the model developed, dashed lines represent the results of extrapolation using the Fair–Tsai model [5, 6], and symbols *1–3* represent the experimental data [26].

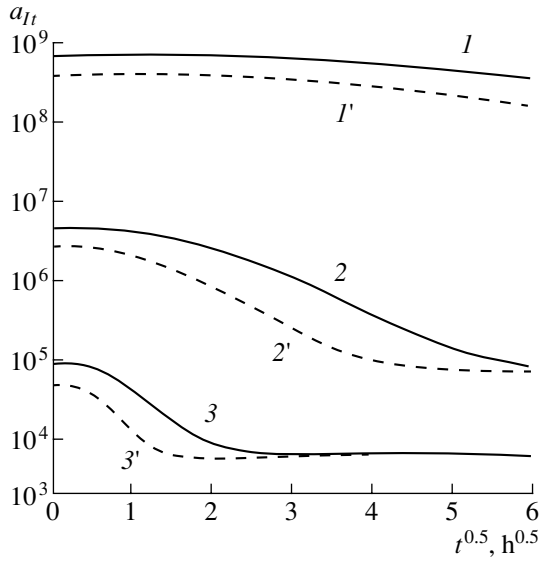

Fig. 7. Dependences of the relative self-interstitial supersaturation on the duration of low-temperature diffusion performed at T = (*1*, *1*') 500, (*2*, *2*') 600, and (*3*, *3*') 700°C. The preceding high-temperature diffusion was performed at T = (*1–3*) 1000 and (*1*'–*3*') 900°C.

until the steady-state distributions $F_I(x)$ and $[I^0](x)$ corresponding to the LTD temperature are established. The degree of the self-interstitial supersaturation at the tail of the concentration profile tends towards a steady-state value that corresponds to the single-stage diffusion described by expression (20).

The inflection point in the phosphorus concentration profile corresponds to the onset of the effect of self-interstitial supersaturation, which causes an enhancement of the diffusion on the concentration profile. The concentration corresponding to the inflection point can be determined from the condition for the equality of the local supersaturation degree to the halved supersaturation degree at the tail; i.e.,

$$a_{It} = 2a_I(n_k). \quad (28)$$

Using formulas (26) and (27) and condition (28), we obtain

$$n_K = \sqrt{n_i^2 + 1/k_{IF}}. \quad (29)$$

As can be deduced from (19) and (20), the same form has the relation for the inflection-point concentration in the case of HTD. It can be seen from expression (29) that the quantity n_K depends only on the temperature of the current diffusion stage (HTD or LTD) and is independent of either the diffusion duration or the surface phosphorus concentration, which is consistent with the experimental data [24–26].

4.2. Parameters

The LTD model parameters supplementary to those used above for HTD are the formation energy of self-interstitials (E_{fI}) and the diffusion coefficients for the neutral pairs P*I* (D_F) and self-interstitials (D_I). The self-interstitial formation energy, which, according to (27), controls the temperature dependence of the initial degree of self-interstitial supersaturation at the tail of the concentration profiles, was determined from the data on the initial portions of the kinetics for the *p–n*-junction displacement at various LTD temperatures [26] (E_{fI} = 2.9 eV).

Of all the published data on D_I, the dependence $D_I = 0.335\exp(-1.86/kT)$ [43] for the temperature range of 460–1200°C satisfies best the condition $E_{MI} + E_{FI} = E_{SD}$ (E_{MI} is the migration energy of self-interstitials, and E_{SD} is the activation energy for self-diffusion in silicon and is approximately equal to 4.8 eV [41, 42]). For the determined E_{FI} and chosen D_I, the temperature dependence $D_F(T)$ was determined from the consistency of the calculated kinetics of the *p–n*-junction displacement during the LTD with experimental data [26]; thus, it was found that $D_F = 2.2 \times 10^{-7}\exp(-1.0/kT)$.

An additional factor influencing a decrease in the diffusion rate for long LTD durations and, correspondingly, a deviation of the $x_j(\sqrt{t})$ dependences from linearity consists in the decrease in the concentration of electrically active phosphorus in the heavily doped region of the concentration profile as a result of the solid-solution decomposition. The parameters of the

decomposition kinetics were taken from previous publications [24, 26].

4.3. Results of Calculations and Discussion

Diffusion equations (11) and (12), with the diffusion coefficients defined by (13) and (14), the initial conditions given by (22), and the boundary conditions defined by (23) and (24), were solved by the finite-difference method using an implicit scheme. The calculated concentration profiles of the total phosphorus [P] and electrically active phosphorus [P^+] before and after the LTD are shown by solid lines in Fig. 5, together with experimental data reported in [26]. As can be seen from Fig. 5, the concentration of electrically active phosphorus decreases in the heavily doped plateau region of the concentration profile in the course of LTD; furthermore, an additional tail becomes distinct in the lightly doped region. The former effect is a result of the decomposition of the phosphorus solid solution, whereas the latter effect is due to the diffusion enhancement by excess self-interstitials accumulated at the HTD stage. As the LTD duration increases, the surface concentration of electrically active phosphorus decreases, whereas the profile tail extends. Figure 6 shows the time dependences of the *p–n*-junction displacement in the course of LTD: $\Delta x_j = x_j - x_{j0}$, where x_{j0} and x_j are the initial and current values of the *p–n*-junction depth. As the LTD duration increases, the dependence $\Delta x_j(\sqrt{t})$ slopes downwards for the temperatures of 600 and 700°C (Fig. 6, curves *2*, *3*). This occurs owing to the exhaustion of the reserve of P*I* pairs, which were accumulated during the HTD, as a result of diffusion-related drain of both the excess self-interstitials and the pairs to the surface. The values of Δx_j calculated by extrapolating the Fair–Tsai model [5, 6] (the dashed lines in Fig. 6) are much smaller than the experimental values, and the difference between calculations and experiment increases with decreasing LTD temperature. The time dependences of the relative self-interstitial supersaturation at the concentration profile tail are shown in Fig. 7 for several LTD temperatures. As can be seen from Fig. 7, the initial degree of supersaturation increases with decreasing LTD temperature and tends towards 10^9 at 500°C. As the HTD temperature increases, supersaturation becomes more pronounced (cf. curves *1–3* and *1'–3'*) as a result of an increase in the equilibrium self-interstitial concentration in expression (27). As the LTD duration increases, the degree of supersaturation decreases with the rate increasing as the temperature increases and tends towards its steady-state value [see (22)]; however, this value is attained during the LTD only at 700°C. For longer LTD stages, a decrease in the surface concentration of electrically active phosphorus, as a result of the solid-solution decomposition, starts to contribute to a decrease in $a_{It}(t)$. The temperature dependence of the concentration n_K corresponding to the deflection point is shown in

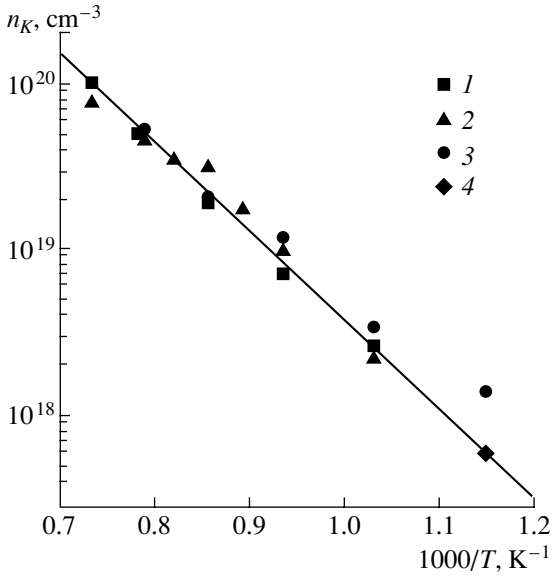

Fig. 8. Temperature dependence of concentration corresponding to the inflection point for the (*1*, *2*) high-temperature and (*3*, *4*) low-temperature diffusion stages. The solid line represents the results of calculations, and symbols *1–4* represent the experimental data taken from (*1*) [44], (*2*) [45], (*3*) [25], and (*4*) [29].

Fig. 8. As can be seen from Fig. 8, the dependence calculated using expression (29) agrees quite well with the data obtained from experiments with both HTD [44, 45] and LTD [25, 29].

5. CONCLUSION

A model of phosphorus diffusion in silicon based on the dual pair mechanism is suggested. In this model, the contribution of various charge states and pair types to diffusion is accounted for by introducing the partial phosphorus diffusivities and the fractions of the vacancy- and interstitial-related diffusion components with allowance made for supersaturation of self-interstitials and undersaturation of vacancies; the latter effects are due to the diffusion of neutral impurity–interstitial pairs (P*I*). In the high-concentration part of the phosphorus concentration profile, phosphorus diffuses predominantly via the neutral (P*V*) and negatively charged (PV^-) phosphorus–vacancy pairs, whereas the positively charged pairs PI^+ predominantly contribute to phosphorus diffusion in the low-concentration region. The neutral P*I* pairs diffuse from the region with the highest concentration to the crystal bulk and give rise to excess self-interstitials that enhance the phosphorus diffusion in the region of the profile tail. The relation between concentrations of electrically active and inactive phosphorus is governed by the processes of cluster formation. It is shown that, during the high-temperature diffusion (HTD) stage, phosphorus diffusion is adequately described by a single diffusion equation with the diffusion coefficient dependent on both

the local and surface phosphorus concentrations and that the phosphorus concentration profiles depend on the reduced depth $x\sqrt{t}$ if the phosphorus surface concentration is constant.

During the subsequent diffusion stage at lower temperatures [the low-temperature diffusion (LTD)], the concentration profiles of the diffusion components (electrically active and inactive phosphorus, neutral pairs P*I*, and negatively charged and neutral self-interstitials) are determined from the simultaneous solution of two diffusion equations for the total concentrations of phosphorus-incorporating and neutral interstitial-incorporating diffusion components; the initial conditions for these equations are the corresponding distributions after the preceding HTD stage. It is shown that an anomalously high diffusion rate early in the LTD is ensured by excess self-interstitials accumulated in the form of P*I* pairs in the doped layer during the HTD stage. As the diffusion duration increases, the LTD rate decreases as a result of drain of excess self-interstitials and P*I* pairs to the surface. The results of the calculations adequately describe the formation of an additional tail in the experimental phosphorus concentration profiles, the effect of temperature of both LTD and HTD on the diffusion rate, and the temperature dependence of the concentration corresponding to the inflection point for both LTD and HTD.

Calculations based on the model make it possible to describe satisfactorily, in quantitative terms, the special features of phosphorus diffusion in a wide range of surface phosphorus concentrations both at high (900–1100°C) and at lower (500–700°C) temperatures. The model involves a minimal number of parameters and can be used in computational programs for the physical and technological simulation of superlarge-scale integrated circuits.

ACKNOWLEDGMENTS

I thank N.N. Afonin and R.Sh. Malkovich for their helpful suggestions and comments.

REFERENCES

1. S. M. Hu, in *Atomic Diffusion in Semiconductors*, Ed. by D. Shaw (Plenum, London, 1973; Mir, Moscow, 1975), Chap. 5.
2. R. B. Fair, in *Impurity Doping Processes in Silicon*, Ed. by F. F. Y. Wang (North-Holland, Amsterdam, 1981), Chap. 7.
3. S. M. Hu, P. Fahey, and R. W. Dutton, J. Appl. Phys. **54**, 6912 (1983).
4. K. O. Petrosyants and O. V. Mazing, Zarubezhn. Élektron. Tekh., Nos. 5–6, 3 (1991).
5. R. B. Fair and J. C. C. Tsai, J. Electrochem. Soc. **124**, 1107 (1977).
6. R. B. Fair, J. Appl. Phys. **50**, 860 (1979).
7. M. Yoshida, Jpn. J. Appl. Phys. **18**, 479 (1979).
8. M. Yoshida and E. Arai, Jpn. J. Appl. Phys. **34**, 5891 (1995).
9. D. Mathiot and J. S. Pfister, J. Phys. Lett. **43**, L453 (1982).
10. V. A. Panteleev, Fiz. Tverd. Tela (Leningrad) **21**, 3388 (1979) [Sov. Phys. Solid State **21**, 1956 (1979)].
11. V. A. Panteleev, M. I. Vasilevskiĭ, G. M. Golemshtok, and V. I. Okulich, Fiz. Tverd. Tela (Leningrad) **28**, 3226 (1986) [Sov. Phys. Solid State **28**, 1820 (1986)].
12. P. M. Fahey, P. B. Griffin, and J. D. Plummer, Rev. Mod. Phys. **61**, 289 (1989).
13. B. J. Mulvaney and W. B. Richardson, Appl. Phys. Lett. **51**, 1439 (1987).
14. M. Orlowski, Appl. Phys. Lett. **53**, 1323 (1988).
15. H. U. Jager, T. Feudel, and S. Ulbricht, Phys. Status Solidi A **116**, 571 (1989).
16. F. F. Morhead and R. F. Lever, Appl. Phys. Lett. **48**, 151 (1986); J. Appl. Phys. **66**, 5349 (1989).
17. D. Mathiot and S. Martin, J. Appl. Phys. **70**, 3071 (1991).
18. D. Mathiot and J. S. Pfister, J. Appl. Phys. **55**, 3518 (1984).
19. W. B. Richardson and B. J. Mulvaney, J. Appl. Phys. **65**, 2243 (1989).
20. B. J. Mulvaney and W. B. Richardson, J. Appl. Phys. **67**, 3197 (1990).
21. M. Budil, H. Potzl, G. Stingeder, *et al.*, Mater. Sci. Forum **38–41**, 719 (1989).
22. B. Baccus, T. Wada, N. Shiguo, *et al.*, IEEE Trans. Electron Devices **39**, 648 (1992).
23. K. Ghaderi and G. Hobler, J. Electrochem. Soc. **142**, 1654 (1995).
24. F. N. Shwettman and D. L. Kendall, Appl. Phys. Lett. **19**, 218 (1971).
25. F. N. Shwettman and D. L. Kendall, Appl. Phys. Lett. **21**, 2 (1972).
26. O. V. Aleksandrov and R. Z. Tumarov, in *Semiconductor Doping* (Nauka, Moscow, 1982), p. 97.
27. O. V. Aleksandrov and V. I. Sokolov, Élektron. Tekh., Ser. 2, No. 6, 38 (1975).
28. O. V. Aleksandrov, R. N. Kyutt, V. I. Prokhorov, and L. M. Sorokin, Fiz. Tverd. Tela (Leningrad) **31** (10), 182 (1989) [Sov. Phys. Solid State **31**, 1754 (1989)].
29. V. I. Prokhorov, V. I. Sokolov, and L. M. Sorokin, Fiz. Tverd. Tela (Leningrad) **23**, 1302 (1981) [Sov. Phys. Solid State **23**, 763 (1981)].
30. R. B. Fair, in *Impurity Doping Processes in Silicon*, Ed. by F. F. Y. Wang (North-Holland, Amsterdam, 1981), Chap. 7.
31. R. Sh. Malkovich, *Mathematics of Diffusion in Semiconductors* (Nauka, St. Petersburg, 1999), Chap. 5.
32. O. V. Aleksandrov, N. V. Ashkinadze, and R. Z. Tumarov, Fiz. Tverd. Tela (Leningrad) **26**, 632 (1984) [Sov. Phys. Solid State **26**, 384 (1984)].
33. O. V. Aleksandrov, R. N. Kyutt, and T. G. Alksnis, Fiz. Tverd. Tela (Leningrad) **22**, 2892 (1980) [Sov. Phys. Solid State **22**, 1688 (1980)].
34. J. P. John and M. E. Law, Appl. Phys. Lett. **62**, 1388 (1993).

35. T. Shimizu, T. Takagi, S. Matsumoto, *et al.*, Jpn. J. Appl. Phys. **37**, 1184 (1998).
36. D. J. Roth and J. D. Plummer, J. Electrochem. Soc. **141**, 1074 (1994).
37. R. L. Meek, T. E. Seidel, and A. G. Cullis, J. Electrochem. Soc. **122**, 786 (1975).
38. R. Sh. Malkovich and V. A. Pokoeva, Fiz. Tverd. Tela (Leningrad) **18**, 2606 (1976) [Sov. Phys. Solid State **18**, 1521 (1976)].
39. G. Weyer, M. Fanciulli, K. Freitag, *et al.*, Mater. Sci. Forum **196–201**, 1117 (1995).
40. W. Frank, Inst. Phys. Conf. Ser. **23**, 23 (1975).
41. K. Taniguchi, D. A. Antoniadis, and Y. Matsushita, Appl. Phys. Lett. **42**, 961 (1983).
42. H. Zimmermann and H. Ryssel, Appl. Phys. A: Solids Surf. **A55**, 121 (1992).
43. T. Y. Tan and U. Gosele, Appl. Phys. A: Solids Surf. **A37**, 1 (1985).
44. N. A. Stolwijk, J. Holzl, W. Frank, *et al.*, Appl. Phys. A: Solids Surf. **A39**, 37 (1986).
45. W. Wijaranakula, J. Appl. Phys. **67**, 7624 (1990).
46. P. B. Griffin, P. M. Fahey, J. B. Plummer, and R. W. Dutton, Appl. Phys. Lett. **47**, 319 (1985).
47. D. B. Lee, Philips Res. Rep. Suppl. **25**, 1 (1974).
48. S. Matsumoto, M. Yoshida, and T. Niimi, Jpn. J. Appl. Phys. **13**, 1899 (1974).

Translated by A. Spitsyn

Semiconductors, Vol. 35, No. 11, 2001, pp. 1242–1248. Translated from Fizika i Tekhnika Poluprovodnikov, Vol. 35, No. 11, 2001, pp. 1299–1305.

ELECTRONIC AND OPTICAL PROPERTIES OF SEMICONDUCTORS

The Impurity Optical Absorption and Conduction Band Structure in 6*H*-SiC

I. S. Gorban'† and A. P. Krokhmal'*

Shevchenko National University, Vladimirskaya ul. 64, Kiev, 01033 Ukraine

** e-mail: krokhmal@mail.univ.kiev.ua*

Received February 27, 2001; accepted for publication April 2, 2001

Abstract—Absorption spectra of nitrogen-doped *n*-type 6*H*-SiC crystals were studied for two orientations of the light wave electric field (**E**) relative to the optical axis (**C**), **E** || **C** and **E** ⊥ **C**, within the range from the near-infrared region to the fundamental band. For **E** || **C**, a weak absorption band peak at 2.85 eV was investigated for the first time. All the absorption bands observed are attributed to donor (nitrogen) photoionization, as a result of which electrons are transferred to the conduction-band upper minima that correspond to different critical points of the Brillouin zone. A combined analysis of the new data obtained in this study, the previous experimental results concerning photoionization of nitrogen, and theoretical data on 6*H*-SiC conduction band structure made it possible to refine the arrangement and symmetry of the additional conduction-band extrema in the Brillouin zone. © *2001 MAIK "Nauka/Interperiodica".*

1. INTRODUCTION

Silicon carbide is finding ever-widening applications in semiconductor electronic and optoelectronic devices operating under extreme conditions [1, 2]. Despite some progress in technology as well as in the study of the electrical and optical properties of 6*H*-SiC, which is one of the most commonly encountered polytypes of silicon carbide, the energy structure of its electron bands, particularly the conduction band, has still not been adequately explored. The most recent findings suggest that the conduction band in 6*H*-SiC has an absolute minimum on the line *M*–*L* at the *U* point rather than at the *M* point [3–7] of the Brillouin zone [8]. The minimum is of the double-valley type, and *M* is a saddle point [9–13]. As far as the higher lying extrema of the conduction band and the additional band edges are concerned, only the energy values for some of them are reliably known [14–16]. The location of the conduction-band additional extrema in the **k** space was presented in theoretical studies [7, 10], with the symmetry of these extrema being determined only at the Γ, *M*, and *K* points of the Brillouin zone [10]; a considerable spread in energy values predicted by different approaches should also be noted. The latter circumstance hinders identification of the conduction-band main features manifesting themselves in fundamental absorption and reflectance spectra, as well as in electroreflection [14, 17–19].

In this study, we analyze the energy structure of the conduction band in 6*H*-SiC and make use of its manifestations in the optical impurity absorption, which is due to the nitrogen (the main donor impurity in SiC) photoionization with the electron transitions to the higher lying minima of the conduction band. This approach requires detailed knowledge of the absorption spectra for the electric field **E** polarization not only relative to the optical axis **C**, coinciding with the main crystallographic axis C_6 (*Z* axis), but also relative to the *X* and *Y* crystallographic axes. It should be mentioned that, in recent studies of 6*H*-SiC, most attention has been given, in **E** || **C** polarization, to a pronounced infrared (IR) doublet band [16, 20–27] with a peak energy of 1.39 eV at liquid-nitrogen temperature and also, in **E** ⊥ **C** polarization, to much weaker and broader bands at about 2 eV [15, 20, 26–28] and 3 eV [29]. Still weaker bands, resulting from nitrogen photoionization involving electron transitions to the higher lying minima of the conduction band, have not been considered yet. This limits the set of available experimental data on the energy sites and other parameters of the conduction-band extra edges.

2. EXPERIMENTAL RESULTS

Spectral dependences of the absorption coefficient α in *n*-type 6*H*-SiC crystals doped in the course of growth with nitrogen are considered for two polarizations, **E** || **C** and **E** ⊥ **C**, within a wide spectral range (from the near-infrared (IR) region up to the fundamental band). For the latter polarization, the electric field of the light wave **E** is parallel to the *X* and *Y* crystallographic axes, or to $\langle 2\bar{1}10 \rangle$ and $\langle 01\bar{1}0 \rangle$ directions. The samples under investigation were single-crystal platelets (parallelepipeds) oriented along the *X*, *Y*, and *Z* crystallographic axes, doped uniformly through the bulk to electron concentra-

† Deceased.

tion $n = N_D - N_A$ from 2.9×10^{17} to 6.1×10^{18} cm^{-3}, and free from polytype heterostructures. In order to measure the absorption in the near-IR range at **E** ∥ **C**, thin plates with a thickness ranging from 50 to 150 μm were cut from the samples with different concentrations of neutral nitrogen. The samples used for other experiments had a thickness in the direction of light propagation in the range from 0.4 to 4 mm. The measurements were carried out at temperature T = 4.5, 77, and 295 K with the help of a special grating monochromator and a modified grating spectrometer on the basis of a DFS-8-2 with reciprocal linear dispersions of 3 and 0.3 nm/mm, respectively.

The absorption spectra typical of the *n*-type 6*H*-SiC crystals at T = 77 K are shown in Fig. 1 for two polarizations, **E** ∥ **C** and **E** ⊥ **C** (curves *1*, *2*). The absorption spectrum is practically unaffected by the cooling of the crystals to 4.5 K. For **E** ∥ **C** polarization, we are likely the first to observe a very weak band with a maximum at photon energy $\hbar\omega$= 2.85 eV [20, 31] and a half-width $\Delta\hbar\omega \approx 0.10$ eV, apart from the well-known pronounced doublet in the IR range [16, 20–27, 30]. The absorption coefficient α at the peak of this band is about 150 times less than that at the peak of the band $\hbar\omega$ = 1.39 eV and increases proportionally to concentration $n = N_D - N_A$ in the samples, as it does similarly for the bands $\hbar\omega$ = 1.39 and 2.02 eV [26]. For eight samples with different concentrations of nitrogen, the absorption coefficient at the peak of the 2.85 eV band is related to the absorption coefficient in the 1.39 eV band and, for **E** ⊥ **C** polarization, to the absorption coefficients in the bands which peaked at 2.02 eV [15, 20, 26–28] and 2.98 eV [29] (see Fig. 2). The relationship turned out to be linear, which suggests that the bands with peaks at 1.39, 2.02, 2.85, and 2.98 eV are of similar chemical nature; specifically, these are related to nitrogen. Here we should note that the IR band arises from the allowed dipole direct transitions of electrons from the three nonequivalent neutral *h* and 2*k* donor states with hexagonal and cubic coordination of the nearest neighbors to the higher lying minimum of the conduction band [16, 27, 30] at the *M* point. At low temperatures and concentrations of neutral nitrogen specified above, the transitions only occur from the $1s(A_1)$ states, which are split off by the orbit–valley interaction [27]. The oscillator strengths of these transitions add up to yield 0.72 [26]. The half-width of the $\hbar\omega$ = 2.85 eV band is somewhat less than that of the IR doublet ($\Delta\hbar\omega \approx 0.17$ eV). This band can also be attributed to the photoionization of nitrogen in *h* and 2*k* sites, but with transitions of electrons to the higher lying minimum, which is also located at the *M* point and is similar in parameters with the minimum [16, 30] responsible for the IR band. In such an event, this band should resemble the IR band in shape, i.e., to be of the doublet type and to display redistribution of components with temperature, similar to [22–27]. This contradicts the experimental data. We determined the oscillator strength of the transitions in the band $\hbar\omega$ =

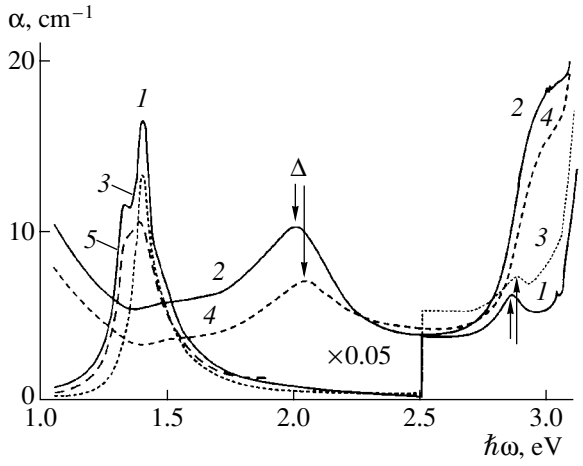

Fig. 1. Absorption spectra of the *n*-6*H*-SiC crystals for two polarizations of light: curves *1* and *2* correspond to *n*-type crystals without acceptor impurity added; curves (*3*–*5*), to *n*-type crystals doped with aluminum. Curves (*1*–*4*) were measured at T = 77 K: *1*, *3*, for **E** ∥ **C**; and *2*, *4*, for **E** ⊥ **C**. Curve *5* was measured at T = 295 K for **E** ∥ **C**.

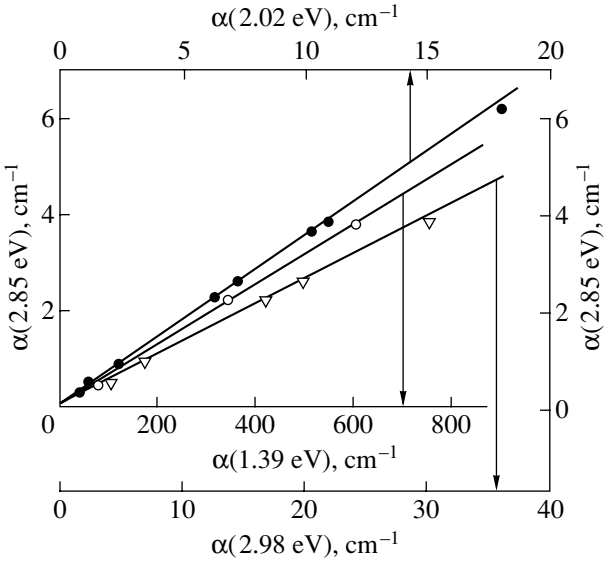

Fig. 2. Correlation between the absorption coefficient at the peak of the 2.85 eV band for crystals with different concentrations of nitrogen and the absorption coefficients at the peaks of the 1.39, 2.02, and 2.98 eV bands.

2.85 eV to be $(1.75 \pm 0.07) \times 10^{-3}$. This value suggests that this band stems from the transitions forbidden in the dipole approximation. If we assume that, similar to the IR band, the band $\hbar\omega$ = 2.85 eV consists of two components, the peaks of which are nearly equal in intensity (in view of the forbidden transitions) and are ~60 meV apart [27, 30], their separation is only possible if the most shallow *h*-donors are completely compensated. Meeting this requirement, the crystals at our disposal were specially doped during growth with both

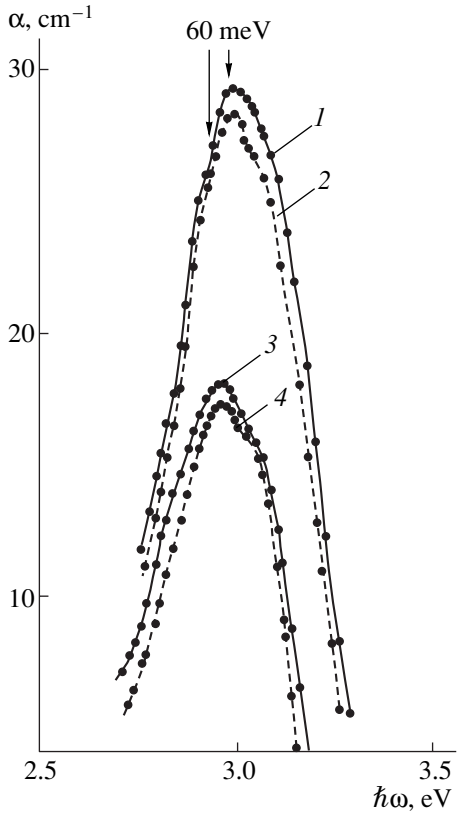

Fig. 3. Absorption spectra of a separate near-edge absorption band for $\mathbf{E} \perp \mathbf{C}$ at T = (*1*, *2*) 77 and (*3*, *4*) 295 K. (*1*, *3*) Corresponds to $\mathbf{E} \parallel Y$; and (*2*, *4*), to $\mathbf{E} \parallel X$. Curves *1*, *2* are shifted up the vertical axis by 10 cm^{-1}.

nitrogen and aluminum, which forms a shallow-level acceptor impurity in SiC. Curve *3* in Fig. 1 depicts an absorption spectrum of one of these 6*H*-SiC crystals. A sufficient amount of acceptors led to the complete compensation of the shallow-level *h* donors (nitrogen) with ionization energy E_D^h = 0.081 eV [23, 31, 32] (according to the published data [5, 33], E_D^h = 0.101 eV) and, as a consequence, to the extinction of the *h* component at 1.33 eV from the IR band at $T \lesssim$ 80 K. At T = 295 K, however, both components are present in the IR band (curve *5*)—the relation between their intensities being the opposite to that for "conventional" (without acceptor impurity specially added) crystals [16, 22–27]. It should be emphasized that the absence of the component with $\hbar\omega$ = 1.33 eV in the IR band in the spectrum of the compensated crystal presents additional proof of this component's connection with the photoionization of nitrogen occupying precisely the *h* site, while the 1.39-eV component is obviously related to the photoionization of nitrogen in the 2*k* sites. The only transitions contributing to the $\hbar\omega$ = 1.33 eV component in compensated crystals at T = 295 K are those from the excited 1*s*(*E*) states of donors in 2*k* sites, which are characterized by nearly the same energy as the 1*s*(A_1) state in the *h* site. It should also be noted that the low-energy component observed at room temperature in the IR band ($\hbar\omega$ = 1.25 eV) in heavily N-doped 6*H*-SiC crystals with an electron concentration $n > 1 \times 10^{19}$ cm^{-3} [20, 21] is associated with band-to-band transitions [20, 24] rather than with the "camel's back" shape of the absolute minimum of the conduction band, as was argued in [34].[1]

The band with $\hbar\omega$ = 2.85 eV is observed in compensated crystals at the steeper near-edge slope, apparently caused by the ionized acceptors photoneutralization with electron transitions to the conduction band, and is shifted to higher energies by approximately 30 meV (curve *3*). After subtraction of this background, the peak of the band in question, contrary to the expectations, displays no shift. This indicates that the *h* component does not contribute to the 2.85 eV band in both compensated and in uncompensated *n*-6*H*-SiC crystals.

Figure 1 (curve *2*) shows an absorption spectrum of 6*H*-SiC crystals with $n \approx (1\text{–}4) \times 10^{18}$ cm^{-3} at T = 77 K; this spectrum is typical of $\mathbf{E} \perp \mathbf{C}$ polarization. In previous studies, the absorption bands at $\hbar\omega$ = 2.02 eV [15, 26, 27] and $\hbar\omega$ = 2.98 eV [29] were considered separately and within limited spectral ranges only. Because of this, certain features of this spectrum were overlooked. Thus, in earlier studies (e.g., [15, 26]), the 2.02 eV band was observed against a background of unknown origin and has a broadened long-wavelength wing. As can be seen from the spectrum, the broad band with its peak at $\hbar\omega$ = 2.02 eV partially overlaps with a broader and more intense near-edge band peaked at $\hbar\omega$ = 2.98 eV and also with a short-wavelength tail of the absorption band, which can be attributed to nitrogen photoionization with the electron transitions to the absolute minimum of the conduction band [37]. It is this partial overlapping of the broad bands that causes the general background of absorption. Moreover, a considerably steep bend of the absorption curve at $\hbar\omega$ = 1.37 eV (with a small inflection at 1.49 eV) most likely indicates the presence of at least one broader and weaker absorption band (peaked possibly at $\hbar\omega \approx$ 1.9 eV), which distorts the shape of the low-energy wing of the 2.02 eV band.

[1] The predicted barrier height dividing two symmetric valleys, which are located at *U* points and the "saddle" at the *M* point, ranges from 3.8 to 5.7 meV [35, 10, 12, 13]. At the lower donor concentration of 5×10^{19} cm^{-3}, the barrier height decreases to 1.3 meV [36]. Absorption spectra of the *n*-type 6*H*-SiC crystals with carrier concentration nearly of the same order of magnitude were studied in [20]. The spectra considered in [20] were recently interpreted in [34] with the double-valley structure of the conduction band taken into account. So small an energy difference cannot be noticed in absorption spectra in the form of a broad band ($\Delta\hbar\omega \approx 0.17$ eV). Even the experiments on hydrostatic compression of 6*H*-SiC crystals at T = 29 K and investigations of extremely narrow PRS lines stemming from the photoluminescence of excitons bound by neutral donors (nitrogen) failed to give evidence for the double-valley structure of the conduction band [35].

The 2.02-eV band is affected also by the photoionization of three nonequivalent nitrogen *h* and 2*k* donors in the course of electron transitions to the higher lying minimum of the conduction band with parameters [15], which essentially differ from those of the minimum responsible for the IR band in the case of **E** || **C** polarization [16, 30]. Therefore, the band at $\hbar\omega = 2.02$ eV should consist of two broad components and should seem structureless. In *n*-6*H*-SiC crystals heavily doped with aluminum, the lack of the *h* component results in a shift of the band peak at $T = 77$ K by $\Delta \approx 35$ meV to higher energies relative to the conventionally observed band at 2.02 eV (Fig. 1, curve *4*). This fact indicates a contribution of the *h* component to the band under discussion in common *n*-type crystals.

Figure 3 depicts the near-edge impurity band that peaked at $\hbar\omega = 2.98$ eV. This band is separated from the absorption spectrum of the *n*-type crystal by subtracting the fundamental absorption in the *p*-type crystal at 77 and 295 K for two polarizations, **E** || *X* and **E** || *Y*. The 2.98-eV band turned out to be a complex consisting of at least three components. The band's half-width is about 0.37 eV. The curve plotted for **E** || *Y* clearly shows an inflection in the vicinity of 2.92 eV, which is also observed in the nonextracted band for **E** ⊥ **C**. In highly compensated crystals, this inflection is missing in the absorption curves. This circumstance suggests that the band at $\hbar\omega = 2.92$ eV is caused by the transitions from the $1s(A_1)$ states of *h* donors. For **E** || *X* and $T = 77$ K, a band at $\hbar\omega = 3.06$ eV is present as well. Note that, at $T = 295$ K and **E** || *X*, the band is also of the doublet type and its peak is temperature-shifted to lower energies by ~20 meV. Although the determination of the precise shape of the band was difficult, we succeeded in estimating the oscillator strength for transitions in this band: $f \approx 0.12$.

3. DISCUSSION

The abundant structural and polarization features of the absorption spectrum of the *n*-6*H*-SiC crystals can hardly be explained on the basis of the miniband model for the conduction band [26, 38]. Within this model, the band at $\hbar\omega = 1.39$ eV corresponds to the allowed dipole electron transitions from the odd (first) to the even (second) miniband, while the band at $\hbar\omega = 2.02$ eV corresponds to the forbidden transitions to the odd (third) miniband. The next bands with $\hbar\omega = 2.85$ eV at **E** || **C** and $\hbar\omega = 2.98$ eV at **E** ⊥ **C** should correspond to the allowed transitions to the higher lying even (fourth) and the forbidden transitions into the odd (fifth) minibands, respectively. The oscillator strengths for these bands are in marked contrast to the model. Moreover, it is difficult to attribute the ~1-eV discontinuities in the electron spectrum to the structural superlattice potential, since the associated structure factors are negligibly small [39].

In many-valley semiconductors, the wave function of an electron bound near a shallow donor is conventionally formed from the Bloch waves at the conduction band bottom of an ideal lattice, with the coefficients $C_{\mathbf{k}}^{l}$ of the initial impurity function

$$\Psi(\mathbf{r}) = \sum_{\mathbf{k}, l} C_{\mathbf{k}}^{l} \Psi_{\mathbf{k}}^{l}(\mathbf{r}) \qquad (1)$$

considered to be negligible everywhere except in the immediate vicinity of the points where the conduction band absolute minimum is located. This approximation is justified for large-radius donor centers with a Bohr radius $a_B \approx 20$–50 Å, when $\Delta k a_B \gg 1$ (here $\Delta\mathbf{k}$ denotes the difference between dissimilar minima in the conduction band) [40, 41]. For small-radius centers (the Bohr radius a_B is comparable with the lattice constant, i.e., $\Delta k a_B \gtrsim 1$), the other minima of the conduction band also contribute to the wave function $\Psi(\mathbf{r})$. For small-radius centers, the wide extent of the impurity wave function in **k**-space also enables the electron transitions from these centers to the conduction band minima located at other points of the Brillouin zone.

According to the empirical estimations [42], the effective Bohr radii of the considered donor states in 6*H*-SiC for *h* and *k* sites amount to $a_B^h = 7.7$ Å and $a_B^k = 6.1$ Å, respectively. These values are consistent with the experiments that yield the respective radii as 7 Å [43] and 5 Å [44]. At the critical point *L*, which is closest to the absolute minimum, the Kittel–Mitchell criterion [40, 41] for donors in the *h* site is $\Delta k_{M-L} a_B^h = 1.6$. At the most remote points Γ and *A*, we have $\Delta k_{M-\Gamma} a_B^h = 9.09$ and $\Delta k_{M-A} a_B^h = 9.23$; i.e., the criterion remains well over unity. For the deeper donors in the *k* sites with ionization energies $E_D^{k_1} = 0.1376$ eV and $E_D^{k_2} = 0.1424$ eV [23, 31, 32] (or $E_D^{k_1} = 0.158$ eV and $E_D^{k_2} = 0.163$ eV [33]), the values given by the criterion are ~1.7 times less than those for the *h* site. Therefore, for donors in *k* sites, the donor wave function (1) contains contributions of all of the conduction band minima in the Brillouin zone, whereas for a shallower donor in the *h* site, it is only the minima close to the absolute one that contribute to the wave function. The intensity and shape of the corresponding absorption bands will depend heavily on the selection rules, the probability density of the impurity wave function in the vicinity of the corresponding minimum in the Brillouin zone, and on the density of states in the minimum considered. From this point of view, the origin of a weak single band with $\hbar\omega = 2.85$ eV at **E** || **C** can be clarified.

The Γ point. It is our opinion that the band at $\hbar\omega = 2.85$ eV is formed by transitions related to the photoionization of nitrogen in the *k* sites with the electron

transitions to the conduction band minimum in the Γ point of the Brillouin zone. In general, the selection rules for donor photoionization are determined by a G^* group, which consists of symmetry elements common to both the wave vector group $G_{\mathbf{k}}$, the star of which includes the considered minimum and the donor point symmetry group G. Substitutional impurity point centers in 6*H*-SiC (C_{6v} class) have C_{3v} symmetry. Consequently, when the donors are photoionized, the only transitions at the center of the Brillouin zone ($G_{\mathbf{k}} \subset C_{6v}$) that can be observed in **E** ∥ **C** polarization are those between $1s(A_1)$ donor states and the Γ_1^* band states of the G^* group. Symmetry of the Γ_1 or Γ_2 band states can be obtained by a reduction of the Γ_1^* representations to the $G_{\mathbf{k}}$ group.

The analytical calculation of the 6*H*-SiC energy spectrum carried out in [3] for only certain symmetric points in the Brillouin zone yielded Γ_1 and Γ_4 symmetries for the lower and upper minima of the conduction band at the center of the Brillouin zone, respectively. More accurate calculation [7], however, provides no data either on the symmetry of irreducible representations for the conduction band singularities at the critical points of the Brillouin zone or on the energy of singularities both at the Γ and M points of the Brillouin zone. In [10], Γ_4 symmetry is attributed to the lower minimum, and Γ_1, to the next two higher lying minima.

According to our data, the conduction band minimum with Γ_1 symmetry is above the absolute minimum by $\Delta E \approx 2.43$ eV at $T \lesssim 80$ K. For this estimation we used the energy of maximum photoionization cross section of donors in k sites in the form $\hbar\omega = (10/9)(\Delta E + E_D)$ [45], where ΔE is the gap between the absolute and the upper minima, and E_D is the energy level measured from the absolute minimum. Taking into account the band gap $E_g = 3.10$ eV, we find that the direct band gap $\Gamma_{6v} - \Gamma_{1c}$ in 6*H*-SiC is equal to 5.53 eV at $T \lesssim 80$ K. This value correlates well with the singularity observed at 5.5 eV in the absorption and reflectance spectra for **E** ⊥ **C** at room temperature [17, 18], as well as with the corresponding theoretical values for the gap $\Gamma_{6v} - \Gamma_{1c} = 5.28$ and 5.70 eV [10]. In what follows we will apply the approach described above and use the band calculations made in [3, 10] to classify the symmetry of other experimentally revealed minima in the 6*H*-SiC conduction band.

The *M* point. In view of the fact that, in 6*H*-SiC, the donor wave functions are formed mainly of the band states with $M(U)$ symmetry, the selection rules at donor photoionization with electron transitions into the upper conduction bands at point M will be governed instead by the $G_{\mathbf{k}} \subset C_{2v}$ group. Let us assume that the symmetry elements σ_v' of the C_{2v} group are oriented in accordance with the elements σ_v' of the C_{6v} group.[2] Then, the X and Y coordinates in the group C_{2v} transform according to the irreducible representations M_3 and M_4, respectively. Then, the consistency relations along the $\Gamma - M(\Sigma)$ line appear in the following form:

$$\begin{aligned} &\Gamma_1 \longrightarrow M_1, \quad \Gamma_2 \longrightarrow M_3, \quad \Gamma_3 \longrightarrow M_2, \\ &\Gamma_4 \longrightarrow M_4, \quad \Gamma_5 \longrightarrow M_1 + M_2, \quad \Gamma_6 \longrightarrow M_3 + M_4. \end{aligned} \tag{2}$$

Taking into account (2) and assuming that the Γ_{1c} band [3] is the lowest at the Γ point, we find that the absolute minimum in 6*H*-SiC should have $U_1(M_1)$ symmetry. In such an event, according to the selection rules, the transitions from $1s(A_1)$ donor states in the h and k sites to the conduction band $U_1(M_1)$ can only be observed in **E** ∥ Z(**C**) polarization. Experimentally [21, 37], transitions into the absolute minimum were observed for **E** ⊥ **C** only; i.e., the transitions are realized to the conduction band of U_3 or U_4 symmetry. The calculations [3, 10] also suggest M_4 symmetry for the minimum of the conduction band in 6*H*-SiC. Thus, according to (2), the lower minimum at the Γ point should be Γ_4, as noted in [10]. It is worth noting that the calculation carried out in [3] yields the Γ_1 symmetry of the upper valence band, while the experimental data was obtained without considering the spin yield Γ_6 [4, 47]. It is evident, therefore, that the notation of irreducible representations for Γ_{1c} and Γ_{4c} bands for the conduction band are mixed up in [3]. Thus, the experimental and theoretical data available suggest that the lower edge of the conduction band has the Γ_4 symmetry at the Γ point and that the direct transitions to this edge from $1s(A_1)$ donor states are forbidden in dipole approximation for either polarization.

Since the IR absorption band is only observed for **E** ∥ **C**, the above considerations suggest that the donor photoionization involves the electron transitions to the higher lying conduction band M_1. The direct band-to-band electron transitions $M_{4c} \longrightarrow M_{1c}$ are forbidden for **E** ∥ **C** polarization by the selection rules; this is confirmed by experiment. The fact that these transitions are forbidden is confirmed in [25] from the analysis of the temperature dependence of absorption in the IR band. Nevertheless, a weak additional absorption band at 1.24 eV was observed in the **E** ∥ **C** polarization at 900 K [24] and was attributed to interband transitions (if nitrogen concentration is high, the observed band evidently results from violation of the **k** selection rules [20, 21]). Following [45], we estimated that the M_1 minimum is located by 1.12 eV above the absolute minimum for both the 1.33 eV and the 1.39 eV bands. This value coincides with the gap $E_0 = 1.11$ eV obtained in [30] from the analysis of the absorption band shapes.

[2] Classes of the symmetry elements and, correspondingly, irreducible representations for C_{6v} group [46] are written down in the correct order. This is important to avoid confusion in view of the present variety in notation of representations.

With allowance made for E_g, the gap $\Gamma_{6v} - M_{1c}$ at $T \leq 80$ K equals 4.22 eV, which agrees well with the high-energy absorption edge of 4.1 eV measured at $T = 300$ K [14]. Another still weaker component of the IR band with a peak at $\hbar\omega = 1.49$ eV should be mentioned. This absorption band was present in the spectra of every *n*-6*H*-SiC sample we studied and shows no variation in intensity from sample to sample. In all likelihood, it is associated with the superlattice. The energy separation between the bands' peaks, $\Delta E = 0.09$ eV, is a reasonable value for discontinuity in the electron spectrum because of a superlattice structure potential.

We attribute the band with $\hbar\omega = 2.98$ eV to the photoionization of nitrogen in the *h* and *k* sites with electron transitions to the conduction band of M_4 symmetry, which, in accordance with the selection rules, should be observed for **E** ∥ *Y* polarization. Calculations [3, 10] also point to the presence of the next higher lying conduction band of M_4 symmetry. According to the selection rules, the band at 3.06 eV corresponds to transitions to the M_3 band. Estimation shows that, at $T \leq 80$ K, the edge of the M_4 band is ~2.54 eV above the absolute minimum. This interpretation is supported by the value of the oscillator strength obtained for transitions in this band ($f \approx 0.12$). Since the **k** quantum number is not yet most appropriate as applied to donors, the bands of absorption transitions to the M_4 and M_3 bands do not separate completely in **E** ∥ *Y* and **E** ∥ *X* polarizations but only "feel" the corresponding polarizations. A small energy gap between M_{4c} and M_{3c} bands, $\Delta E \approx 0.08$ eV, may also be due to the superlattice [7].

The *F* point. According to [31], the absorption band $\hbar\omega = 2.02$ eV is observed both in **E** ⊥ **C** and **E** ∥ **C** polarizations. Moreover, we revealed that there was no sensitivity of this band to **E** ∥ *Y* or **E** ∥ *X* polarizations. Depolarized transitions of electrons can only be observed from donors to the minimum located at the *F* point, i.e., on the $R - \Sigma$ line, and the G^* group corresponds to the C_s symmetry with the reflection plane $(\sigma'_v|0)$. Since transitions from *h* donors contribute to the band $\hbar\omega = 2.02$ eV, the corresponding minimum of the conduction band should not be too far from the *M* point. Estimations show that this minimum is above the absolute one by 1.68 eV. With respect to E_g, the gap $\Gamma_{6v} - F_{c1,2} = 4.78$ eV.

The *K* point. According to [3, 10], the minimum of the conduction band at the *K* point has K_3 symmetry. The transitions from the donor states $1S(A_1)$ to the conduction band K_3 ($G_{\mathbf{k}} \subset C_{3v}$) are allowed by selection rules at **E** ⊥ **C**. It is likely that the additional broad and weak band appearing at **E** ⊥ **C**, with its peak presumed to be at $\hbar\omega = 1.9$ eV, is caused by nitrogen photoionization involving the electron transitions to the K_3 conduction band with the gap $\Gamma_{6v} - K_{3c} \approx 4.6$ eV, which is in agreement with the onset of the indirect edge of fundamental absorption at $\hbar\omega \approx 4.6$ eV [14] and with the corresponding theoretical values of 4.4 eV [10] and 4.56 eV [11] as well.

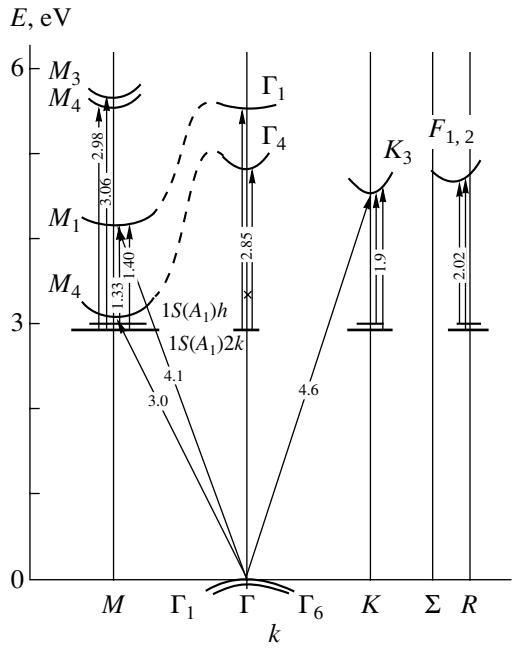

Fig. 4. A fragment of 6*H*-SiC conduction-band structure $E(k)$. Vertical arrows indicate the transitions from nitrogen levels to the corresponding minima of the conduction band at $T = 77$ K. Slanting arrows correspond to transitions observed within the fundamental absorption at $T = 300$ K [9]. The levels' length and thickness schematically depict the extent and probability density of the impurity wave function in the vicinity of the corresponding minima for $1S(A_1)$ donor states in nonequivalent *h* and 2*k* sites.

CONCLUSION

Summarizing the above, we applied a new approach to gain insight into the origin of the absorption bands resulting in 6*H*-SiC from donor (nitrogen) photoionization accompanied by electron transitions to the higher lying edges of the conduction band. Using relevant group-theory analysis and generalizing the new and previous experimental and theoretical data, we managed to classify the conduction band edges which manifested themselves in the experiment by their symmetry types in the Brillouin zone, and we reported their energies (Fig. 4). We believe that these data could be useful for improving the knowledge of the conduction band structure in 6*H*-SiC.

REFERENCES

1. P. A. Ivanov and V. E. Chelnokov, Fiz. Tekh. Poluprovodn. (St. Petersburg) **29**, 1921 (1995) [Semiconductors **29**, 1003 (1995)].
2. A. A. Lebedev and V. E. Chelnokov, Fiz. Tekh. Poluprovodn. (St. Petersburg) **33**, 1096 (1999) [Semiconductors **33**, 999 (1999)].

3. H. G. Junginger and W. van Haeringen, Phys. Status Solidi **37**, 709 (1970).
4. V. I. Sankin, Fiz. Tverd. Tela (Leningrad) **15**, 961 (1973) [Sov. Phys. Solid State **15**, 671 (1973)].
5. B. W. Wessels and H. C. Gatos, J. Phys. Chem. Solids **38**, 345 (1977).
6. I. S. Gorban', V. A. Gubanov, V. D. Kulakovskiĭ, *et al.*, Fiz. Tverd. Tela (Leningrad) **30**, 1605 (1988) [Sov. Phys. Solid State **30**, 928 (1988)].
7. V. I. Gavrilenko, A. V. Postnikov, N. I. Klyui, and V. G. Litovchenko, Phys. Status Solidi B **162**, 477 (1990).
8. P. J. Collwell and M. V. Klein, Phys. Rev. B **6**, 498 (1972).
9. N. T. Son, O. Kordina, A. O. Konstantinov, *et al.*, Appl. Phys. Lett. **65**, 3209 (1994).
10. C. Persson and U. Lindefelt, J. Appl. Phys. **82**, 5496 (1997).
11. W. R. L. Lambrecht, S. Limpijumnong, S. N. Rashkeev, and B. Segall, Phys. Status Solidi B **202**, 5 (1997).
12. C. Persson and U. Lindefelt, J. Appl. Phys. **86**, 5036 (1999).
13. B. K. Meyer, D. M. Hofmann, D. Volm, *et al.*, Phys. Rev. B **61**, 4844 (2000).
14. W. J. Choyke and L. Patrick, Phys. Rev. B **172**, 769 (1968).
15. G. B. Dubrovskiĭ and E. I. Radovanova, Fiz. Tverd. Tela (Leningrad) **11**, 680 (1969) [Sov. Phys. Solid State **11**, 549 (1969)].
16. O. V. Vakulenko and O. A. Govorova, Fiz. Tverd. Tela (Leningrad) **12**, 1857 (1970) [Sov. Phys. Solid State **12**, 1478 (1970)].
17. V. V. Makarov, Fiz. Tekh. Poluprovodn. (Leningrad) **6**, 1805 (1972) [Sov. Phys. Semicond. **6**, 156 (1972)].
18. B. E. Wheeler, Solid State Commun. **4**, 173 (1966).
19. V. I. Gavrilenko, V. A. Zuev, G. A. Katrich, and D. T. Tarashchenko, Fiz. Tekh. Poluprovodn. (Leningrad) **12**, 1621 (1978) [Sov. Phys. Semicond. **12**, 959 (1978)].
20. E. Biederman, Solid State Commun. **3**, 343 (1965).
21. B. Ellis and T. S. Moss, Proc. R. Soc. London, Ser. A **299**, 393 (1967).
22. I. S. Gorban', Yu. A. Marazuev, and A. S. Skirda, Fiz. Tverd. Tela (Leningrad) **14**, 780 (1972) [Sov. Phys. Solid State **14**, 664 (1972)].
23. M. P. Lisitsa, O. V. Vakulenko, Yu. S. Krasnov, and V. N. Solodov, Fiz. Tekh. Poluprovodn. (Leningrad) **5**, 2047 (1971) [Sov. Phys. Semicond. **5**, 1785 (1971)].
24. I. S. Gorban', V. P. Zavada, and A. S. Skirda, Fiz. Tverd. Tela (Leningrad) **14**, 3097 (1972) [Sov. Phys. Solid State **14**, 2654 (1972)].
25. O. V. Vakulenko, O. A. Govorova, and B. M. Shutov, Fiz. Tverd. Tela (Leningrad) **14**, 291 (1972) [Sov. Phys. Solid State **14**, 242 (1972)].
26. G. B. Dubrovskiĭ, A. A. Lepneva, and E. I. Radovanova, Phys. Status Solidi B **57**, 423 (1973).
27. I. S. Gorban' and A. S. Skirda, Ukr. Fiz. Zh. **26**, 228 (1981).
28. G. N. Violina, L. H. Yeh, and G. F. Kholuyanov, Fiz. Tverd. Tela (Leningrad) **5**, 3406 (1963) [Sov. Phys. Solid State **5**, 2500 (1963)].
29. G. N. Violina, B. I. Seleznev, and Yu. M. Tairov, Fiz. Tekh. Poluprovodn. (Leningrad) **7**, 1821 (1973) [Sov. Phys. Semicond. **7**, 1215 (1973)].
30. O. V. Vakulenko and B. M. Shutov, Fiz. Tekh. Poluprovodn. (Leningrad) **13**, 2002 (1979) [Sov. Phys. Semicond. **13**, 1166 (1979)].
31. Th. Stiasny and R. Helbig, Phys. Status Solidi A **162**, 239 (1997).
32. W. Suttrop, G. Pensl, W. J. Choyke, *et al.*, J. Appl. Phys. **72**, 3708 (1992).
33. O. V. Vakulenko and O. A. Guseva, Fiz. Tekh. Poluprovodn. (Leningrad) **15**, 1528 (1981) [Sov. Phys. Semicond. **15**, 886 (1981)].
34. S. Limpijumnong, W. R. L. Lambrecht, S. Rashkeev, and B. Segall, Phys. Rev. B **59**, 12890 (1999).
35. F. Engelbrecht, J. Zeman, G. Wellenhofer, *et al.*, Phys. Rev. B **56**, 7348 (1997).
36. C. Persson, U. Lindefelt, and B. E. Sernelius, Phys. Rev. B **60**, 16 479 (1999).
37. A. Imai, J. Phys. Soc. Jpn. **21**, 2610 (1966).
38. G. B. Dubrovskiĭ and A. A. Lepneva, Fiz. Tverd. Tela (Leningrad) **19**, 1252 (1977) [Sov. Phys. Solid State **19**, 729 (1977)].
39. A. H. G. de Mesquita, Acta Crystallogr. **23**, 610 (1967).
40. C. Kittel and A. Mitchell, Phys. Rev. **96**, 1488 (1954).
41. J. M. Luttinger and W. Kohn, Phys. Rev. B **97**, 869 (1955).
42. M. Ikeda, H. Matsunami, and T. Tanaka, Phys. Rev. B **22**, 2842 (1980).
43. A. I. Veĭnger, Fiz. Tekh. Poluprovodn. (Leningrad) **3**, 70 (1969) [Sov. Phys. Semicond. **3**, 52 (1969)].
44. G. E. Hardeman and G. V. Gerritsen, in *Silicon Carbide-1968*, Ed. by H. K. Henisch and R. Roy (Pergamon, Oxford, 1968; Mir, Moscow, 1972), Mater. Res. Bull. **4**, 261 (1969).
45. B. K. Ridley, *Quantum Processes in Semiconductors* (Clarendon, Oxford, 1982; Mir, Moscow, 1986), Chap. 5.
46. I. S. Gorban', V. A. Gubanov, and V. F. Orlenko, Fiz. Tverd. Tela (Leningrad) **23**, 525 (1981) [Sov. Phys. Solid State **23**, 295 (1981)].
47. I. S. Gorban', A. P. Krokhmal', and I. A. Rozhko, Fiz. Tverd. Tela (Leningrad) **31** (12), 126 (1989) [Sov. Phys. Solid State **31**, 2095 (1989)].

Translated by A. Sidorova-Biryukova

Semiconductors, Vol. 35, No. 11, 2001, pp. 1249–1251. Translated from Fizika i Tekhnika Poluprovodnikov, Vol. 35, No. 11, 2001, pp. 1306–1308.

ELECTRONIC AND OPTICAL PROPERTIES OF SEMICONDUCTORS

Magnetic Properties of $Pb_{1-x}Ge_xTe$ Alloys Doped with Ytterbium

E. P. Skipetrov*, N. A. Chernova*, L. A. Skipetrova*, A. V. Golubev*, and E. I. Slyn'ko**

** Moscow State University, Vorob'evy gory, Moscow, 119899 Russia*

e-mail: skip@mig.phys.msu.su

*** Institute of Material Science Problems, Chernovtsy, 274001 Ukraine*

Submitted February 14, 2001; accepted for publication April 2, 2001

Abstract—Temperature dependences of magnetic susceptibility and magnetic-field dependences of magnetization in the $Pb_{1-x-y}Ge_xYb_yTe$ ($0 \le x \le 0.02$, $y \le 0.065$) solid solutions were studied. It was found that diamagnetic response was replaced by the Curie–Weiss paramagnetic response as temperature decreased. This indicates that $Yb^{3+}(4f^{13})$ magnetic ions are present in the alloys. The magnetic ion concentration and the occupancy of the Yb-induced impurity band were determined from the experimental data. © *2001 MAIK "Nauka/Interperiodica".*

Doping of the IV–VI compounds and the corresponding alloys with variable-valence impurities radically affects the energy spectrum of the charge carriers. This circumstance gives rise to deep impurity levels (impurity bands) the energy position of which depends on the type of impurity, the alloy composition, temperature, pressure, and magnetic field [1, 2]. Due to this fact, a number of new physical effects are observed in the IV–VI doped semiconductors (Fermi-level pinning by the impurity level, slow relaxation of the nonequilibrium charge carriers, metal–insulator transitions in a quantizing magnetic field and under pressure, and others) which allow one to include them in a specific class of doped semiconductor materials. Initially only Group III elements (Al, Ga, In, and Tl) represented impurities with a variable valence. However, in recent years, this group of impurities was significantly expanded due to inclusion of the Cr, Yb, Eu, Gd, and Ce transition elements. Doping with these elements transforms IV–VI semiconductors into semimagnetic semiconductors [3–7].

Ytterbium holds a special place among all the impurities mentioned above. The reason for this is that the *f*-shell of Yb atoms is completely filled with electrons. Ytterbium ions substituting for the metal atoms in a crystal lattice can be both in magnetic and nonmagnetic states. The magnetic activity of these ions is directly related to their charge state and is controlled by the energy position of the deep impurity level relative to the band edges of the energy spectrum. The Yb ions in the Yb^{2+} ($4f^{14}5s^25p^6$) state, which form impurity levels occupied by electrons, are nonmagnetic and electrically neutral relative to the metal sublattice. At the same time, the Yb ions in the Yb^{3+} ($4f^{13}5s^25p^6$) state with unoccupied impurity levels are electrically active, and they have a localized magnetic moment. On the other hand, the degree of the impurity state occupation by electrons can vary due to redistribution of electrons between the level and the band as the alloy composition varies, as well as under the effect of external factors [8]. Therefore, the main aim of this study was to determine the concentration of the magnetic ions and the impurity band occupancy in the $Pb_{1-x}Ge_xTe$:Yb alloys with different Yb and Ge content. It was assumed that Ge concentration variation will enable us to change the impurity band position relative to the valence-band top, and that the variation in the Yb content will make it possible to change the position and total capacity of the impurity band.

Single crystal $Pb_{1-x-y}Ge_xYb_yTe$ ingots ($0 \le x \le 0.02$, $y \le 0.065$) were synthesized by the Bridgman–Stockbarger method. The germanium and ytterbium content was measured by X-ray fluorescence analysis. Samples in the shape of thick disks weighing 0.7–0.8 g were studied using an EG&G PARC M155 vibration-coil magnetometer. Temperature dependences of magnetic susceptibility χ and magnetic-field dependences of magnetization M were measured for each sample at temperatures of $5\ K \le T \le 300\ K$ in the magnetic fields as high as 0.5 T.

Typical temperature dependences of magnetic susceptibility for the alloys with different Yb content are shown in Fig. 1. Alloy magnetic susceptibility is a sum of two components: a diamagnetic χ_0 component, which, apparently, is temperature-independent (curve *1*), and a paramagnetic component, which rapidly increases as temperature decreases. The diamagnetic contribution, which is usually related to the susceptibility of the crystal lattice, is in good agreement with the well-known experimental data for undoped PbTe and $Pb_{1-x}Sn_xTe$ [9, 10] and decreases steadily with increasing Yb content. Such a decrease in the diamagnetic contribution

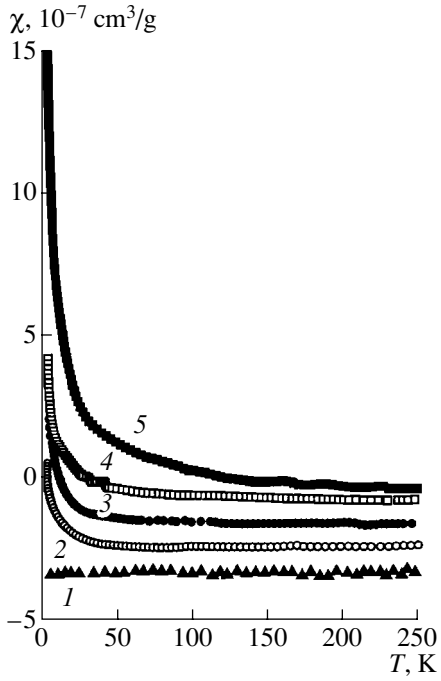

Fig. 1. The temperature dependences of magnetic susceptibility in $Pb_{1-y}Yb_yTe$ with Yb content y = (*1*) 0.0003, (*2*) 0.005, (*3*) 0.008, (*4*) 0.015, and (*5*) 0.065.

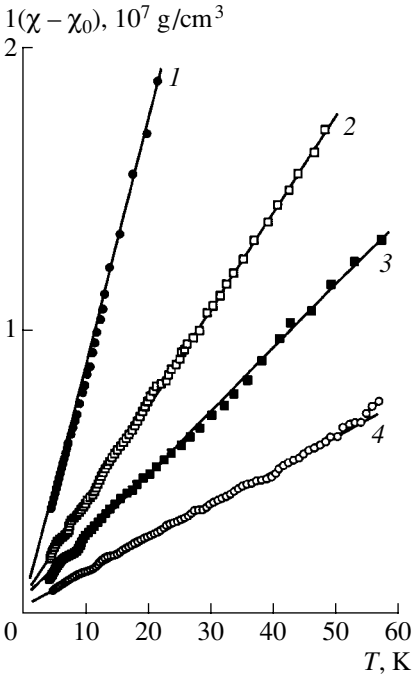

Fig. 2. Temperature dependences of reciprocal magnetic susceptibility of $Pb_{1-x-y}Ge_xYb_yTe$ (x = 0.02) with Yb content y = (*1*) 0.007, (*2*) 0.01, (*3*) 0.014, and (*4*) 0.019.

with increasing impurity concentration can be caused by an increase in the density of electron states in the impurity band, which stabilizes the Fermi level in the investigated alloys. In this case, an additional paramagnetic contribution to the magnetic susceptibility of the impurity band electrons is controlled by the density of states at the Fermi level located within the impurity band [11]. Previously, a similar decrease in the diamagnetic response has been observed, for example, when the Fermi level was brought into the impurity band of thallium as the hole concentration in PbTe doped with Tl increased [9].

Parameters of the $Pb_{1-x-y}Ge_xYb_yTe$ samples

Sample no.	x	y	$N_{Yb^{3+}}$, 10^{19} cm^{-3}	N_{Yb}, 10^{20} cm^{-3}	$N_{Yb^{3+}}/N_{Yb}$
1	0	0.0003	–	0.044	–
2	0	0.005	1.1	0.80	0.14
3	0	0.008	1.7	1.2	0.13
4	0	0.015	2.4	2.2	0.11
5	0	0.030	6.6	4.6	0.14
6	0	0.065	8.4	9.6	0.09
7	0.02	0.007	0.97	1.0	0.09
8	0.02	0.010	2.4	1.5	0.16
9	0.02	0.014	3.7	2.1	0.18
10	0.02	0.019	7.6	2.8	0.27

At low temperatures, a linear increase in magnetization typical of paramagnets is observed in weak magnetic fields. In this case, the magnetic susceptibility temperature dependences obey the Curie–Weiss law (Fig. 2):

$$\chi = \chi_0 + C/(T - \Theta), \quad (1)$$

where C is the Curie–Weiss constant, and Θ is the Curie temperature. Experimental data shown in Fig. 2 can be extrapolated by straight lines which intersect the abscissa at a small negative temperature ($\Theta \approx -2$ K). This indicates the existence of weak antiferromagnetic interaction between the magnetic centers. The Curie constant values calculated from the line slopes were used to estimate the magnetic center concentration. In this case, we assume that individual Yb^{3+} ions are the magnetic centers in the alloys under study. The ground electron state of these centers in the cubic crystalline field is the Γ_6 doublet. According to electron spin resonance data, the g-factor of this state is equal to 2.52, and the effective spin S = 1/2 [12]. In this case, the magnetic ion concentration $N_{Yb^{3+}}$ can be calculated from the Curie constant C obtained from the experiment:

$$N_{Yb^{3+}} = 3k_BC/(g^2\mu_B^2S(S+1)), \quad (2)$$

where k_B is the Boltzmann constant, and μ_B is the Bohr magneton.

Calculated concentrations $N_{Yb^{3+}}$ are listed in the table. Total concentrations of the ytterbium atoms N_{Yb} in the alloys were determined from the X-ray fluorescence analysis and are also given in the table. Comparison of these data shows that a fraction of the magnetic ions $N_{Yb^{3+}}/N_{Yb}$ in $Pb_{1-y}Yb_yTe$ is equal to 10–15% of the total Yb content, and is almost independent of the alloy composition. In Ge-containing alloys, the fraction of the magnetic ions is somewhat greater than in $Pb_{1-y}Yb_yTe$, and it increases with Yb concentration. At the same time, the magnetic center concentration increases steadily as the Yb concentration in the alloys increases.

In terms of the energy-band diagram of the Yb-doped $Pb_{1-x}Ge_xTe$ alloys, the magnetically active Yb^{3+} ion concentration corresponds to the concentration of unoccupied electron states in the Yb impurity band. In $Pb_{1-y}Yb_yTe$ crystals with a relatively low Yb concentration ($y \lesssim 0.03$), the impurity band is located in the valence band, and at low temperatures it pins the Fermi level near its edge [8]. As the Yb concentration increases, the impurity band apparently approaches the valence band edge, crosses it, and enters the band gap. A similar transformation of the energy spectrum also occurs as the Ge concentration in $Pb_{1-x-y}Ge_xYb_yTe$ increases, so that the impurity band is located in the band gap for any Yb concentration in the alloys with $x = 0.02$. In these conditions, the unoccupied states in the impurity band are obviously caused by the electron transitions from this band to the unoccupied states of the valence band. Concentration of these states is controlled mainly by the native structure defects of the acceptor type associated with the deviation from stoichiometry.

In the context of this model, an increase in the fraction of unoccupied electron states in the impurity band as the Ge concentration increases is quite understandable because all unoccupied states of the $Pb_{1-x-y}Ge_xYb_yTe$ ($x = 0.02$) valence band are occupied by electrons from the impurity band. In $Pb_{1-y}Yb_yTe$, only the states below the Fermi level located in the valence band are occupied. A steady increase in the magnetic Yb ion concentration (concentration of the unoccupied states in the impurity band) indicates that the deviation from the stoichiometric composition increases as the impurity concentration increases. Therefore, we may conclude that doping with Yb (as well as in other doped IV–VI semiconductors [13]) gives rise to self-compensation, i.e., the fractional compensation of the donor effect of the impurity by the native structure defects.

ACKNOWLEDGMENTS

This study was supported by the Russian Foundation for Basic Research, project no. 00-15-96784.

REFERENCES

1. V. I. Kaĭdanov and Yu. I. Ravich, Usp. Fiz. Nauk **45**, 51 (1985) [Sov. Phys. Usp. **28**, 31 (1985)].
2. B. A. Akimov, A. V. Dmitriev, D. R. Khokhlov, and L. I. Ryabova, Phys. Status Solidi A **137**, 9 (1993).
3. T. Story, Z. Wilamowski, E. Grodzicka, *et al.*, Acta Phys. Pol. A **84**, 773 (1993).
4. E. Grodzicka, W. Dobrowolski, T. Story, *et al.*, Acta Phys. Pol. A **90**, 801 (1996).
5. R. Denecke, L. Ley, G. Springholz, and G. Bauer, Phys. Rev. B **53**, 4534 (1996).
6. T. Story, M. Gorska, A. Lusakowski, *et al.*, Phys. Rev. Lett. **77**, 3447 (1996).
7. X. Gratens, S. Charar, M. Averous, *et al.*, Phys. Rev. B **56**, 8199 (1997).
8. E. P. Skipetrov, N. A. Chernova, E. L. Slyn'ko, and Yu. K. Vygranenko, Phys. Rev. B **59**, 12928 (1999).
9. K. I. Andronik, M. P. Boĭko, and A. V. Luzhkovskiĭ, Fiz. Tekh. Poluprovodn. (Leningrad) **22**, 1878 (1988) [Sov. Phys. Semicond. **22**, 1190 (1988)].
10. L. A. Fal'kovskiĭ, A. V. Brodovoĭ, and G. V. Lashkarev, Zh. Éksp. Teor. Fiz. **80**, 334 (1981) [Sov. Phys. JETP **53**, 170 (1981)].
11. S. V. Vonsovskiĭ, *Magnetism* (Nauka, Moscow, 1971; Wiley, New York, 1974).
12. S. Isber, S. Charar, X. Gratens, *et al.*, Phys. Rev. B **54**, 7634 (1996).
13. V. I. Kaĭdanov, S. A. Nemov, and Yu. I. Ravich, Fiz. Tekh. Poluprovodn. (St. Petersburg) **28**, 369 (1994) [Semiconductors **28**, 223 (1994)].

Translated by I. Kucherenko

Semiconductors, Vol. 35, No. 11, 2001, pp. 1252–1253. Translated from Fizika i Tekhnika Poluprovodnikov, Vol. 35, No. 11, 2001, pp. 1309–1310.

ELECTRONIC AND OPTICAL PROPERTIES OF SEMICONDUCTORS

On the Charge Transport Mechanism in *n*-InSb Films

Yu. A. Nikol'skiĭ

Borisoglebsk State Pedagogical Institute, Borisoglebsk, Voronezh oblast, 397160 Russia

Submitted January 22, 2001; accepted for publication April 3, 2001

Abstract—The structure of the conduction band bottom of polycrystalline and recrystallized *n*-InSb films grown on silicon dioxide substrates has been studied by measuring the temperature dependence of the electrical conductivity in the intrinsic conductivity range. Linear dependences $\ln\sigma = f(10^3/T)$ with different slopes can be observed in heterogeneous semiconductors in the intrinsic conductivity range. The percolation level has been determined from the average of ΔE_1, ΔE_2, …, ΔE_n to be 0.165 eV for polycrystalline and 0.2 eV for recrystallized films. *© 2001 MAIK "Nauka/Interperiodica".*

Heterogeneous structures characterized by an apparently anomalous conductivity mechanism and by optical, photoelectric, and other phenomena have recently attracted much attention from researchers working in the field of semiconductor physics. The intense interest in heterogeneous media is due to the fact that, in some cases, the appearing anomalies give rise to fundamentally new physical phenomena in semiconductors and in multi-layer semiconductors and other structures. It is desirable to understand these anomalous properties in order to create new semiconductor devices.

Many researchers have been developing models that can describe these phenomena in heterogeneous structures.

The fundamentals of the theory of percolation conduction in heterogeneous media were presented in [1]. Concrete problems were solved for heterogeneous media with high- and low-resistance inclusions in [2]. There have been reports providing a satisfactory description of the anomalous behavior of the Hall effect and photoconductivity in heterogeneous *n*-InSb films [3, 4].

We made an attempt to model the charge transport mechanism in polycrystalline and recrystallized *n*-InSb films grown on silicon dioxide substrates, on the basis of experimental data and theoretical results [5, 6].

Polycrystalline *n*-InSb films were prepared by the discrete evaporation of crystalline *n*-InSb powder with carrier density $n \le 2 \times 10^{15}$ cm^{-3} at room temperature onto silicon dioxide substrates kept at 300, 350, and 400°C.

Recrystallized *n*-InSb films were obtained by thermal recrystallization of polycrystalline films.

Results of the structural investigations of the polycrystalline and recrystallized *n*-InSb films were reported in [7]. The thickness of the polycrystalline and recrystallized films was 1.0–2.0 μm. The carrier density was determined from Hall measurements to be in the range 5×10^{16}–5×10^{17} cm^{-3} at room temperature.

The primary goal of this study was to elucidate the conduction band structure in these films. If acceptors are also present in an *n*-type semiconductor, then, at exact compensation when N_D and N_A are rather close, the electronic gas is nonideal. Electrons are in a field with random potential induced by donors and acceptors. The random potential can be regarded as a deformation of the conduction band bottom ε_c. At extremely exact compensation, the characteristic amplitude of the random potential becomes larger than ε_F defined by

$$\varepsilon_F = (3\pi^2)^{2/3}\hbar^2 n^{2/3}/2m.$$

In this case, electrons only reside in the deepest places of the potential relief, forming isolated droplets (Fig. 1). The electrical conduction is effected by thermal activation of electrons to the so-called percolation level.

Intrinsic conduction occurs in *n*-InSb beginning at temperatures $\gtrsim 300$ K for samples with a carrier density of $\sim 5 \times 10^{16}$ cm^{-3}. We propose to study the structure of the conduction band bottom by measuring the temperature dependence of the electrical conductivity in the intrinsic conduction mode. To determine accurately the activation energy from conductivity measurements, knowledge of how the carrier mobility depends on temperature is necessary. Since the key mechanism determining the *n*-InSb mobility at $T >$ 200 K is scattering on polar phonons, it can be assumed that, at these temperatures, $\mu \propto T^{-\alpha}$, where $\alpha = 3/2$. Then, ΔE, determined from the dependence $\ln(\sigma T^{(\alpha - 3/2)}) = f(10^3/T)$, can be simply found from the dependence $\ln\sigma = f(10^3/T)$. The electronic wave function is strongly distorted in heterogeneous semiconductors because of the carrier interaction with heterogeneities, which leads to a substantial change in the parabolic shape of the conduction band bottom. As a result, it is possible that no linear dependence is observed in the $\ln\sigma = f(10^3/T)$ plot in the intrinsic conductivity mode. Deviation from linear dependence in the intrinsic conductivity range may occur at a high temperature

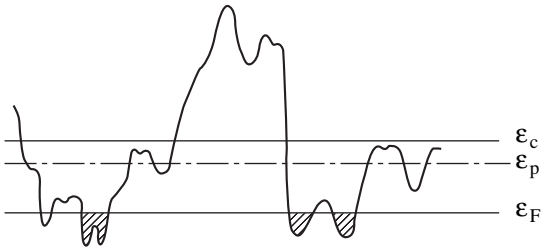

Fig. 1. Energy diagram of a compensated semiconductor. Wavy line represents local deformations of the conduction band bottom; ε_c is the conduction band bottom in the absence of impurity potential, ε_F is the Fermi level, and ε_p is the percolation level. Regions occupied by electrons (electronic droplets) are shaded.

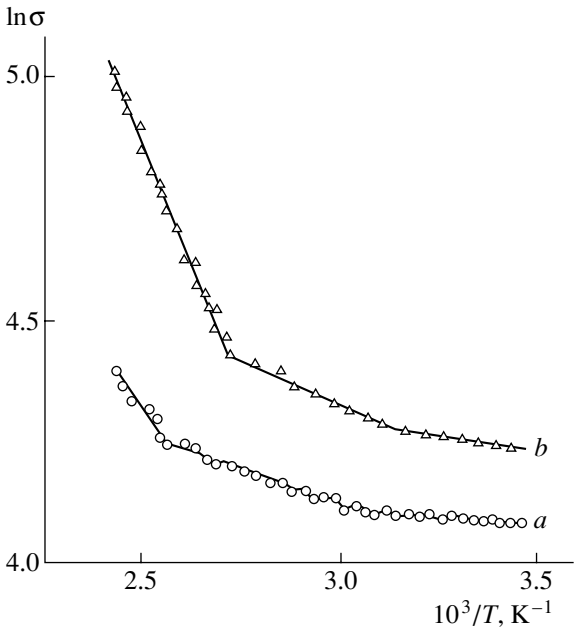

Fig. 2. Typical temperature dependence of the electrical conductivity of (*a*) polycrystalline and (*b*) recrystallized *n*-InSb films (t_n = 300°C). σ is given in Ω^{-1} cm^{-1}.

owing to degeneracy. However, since $T < 400$ K in our measurements, and the maximum kT is ≈0.035 eV, degeneracy does not occur.

Repeated measurements on polycrystalline and recrystallized films in the intrinsic conductivity mode give a set of linear portions, which can be used to estimate the activation energies corresponding to the energy of carrier transition from the valence to the conduction band (Figs. 2a and 2b). Having determined these values ΔE_1, ΔE_2, …, ΔE_n ($\Delta E = 2kT_1T_2\ln(\sigma_2/\sigma_1)/(T_2 - T_1)$) and having found the arithmetic mean, we can thus estimate the average activation energy. This value is called the percolation level. For example, the percolation level is, respectively, 0.053, 0.165, and 0.275 eV for polycrystalline films obtained at substrate temperatures of 300, 350, and 400°C, and 0.2 eV for a recrystallized film.

The study of the structure of the conduction band bottom in polycrystalline *n*-InSb films indicates that, with increasing substrate temperature, i.e., improving the equilibrium conditions of film growth, the samples approach stoichiometric composition and, thus, the carrier density becomes lower. Therefore, we have intrinsic conduction at lower temperatures in samples with a higher substrate temperature and, consequently, the percolation level approaches the energy gap.

The heterogeneous structure formed in recrystallized films grown on silicon dioxide substrates strongly departs from equilibrium because of the presence of macroscopic defects in the process of recrystallization. The percolation level found in the high-temperature range is 0.2 eV.

REFERENCES

1. B. I. Shklovskiĭ and A. L. Éfros, Usp. Fiz. Nauk **117**, 401 (1975) [Sov. Phys. Usp. **18**, 845 (1975)].
2. E. V. Kuchis, *Galvanomagnetic Effects and Methods for Studying Them* (Nauka, Moscow, 1990).
3. Yu. A. Nikol'skiĭ, Fiz. Tekh. Poluprovodn. (Leningrad) **24**, 1322 (1990) [Sov. Phys. Semicond. **24**, 831 (1990)].
4. Yu. A. Nikol'skiĭ, Fiz. Tekh. Poluprovodn. (Leningrad) **28**, 1972 (1994) [Semiconductors **28**, 1087 (1994)].
5. Yu. A. Nikol'skiĭ and S. E. Zyuzin, in *Bulletin of Voronezh State Technical University, Series Material Science* (Voronezh. Gos. Tekh. Univ., Voronezh, 1998), p. 90.
6. Yu. A. Nikol'skiĭ and V. V. Polyakov, in *Collection of Scientific Works of Borisoglebsk Pedagogical Institute* (Borisogl. Ped. Inst., Borisoglebsk, 1996), p. 76.
7. V. A. Kas'yan, P. I. Ketrush, Yu. A. Nikol'skiĭ, and F. I. Pasechnik, *Thin Films of Indium Antimonide* (Shtinitsa, Kishinev, 1989).

Translated by S. Ktitorov

Semiconductors, Vol. 35, No. 11, 2001, pp. 1254–1258. Translated from Fizika i Tekhnika Poluprovodnikov, Vol. 35, No. 11, 2001, pp. 1311–1315.

ELECTRONIC AND OPTICAL PROPERTIES OF SEMICONDUCTORS

Effect of Bismuth Impurity on Carrier Density in PbSe:Bi:Se Epitaxial Layers

V. A. Zykov, T. A. Gavrikova, V. I. Il'in, S. A. Nemov, and P. V. Savintsev

St. Petersburg State Technical University, St. Petersburg, 195251 Russia

Submitted March 12, 2001; accepted for publication April 3, 2001

Abstract—The dependence of the Hall carrier density on bismuth concentration, n, $p = f(N_{Bi})$, in PbSe:Bi:Se/BaF_2 films has been studied. The films were grown by vacuum condensation from two independent molecular beams (PbSe:Bi and Se_2) mixed directly at the surface of a (111)BaF_2 substrate heated to 350°C. The bismuth concentration in the stock was 0–0.3 at. %. Two specific portions can be distinguished in the experimental n, $p = f(N_{Bi})$ dependence. At $N_{Bi} > 0.0375$ at. %, the electron density is close to N_{Bi}; at low bismuth concentrations, $N_{Bi} < 0.0375$ at. %, the linear run of the $n = f(N_{Bi})$ dependence is violated, and the conduction changes to p-type. All the doped films under study are saturated with selenium. This is a necessary condition for obtaining the highest electron densities in the films at N_{Bi} corresponding to the linear portion of the $n = f(N_{Bi})$ dependence. The results are discussed in terms of a thermodynamic model of the impurity interaction with intrinsic defects in PbSe, taking into account the amphoteric behavior of bismuth atoms in lead selenide. © *2001 MAIK "Nauka/Interperiodica".*

The manifestation of the electrical properties of an impurity in lead chalcogenides largely depends on its interaction with the intrinsic defects of a compound. This statement finds numerous verifications in experimental data on the electrical properties of crystals and films of binary and ternary lead chalcogenides doped with elements of Groups I, III, and VII of the periodic table [1, 2]. These impurities are characterized by a strictly defined position of their atoms in one of the sublattices of a compound. For Group V impurity atoms, the interaction with intrinsic defects is complicated by the possibility of these atoms residing in both sublattices with probabilities dependent on the type and density of predominant intrinsic defects, similar to the behavior of Ge or Si in GaAs [3]. Amphoteric behavior of antimony in lead chalcogenides was observed by Mössbauer spectroscopy in the studies of Sb localization in the sublattices of PbS [4] and PbTe [5], which appeared to depend directly on how the stoichiometry was violated. It has been established that antimony preferentially resides in the anion sublattice in lead-rich samples and in the cation sublattice in chalcogen-rich samples.

Data on Bi behavior in lead chalcogenides are somewhat contradictory. Some authors suppose that Bi in lead chalcogenides resides only in the cation sublattice, behaving as a donor [6, 7]. By contrast, data on the electrical properties of PbTe:Bi crystals with an excess of Te [8] indicate a possible acceptor behavior of bismuth, which implies the residing of Bi in the anion sublattice. In our study of the electrical properties of Bi-doped PbSe films, we also obtained indirect evidence of the amphoteric behavior of this impurity [9].

The clearest evidence of the possible redistribution of bismuth between the sublattices in a compound is furnished by data concerning the influence exerted by the excess of a component of the compound on the electrical properties of PbSe:Bi films with fixed impurity content ($N_{Bi} = 0.075$ at. %) [9]. Deviations from stoichiometry in PbSe:Bi films were controlled by introducing excess [Se] or [Pb] into the vapor phase during deposition. An increase in the donor concentration in a PbSe:Bi film was observed on raising the Se content in the vapor, which contradicts the assumption of the acceptor behavior of super-stoichiometric Se (the source of acceptor lead vacancies) in pure PbSe. At a higher excess of selenium, the density of free carriers became close to the bismuth concentration in the stock and remained unchanged with the further increase in Se content. This fact was interpreted as resulting from the transfer of the entire amount of bismuth into the lead sublattice (Bi_{Pb}), where this impurity behaves as a donor donating one electron per impurity atom into the conduction band. In doing so, it is assumed that the role of the excess selenium is limited to the generation of vacancies in the cation sublattice. For lead-rich films, the pattern seems to be more complicated. In the range where the concentrations $[Bi_{Pb}]$ and $[Bi_{Se}]$ are close (a small excess of lead), the carrier density is governed by interstitial lead behaving as a single-ionized donor [10]. At a high excess of lead, acceptor centers appear in the film, which correspond to the transfer of bismuth into the chalcogen sublattice (Bi_{Se}). The appearance of acceptor centers in PbSe:Bi films with a high excess of lead is, in itself, a strong argument in favor of the model assuming that bismuth resides in the anion sublattice,

since thermal generation of holes from Bi atoms is only possible in this position.

The subject of discussion in the present study is how carrier density depends on the bismuth content in PbSe films fabricated under conditions most favorable for bismuth localization in the cation sublattice.

The films were grown by vacuum epitaxy from molecular beams by the method described elsewhere [9]. The deposition was performed from two independent sources, one with bismuth-containing lead selenide, and the other, with elementary selenium. The bismuth content of the stock was varied in the range 0.02–0.4 at. %. The vapor beams were mixed directly on the substrate surface. The process parameters were as follows: substrate temperature T_S = 350°C; PbSe:Bi source temperature 700°C; the selenium source temperature T_{Se} was varied depending on bismuth content and was chosen so as to ensure the maximum possible saturation of the doped sample with selenium. Previous experiments have shown that under these conditions all bismuth is transferred from the stock into a film [9].

The electrical properties of PbSe:Bi:Se films were studied by measuring the Hall effect and conductivity. Figures 1 and 2 present the Hall carrier density, n, p (T = 300 K) in relation to the Bi content of the stock for films saturated with selenium. The experimental $n, p = f(N_{Bi})$ dependence in Fig. 1 can be divided into two portions. At bismuth concentrations 0.05–0.3 at. %, the films are n-type, with a linear relation between n and N_{Bi} (Fig. 2) and $n = N_{Bi}$. At bismuth concentrations in the stock lower than 0.05 at. %, the behavior of the $n = f(N_{Bi})$ dependence changes. In this range, the dependence is no longer linear, the electron density falls steeply with decreasing bismuth concentration, and, at $N_{Bi} < 0.0375$ at. %, holes become the dominant carriers—their density in undoped film (N_{Bi} = 0) reaching values of about $(2–5) \times 10^{18}$ cm^{-3}.

With bismuth assumed to reside in the cation sublattice, where it behaves as a donor giving one electron per impurity atom, the electroneutrality equation can be written as

$$n - p = [Bi^{+}_{Pb}] - 2[V^{2-}_{Pb}].$$

Analysis of this expression offers a qualitative explanation of the obtained experimental dependence $n - p = f(N_{Bi})$. Indeed, at high N_{Bi}, when $[Bi^{+}_{Pb}] \gg 2[V^{2-}_{Pb}]$, the vacancies in the lead sublattice can be disregarded, and the electroneutrality equation takes the form $(n - p) = [Bi^{+}_{Pb}]$, which is in satisfactory agreement with the experiment (Fig. 2). At low bismuth concentrations (in the experiment, below 0.05 at. %), such that $[V^{2-}_{Pb}] \gg [Bi^{+}_{Pb}]$, the effect of the acceptor vacancies cannot be neglected. This must disrupt the linear run of the $n - p = f(N_{Bi})$ dependence because of increasing hole density, inversion of the conductivity type, and attainment of a

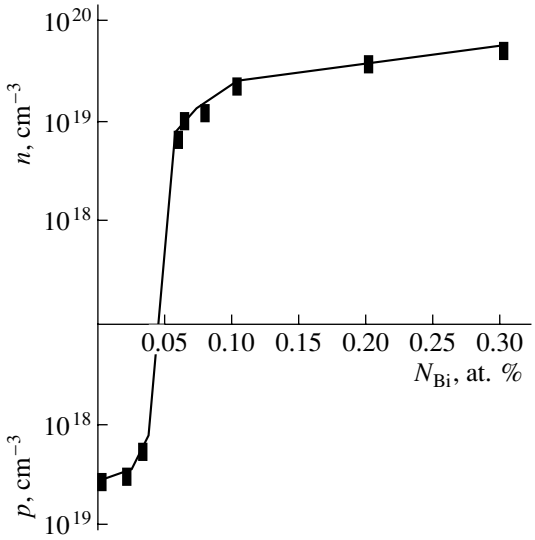

Fig. 1. Hall carrier density vs. bismuth content in PbSe:Bi films saturated with Se (T = 300 K).

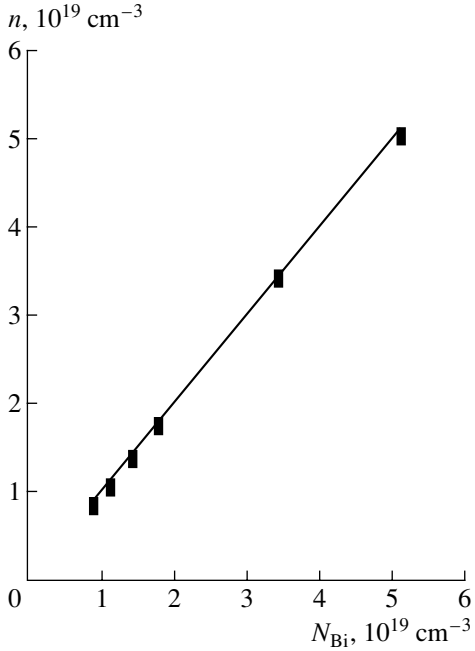

Fig. 2. Linear portion of the dependence of the Hall carrier density on bismuth content in PbSe:Bi films saturated with Se (T = 300 K).

value $p \approx (2–5) \times 10^{18}$ cm^{-3} corresponding to the limiting solubility of selenium in pure PbSe at $T = T_S$.

As can be seen, the analysis of electroneutrality in doped lead selenide films allows a qualitatively correct description of their electrical properties. However, this analysis is far from being complete, since it fails to take into account the fact that all the presented experimental data refer to films saturated with selenium to the maximum possible extent. The last remark is important,

since variation of the selenium content in the vapor and solid phases can change the carrier density in PbSe:Bi films by several orders of magnitude [9]. Taking this fact into account requires an approach other than just a simple analysis of the complete equilibrium of intrinsic defects in a semiconductor compound in the presence of an impurity, as was done, e.g., in [6]. In the present study, we make an attempt to analyze the $n - p = f(N_{Bi})$ dependence, taking into consideration the possible redistribution of impurities between the sublattices of a compound. Our analysis is based on the approach developed in [3, 11] to describe the behavior of amphoteric impurities in III–V semiconductor compounds.

In terms of the concept of the amphoteric behavior of bismuth in lead selenide, the equilibrium distribution of impurities between the sublattices of the compound is described by the reaction

$$\mathrm{Bi}_{\mathrm{Se}}^0 + V_{\mathrm{Pb}}^0 = \mathrm{Bi}_{\mathrm{Pb}}^0 + V_{\mathrm{Se}}^0, \quad (1)$$

where V_{Pb} and V_{Se} denote the lead and selenium vacancies, and the subscript "0" designates electrically neutral particles. For this reaction, the chemical potentials are related by

$$\mu(\mathrm{Bi}_{\mathrm{Se}}^0) + \mu(V_{\mathrm{Pb}}^0) = \mu(\mathrm{Bi}_{\mathrm{Pb}}^0) + \mu(V_{\mathrm{Se}}^0). \quad (2)$$

Assuming, as in [3], that point defects, as well as impurities, form an ideal diluted solution in a PbSe crystal, we obtain an expression for the ratio of the Bi concentrations in the sublattices:

$$\frac{[\mathrm{Bi}_{\mathrm{Se}}^0]}{[\mathrm{Bi}_{\mathrm{Pb}}^0]} = \frac{[V_{\mathrm{Se}}^0]}{[V_{\mathrm{Pb}}^0]} \times \exp\left[\frac{g(\mathrm{Bi}_{\mathrm{Pb}}^0) - g(\mathrm{Bi}_{\mathrm{Se}}^0) + g(V_{\mathrm{Se}}^0) - g(V_{\mathrm{Pb}}^0)}{kT}\right]. \quad (3)$$

Here, $g(V_{\mathrm{Se}}^0)$ and $g(V_{\mathrm{Pb}}^0)$ are the free energies of vacancy formation, and $g(\mathrm{Bi}_{\mathrm{Se}}^0)$ and $g(\mathrm{Bi}_{\mathrm{Pb}}^0)$, the free energies of Bi dissolution in, respectively, the cation and anion sublattices of PbSe.

The expression for the ratio of the vacancy concentrations $[V_{\mathrm{Se}}^0]/[V_{\mathrm{Pb}}^0]$, obtained in the analysis of the complete equilibrium of intrinsic defects in pure PbSe with account of [3, 10], has the form

$$\frac{[V_{\mathrm{Se}}^0]}{[V_{\mathrm{Pb}}^0]} = \frac{K_2^2}{K_1} P_{\mathrm{Se}_2}^{-1}, \quad (4)$$

where

$$K_1 = N^2 \exp\left[-\frac{g(V_{\mathrm{Se}}^0) + g(V_{\mathrm{Pb}}^0)}{kT}\right]$$

is the equilibrium constant of the reaction of lead and selenium vacancy formation;

$$K_2 = N \exp\left[\frac{\mu(\mathrm{Se}_{\mathrm{Se}}^0) - g(V_{\mathrm{Se}}^0) - \varphi(T)}{kT}\right]$$

is the constant determining the equilibrium concentrations of intrinsic defects depending on the selenium content in vapor; N is the number of sites in the anion (cation) sublattice of PbSe; and P_{Se_2} is the partial pressure of selenium in the vapor phase. Substituting (4) into (3), we obtain

$$\frac{[\mathrm{Bi}_{\mathrm{Se}}^0]}{[\mathrm{Bi}_{\mathrm{Pb}}^0]} = a P_{\mathrm{Se}_2}^{-1}, \quad (5)$$

where

$$a = A(T) \exp\left[\frac{g(\mathrm{Bi}_{\mathrm{Pb}}^0) - g(\mathrm{Bi}_{\mathrm{Se}}^0)}{kT}\right],$$

and $A(T)$ depends only on temperature. On augmenting (5) with the condition $[\mathrm{Bi}_{\mathrm{Se}}^0] + [\mathrm{Bi}_{\mathrm{Pb}}^0] = N_{\mathrm{Bi}}$ (N_{Bi} is the total amount of introduced bismuth), we have

$$[\mathrm{Bi}_{\mathrm{Pb}}^0] = \frac{N_{\mathrm{Bi}} P_{\mathrm{Se}_2}}{(a + P_{\mathrm{Se}_2})}. \quad (6)$$

Relation (6) offers a satisfactory qualitative description of the experimental data on the influence exerted by an excess of selenium on the electrical properties of PbSe:Bi films, indicating that the introduction of excess selenium favors localization of bismuth in the cation sublattice where Bi behaves as a donor; moreover, at high enough P_{Se_2}, practically the whole amount of Bi is in $\mathrm{Bi}_{\mathrm{Pb}}$ sites. Indeed, if P_{Se_2} is so small that the condition $a > P_{\mathrm{Se}_2}$ is satisfied, $(a + P_{\mathrm{Se}_2}) \approx a$, and the bismuth concentration in the cation sublattice depends linearly on the partial pressure of selenium, $[\mathrm{Bi}_{\mathrm{Pb}}^0] = N_{\mathrm{Bi}} P_{\mathrm{Se}_2}/c$, where c is a constant. By contrast, at high P_{Se_2}, sufficient for the condition $a \ll P_{\mathrm{Se}_2}$ to be satisfied, $(a + P_{\mathrm{Se}_2}) \approx P_{\mathrm{Se}_2}$ and $[\mathrm{Bi}_{\mathrm{Pb}}^0] = N_{\mathrm{Bi}}$, which means that the whole amount of bismuth is transferred to the cation sublattice. The leveling-off of the carrier density in the isothermal (T_S = const) curve describing the dependence $n - p = f(P_{\mathrm{Se}_2})$ [8] corresponds to this range of P_{Se_2} values. It is noteworthy that for the discussed limiting case of Bi residing solely in the cation sublattice of PbTe, the general tendency for the bismuth solubility to increase has also been predicted by thermodynamic calculations [6].

Taking into account the statistics of the electron gas [3] in the case of the simultaneous existence of donor

(Bi_{Pb}) and acceptor (Bi_{Se}) centers in PbSe gives the concentration ratio of the ionized impurities:

$$\frac{[Bi^+_{Pb}]}{[Bi^-_{Se}]} = \frac{[Bi^0_{Pb}]}{[Bi^0_{Se}]}\frac{N_C}{N_V}\frac{p}{n}\exp\left(-\frac{\Delta E_D - \Delta E_A}{kT}\right), \quad (7)$$

which, in view of Eq. (4), transforms into

$$\frac{[Bi^+_{Se}]}{[Bi^-_{Pb}]} = K_3\left(\frac{n}{n_i}\right)^2,$$
$$K_3 = \frac{N_V a}{N_C}P^{-1}_{Se_2}\exp\left(\frac{\Delta E_D - \Delta E_A}{kT}\right). \quad (8)$$

Here, N_C and N_V are the densities of states in the conduction and valence bands; ΔE_D and ΔE_A are the ionization energies of the bismuth impurity in donor and acceptor states, respectively; and n_i is the intrinsic carrier concentration. At high temperatures, where all impurity centers are ionized,

$$\frac{[Bi^0_{Se}]}{[Bi^0_{Pb}]} = K_3\left(\frac{n}{n_i}\right)^2. \quad (9)$$

The obtained relation shows that the incorporation of impurities into the sublattices of a compound depends on the partial pressure of the component vapor and the carrier density. According to (8) and (9), an increase in P_{Se_2} leads to a decrease in the $[Bi^0_{Se}]/[Bi^0_{Pb}]$ ratio, i.e., to an increasing bismuth fraction in the cation sublattice. By contrast, with increasing electron density in the film, the fraction of bismuth in lead sites decreases in proportion to n^{-2}. For films of *n*-type conduction, with $n/n_i > 1$, the condition for bismuth to reside predominantly in the cation sublattice is $K_3 < 1$.

Taking into account that the electrical properties of PbSe:Bi films were measured at $T_0 = 300$ K, which differed from the film growth temperature T_S, the electron density and the concentration of an amphoteric impurity in an *n*-type semiconductor without permanent compensation are related by [11]:

$$N_{Bi} = \frac{1 + (K_3/4)D^2}{1 - (K_3/4)D^2},$$
$$D = n_0/n_i + [4 + (n_0/n_i)^2]^{1/2}, \quad (10)$$

where n_0 is the electron density at $T = T_0$, and n_i is the intrinsic carrier density at $T = T_S$. The run of the $n_0 = f(N_{Bi})$ dependence, i.e., the experimental curve we study, depends on the ratio of the room temperature electron density to the intrinsic density at T_S, which is equal to 1.7×10^{18} cm^{-3} at $T_S = 350$°C.

Correlating the experimental carrier densities with n_i, we can conclude that, for the linear portion of the $n_0 = f(N_{Bi})$ dependence, the ratio $n_0/n_i > 1$, or even $n_0/n_i \gg 1$. In this case, expression (10) transforms for very small K_3 values into

$$N_{Bi} = n_0\frac{1 + K_3(n_0/n_i)^2}{1 - K_3(n_0/n_i)^2}. \quad (11)$$

When the term $K_3(n_0/n_i)^2$ is small compared with unity, $N_{Bi} = n_0$. In its turn, the smallness of $K_3(n_0/n_i)^2$ means, according to (9), that the ratio $[Bi^0_{Se}]/[Bi^0_{Pb}]$ is also small, i.e., bismuth mainly resides in the cation sublattice.

The problem becomes somewhat more complicated if the compensation by intrinsic defects (in our experiment, the acceptor vacancies of lead, V_{Pb}) is taken into account. In this case, the electroneutrality equation has the form

$$2[V^{2-}_{Pb}] + n_0 = [Bi^-_{Se}] - [Bi^+_{Pb}], \quad (12)$$

and n_0 and N_{Bi} are related by

$$N_{Bi} = (n_0 + 2[V^{2-}_{Pb}])\frac{1 + K_3(n_0/n_i)^2}{1 - K_3(n_0/n_i)^2}. \quad (13)$$

Evidently, at carrier densities n_0 comparable with or lower than $[V^{2-}_{Pb}]$, a deviation from the linearity of $n_0 = f(N_{Bi})$ must be observed, accompanied by a decrease in the electron density, which is actually the case in this experiment.

Thus, it is possible to describe both the dependence of the carrier density on the bismuth content and the unusual influence of selenium on the carrier density in PbSe:Bi by invoking the concept of the amphoteric behavior of bismuth in lead selenide films obtained by vacuum deposition from PbSe:Bi stock with a strong excess of selenium in the vapor phase. Undoubtedly, the proposed model is formal and gives no insight into the physical factors determining where an impurity atom resides in the PbSe crystal lattice. Analysis of the obtained expressions shows that the $[Bi^0_{Se}]/[Bi^0_{Pb}]$ value depends on pressure P_{Se_2} and also on the carrier density as $(n_0/n_i)^2$; however, we believe that a substantial, and, possibly, key contribution is made by the relation between the energies $g(Bi^0_{Pb})$ and $g(Bi^0_{Se})$, on which $[Bi^0_{Se}]/[Bi^0_{Pb}]$ depends exponentially [see (3)]. According to [11], these energies are determined by the energies of chemical bonding between the impurity atoms and the host material and also by the energy of elastic deformation of the lattice, which is to be taken into account because of the different sizes of the impurity and the substituted host atom. Finally, we cannot exclude the influence of the electron subsystem on the impurity distribution, e.g., via the self-compensation mechanism, which is effective in a number of semiconductors including lead chalcogenides [8, 12].

To conclude, it is worth noting that the PbSe:Bi:Se films under study have been fabricated by a technology which prevents the formation of interstitial lead in the matrix; at the same time, these films have *n*-type conduction, which means that they can interact with oxygen and, therefore, are of interest as starting materials for the fabrication of photosensitive devices by conventional lead chalcogenide technologies.

REFERENCES

1. R. Dornhaus, G. Nimtz, and B. Schlicht, *Narrow-Gap Semiconductors* (Springer-Verlag, Berlin, 1983).
2. V. I. Kaĭdanov, S. A. Nemov, and Yu. I. Ravich, Fiz. Tekh. Poluprovodn. (St. Petersburg) **28**, 360 (1994) [Semiconductors **28**, 223 (1994)].
3. N. S. Ratova and V. I. Fistul', Fiz. Tekh. Poluprovodn. (Leningrad) **4**, 1109 (1970) [Sov. Phys. Semicond. **4**, 939 (1970)].
4. V. F. Masterov, F. S. Nasredinov, P. P. Seregin, *et al.*, Fiz. Tekh. Poluprovodn. (St. Petersburg) **33**, 913 (1999) [Semiconductors **33**, 836 (1999)].
5. V. F. Masterov, F. S. Nasredinov, S. A. Nemov, *et al.*, Fiz. Tekh. Poluprovodn. (St. Petersburg) **31**, 1321 (1997) [Semiconductors **31**, 1138 (1997)].
6. N. S. Golovanova, V. P. Zlomanov, O. I. Tananaeva, and L. D. Licheva, Izv. Akad. Nauk SSSR, Neorg. Mater. **20** (4), 574 (1984).
7. T. C. Harman, J. Nonmet. **1**, 183 (1973).
8. L. I. Bytenskiĭ, V. I. Kaĭdanov, V. P. Maksenko, *et al.*, Fiz. Tekh. Poluprovodn. (Leningrad) **18**, 489 (1984) [Sov. Phys. Semicond. **18**, 303 (1984)].
9. T. A. Gavrikova, V. A. Zykov, and S. A. Nemov, Fiz. Tekh. Poluprovodn. (St. Petersburg) **29**, 309 (1995) [Semiconductors **29**, 154 (1995)].
10. A. V. Novoselova and V. P. Zlomanov, Curr. Top. Mater. Sci. **7**, 643 (1981).
11. V. I. Fistul', *Amphoteric Impurities in Semiconductors* (Metallurgiya, Moscow, 1992).
12. N. V. Agrinskaya and T. V. Mashovets, Fiz. Tekh. Poluprovodn. (St. Petersburg) **28**, 1505 (1994) [Semiconductors **28**, 843 (1994)].

Translated by D. Mashovets

Semiconductors, Vol. 35, No. 11, 2001, pp. 1259–1262. Translated from Fizika i Tekhnika Poluprovodnikov, Vol. 35, No. 11, 2001, pp. 1316–1319.

ELECTRONIC AND OPTICAL PROPERTIES OF SEMICONDUCTORS

Photoelectric Phenomena in ($\mu c_x a_{1-x}$)-Si:H/*c*-Si Heterostructures

H. Mell*, Yu. A. Nikolaev, V. Yu. Rud'***, Yu. V. Rud'**, and E. I. Terukov****

** Phillips-University, D-35032, Marburg, Germany*

*** Ioffe Physicotechnical Institute, Russian Academy of Sciences, Politekhnicheskaya ul. 26, St. Petersburg, 194021 Russia*

e-mail: yu.nikolaev@pop.ioffe.rssi.ru

**** St. Petersburg State Technical University, ul. Politekhnicheskaya 29, St. Petersburg, 195251 Russia*

Submitted April 11, 2001; accepted for publication April 19, 2001

Abstract—Heterostructures ($\mu c_x a_{1-x}$)-Si:H/*c*-Si with a various volume fraction *x* of microcrystalline and amorphous Si phases were obtained by plasmochemical deposition. The fraction variation was achieved by changing the silane content in H_2. The steady-state current–voltage characteristics and spectral dependences of photosensitivity of the structures obtained were investigated. The latter dependences were recorded by exposing the samples to the natural and linearly polarized light in relation to the phase composition of thin ($d_1 \cong 0.6$–0.8 μm) films of microcrystalline and amorphous Si. The photovoltaic effect and induced photopleochroism of the structures obtained were detected. The prospects of using a new type of heterojunction in photoconverters of natural and linearly polarized light were assessed. © *2001 MAIK "Nauka/Interperiodica".*

The discovery of efficient photoluminescence and electroluminescence of porous Si (*P*-Si) at room temperatures in the visible spectral range revealed new possibilities of controlling the fundamental properties of semiconductors solely by decreasing their dimensionality [1, 2]. Simultaneously, this discovery stimulated the development of new processes of fabricating thin-film materials, which include nanocrystallites and microcrystallites. The glow-discharge plasmochemical deposition from silane diluted by H_2 (H_2 content less than 3%) makes it possible to obtain thin Si films in the form of an amorphous (*a*-Si:H) matrix with inclusions of Si microcrystallites (μ*c*) [3–6]. The size of Si crystallites in these films is usually within the range of 3.6–5.7 nm, and their volume fraction *x* can be changed from ≈15 to 100% by varying the deposition conditions [4, 6]. It was also demonstrated that the analysis of Raman spectra makes it possible to measure the *x* value for the films deposited on the quartz or Si substrates. In this paper, the results of the first investigations of the photoelectric properties of a new type of heterostructure (HS) are reported. These HSs are based on the contact of two-phase ($\mu c_x a_{1-x}$)-Si:H films with the *c*-Si single-crystal substrate.

The ($\mu c_x a_{1-x}$)-Si:H films were grown by the plasma technique with the use of silane (SiH_4) diluted by H_2. The SiH_4 content in H_2, which was used for obtaining these films, is given in the table. The ($\mu c_x a_{1-x}$)-Si:H films were deposited on polished *p*-Si(100) ~0.4 μm thick substrates with a resistivity of 20 Ω cm. The deposition temperature was T_s = 160°C. The analysis of Raman spectra demonstrated that variation in the *f* magnitude makes possible the reproducible control of the volume ratio between the microcrystalline and amorphous Si phases (see table).

The steady-state current–voltage (*I–V*) characteristics and spectra of the relative quantum efficiency of the photoconversion η of natural and linearly polarized radiation (LPR) for the HSs obtained were investigated. Certain photoelectric parameters of the HSs, which depended on the conditions under which these were obtained, are given in the table. The main results of the conducted investigations are as follows.

1. Typical *I–V* characteristics of two HSs grown with different SiH_4 contents in H_2, which makes it possible to control the ratio between crystalline and amorphous Si phases (see the table), are shown in Fig. 1. It can be seen that the HSs obtained manifest clearly pronounced rectification irrespective of the ratio between the volumes of microcrystalline and amorphous Si phases. The negative polarity of the external bias across the ($\mu c_x a_{1-x}$)-Si:H layer always corresponds to forward portions of *I–V* characteristics. For the bias range $U <$ 0.6–0.8 V, forward portions of *I–V* characteristics at 300 K are described by the conventional diode equation with a high nonideality factor ≅4.5–6 for various HSs. This may be caused by the influence of high series resistance. As a result, it is difficult to judge the forward current mechanism for these HSs. For bias voltages $U >$ 1 V, the forward portions of *I–V* characteristics for all HSs investigated are controlled by the relationship $I = (U - U_0)/R_r$. The cutoff voltage U_0 is within the range of 0.6–0.9 V for various HSs. No unique relation of the cutoff voltage to the phase composition of the films was

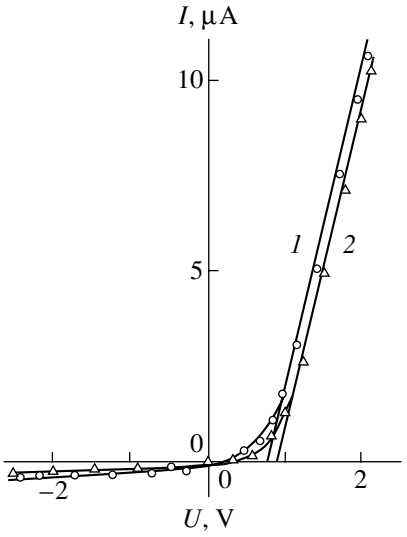

Fig. 1. Steady-state *I–V* characteristics of $(\mu c_x a_{1-x})$-Si:H/*c*-Si heterostructures. $T = 300$ K. (*1*) Sample *D*44 and (*2*) sample *D*56.

observed. A similar conclusion may be drawn for the magnitude of the residual resistance of the structures R_r (see table). It is necessary only to mention the tendency for an increase in R_r in passing to the HSs based on amorphous ($x = 0$) Si films. For this reason, as can be seen from Fig. 1, the linear part of the forward portion of the *I–V* characteristic is shifted to higher forward biases. It is known that the resistivity of such two-phase films increases by 6–8 orders of magnitude with decreasing *x* from 90 to 0% [6]. This circumstance did not actually manifest itself in the *I–V* characteristics of the HSs, possibly due to both the conduction anisotropy for the films with columnar structure and the low film thicknesses d_1 for the HSs investigated (see the table). For $U \le 5$ V, the reverse currents across these HSs are rather low. Specifically, they are usually no larger than $(2–5) \times 10^{-7}$ A at $T = 300$ K. In general, it should be noted that the controllable volume ratio between microcrystalline and amorphous Si phases in the films of HSs obtained, which was permitted by the technology used, does not actually affect the current flow in these very specific structures. It is evident that the electrical properties of these structures should be determined by at least two different types of heterojunctions, namely, $(\mu c_x a_{1-x})$-Si:H/*c*-Si and *a*-Si:H/*c*-Si. The *I–V* characteristics were independent of *x*. This fact suggests that the energy barrier is determined mainly by a short-range order, which is actually similar for both crystalline and amorphous phases.

2. On illumination of all HSs obtained, the photovoltaic effect appears; its sign is independent of the localization of the illuminating beam (with diameter of ~0.2 mm) on the structure surface and energy of incident photons. For this reason, we may assume that, in such cases, the photovoltaic effect is determined by a single energy barrier, which appears due to the deposition of thin films on the *c*-Si substrate. As a rule, the HS photosensitivity prevails if measurements are carried out when illuminating the HS from the thin film side. The largest values of the voltaic sensitivity S_U^{m} and current sensitivity S_I^{m} are given in the table. An unambiguous relation of the HS photosensitivity to *f* and x quantities was not found. It seems possible to note only that the largest photosensitivity is realized in the structures with two-phase films ($x = 0.81$ and 0.5). The films are always negatively charged, which corresponds to the rectifying direction.

Spectral dependences of the relative quantum efficiency η for the HSs exposed to unpolarized light from the thin film side are shown in Fig. 2. It can be seen that the photovoltaic effect for all structures is a broadband one. The long-wavelength edge of photosensitivity is caused by band-to-band transitions in the substrate of the HS. High photosensitivity is observed deep within the fundamental absorption band for crystalline Si, and its spectral range $\Delta\hbar\omega^{\mathrm{m}}$ (see table) and magnitude are nearly constant from 1.3 to 1.7 eV. The full width at half the maximum $\delta_{1/2}$ of the photosensitivity band for the HSs obtained is given in the table. The $\delta_{1/2}$ quantity is fairly large, which is indicative of a rather high quality of the heterointerface. It should also be noted that the width η of the band increases with increasing the volume fraction of microcrystallites embedded in the amorphous Si matrix. This permits us to consider that the recombination rate of photogenerated pairs at the heterointerface between the two-phase

Photoelectric properties of $(\mu c_x a_{1-x})$-Si:H/*c*-Si heterostructures ($T = 300$ K)

Sample no.	*f*, %	d_1, μm	*x*, %	U_0, V	$R_r \times 10^{-4}$, Ω	S_U^{m}, V/W	S_I^{m}, μA/W	$\Delta\hbar\omega^{\mathrm{m}}$, eV	$\delta_{1/2}$, eV	i_{m}^P / i_0	P_I, % ($\Theta = 75°$)
*D*44	1.5	0.65	86	0.85	20	10	12	1.32–1.55	0.83	1.75	56
*D*45	2.0	0.75	81	0.66	8.6	730	80	1.32–1.65	0.81	1.77	55
*D*46	2.5	0.70	65	0.80	37	74	8	1.35–1.68	0.78	1.70	58
*D*47	3.0	0.65	50	0.62	15	8300	66	1.60–1.70	0.77	1.73	55
*D*48	3.5	0.70	0	0.61	50	86	14	1.32–1.74	0.75	1.74	58
*D*56	8.0	0.80	0	0.90	26	145	48	1.35–1.65	0.72	1.70	57

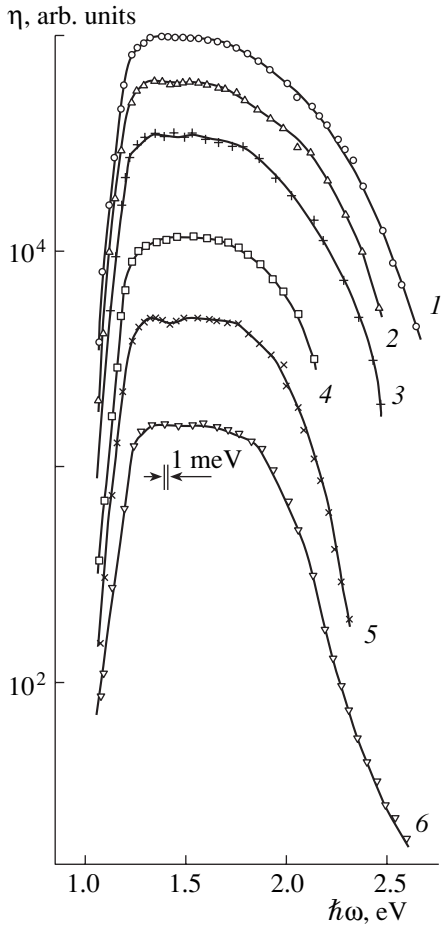

Fig. 2. Spectral dependences of relative quantum efficiency of photoconversion for $(\mu c_x a_{1-x})$-Si:H/*c*-Si HSs exposed to the natural light at $T = 300$ K. (*1*) Sample *D*44, (*2*) sample *D*45, (*3*) sample *D*46, (*4*) sample *D*47, (*5*) sample *D*48, and (*6*) sample *D*56. Structures are illuminated from the side of the $(\mu c_x a_{1-x})$-Si:H layers. Curves are shifted along the η axis.

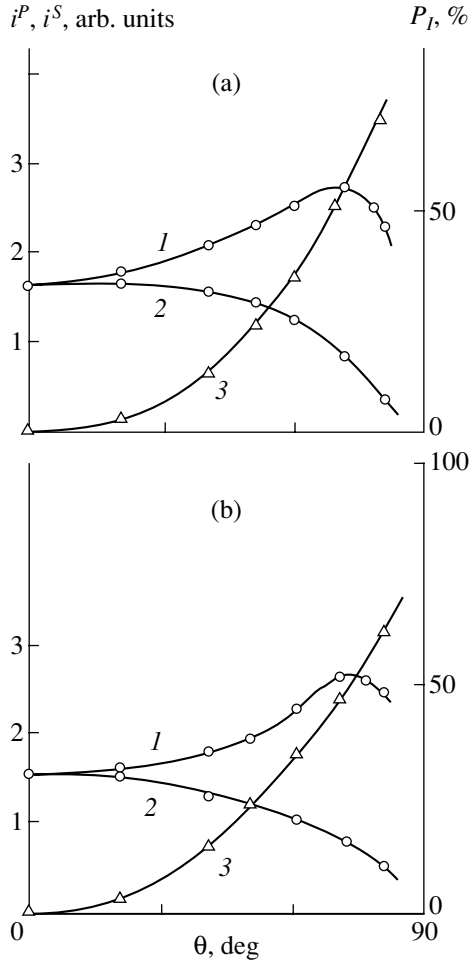

Fig. 3. Photocurrents (*1*) i^P, (*2*) i^S, and (*3*) coefficient P_I of the photopleochroism induced in relation to the angle of LPR incidence on the plane of $(\mu c_x a_{1-x})$-Si:H layers at $T = 300$ K. (a) Sample *D*44 and (b) sample *D*56).

$(\mu c_x a_{1-x})$-Si:H and single-crystal Si, as well as optical losses in the two-phase film, are no higher than in the *a*-Si:H/*c*-Si HS. This may be due to an increase in the band gap of Si microcrystallites embedded in the amorphous matrix [5]. It seems likely that obtaining the HSs with $x > 86\%$ makes it possible for a further increase $\delta_{1/2}$ in the spectral range best suited to solar cells.

3. Investigations of the photosensitivity of the $(\mu c_x a_{1-x})$-Si:H/*c*-Si HSs for the LPR demonstrated that, if they are illuminated from the side of the thin $(\mu c_x a_{1-x})$-Si:H films along the normal to their surface, no polarization photosensitivity is observed, and photopleochroism $P_I = 0$ [7, 8]. This circumstance corresponds to isotropic photoactive absorption in the substrate and thin films forming the HSs under study. The photosensitivity to the orientation of the electric-field vector of the optical wave **E** for the obtained HSs appears only for inclined LPR incidence on the HSs plane [8]. Examples of typical experimental dependences of photocurrents i^P (vector **E** is parallel to the plane of incidence) and i^S (vector **E** is normal to the plane of incidence) as a function of the angle of incidence θ on the plane of the $(\mu c_x a_{1-x})$-Si:H/*c*-Si HSs are shown in Figs. 3a and 3b. It can be seen that the angular dependences of photocurrents i^P and i^S in these HSs are in agreement with Fresnel relationships for amplitude coefficients of the LPR transmission for various azimuths of the interface between air and a $(\mu c_x a_{1-x})$-Si:H film [8]. Actually, over the entire photosensitivity region for the HSs investigated, the photocurrent i^P initially increases with increasing θ, passes through a maximum i_m^P, and then decreases. This increase, which is caused by a decrease in the radiation losses by reflection, is observed for a rather high-quality HS surface [9]. The ratios of the largest photocurrent to the photo-

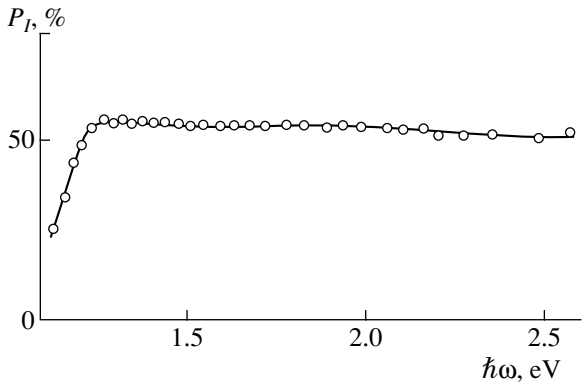

Fig. 4. Spectral dependences of the coefficient P_I of the photopleochroism induced for the $(\mu c_x a_{1-x})$-Si:H/*c*-Si heterostructure. T = 300 K, sample *D*46, and $\theta = 75°$.

current at $\theta = 0$ i_m^P/i_0 for all HSs obtained within the sensitivity region were close to each other (see table) and characterize the surface of $(\mu c_x a_{1-x})$-Si:H layers as perfect. As can be seen from Fig. 3 (curve *2*), the photocurrent i^S for all HSs decreases with increasing θ. In view of previous results [10, 11], this could be the basis for the conclusion that no LPR interference is observed in the thin films of the entrance windows of the HSs. The coefficient P_I of photopleochroism, induced by the inclined LPR incidence for the $(\mu c_x a_{1-x})$-Si:H/*c*-Si HSs obtained, follows the quadratic law $P_I \propto \theta^2$ with increasing angle of incidence over the entire photosensitivity region (Fig. 3, curve *3*). Similarly to surface-barrier structures [7, 8], the coefficient of photopleochroism induced for these HSs at θ = const is actually constant over their photosensitivity region (Fig. 4). It should be noted that the P_I value for these HSs is in agreement with the refractive index of bulk *c*-Si [8]. This is also typical of the surface-barrier structures [7].

Thus, the HSs based on thin two-phase films, which consist of Si microcrystalline inclusions in the amorphous Si matrix, feature rectification and a broad-band photovoltaic effect, which can be realized in photoconverters of natural and linearly polarized radiation.

ACKNOWLEDGMENTS

This study was supported by the program COPERNICUS, grant no. IC15CT98-0819, TIMOC; and by the Ministry of Industry, Science, and Technologies, Program on Laser Physics (project no. 08.01.100f).

REFERENCES

1. L. T. Canham, Appl. Phys. Lett. **57**, 1046 (1990).
2. N. Koshida and H. Koyama, Appl. Phys. Lett. **60**, 347 (1992).
3. Y. He, C. Yin, G. Geng, *et al.*, J. Appl. Phys. **75**, 797 (1994).
4. E. I. Terukov, V. Kh. Kudoyarova, V. Yu. Davydov, *et al.*, Mater. Sci. Eng. B **B69–70**, 266 (2000).
5. X. N. Liu, X. W. Wu, X.-M. Bao, and Y. L. He, Appl. Phys. Lett. **64**, 220 (1994).
6. D. Ruff, *Elektrischer Transport in mikrokristal len Silizium* (Philips–University, Marburg, 1999).
7. S. G. Konnikov, D. Melebaev, V. Yu. Rud', and M. Serginov, Pis'ma Zh. Tekh. Fiz. **18** (12), 39 (1992) [Sov. Tech. Phys. Lett. **18**, 382 (1992)].
8. F. P. Kesamanly, V. Yu. Rud', and Yu. V. Rud', Fiz. Tekh. Poluprovodn. (St. Petersburg) **33**, 513 (1999) [Semiconductors **33**, 483 (1999)].
9. Yu. V. Zhilyaev, N. Nazarov, V. Yu. Rud', *et al.*, Fiz. Tekh. Poluprovodn. (St. Petersburg) **27**, 1610 (1993) [Semiconductors **27**, 890 (1993)].
10. V. Yu. Rud', Yu. V. Rud', and H. W. Shock, Semicond. Sci. Technol. **15**, 625 (2000).
11. V. Yu. Rud' and Yu. V. Rud', Fiz. Tekh. Poluprovodn. (St. Petersburg) **31**, 245 (1997) [Semiconductors **31**, 197 (1997)].

Translated by N. Korovin

Semiconductors, Vol. 35, No. 11, 2001, pp. 1263–1269. Translated from Fizika i Tekhnika Poluprovodnikov, Vol. 35, No. 11, 2001, pp. 1320–1325.

ELECTRONIC AND OPTICAL PROPERTIES OF SEMICONDUCTORS

A Pulsed Synthesis of β-$FeSi_2$ Layers on Silicon Implanted with Fe^+ Ions

R. I. Batalov*, R. M. Bayazitov*, E. I. Terukov, V. Kh. Kudoyarova**, G. Weiser***, and H. Kuehne*****

** Kazan Physicotechnical Institute, Kazan Scientific Center, Russian Academy of Sciences, Sibirskiĭ trakt 10/7, Kazan 29, 420029 Tatarstan, Russia*

e-mail: bayaz@kfti.knc.ru

*** Ioffe Physicotechnical Institute, Russian Academy of Sciences, Politekhnicheskaya ul. 26, St. Petersburg, 194021 Russia*

**** Philipps University of Marburg, Renthof 5, D-35032, Germany*

Submitted April 4, 2001; accepted for publication April 19, 2001

Abstract—Continuous layers and fine-grained films of β-$FeSi_2$ were synthesized using the implantation of Fe^+ ions into Si(100) with subsequent pulsed nanosecond ion-beam treatment of the implanted layers. The X-ray diffraction studies showed that the pulsed ion-beam treatment brings about the formation of a mixture of two phases: FeSi and β-$FeSi_2$ with strained crystal lattices. Subsequent rapid thermal annealing led to the complete transformation of the FeSi phase into the β-$FeSi_2$ phase with the formation of a textured layer. The data obtained using Raman spectroscopy corroborate the formation of the β-$FeSi_2$ phase with a high degree of silicon crystallinity. The results of measuring the optical absorption point to the formation of β-$FeSi_2$ layers and precipitates with a direct-gap structure, an optical gap of $E_g \approx 0.83$ eV, and an Urbach tail extent of $E_0 \approx 220$ meV. The photoluminescence band peaked at $\lambda \approx 1.56$ μm and caused by direct band-to-band transitions in β-$FeSi_2$ was observed at temperatures lower than 210 K. © *2001 MAIK "Nauka/Interperiodica".*

1. INTRODUCTION

One of the most important problems in Si-based optoelectronics is the development of thin-film structures that emit in the region of 1.5 μm, which falls within the transmission window of silicon and silicon dioxide. In the last 10–15 years, the most popular approach to solving this problem has been related to the formation of solid solutions of Er in Si [1, 2]. The Si:Er layers emit at a wavelength of 1.54 μm by the $^4I_{13/2} - {}^4I_{15/2}$ transitions in the inner 4*f* shell of an Er^{3+} ion in the optically active state. However, the low solubility of the rare-earth elements in Si and their tendency towards the formation of optically inactive clusters appreciably limit the intensity of intracenter luminescence at room temperature [3].

In the last five years, a new and alternative approach to solving the problem related to the synthesis of compounds and their clusters in Si has been actively developed. One of such compounds is iron disilicide (β-$FeSi_2$); this is a semiconducting direct-gap material with an optical band gap of about 0.85 eV, which corresponds to a wavelength close to 1.5 μm [4]. Low-temperature (~200 K) photoluminescence (PL) has already been observed in the β-$FeSi_2$ layers [5–7], and the first light-emitting diodes with active regions incorporating the β-$FeSi_2$ precipitates and operating under the forward bias at 80 K [8] and 300 K [9] have been fabricated. The main methods for fabricating the diode structures are ion implantation and molecular-beam epitaxy with subsequent high-temperature (up to 900°C) and long (up to 20 h) heat treatments. However, such thermal treatments are undesirable in microelectronics for the fabrication of integrated circuits because these treatments give rise to an appreciable diffusion of Fe atoms into the base Si layer due to a large diffusion coefficient of Fe at high temperatures ($D \approx 5 \times 10^{-6}$ cm^2/s at $T \approx 1000$°C), which results in the deterioration of the main parameters of silicon devices [10].

In order to obviate the above limitations, one can use pulsed-beam (laser, ion, and electron) treatments that affect only the surface layers of the material (~1 μm) during a short time (<1 μs), which eliminates the unwanted impurity diffusion into the base material. In addition, the high rates of heating, melting, and subsequent solidification (~1 m/s) result in the formation of defect-free, epitaxial, and heavily doped Si layers

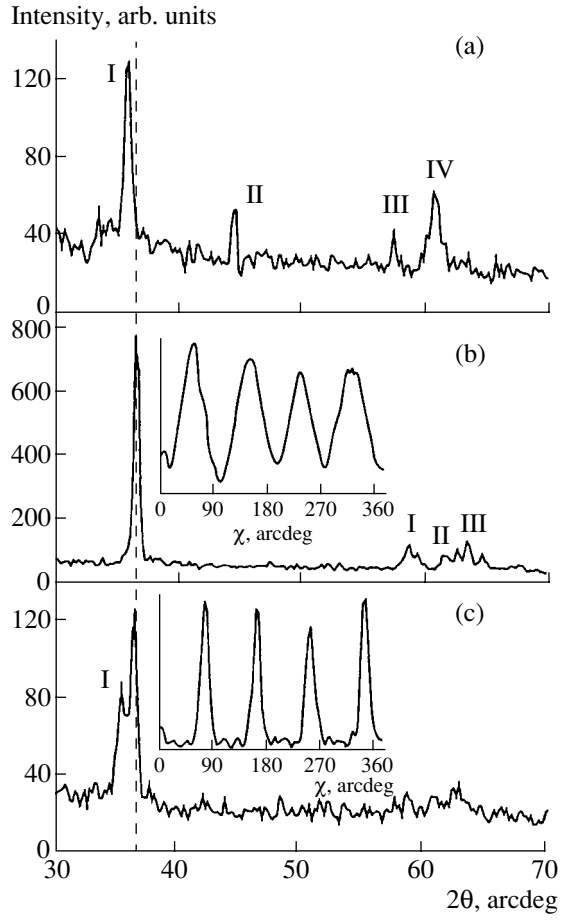

Fig. 1. The spectra of glancing X-ray diffraction for Si implanted with Fe^+ ions with the doses of (a, b) 1.8×10^{17} and (c) 1×10^{16} cm^{-2} after (a) pulsed ion-beam treatment (PIBT) (a 50-ns-width pulse with 50 A/cm^2), (b) PIBT and additional thermal annealing (TA) (for 20 min at 800°C), and (c) PIBT and additional TA. In the insets, we show the azimuthal dependences of the diffraction peak (202)/(220): (a) the diffraction peaks corresponding to (I) β-$FeSi_2$ (202)/(220), (II) FeSi(111); (III) FeSi(210), (IV) β(041); (b) the diffraction peaks corresponding to (I) β(313)/(331), (II) β(041), and (III) β(422); and (c) the diffraction peaks (I) for Si(111).

[11–13]. A characteristic special feature of the pulsed ion-beam treatment (PIBT), compared to the pulsed laser treatment, is the deeper and more uniform distribution of the ion energy losses in the material, which results in a less profound superheating and less severe surface damage; an additional advantage is the independence of the treatment outcome from the optical properties of the irradiated material [14].

In this study, we formed thin β-$FeSi_2$ films using PIBT of Si layers implanted with Fe^+ ions at doses corresponding to the formation of continuous layers and fine-grained films [15]. The synthesized β-$FeSi_2$ films were studied by glancing X-ray diffraction, Raman scattering, Rutherford backscattering (RBS), and optical and photoluminescence spectroscopies.

2. EXPERIMENTAL

The wafers of single-crystal *n*-Si(100) grown by the Czochralski method were implanted with 40-keV Fe^+ ions at doses of 1×10^{16} and 1.8×10^{17} cm^{-2}, with the ion-current density being equal to 5 μA/cm^2. Subsequent to implantation, the samples were subjected to PIBT using a high-power nanosecond ion beam (80% of C^+, 20% of H^+, E = 300 keV, τ = 50 ns, and $j \approx$ 50 A/cm^2; from two to three pulses were used) [14]. The total dose of C^+ and H^+ ions in the course of PIBT did not exceed 1×10^{14} cm^{-2}. Thermal annealing (TA) of implanted samples was performed in a quartz furnace in a nitrogen atmosphere for 20 min at a temperature of 800°C.

The structure and phase composition of the implanted and annealed layers were studied by glancing X-ray diffraction (the angle of incidence of the beam φ ≈ 1°) using the Fe K_α radiation (λ = 1.9373 Å). The azimuthal dependence of the most intense diffraction peak was recorded by orienting the detector to the position of a given reflection spot with subsequent azimuthal scanning in the angle range of χ = 0°–360°. Distribution of implanted Fe atoms over depth was studied by RBS spectroscopy using a deuteron ($^2D^+$) beam with an energy of 0.9 MeV and at the scattering angle of 135°. The microstructure of the samples was studied using Raman spectroscopy. The Raman spectra were recorded using a JY U1000 Raman system. All the spectra were recorded at 300 K in the range of 0–600 cm^{-1} with a resolution of 3 cm^{-1}. An Ar laser (λ = 514.5 nm) was used as the source of pump radiation. The use of this laser beam allowed us to gain insight into the microstructure of both the β-$FeSi_2$ film and the crystalline Si, since the optical-probing depths in a β-$FeSi_2$ layer and Si are equal to ~18 and ~760 nm, respectively [16].

Infrared (IR) spectroscopy under conditions of reflection and transmission was used to determine the band gap of the formed silicide. A Hitachi-330 spectrophotometer was used for measuring the spectra at 300 K in the spectral range of 1000–2000 nm. The photoluminescence (PL) of synthesized β-$FeSi_2$ films was studied in the near-IR region of the spectrum (λ = 1.0–1.7 μm) in the temperature range of 77–250 K. An Ar laser (λ = 514.5 nm and P = 50 mW) was used to excite the PL signal detected with a Ge photodiode cooled to 77 K.

3. RESULTS AND DISCUSSION

3.1. X-ray Diffraction Analysis

There are no reflections in the spectrum of X-ray diffraction measured immediately after ion implantation (this spectrum is not shown); this indicates that the implanted layer is completely amorphized. In Fig. 1, we show the X-ray diffraction spectra of the samples implanted with two doses of Fe^+ ions (1×10^{16} or 1.8×10^{17} cm^{-2}) and then subjected to PIBT (for 50 ns with 50 A/cm^2) and to an additional TA (for 20 min at 800°C). It can be seen from Fig. 1a that a mixture of two phases (metallic FeSi and semiconducting β-$FeSi_2$) is formed as a result of the PIBT. The peak with the highest intensity in the spectrum is caused by the Bragg reflection from the (202)/(220) planes in β-$FeSi_2$. The angular position of this peak ($2\theta = 36.2°$) differs appreciably from the tabulated value ($2\theta = 36.9°$), which can be attributed to a stressed state of the disilicide crystal lattice; the stresses are caused by the rapid liquid-phase crystallization of the ion-implantation layer. In order to relieve the stress and transform completely the residual FeSi phase into the β-$FeSi_2$ phase, we used a TA (for 20 min at 800°C) in a nitrogen atmosphere. The X-ray diffraction spectrum after the above TA is shown in Fig. 1b. As can be seen, the intensity of the (202)/(220) peak increased significantly, and the peak itself shifted to $2\theta = 36.9°$, which indicates that the stresses in the disilicide lattice were relieved. In addition, the reflections corresponding to the FeSi phase disappeared. The ratio of the peak intensities $I_{220} : I_{422} = 8.5$, whereas this ratio is equal to 1.25 in the randomly oriented β-$FeSi_2$ powders. This fact indicates that there is a preferential orientation (a texture) in the β-$FeSi_2$ layer. In the inset in Fig. 1b, we show the azimuthal dependence of the (220) peak; four intense peaks related to the growth of β-$FeSi_2$ layer on Si(100) are characteristic of this dependence. It should be noted that, if ion-implanted Si was subjected solely to a TA, a very poorly pronounced texture is observed; in addition, the intensity of the main diffraction peak was lower by almost a factor of 3 (the corresponding spectrum is not shown). In Fig. 1c, we show the X-ray diffraction spectrum of Si implanted with the 1×10^{16} cm^{-2} dose and then subjected to PIBT and TA. As can be seen, the reflections corresponding to the β-$FeSi_2$ phase (without inclusions of the metallic FeSi phase) are present in the spectrum; in addition, a reflection from the Si(111) matrix is observed, which indicates that the surface regions of the Si matrix have a polycrystalline structure. The curve shown in the inset in Fig. 1c suggests that the β-$FeSi_2$ precipitates are oriented predominantly in the ⟨110⟩ direction. Calculations of the average size of the β-$FeSi_2$ precipitates using the MAUD program [17] yield the value of ~40 nm, which is close to the data obtained under similar implantation conditions [15, 18].

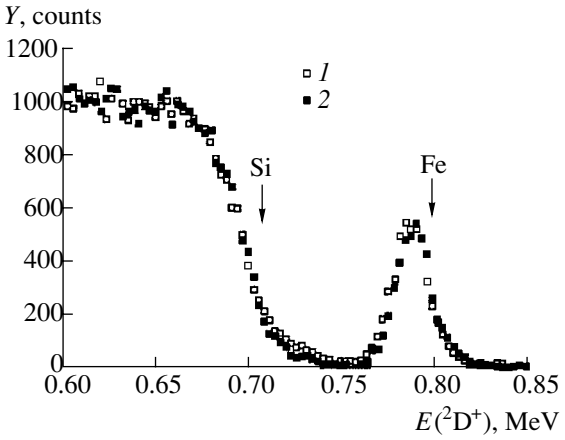

Fig. 2. The Rutherford backscattering spectra for Si implanted with Fe^+ ions with a dose of 1.8×10^{17} cm^{-2} after (*1*) a pulsed ion-beam treatment (50 A/cm^2) and additional thermal annealing (TA) (for 20 min at 800°C) and (*2*) merely the TA for 20 min at 800°C. The arrows indicate the position of the surface for Fe and Si.

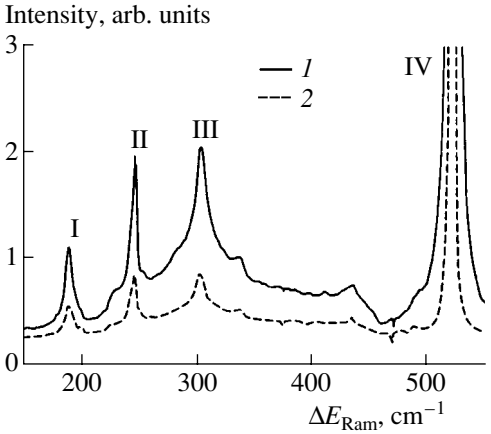

Fig. 3. The Raman spectra of Si implanted with doses of Fe^+ ions equal to (*1*) 1.8×10^{17} and (*2*) 1×10^{16} cm^{-2} and then subjected to pulsed ion-beam treatment (pulse width of 50 ns and current density of 50 A/cm^2) and thermal annealing for 20 min at 800°C. The positions of the peaks are (I) 190.4 (β-$FeSi_2$); (II) 246.2 (β-$FeSi_2$); (III) 301.5 (Si, 2TA); and (IV) 521.2 cm^{-1} (Si, TO).

In Fig. 2, we show the random RBS spectrum of ion-implanted Si after the PIBT with subsequent TA (*1*) and the corresponding spectrum for Si subjected only to a postimplantation TA (*2*). In both cases, the β-$FeSi_2$ layer is formed in the vicinity of the surface and extends to a depth of ~100 nm. An appreciable Fe redistribution caused either by diffusion or by segregation to the surface is not observed. The absence of the characteristic steps caused by the formation of stoichiometric $FeSi_2$ in

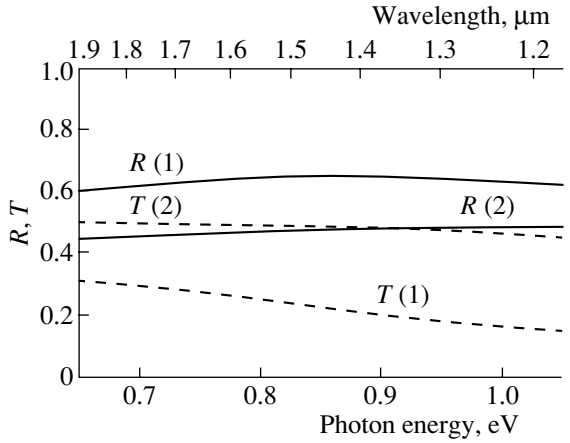

Fig. 4. The transmission (*T*) and reflection (*R*) spectra of Si implanted with the Fe^+ doses of (*1*) 1.8×10^{17} and (*2*) 1×10^{16} cm^{-2} and then subjected to pulsed ion-beam treatment (50 ns, 50 A/cm^2) and thermal annealing for 20 min at 800°C.

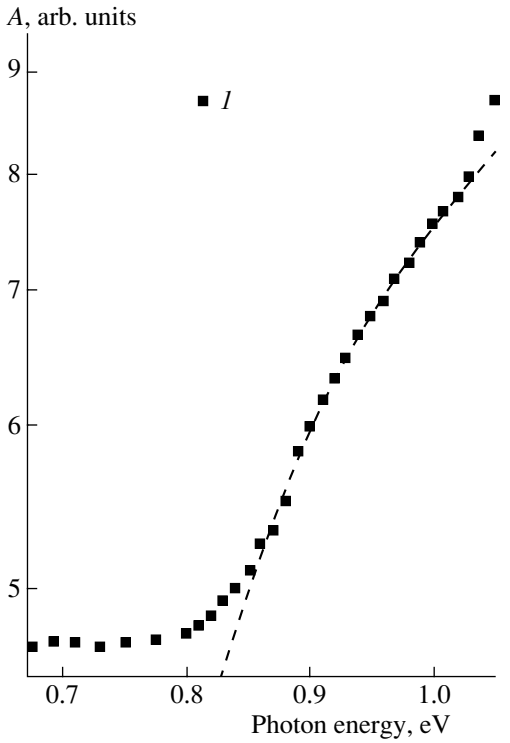

Fig. 5. The absorbance spectrum of Si implanted with 1×10^{16} cm^{-2} of Fe^+ ions after pulsed ion-beam treatment (50 ns, 50 A/cm^2) and additional thermal annealing for 20 min at 800°C. Dashed line represents the results of approximation of experimental data using expression (1) and the symbols (*1*) represent the experimental data.

the RBS-spectrum regions corresponding to Si and Fe may be attributed to the insufficient resolution (12 keV) of the detector of scattered deuterons.

3.2. Raman Spectroscopy

The Raman spectra of Si implanted with Fe^+ ions using doses of 1×10^{16} and 1.8×10^{17} cm^{-2} and then subjected to PIBT and TA are shown in Fig. 3. The four most intense lines, peaked at 190, 246, 301, and 521 cm^{-1}, can be seen. The last two lines are related to the transverse optical (TO) phonons and to the two-phonon processes (2TA) in the bulk crystalline Si (*c*-Si). It should be noted that the line peaked at 301.5 cm^{-1} was observed only in the defect-free *c*-Si crystals and not in the β-$FeSi_2$ layers obtained by ion implantation with subsequent TA [19]. This indicates that the deeper Si layers have a low concentration of defects. As for the Raman lines that peaked at 190 and 246 cm^{-1}, these are caused by the presence of β-$FeSi_2$. The β phase of iron disilicide crystallizes according to the orthorhombic space group D_{2h}^{18}. For Raman spectroscopy, the factor group-theory analysis predicts 12 active internal modes, which probably produce most of the 14 Raman lines. In addition, the Raman activity of the three A_g modes should not be changed when polarization of the pump field is rotated with respect to polarization of the scattered light. This occurs for the three most intense lines of the transverse-polarized spectrum with peaks at 197, 253, and 346 cm^{-1}, which were observed in the 1-μm-thick β-$FeSi_2$ film on the FeSi substrate. The Raman lines peaked at 178, 201, and 252 cm^{-1} were observed for bulk polycrystalline β-$FeSi_2$. For the 200-nm-thick β-$FeSi_2$ film grown on the Si substrate, the main Raman lines that peaked at 176, 195/200, and 247 cm^{-1} have been observed [16, 20]. It should be noted that the peak at 247 cm^{-1} (the A_g mode) has been invariably the most intense; for this reason, many researchers have concentrated their attention on this peak alone. As can be seen from Fig. 3, the intensity of the peak at 246 cm^{-1} increases as the dose of implanted Fe^+ ions increases, which can be attributed to an increase in the amount of the synthesized β-$FeSi_2$ phase.

3.3. Optical IR Spectroscopy

Figure 4 shows the transmission (*T*) and reflection (*R*) spectra in the spectral region corresponding to the transparency of the silicon substrate for two ion-implanted samples after PIBT and TA. Similar shapes of the transmission and reflection curves are observed for both samples; i.e., there is a steady decrease in transmittance and a slight increase in reflectance with increasing photon energy. The distinction in absolute values in the *T* and *R* spectra is attributed to a difference in the microstructure of the formed β-$FeSi_2$ films; i.e., a continuous layer is formed for the dose of 1.8×10^{17} cm^{-2}, whereas, for the dose of 1×10^{16} cm^{-2}, there is a fine-grained film composed of β-$FeSi_2$ precipitates with a size of about 40 nm. In Fig. 5, we show the

absorbance A of the sample as a function of the photon energy. The drastic increase in the absorbance for $E >$ 1 eV is caused by fundamental absorption in silicon. The spectral range of 0.8–1.0 eV corresponds to the β-$FeSi_2$ band gap, the value of which can be determined from the following approximate expression for the direct band-to-band transitions [21]:

$$\alpha = C(E - E_g^d)^{1/2}. \quad (1)$$

Here, α is the absorption coefficient, E is the photon energy, C is a constant related to the special features of the band structure, and E_g^d is the direct band gap. The obtained value of the band gap $E_g^d \approx 0.83$ eV is slightly larger than that reported in [6, 18]. In Fig. 6, we show the squared absorption exponent $(\alpha d)^2$ (d is the thickness of the silicide layer) as a function of E for Si implanted with a high dose (1.8×10^{17} cm^{-2}) of Fe^+ ions; this dependence was plotted using the formula

$$\alpha d = \ln\left(\frac{1-R}{T}\right). \quad (2)$$

The extrapolation of the linear portion of the curve in Fig. 6 to the intersection with the E axis yields $E_g^d \approx$ 0.83 eV for the continuous β-$FeSi_2$ layer, which corresponds to the values of E_g for β-$FeSi_2$ reported elsewhere [4, 5, 22, 23].

At energies lower than those corresponding to the fundamental absorption in silicide, an appreciable subgap absorption (the Urbach tail) is observed; this absorption is caused by defects and can be described by the following empirical formula [24]:

$$\alpha = \alpha_0 \exp\left(\frac{E - E_g}{E_0}\right). \quad (3)$$

Here, α_0 is a constant, and E_0 is the Urbach tail extent. The value of E_0 indicates that both static structural disorder and dynamic thermal disorder contribute to the absorption at the photon energies smaller than the direct band gap. It has been shown that structural disorder, due to grain boundaries and other structure defects, contributes predominantly to the Urbach tail [22]. The results of fitting formula (3) to describe the absorption by defects for $E < E_g$ are shown in the inset in Fig. 6. The obtained value of $E_0 \approx 0.22$ eV indicates that the silicide layer includes a large concentration of residual defects. For β-$FeSi_2$, synthesized using a long TA, $E_0 \approx$ 0.05 eV [25]. Obviously, in order to reduce the number of defects in the β-$FeSi_2$ layer, one should search for optimal conditions of ion implantation, PIBT, and TA.

3.4. Photoluminescence Spectroscopy

Figure 7 shows the PL spectrum recorded at 77 K in the range of 0.7–1.2 eV for a β-$FeSi_2$ film synthesized by implantation of Fe^+ ions with a dose of 1×10^{16} cm^{-2} with subsequent PIBT and TA. The PL spectrum for a sample implanted with a dose of 1.8×10^{17} cm^{-2} is not shown because it was comparable to the background at 77 K. The latter is attributed to a high concentration of defects in the synthesized continuous β-$FeSi_2$ layer. A similar pattern of the small-amplitude PL signal from

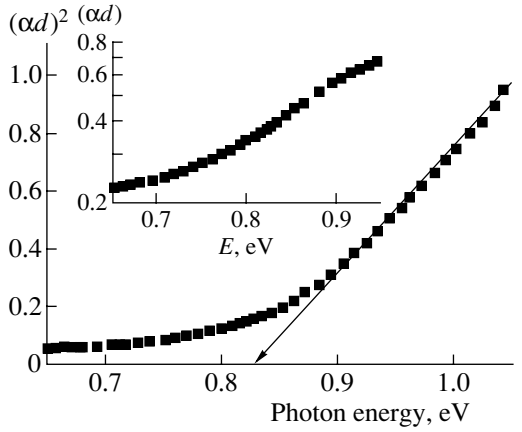

Fig. 6. Dependence of the squared exponent of absorbance on the photon energy for Si implanted with 1.8×10^{17} cm^{-2} of Fe^+ ions after subsequent pulsed ion-beam treatment and additional thermal annealing. The solid line corresponds to extrapolation of experimental data for determining the direct band gap. The dependence of the absorbance exponent on the photon energy is shown in the inset.

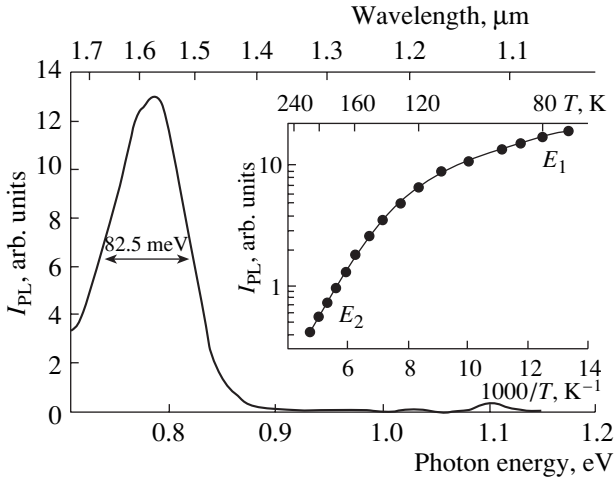

Fig. 7. The photoluminescence spectrum of Si implanted with 1×10^{16} cm^{-2} of Fe^+ ions after pulsed ion-beam treatment and additional thermal annealing; the spectrum was measured at 77 K with the pump power being equal to 50 mW. In the inset, we show the temperature dependence of the PL-signal intensity for two activation energies (E_1 and E_2) determined from fitting expression (4) to experimental data (dots).

a continuous β-$FeSi_2$ layer has been reported previously [5, 15].

The peaks at ~0.78 and ~1.11 eV can be seen in the PL spectrum in Fig. 7. The latter peak ($E \approx 1.11$ eV) is related to indirect transitions through the Si band gap. The most intense band peaked at 0.78 eV (1.56 μm) and is related to the direct band-to-band transitions through the band gap of β-$FeSi_2$. It should be noted that the dislocation-related PL peaks *D*2–*D*4 [26] are absent in the spectrum under consideration; these peaks have been observed in the low-temperature PL spectra of the β-$FeSi_2$ precipitates synthesized using ion implantation [6, 18]. As for the most intense dislocation-related peak *D*1, the position of which (0.81 eV) is close to the position of the observed PL peak (0.78 eV), its origin will be discussed below. The distinction between the obtained value of the band gap (~0.83 eV at 300 K) and the experimental position of the PL peak (~0.78 eV at 77 K) is possibly caused by the introduction of the defect- and impurity-related levels into the β-$FeSi_2$ band gap in the course of ion implantation and PIBT. The presence of these levels brings about the pronounced quenching of the PL signal at temperatures higher than 100 K and its disappearance at temperatures above 210 K (see the inset in Fig. 7). The temperature dependence of the PL-signal amplitude $I(T)$ can be adequately approximated by the following expression that contains two activation energies (E_1 and E_2):

$$I_{PL}(T) = \frac{I(0)}{1 + A\exp\left(\frac{-E_1}{kT}\right) + B\exp\left(\frac{-E_2}{kT}\right)}. \quad (4)$$

Here, A and B are weighting coefficients, and $I(0)$ is the PL intensity at a temperature close to absolute zero. The values of the activation energies ($E_1 = 23$ meV and $E_2 = 110$ meV) were determined by fitting the theoretical curve to the experimental data. A comparison of the obtained values of E_1 and E_2 with the activation energy for the dislocation-related level *D*1 (~10 meV) [5] shows that these energies are quite different. This difference and also the absence of other dislocation-related peaks (*D*2–*D*4) in the PL spectrum make it possible to rule out the contribution of dislocations to the PL peak in the vicinity of 1.5 μm and to attribute this peak to the direct band-to-band transitions in the β-$FeSi_2$ precipitates.

4. CONCLUSION

We synthesized β-$FeSi_2$ continuous layers and fine-grained films by implanting Fe^+ into Si(100) at doses of 1×10^{16} and 1.8×10^{17} cm^{-2} with subsequent nanosecond-duration pulsed ion-beam treatment (PIBT) of the ion-implanted layers. The X-ray diffraction analysis showed that PIBT results in the formation of a mixture of two phases (FeSi and β-$FeSi_2$) with strained crystal lattices. Subsequent thermal annealing (for 20 min at 800°C) leads to the complete transformation of the FeSi phase into the β-$FeSi_2$ phase with the formation of a textured layer. The results of measuring the optical absorption indicate that direct-gap structures are formed in the samples; these structures have an optical band gap $E_g \approx 0.83$ eV and an Urbach tail extent $E_0 \approx 220$ meV. It is shown that the photoluminescence peaked at $\lambda \approx 1.56$ μm and observed at temperatures of up to 210 K is related to the direct band-to-band transitions in the synthesized β-$FeSi_2$ precipitates.

ACKNOWLEDGMENTS

We thank V.A. Shustov for X-ray diffraction measurements and V.M. Lebedev for the measurements of the Rutherford backscattering.

This study was supported by the Russian Foundation for Basic Research (project nos. 00-15-96615 and 01-02-16649), the Foundation for Research and Development of the Tatarstan Republic (project no. 06-6.4-86/2001), and the Research and Education Center of Kazan State University under the program "Materials and Technologies of XXI Century (grant no. BRHE REC-007).

REFERENCES

1. H. Ennen, J. Schneider, G. Pomrenke, and A. Axmann, Appl. Phys. Lett. **43**, 943 (1983).
2. H. Ennen, G. Pomrenke, A. Axmann, *et al.*, Appl. Phys. Lett. **46**, 381 (1985).
3. S. Coffa, C. Franzo, F. Priolo, *et al.*, Phys. Rev. B **49**, 16313 (1994).
4. M. C. Bost and J. E. Mahan, J. Appl. Phys. **58**, 2696 (1985); **64**, 2034 (1988).
5. H. Katsumata, Y. Makita, N. Kobayashi, *et al.*, J. Appl. Phys. **80**, 5955 (1996).
6. M. G. Grimaldi, S. Coffa, C. Spinella, *et al.*, J. Lumin. **80**, 467 (1998).
7. T. Suemasu, Y. Iikura, K. Takakura, and F. Hasegawa, J. Lumin. **87/89**, 528 (2000).
8. K. P. Homewood, K. J. Reeson, R. M. Gwilliam, *et al.*, Thin Solid Films **381**, 188 (2001).
9. T. Suemasu, Y. Negishi, K. Takakura, and F. Hasegawa, Jpn. J. Appl. Phys. **39**, L1013 (2000).
10. B. O. Kolbesen and H. Cerva, Phys. Status Solidi B **222**, 303 (2000).
11. R. Hodgson, J. E. E. Baglin, R. Pal, *et al.*, Appl. Phys. Lett. **37**, 187 (1980).
12. L. J. Chen, L. S. Hung, J. W. Mayer, *et al.*, Appl. Phys. Lett. **40**, 595 (1982).
13. R. M. Bayazitov, L. Kh. Zakirzyanova, I. B. Khaibullin, *et al.*, Vacuum **43**, 619 (1992).
14. R. M. Bayazitov, L. Kh. Antonova, I. B. Khaibullin, and G. E. Remnev, Nucl. Instrum. Methods Phys. Res. B **139**, 418 (1998).

15. K. J. Reeson, M. S. Finney, M. A. Harry, *et al.*, Nucl. Instrum. Methods Phys. Res. B **106**, 364 (1995).

16. A. G. Birdwell, R. Glosser, D. N. Leong, and K. P. Homewood, J. Appl. Phys. **89**, 965 (2001).

17. M. Ferrari and L. Lutterotti, J. Appl. Phys. **76**, 7246 (1994).

18. K. Oyoshi, D. Lenssen, R. Carius, and S. Mantl, Thin Solid Films **381**, 194 (2001).

19. Y. Maeda, K. Umezawa, Y. Hayashi, and K. Miyake, Thin Solid Films **381**, 219 (2001).

20. K. Lefki, P. Muret, E. Bustarret, *et al.*, Solid State Commun. **80**, 791 (1991).

21. J. Pankove, in *Optical Processes in Semiconductors* (Dover, New York, 1971), p. 34.

22. Z. Yang, K. P. Homewood, M. S. Finney, *et al.*, J. Appl. Phys. **78**, 1958 (1995).

23. V. Daraktchieva, M. Baleva, E. Goranova, and Ch. Angelov, Vacuum **58**, 415 (2000).

24. F. Urbach, Phys. Rev. **92**, 1324 (1953).

25. Z. Yang and K. P. Homewood, J. Appl. Phys. **79**, 4312 (1996).

26. N. A. Drozdov and A. A. Patrin, Pis'ma Zh. Éksp. Teor. Fiz. **23**, 651 (1976) [JETP Lett. **23**, 597 (1976)].

Translated by A. Spitsyn

Semiconductors, Vol. 35, No. 11, 2001, pp. 1270–1278. Translated from Fizika i Tekhnika Poluprovodnikov, Vol. 35, No. 11, 2001, pp. 1326–1334.

SEMICONDUCTOR STRUCTURES, INTERFACES, AND SURFACES

Generation–Recombination and Diffusion Currents in HgMnTe n^+–p Junctions

L. A. Kosyachenko, A. V. Markov, S. É. Ostapov, and I. M. Rarenko

Chernovtsy National University, Chernovtsy, 58012 Ukraine

Submitted February 5, 2001; accepted for publication April 2, 2001

Abstract—Special features of the distributions of the space charge, the electric-field strength, and potential in the p–n junction in the narrow-gap HgMnTe semiconductor were considered using the Poisson equation. It is shown that, as the band gap narrows, the effect of free charge carriers induces the coordinate dependence of electric-field strength to deviate from the linear dependence and that of the potential to deviate from the quadratic dependence. As a result of this, and also because of an appreciable increase in the diffusion potential in the n^+–p junction with the degenerate n^+ region, the mechanisms of the charge transport become peculiar: the voltage dependence of the recombination current deviates from those following from the conventionally used analytical expressions, whereas for higher bias voltages, the diffusion current of holes from the lightly doped p region into the n^+ region is prevalent. © *2001 MAIK "Nauka/Interperiodica".*

1. INTRODUCTION

Diode structures based on $Hg_{1-X}Cg_XTe$ ($X \approx 0.2$) with p–n junctions incorporating a heavily doped n region (i.e., with n^+–p junctions) are used to detect infrared radiation in the spectral region of 8–14 μm [1]. Such structures are most suitable also when other ternary semiconductors are used, in particular, the $Hg_{1-X}Mn_XTe$ ($X \approx 0.1$) solid solution; the latter features a higher stability of the crystal lattice and the surface [2]. The characteristics of HgMnTe-based n^+–p junctions formed by ion implantation or ion etching of the p-type material [2, 3] have been analyzed in detail, taking into account various mechanisms of charge transport [2] and using the well-known models developed for p–n junctions [4, 5].

However, detailed studies of the electrical characteristics of $Hg_{1-X}Mn_XTe$ ($X \approx 0.1$, $E_g \approx 0.1$ eV) n^+–p junctions have shown that these characteristics have important special features, which are inconsistent with the above models: the current–voltage characteristic measured under the forward-bias voltage deviates from the dependence $I \propto \exp(eV/2kT)$ typical of the recombination current, the diffusion current [$I \propto \exp(eV/kT)$] manifests itself only at excessively high forward-bias voltages, the ratio between the forward and reverse current is typically no larger than 10^2, and so on [3, 6, 7]. As an illustration, Fig. 1a shows typical current–voltage characteristics of the HgMnTe-based diodes. Differences in the reverse currents can be attributed to the inhomogeneity of the material; however, the forward portions exhibit a reasonably good reproducibility both of the magnitude of current and of the characteristic shape of the $I(V)$ curve. As has been shown previously [3, 7], in order to explain the observed deviation of the recombination current from the $\exp(eV/2kT)$ dependence, it is sufficient to take into account the fact that levels of the most effective recombination centers are not exactly located at the midgap. Other special features of processes occurring in the p–n junction based on a narrow-gap semiconductor were not considered in [3, 7].

The results of this study show that the observed special features of electrical characteristics of HgMnTe-based diodes can be satisfactorily explained if one uses a junction model accounting for degeneracy of the n^+ region and for the resulting distributions of the space charge, potential, and electric-field strength in the p–n junction in a narrow-gap semiconductor. This approach seems topical since, in $Hg_{1-X}Mn_XTe$ with a band gap of about 0.1 eV (a threshold wavelength of ~12 μm), the effective electron mass is smaller by almost two orders of magnitude than the free-electron mass, and an appreciable degeneracy is observed even for the electron concentration $n \approx 10^{16}$ cm^{-3}. Similar behavior is also observed in other narrow-gap semiconductors, in particular, $Hg_{1-X}Mn_XTe$.

2. DISTRIBUTIONS OF THE SPACE CHARGE AND THE ELECTRIC-FIELD STRENGTH IN THE p–n JUNCTION BASED ON A NARROW-GAP SEMICONDUCTOR

We consider the junction between an electron semiconductor with a donor concentration equal to N_d for $x < 0$ and a hole semiconductor with an acceptor concentration equal to N_a for $x > 0$ (Fig. 1b). As is well known, the assumed step-function impurity distribution adequately describes the junctions formed by ion implantation and by ion etching of p-HgMnTe, and also the epitaxial and even shallow diffused p–n junctions

1063-7826/01/3511-1270$21.00

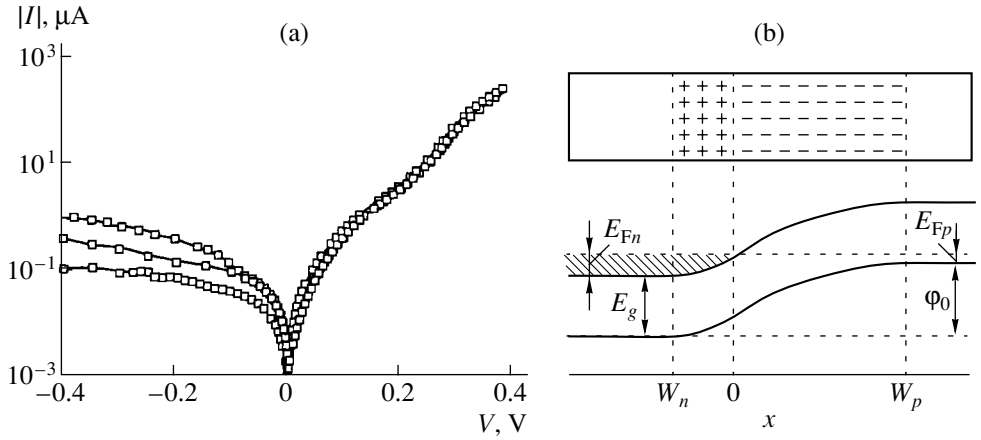

Fig. 1. (a) The current–voltage characteristics of several diodes based on $Hg_{1-X}Mn_XTe$ (E_g = 0.12 eV) with n^+–p junction at 80 K (the diode area is 5×10^{-5} cm^2); (b) the energy-band diagram for the p–n junction under consideration.

[1–4]. Such a model is quite justified only if the layer within which the impurity concentration changes is much thinner than the space-charge region.

In the approximation of a step junction, the ionized donors form the space charge eN_d in the region of $x < 0$, whereas the ionized acceptors give rise to the space charge $-eN_a$ in the region of $x > 0$ (if the n and p regions are formed of compensated semiconductors, N_d and N_a should be replaced with concentrations of uncompensated impurities). For a wide-gap semiconductor, it is typically assumed that the concentration of free (majority) charge carriers at the outer boundaries of the depletion layer (the coordinates W_n and W_p in Fig. 1b) decreases rapidly upon entering deeper lying regions of the p–n junction; therefore, the space-charge densities to the left and to the right of the p–n junction may be considered as coordinate-independent and equal to eN_d and $-eN_a$, respectively (it is assumed that impurities have shallow levels and that the temperature is not too low). For a narrow-gap semiconductor with $E_g \approx 0.1$ eV, in which case the potential-barrier height (the diffusion potential) in the p–n junction is much smaller, the free-carrier contribution to the charge transport cannot be neglected. If, in addition, the p–n junction is asymmetric, and, especially, if one of the regions is degenerate, one should also consider the contribution of minority charge carriers, which come to the lighter doped region from the heavier doped region.

Taking the above into account, we can write the Poisson equations for potential energy $\varphi(x)$ in the one-dimensional case as

$$\frac{d^2\varphi}{dx^2} = \frac{e^2[N_d - n(x) + p(x)]}{\varepsilon\varepsilon_0} \quad \text{for} \quad x < 0, \qquad (1)$$

$$\frac{d^2\varphi}{dx^2} = -\frac{e^2[N_a - p(x) + n(x)]}{\varepsilon\varepsilon_0} \quad \text{for} \quad x > 0, \qquad (2)$$

where ε is the relative permittivity of the semiconductor, ε_0 is the permittivity of free space, and e is the elementary charge.

We will measure the electron energy from the conduction-band bottom in the n^+ region of the diode, and we denote the Fermi energy in the n^+ region by E_{Fn} (Fig. 1b). The electron concentration in the conduction band can then be expressed as

$$n(x, V) = \int_0^\infty \frac{\rho_c(E)dE}{\exp\left(\dfrac{E - E_{Fn} + \varphi(x, V)}{kT}\right) + 1}, \qquad (3)$$

where V is the bias voltage and $\rho_c(E)$ is the density of states in the conduction band. We take into account the nonparabolicity of the latter band using the dispersion law in the widely used Kane model [8]

$$E_c(k) = \frac{\hbar^2 k^2}{2m_e} + \frac{1}{2}\left[\sqrt{E_g^2 + \frac{8}{3}P^2k^2} - E_g\right]. \qquad (4)$$

Using (4), we readily obtain [9]

$$\rho_c(E) = \frac{\sqrt{2}m_e^{3/2}}{\pi^2\hbar^3}E^{1/2}\left(1 + \frac{E}{E_g}\right)^{1/2}\left(1 + 2\frac{E}{E_g}\right), \qquad (5)$$

where $m_e = 3\hbar^2E_g/4P^2$ is the effective electron mass at the conduction-band bottom, and P is a parameter defined by the matrix element of the angular momentum [the expression for the density of states for a parabolic band follows from (5) if we set $E/E_g \ll 1$].

Since the hole concentration in the p region of the diodes under consideration is typically close to 10^{16} cm^{-3} (in any case, it is no higher than 10^{17} cm^{-3}) and the effective hole mass $m_h \approx 0.55m_0$ (m_0 is the electron rest mass), we may disregard the effects of degen-

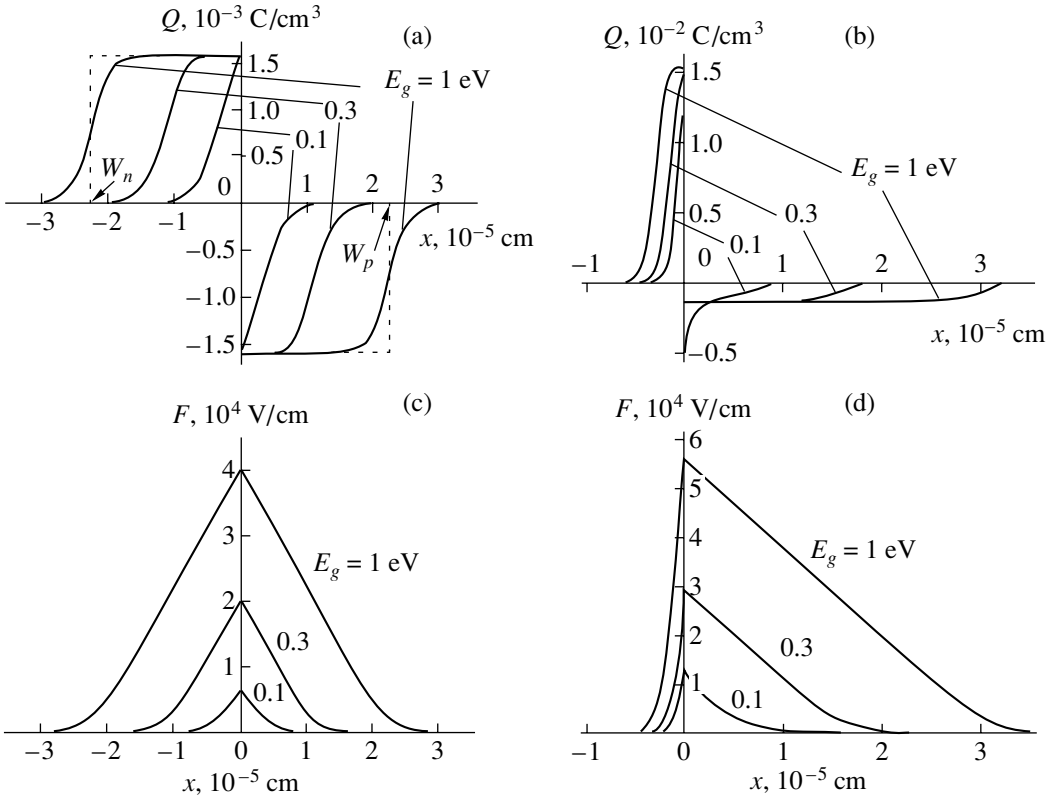

Fig. 2. Distributions of (a, b) the space-charge density and (c, d) the electric-field strength in (a, c) a symmetric p–n junction with $N_a = N_d = 10^{16}$ cm^{-3} and (b, d) an asymmetric junction with $N_a = 10^{16}$ cm^{-3} and $N_d = 10^{17}$ cm^{-3} for three values of the band gap E_g at $T = 77$ K (indicated for each curve).

eracy in the valence band; as a result, the free-hole concentration can be expressed as

$$p(x, V) = \frac{N_v}{\exp\left(\dfrac{E_{Fp} + \varphi_0 - eV - \varphi(x, V)}{kT}\right) + 1}, \quad (6)$$

where E_{Fp} is the distance between the Fermi level and the valence-band top in the p-region bulk, φ_0 is the barrier height in the p–n junction for $V = 0$, and N_v is the effective density of states in the valence band and is equal to $2(m_h kT/2\pi\hbar^2)^{3/2}$ (for the sake of simplicity, we consider only a single type of holes).

Poisson Eqs. (1) and (2), with allowance made for expressions (3)–(6), were solved by the Runge–Kutta [10] method as a system of the first-order differential equations

$$\frac{1}{e}\frac{d\varphi}{dx} = F(x, \varphi), \quad (7)$$

$$\frac{dF}{dx} = \frac{1}{\varepsilon\varepsilon_0}Q(x, \varphi) \quad (8)$$

for the electric-field strength $F(x, V)$ and the space-charge density $Q(x, V)$, respectively. The integration constants were determined from the condition that both equations should yield the same results both for the potential and the electric-field strength at the point $x = 0$. Deep into the n and p regions, the electric-field strength and the space charge were assumed to be equal to zero. For a given free-carrier concentration, the Fermi level position and, therefore, the barrier height in the junction were determined, which represented another condition when solving Eqs. (1) and (2). The calculations were carried out for $T = 77$ K, since the photodiodes for the spectral region of 8–14 μm typically operate at the liquid-nitrogen temperature. The relative permittivity was assumed to be equal to 17 [2].

In Fig. 2, we show the obtained space-charge distribution $Q(x)$, i.e., $e[N_d - n(x) + p(x)]$ for the n-type region, $-e[N_a - p(x) + n(x)]$ for the p-type region (Figs. 2a, 2b), and the distribution of the electric-field strength $F(x)$ for both regions (Figs. 2c, 2d). The calculations were performed for semiconductors with band gaps of 1, 0.3, and 0.1 eV; the effective masses of electrons and holes were assumed to be identical initially: $m_e = m_h = 0.55m_0$. The results of the calculations for a symmetric p–n junction with $N_d = N_a = 10^{16}$ cm^{-3} are shown on the left. As might be expected, the space-charge densities on both sides of the interface are found to be constant within most of the depletion layer for $E_g = 1$ eV; the space-charge density varies gradually

only at the periphery of the depletion layer (the volume density of electric charge equal to 1.6×10^{-3} C cm^{-3} corresponds to the charge of singly ionized impurities with a concentration of 10^{16} cm^{-3}). For $E_g = 0.3$ eV, the transitional region encompasses already an appreciable portion of the depletion layer. For $E_g = 0.1$ eV, the space charge is not constant within the entire depletion layer. The values of W_n and W_p indicated in Fig. 2 correspond to the thickness of the depletion layers in the n and p regions, respectively, for $E_g = 1$ eV if the free charge carriers are disregarded (in order to avoid encumbering Fig. 2 with details, the coordinates W_n and W_p are not indicated for $E_g = 0.3$ and 0.1 eV).

Thus, the above assumption that the role of free charge carriers in the formation of the p–n-junction space charge becomes more important in a narrow-gap semiconductor is verified. Moreover, it can be seen from Fig. 2 that the role of the free charge carriers is found to be prevalent for $E_g \approx 0.1$ eV. As has been noted previously, this is caused by a small (compared to the diodes based on wide-gap semiconductors) contact potential difference, rather than by any other factors. This inference is supported by the fact that the solution of Eqs. (1) and (2), for a reverse-bias voltage of $V = -0.9$ eV, yields nearly the same space-charge profile as in the case of $E_g = 1$ eV and $V = 0$.

It can also be seen from Fig. 2 that the changes in the shape of the space-charge distribution affect the distribution of the electric-field strength in the p–n junction. For $E_g = 1$ eV, the field strength F decreases linearly as the distance from the metallurgical interface increases (this is a well-known fact); for $E_g = 0.3$ eV, the linear portion narrows; and, for $E_g = 0.1$ eV, the dependence $F(x)$ changes radically.

The special features under consideration manifest themselves in an asymmetric p–n junction as well (Figs. 2b, 2d). As E_g decreases, the portions with a constant space-charge density and, correspondingly, with a linear coordinate dependence of the electric-field strength and a quadratic coordinate dependence of potential become narrower both in the p region and in the more heavily doped n region. A distinctive dissimilarity from a symmetric junction consists in the fact that, for a narrow-gap semiconductor ($E_g = 0.1$ eV), the space-charge density increases drastically in the layer adjoining the $x = 0$ boundary from the side of the lightly doped p region owing to the electron transport from the n region (which was mentioned above). This effect becomes more pronounced if there is a large difference between the concentrations N_d and N_a, which is quite possible in the HgMnTe-based n^+–p junctions [2, 3].

Thus, an extension of the model of the p–n junction in a wide-gap semiconductor to the diodes in narrow-gap semiconductors is not quite correct, especially if we are dealing with processes that depend on the potential profile and on the distribution of the electric-field strength in the depletion layer (the processes of generation–recombination, tunneling, and so on).

3. THE ROLE OF DEGENERACY IN THE n REGION

In order to render the effects caused by the narrowing of the semiconductor band gap more pronounced, we assumed that the effective masses of electrons and holes are identical in the above calculations. What actually happens is that the effective electron mass m_e in $Hg_{1-X}Mn_XTe$ (as in $Hg_{1-X}Cd_XTe$) decreases rapidly with decreasing E_g; consequently, the relation $m_e = 0.01m_0$ may be considered typical for $E_g \approx 0.1$ eV [1, 2]. The density of states in the conduction band decreases drastically simultaneously with a decrease in m_e; as a result, as was mentioned above, the degeneracy of an electron gas is observed for the charge-carrier concentrations that are unusually low for a wide-gap semiconductor. The relation between the Fermi energy E_{Fn} and the electron concentration n is given by

$$n(E_{Fn}) = \int_0^\infty \frac{\rho_c(E)dE}{\exp\left(\frac{E - E_{Fn}}{kT}\right) + 1}, \qquad (9)$$

where expression (5) should be used for $\rho_c(E)$. It follows from (9) that, for a semiconductor with $E_g = 0.1$ eV and $m_e = 0.01m_0$, the Fermi level crosses the conduction-band bottom already for $n \approx 3 \times 10^{15}$ cm^{-3} and is found above this bottom by several tenths of an electronvolt for $n \gtrsim 10^{18}$ cm^{-3}. A deviation of the dispersion law in the valence band from the parabolic law (as a variation in the effective hole mass m_h with a narrowing band gap in semiconductors of the HgMnTe type) is typically disregarded; i.e., formula (6) can be used to calculate the hole concentration.

Profound degeneracy of electrons in the n-type region of the diode structure accounts for the experimental fact that the barrier height φ_0 in the n^+–p junction may exceed the semiconductor band gap by a factor of 2–3 [3, 7]. Indeed, in this case we have

$$\varphi_0 = E_g - E_{Fp} + E_{Fn}. \qquad (10)$$

In accordance with (6), the value of E_{Fp} is equal to about 0.025 eV for $p = 3 \times 10^{16}$ cm^{-3} and $T = 77$ K, whereas the barrier height is $\varphi_0 = 0.25$ eV for the n-region electron concentration somewhat higher than 10^{18} cm^{-3}; the latter value is quite realistic.

With allowance made for the aforesaid, Fig. 3 shows the results of solving the Poisson equations (1) and (2) for a semiconductor with a band gap equal to 0.1 eV and parameters typical of the HgMnTe-based p–n junctions ($m_h = 0.55m_0$, $m_e = 0.01m_0$, and $N_a = 10^{16}$ cm^{-3}) for the donor concentrations equal to 10^{16}, 10^{17}, and 10^{18} cm^{-3}. As can be seen from Fig. 3, the energy-band

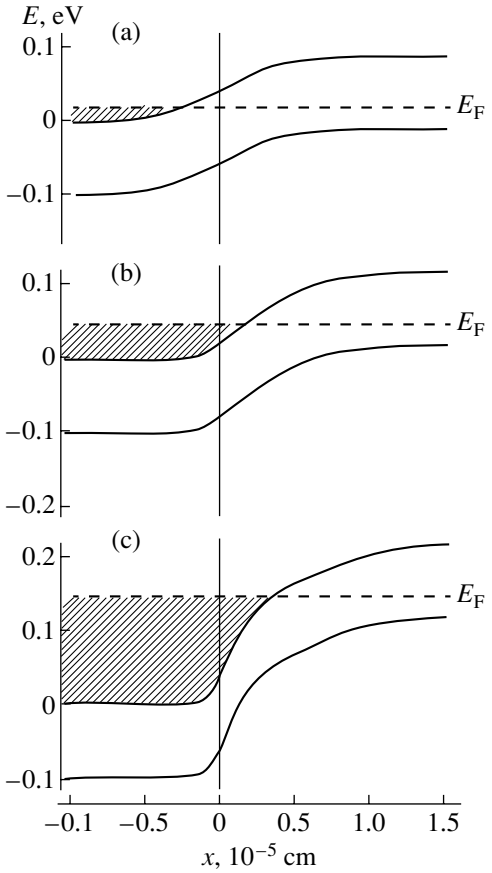

Fig. 3. The energy-band diagram for the junctions with the acceptor concentration $N_a = 10^{16}$ cm^{-3} in the *p*-type substrate and the donor concentrations in the *n*-type layer N_d = (a) 10^{16}, (b) 10^{17}, and (c) 10^{18} cm^{-3}. $E_g = 0.1$ eV, $m_e = m_h = 0.55m_0$, $T = 77$ K, and E_F denotes the Fermi level.

diagram of the *p*–*n* junction for $N_d = 10^{16}$ cm^{-3} resembles that for a step *p*–*n* junction in a wide-gap semiconductor with a degenerate *n* region. However, for $N_d = 10^{17}$ and 10^{18} cm^{-3}, the junction energy-band diagram becomes radically modified. An insignificant voltage drop (0.03–0.04 V) falls within the depletion layer in the n^+-type region, whereas an inversion layer forms in the *p*-type region (as a result of electron injection); this is similar to what occurs at the metal–semiconductor contact or in the surface-barrier diode if there is a large band bending (for a high barrier). Moreover, electrons are in the degenerate state in the inversion layer. The layer with intrinsic conductivity (the *i* layer) and, consequently, the *p*–*n* junction itself are located in the *p*-type region at a considerable distance from the metallurgical interface between the n^+- and *p*-type regions. All of the above suggests that the electrical properties of the diodes under investigation are predominantly governed by the processes in the *p*-type region.

4. GENERATION–RECOMBINATION CURRENTS IN A n^+–*p* JUNCTION

The generation–recombination of charge carriers in the space-charge region is one of the main mechanisms that govern electrical properties of the infrared photodiodes based on HgCdTe and HgMnTe [1–3]. Typically, the generation–recombination processes are accounted for in the context of the Sah–Noyce–Shockley model suggested originally for the interpretation of the characteristics of silicon *p*–*n* junctions [11]. A consideration of the statistics for recombination via a single-type of center yields the following expression for the steady-state recombination rate [12]:

$$U(x, V) = \frac{n(x, V)p(x, V) - n_0p_0}{\tau_{p0}[n(x, V) + n_1] + \tau_{n0}[p(x, V) + p_1]}. \quad (11)$$

Here, $n(x, V)$ and $p(x, V)$ are the concentrations of free charge carriers in the conduction and valence bands, respectively; n_0 and p_0 are the corresponding equilibrium concentrations; and τ_{n0} and τ_{p0} are the lifetimes of electrons and holes in the *p*- and *n*-type semiconductors, respectively. The quantities n_1 and p_1 are numerically equal to the equilibrium concentrations of electrons and holes, on the condition that the Fermi level coincides with the recombination-center level; i.e., n_1 and p_1 are the quantities that control the recombination-rate $U(x, V)$ dependence on the recombination-level depth. Denoting by E_t the energy distance between the recombination level and the conduction-band bottom, we can write the following expressions for n_1 and p_1:

$$n_1 = \frac{N_c}{\exp\left(\frac{E_t}{kT}\right) + 1}, \quad (12)$$

$$p_1 = \frac{N_v}{\exp\left(\frac{E_g - E_t}{kT}\right) + 1}. \quad (13)$$

Integration of $U(x, V)$ over the entire space-charge region yields the following density of the generation–recombination current:

$$J_{gr} = e\int U(x, V)dx. \quad (14)$$

Using formula (14) and expressions (11)–(13), we can derive (with certain simplifications) the analytical expressions for the recombination current under a forward bias voltage and for the generation current under a reverse bias voltage ($eV \gg kT$); these analytical expressions are widely used for a *p*–*n* junction and are written as

$$J_r = \frac{en_iW}{\sqrt{\tau_{n0}\tau_{p0}}}\exp\left(\frac{eV}{2kT}\right), \quad (15)$$

$$J_g = \frac{en_i W}{\sqrt{\tau_{n0}\tau_{p0}}}, \quad (16)$$

where n_i is the intrinsic carrier concentration, W is the width of the space-charge region, and $(\tau_{n0}\tau_{p0})^{1/2} = \tau_0$ is the effective lifetime of charge carriers in this region. The right-hand side of formula (15) is sometimes supplemented with the factor $kT/(\varphi_0 - eV)$, which accounts for the fact that the recombination occurs only in a part of the space-charge region, rather than uniformly over the entire extent of this region.

As follows from the above, the application of expressions (15) and (16) to the HgMnTe-based n^+–p junctions is not quite correct because these expressions were derived without taking into account the special features related to the narrow band gap and profound degeneracy in the n^+-type region. In order to determine the generation–recombination currents in such junctions, we should refer to expressions (11)–(14) using formulas (3) and (6) for $n(x, V)$ and $p(x, V)$. Since there are quite a number of various levels (impurity- and defect-related) in the HgMnTe band gap, we may assume that the most effective recombination centers (according to the Sah–Noyce–Shockley model) are those that have levels with the following depth:

$$E_t = \frac{E_g}{2} - \frac{kT}{2}\ln\left(\frac{\tau_{n0}N_v}{\tau_{p0}N_c}\right). \quad (17)$$

In Fig. 4a, we show the recombination-rate distribution $U(x)$ calculated for the n^+–p junction using formula (11) for various forward-bias voltages. As can be seen, recombination occurs in a relatively narrow space-charge layer in the p-type region of the diode biased by low voltages (the logarithmic scale is used for U). As the voltage increases, the region of the most effective recombination shifts to the n^+–p interface (simultaneously with the narrowing of the space-charge region). Furthermore, the recombination rate at the periphery of the space-charge region increases with voltage more rapidly than in the layer of the most effective recombination; as a result, the recombination rate becomes almost uniform over the entire depletion layer in the p-type region as eV approaches φ_0.

For a reverse bias voltage [in this circumstance, $U < 0$ according to formula (11)], generation occurs also in the p-type diode region, and at notably low voltages in a narrow space-charge region as well (Fig. 4b). As the voltage increases, this layer widens (for a constant recombination rate at its maximum) and ultimately encompasses the entire depletion layer in the p-type region (its thickness increases with voltage).

In Fig. 5, we show the voltage dependences of the generation–recombination current; these dependences were obtained by integrating the $U(x, V)$ function over the entire space-charge region, i.e., from $-W_n$ to W_p. The calculations were performed for the donor concentration of $N_d = 10^{18}$ cm^{-3} in the n^+ layer and for the acceptor concentrations in the p-type substrate equal to $N_a = 10^{16}$, 3×10^{16}, and 10^{17} cm^{-3}. The calculations car-

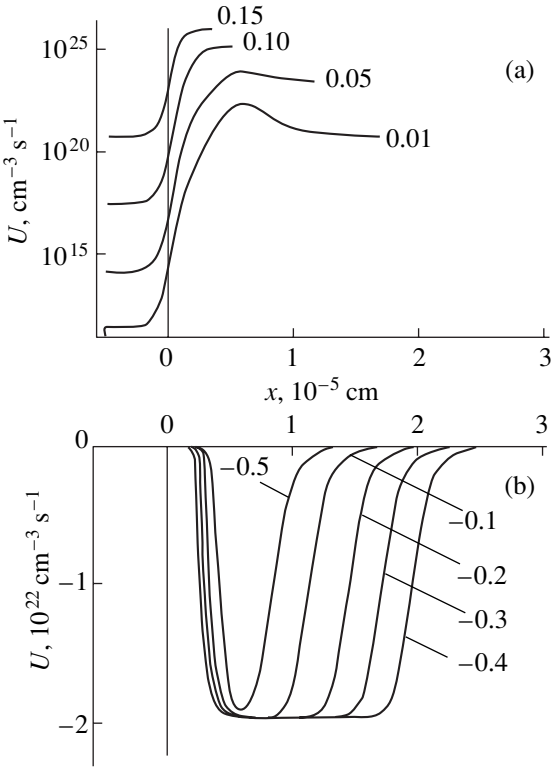

Fig. 4. Distributions of (a) the recombination rate under the forward-bias voltages and (b) the generation rate for the reverse-bias voltages in the n^+–p junction with $N_a = 10^{16}$ cm^{-3} and $N_d = 10^{18}$ cm^{-3} (numbers at the curves indicate the bias voltage expressed in volts).

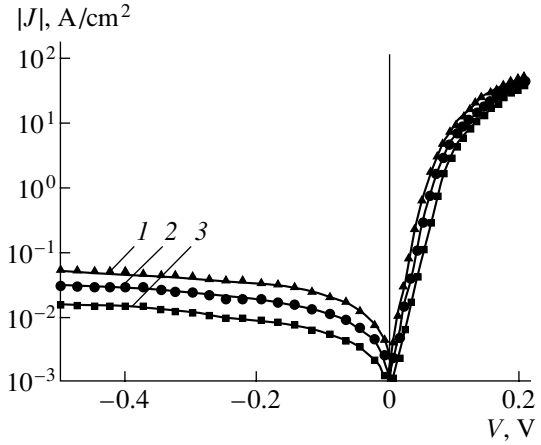

Fig. 5. Calculated dependences of the generation–recombination current density J on the voltage V in the n^+–p junction with $N_d = 10^{18}$ cm^{-3} and the acceptor concentrations in the substrate N_a = (*1*) 10^{16}, (*2*) 3×10^{16}, and (*3*) 10^{17} cm^{-3}.

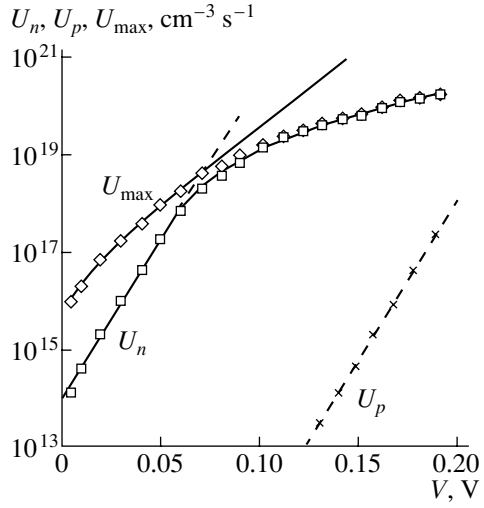

Fig. 6. The voltage dependences of recombination rates at the interfaces of the depletion region with the *p*-type region (U_n) and with the n^+-type region (U_p) and of the recombination rate at its maximum U_{max}. The solid and dashed straight lines correspond to $U \propto \exp(eV/kT) - 1$.

ried out for a fixed value of N_a and various values of N_d show that the current–voltage characteristic is almost independent of N_d in a wide range of its variation (from 3×10^{17} to 3×10^{18} cm^{-3}) [3]. This is understandable since the generation–recombination processes in the junction occur, as follows from Fig. 4, mainly in the *p*-type region of the diode.

A comparison of the results illustrated in Figs. 5 and 1 shows, first of all, that the measured reverse currents are greatly in excess of the calculated currents and, in addition, depend more heavily on the voltage. This is explained by the fact that the reverse currents in the HgMnTe-based diodes at low temperatures (77 K) are controlled by high-field effects (tunneling and the avalanche multiplication of charge carriers); it is only at 180–200 K that the generation current becomes prevalent [3].

The calculated forward current at low bias voltages (lower than 0.07–0.08 V) obeys the dependence given by formula (15) and, for higher voltages, deviates from this dependence to lower values of the current, which is consistent with the behavior of experimental curves. Notably, a deviation from the above dependence is not observed if we assume that $m_e = m_h = 0.55m_0$ and increase the diffusion potential by setting E_g = 0.2–0.3 eV. As for the absence of a new increase in the current in the bias-voltage region above ~0.25 V in the calculated curves (Fig. 5), in contrast to the experimental curves (Fig. 1), this is explained by the fact that the above-barrier transport of charge carriers was disregarded in the above calculations; i.e., the diffusion currents of the minority charge carriers were ignored.

5. THE ROLE OF DIFFUSION CURRENTS

The electron and hole diffusion currents under the forward-bias voltage can be determined using the results of the calculation of the recombination rate in the junction (Fig. 4a). Assuming that the concentration of electrons injected into the neutral *p*-type region ($x > W_p$) decreases with the coordinate as $\exp(-x/L_n)$ (L_n is the electron diffusion length) [4, 5], we can obtain the density J_n of the electron diffusion current by multiplying the recombination rate at the point $x = W_p$ by L_n; i.e.,

$$J_e = eU_n(x = W_p)L_n.$$

Similarly, the hole diffusion current is given by

$$J_p = eU_p(x = W_n)L_p,$$

where L_p is the hole diffusion length.

Dependences of recombination rates U_p and U_n at the points $x = W_p$ and $x = -W_n$ on the voltage V and the dependence of U_{max} at its maximum on V are shown in Fig. 6. Comparing the curves, we may immediately conclude that the electron diffusion current cannot give rise to inflection in the current–voltage characteristic at $V \approx 0.25$ V observed experimentally, because, in this voltage region, the dependence $U_n(V)$ is nearly the same as $U_{max}(V)$ (the dependence $I \propto \exp(eV/kT)$ typical of the above-barrier current is observed only at low voltages). However, this is not the case for the hole diffusion current: the dependence $U_p(x = W_n)$ on V follows the law $\exp(eV/kT)$ in the entire voltage range. This is understandable because the potential barrier for holes in the n^+–*p* junction is fairly high (in contrast to the barrier for electrons, as can be seen from Fig. 3); therefore, the concentration of holes that can penetrate into the n^+-type region is controlled by the Boltzmann factor of the form $\exp[-(\varphi_0 + E_{F_p} - eV)/kT] \propto \exp(eV/kT)$. Thus, the diffusion current of holes from the lightly doped *p* region (rather than the electron current from the heavily doped n^+-type region, as might be assumed [4, 5]) gives rise to the inflection observed in the measured current–voltage characteristics in the region of V = 0.25–0.3 V.

In order to estimate quantitatively the contribution of the hole diffusion current, we use the expressions $L_p = (D_p\tau_p)^{1/2}$ and $eD_p/kT = \mu_p$, where D_p, τ_p, and μ_p are the diffusion coefficient, lifetime, and mobility of holes, respectively. Assuming that $\mu_p = 10^3$ cm^2 V^{-1} s^{-1}, we obtain $D_p \approx 10$ cm^2/s at 77 K. The lifetime of holes τ_p can be determined by comparing the results of calculation with experimental data. In so doing, we should bear in mind that the lifetime may be found to be shorter by several orders of magnitude than the adopted value of 10^{-6} s (quite acceptable for the layer depleted of the charge carriers) due to the intense Auger recombination in the heavily doped n^+ region [2].

Taking into account the aforesaid, we show in Fig 7 the results of calculating the current–voltage character-

istics of the n^+–p junction for several values of τ_p taking into account two current components: the recombination current in the space-charge region and the diffusion current of holes. We used the parameters realistic for a HgMnTe-based diode: $N_a = 3 \times 10^{16}$ cm^{-3}, $N_d = 10^{18}$ cm^{-3}, $(\tau_{n0}\tau_{p0})^{1/2} = \tau_0 = 10^{-6}$ s, and the junction area $A = 5 \times 10^{-5}$ cm^2; the hole lifetime was used as an adjustable parameter, which was varied in a wide range of 10^{-6}–10^{-10} s [3].

As can be seen, consideration of the hole diffusion current gives rise to the sought-for additional increase in the current for $V > 0.15$–0.25 V. To ensure that the onset of this increase corresponds to the inflection in experimental curves (Fig. 1), the hole lifetime should be set equal to 10^{-8}–10^{-9} s. However, the calculated curve runs much steeper than experimental curves for large currents. This discrepancy can be easily explained by the fact that, in this region of currents, an appreciable portion of the voltage applied to the diode drops on the substrate series resistance R_s, which amounts to 100–300 Ω for the HgMnTe-based diodes [3]. If the voltage drop across R_s is taken into account, the calculated dependence becomes much like the experimental curve (the dashed line). The determining contribution of the hole diffusion current at large currents does not exclude the important role of the electron diffusion current at low forward-bias voltages.

Despite the lower recombination rate at the interface between the depletion layer and the neutral p region ($U_n < U_{max}$ in Fig. 6), the electron diffusion current may become important for a certain relation between the parameters owing, in particular, to a larger diffusion length of electrons.

Concluding the presentation of the results obtained, let us analyze the applicability of the model used for calculating the currents. Under the conditions of the forward bias, formulas (3) and (6) are valid only if the recombination current is much smaller than the diffusion current of charge carriers in any cross section of the junction; i.e., in this case, the diffusion current is nearly balanced by the drift current (see [5], pp. 189–190). Let us compare the recombination current J_r represented in Fig. 7 with the diffusion currents of electrons $J_e = eD_n dn/dx$ and holes $J_h = eD_p dn/dx$ in the junction cross section where the recombination rate is at its maximum. For each value of V, the coordinate x corresponding to $U = U_{max}$ can be determined from the results shown in Fig. 4a; the dependences $n(x, V)$ and $p(x, V)$ can be derived from formulas (3) and (6) if the potential $\varphi(x, V)$ at the same point is known.

The electron diffusion current calculated in the above manner for a diode with $N_a = 10^{16}$ cm^{-3} and $N_d = 10^{18}$ cm^{-3} is found to exceed the recombination current by about a factor on the order of 30 in the entire voltage range; the ratio between the hole diffusion current and the recombination current is even greater (10^3). We emphasize that this is valid for the p–n-junction cross section where the recombination rate is at its maximum; in other regions of the p–n junction, the inequalities $J_r \ll J_e$ and $J_r \ll J_h$ are satisfied with an even greater margin. Thus, we may assume that recombination hardly distorts the charge-carrier distribution given by formulas (3) and (6).

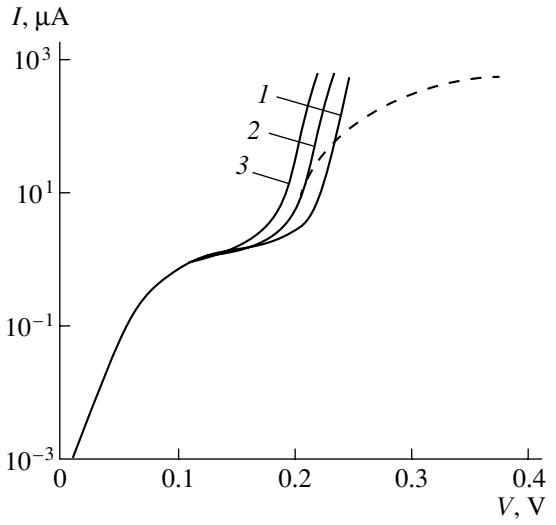

Fig. 7. The forward current–voltage characteristics of n^+–p junction ($E_g = 0.1$ eV) for $N_a = 3 \times 10^{16}$ cm^{-3} and $N_d = 10^{18}$ cm^{-3}. When calculating the recombination current, the carrier lifetime in the depletion region τ_0 was assumed equal to 10^{-6} s. The diffusion current of holes was calculated using the values of the hole lifetime in the n^+-type region τ_p equal to (*1*) 10^{-10}, (*2*) 10^{-8}, and (*3*) 10^{-6} s. Dashed line represents the result of calculation with $\tau_p = 10^{-8}$ s taking into account the voltage drop across the substrate series resistance $R_s = 250$ Ω.

6. CONCLUSION

The distributions of the space-charge density, the electric-field strength, and potential in a p–n junction change radically if one passes from a wide-gap semiconductor to a semiconductor that has a narrower band gap and is suitable for detection of infrared radiation within the atmospheric window of 8–14 μm ($E_g \approx 0.1$ eV). These changes are mainly caused by the effect of the majority charge carriers; however, the role of minority charge carriers is also important in an asymmetric p–n junction with a degenerate n^+ region. As a result, the coordinate dependences of the electric-field strength and potential cease to be linear and quadratic, respectively; in addition, the space-charge density ceases to be coordinate-independent. Owing to these effects, the voltage dependence of the recombination current in a narrow-gap semiconductor differs from that described by the conventional analytical expression ($I \propto \exp(eV/2kT) - 1$). For high forward-bias voltages, diffusion of minority charge carriers from the lightly

doped p region to the degenerate n^+ region (rather than from the n^+ region to the p region) makes an appreciable contribution to the charge transport in a n^+–p junction. The current–voltage characteristics calculated, taking into account the special features of the processes occurring in the n^+–p junction in a narrow-gap semiconductor, describe adequately the experimental curves measured for the HgMnTe-based diodes.

The results of this study may be used to calculate the tunneling current and (taking into account all the possible mechanisms of the charge transport) to determine one of the key parameters of an infrared detector, i.e., the differential resistance of the diode R_0 under zero bias. However, these issues require special consideration.

ACKNOWLEDGMENTS

We are grateful to Sun Weiguo for providing us with the samples of HgMnTe-based diodes and to V.M. Sklyarchuk who performed measurements.

REFERENCES

1. A. Rogalski, Infrared Phys. **28**, 139 (1988).
2. A. Rogalski, Infrared Phys. **31**, 117 (1991).
3. L. A. Kosyachenko, I. M. Rarenko, Sun Weiguo, and Lu Zheng Xiong, Solid-State Electron. **44**, 1197 (2000).
4. S. M. Sze, *Physics of Semiconductor Devices* (Wiley, New York, 1981; Mir, Moscow, 1984), Vol. 1.
5. G. E. Pikus, *The foundations of Theory of Semiconductor Devices* (Nauka, Moscow, 1965).
6. L. A. Kosyachenko, I. M. Rarenko, O. A. Bodnaruk, and Sun Weiguo, Fiz. Tekh. Poluprovodn. (St. Petersburg) **33**, 1438 (1999) [Semiconductors **33**, 1293 (1999)].
7. L. A. Kosyachenko, S. É. Ostapov, and Sun Weiguo, Fiz. Tekh. Poluprovodn. (St. Petersburg) **34**, 695 (2000) [Semiconductors **34**, 668 (2000)].
8. E. O. Kane, J. Phys. Chem. Solids **1**, 249 (1957).
9. P. S. Kireev, *Physics of Semiconductors* (Vysshaya Shkola, Moscow, 1975).
10. L. I. Turchak, *Basics of Numerical Methods* (Nauka, Moscow, 1987).
11. C. Sah, R. Noyce, and W. Shockley, Proc. IRE **45**, 1228 (1957).
12. W. Shockley and W. T. Read, Jr., Phys. Rev. **17**, 835 (1952).

Translated by A. Spitsyn

Semiconductors, Vol. 35, No. 11, 2001, pp. 1279–1281. Translated from Fizika i Tekhnika Poluprovodnikov, Vol. 35, No. 11, 2001, pp. 1335–1337.

SEMICONDUCTOR STRUCTURES, INTERFACES, AND SURFACES

Effect of Surface Orientation of $Cd_xHg_{1-x}Te$ Crystals on the Properties of Surface Anodic Oxides

V. G. Sredin*, Yu. S. Mezin, and V. M. Ukrozhenko***

** Military Academy of Strategic Rocket Forces, Moscow, 103074 Russia*

*** RD&P Center "Orion", Moscow, 111123 Russia*

Submitted February 8, 2001; accepted for publication April 2, 2001

Abstract—Electron spectroscopy for chemical analysis was used to study the effect of surface orientation of $Cd_xHg_{1-x}Te$ crystals ($x = 0.19$) on the composition of anodic oxide. It is found that anodic oxide compositions on the (111) and (100) crystal surfaces are identical and change gradually from the substrate to the outer surface, whereas the oxide on the (110) surface contains an interlayer of unoxidized Te. This result correlates with some properties known for $Cd_xHg_{1-x}Te$ oxides. © *2001 MAIK "Nauka/Interperiodica".*

The properties of semiconductors depend heavily on the quality of surface insulator layers, which, in most cases, are produced, similarly to Si, by oxidizing the crystal surface. Layers, obtained in this way in compound semiconductors consist of a combination of various oxides of different composition as a result of variation in oxidation rates for the elements incorporated in the crystal. This brings about a strong dependence of the physical properties of oxides and oxide/semiconductor interfaces on the oxidation technology and initial state of the surface. For certain semiconductor materials, the surface oxides are unstable because of chemical reactions occurring in the solid phase of layers and at a contact with the crystal surface. As a result, the oxide can contain the elements incorporated in a semiconductor or the compounds of these elements. These issues have been considered in detail previously [1, 2]. As an alternative method for protecting the surfaces of device structures obtained on the basis of compound semiconductors, one can use the growth of insulating layers or the passivation of the surface [3]. However, the sulfate, selenide, and fluoride layers on the surface of $Cd_xHg_{1-x}Te$ are, like the layers of its native oxide, also unstable [1].

It has been shown previously for crystals of the $Cd_xHg_{1-x}Te$ solid solution with the sphalerite structure that there exists a certain correlation between the properties of a surface anodic oxide and the crystallographic orientation of the surface on which it was grown [4]. For example, the growth rate of the oxide on the (110) crystallographic plane is the lowest in comparison with the growth rate on the (100) and (111) planes (see Fig. 1). It can be seen that only the growth curves for the (110) plane do not show kinks which are indicative of the change in growth rate associated with the change of oxide composition in the course of its formation.

In this study, we attempt to make a direct comparison between the chemical compositions of the anodic oxide layers grown on differently oriented planes of the crystals of $Cd_xHg_{1-x}Te$ solid solutions with $x = 0.19$. For the experiments, samples with approximately the same electrical properties (*p*-type conductivity with charge carrier concentration of about 8×10^{15} cm^{-3} and mobility of about 3×10^2 cm^2 V^{-1} s^{-1} at 77 K) were chosen. According to X-ray data, the orientation of the crystal surfaces coincided with the crystallographic (100), (110), and (111) planes within 6°. The oxide layers were grown under identical conditions on the crystal surfaces: they were etched preliminarily in a standard bromine etchant by anodizing in 0.1 N solution of KOH in ethyleneglycol. The thickness of the oxide layers was 100–130 nm.

The composition of oxides was studied by electron spectroscopy for chemical analysis (ESCA) under high-vacuum conditions (the residual pressure was lower than 10^{-9} Torr) in a MIKROLAB-MK-II two-chamber system. The characteristic spectra of the ele-

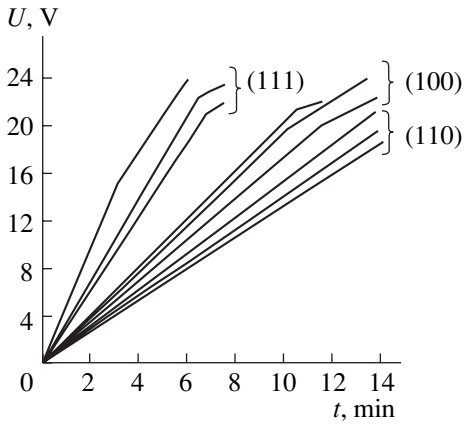

Fig. 1. Kinetic curves of growth of anodic oxide on the oriented surfaces of $Cd_{0.19}Hg_{0.81}Te$ single crystals.

1063-7826/01/3511-1279$21.00 © 2001 MAIK "Nauka/Interperiodica"

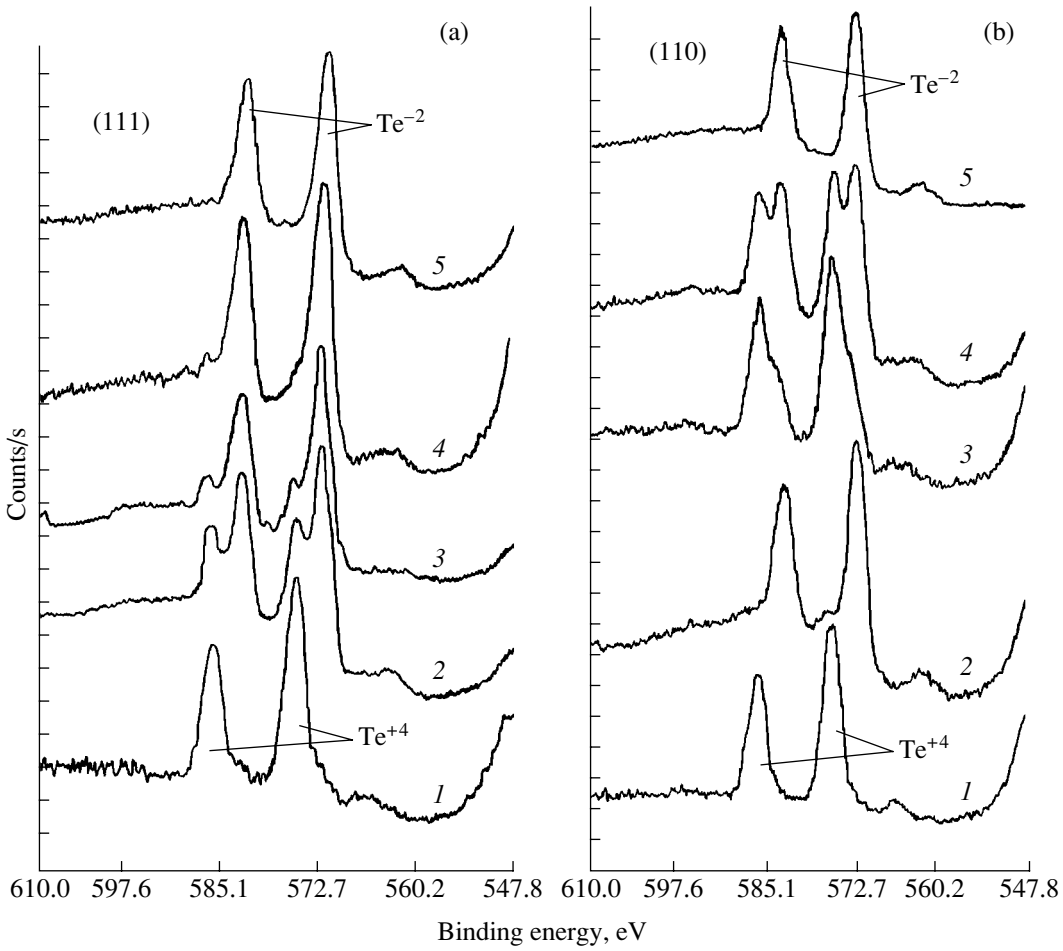

Fig. 2. ESCA spectra of anodic oxides on the surfaces of $Cd_{0.19}Hg_{0.81}Te$ single crystals with (a) (111) and (b) (110) orientations measured after the successive (*1–5*) layer-by-layer etching off the oxide from (*1*) its outer surface down to (*5*) the crystal surface.

ments were excited by X-rays with a photon energy of 1253.6 eV. In order to remove adsorbed impurities from the surface of anodic oxide, the samples were etched for a short time prior to measurements by singly ionized argon ions at an energy of 10 keV in a sample-preparation chamber preliminarily evacuated to a pressure lower than 10^{-9} Torr. The conditions of ion etching allowed for the measurement of 4–5 spectra for a given thickness of a layer. The main results are shown in Fig. 2.

The recorded spectra contain lines resulting from the excitation of photoelectrons from the core states in Cd, Hg, and Te ions. The lines of the elements analyzed in this study have a doublet structure (Fig. 2); however, it is sufficient to monitor the evolution of only one component of a doublet. The largest chemical shift resulting from the change in ion surroundings is observed for Te. Its lines correspond to the $3d_{5/2}$ state with the energies of 576.1 eV for Te^{+4} in TeO_2, $CdTeO_3$, and $HgTeO_3$ oxides, and 572.6 eV for Te^{-2} in the crystal. The position of the unshifted line for atomic Te corresponds to the energy of 572.6 eV. The chemical shifts for cations in these materials are small in contrast to those in Te because the sign of a shift, contrary to the case of Te, is not changed when a cation passes from crystal to oxide. Therefore, the change in Cd and Hg surroundings in oxides, in comparison with a substrate, manifests itself only as a broadening of $4f_{7/2}$ Hg and $3d_{5/2}$ Cd lines, which is quite large: the line width for Hg increases approximately from 1 eV in crystal to 1.5 eV in oxide; the line width for Cd, from 1.2 to 1.5 eV. Generally, the results obtained are consistent with the data published in [5, 6]; however, the studies of changes in oxide composition relative to the depth revealed a certain orientational effect. Our measurements show that the composition of the oxide on the (111) and (100) crystal faces changes gradually from the substrate to the outer surface (see Fig. 2a), while, for the oxide grown on the (110) face, the precipitation of unoxidized Te within a certain interval of depth is observed (Fig. 2b, curve *2*). The formation of an interlayer containing unoxidized Te at different distances from the outer surface was

observed only for the oxide grown on the (110) face. The occurrence of a certain amount of unoxidized, possibly amorphous, Te on the (111) surface immediately under the oxide layer and inside the layer (Fig. 2a, curves *3*, *4*) may be caused by the precipitation of Te as a product of the reaction during the chemical etching prior to oxide growth, as was reported in [6]. As can be seen in Fig. 2b, the content of this Te phase decreases gradually with the distance from the crystal/oxide interface. Near the outer surface of the oxide, the layers contain completely oxidized Te (Fig. 2b, curve *1*). The composition of the oxide on the (111) surface depends on depth in the same monotonic way. The occurrence of an interlayer of unoxidized Te in the oxide under the (110) surface may result from a solid-phase reaction. It is known that Cd and Hg oxides are unstable when they come into contact with the surface of a solid solution. It still remains unclear why the suggested reactions occur only for one of many possible orientations.

Thus, our measurements showed a similarity in the compositions of anodic oxides on the (100) and (111) surfaces, in contrast to the (110) surface, and revealed a correlation between the properties of the oxides and their composition. Indeed, the twofold higher density of built-in charge [4] on the (110) surface can be attributed to the presence of unoxidized Te in this layer. The kinks in the growth curves for the oxides on the (100) and (111) surfaces may indicate the gradual disappearance of this ion from the oxide layer (Fig. 2a, curves *2*–*4*). Indeed, the oxidation rate for Te is higher than for Hg and Cd; therefore, the growth rate of a surface layer after the complete oxidation of Te decreases, which is observed in kinetic curves of growth (Fig. 1).

We may assume that the observed orientational effects are related to the common features of the physicochemical properties of materials with a sphalerite structure. The (110) plane in this structure is known to be a cleavage plane and is characterized by a zero surface charge density, while the (111) plane is a polar one and carries a positive charge, if it consists of cations, and a negative charge, if it contains anions. The density of a surface charge in the latter case is highest for the crystals with a sphalerite structure. This distinction, as well as the difference in chemical composition of the surfaces, are apparently responsible for the anisotropy of some physical properties. Indeed, it was shown that the energy of bonding ions to the surface of $Cd_xHg_{1-x}Te$ depends on the crystallographic orientation of the surface [7]. The processes of crystal formation also depend heavily on orientation. For example, the (111) plane in crystals with a sphalerite structure is a plane of the highest growth rate, which is experimentally confirmed for CdTe [8] and $Cd_xHg_{1-x}Te$ [9]. It has also been found that the diffusion rate of Ga in $Cd_xHg_{1-x}Te$ depends more heavily on orientation and changes by more than an order of magnitude for various crystallographic orientations [10]. The orientational dependence of the growth rate of a surface layer was observed for GaAs [3] and InSb [11]. Thus, the orientation-dependent properties and composition of surface anodic $Cd_xHg_{1-x}Te$ oxides correlate with the orientational features of the surfaces of other materials with a sphalerite structure and should be taken into consideration in the development of device structures.

ACKNOWLEDGMENT

The authors thank A.V. Voĭtsekhovskiĭ for his participation in discussing the results.

REFERENCES

1. C. R. Hill, J. Vac. Sci. Technol. A **8** (2), 1778 (1990).
2. A. V. Voĭtsekhovskiĭ and V. N. Davydov, *Photoelectric Metal-Insulator-Semiconductor Structures Based on Narrow-Gap Semiconductors* (Radio i Svyaz', Tomsk, 1990).
3. V. N. Bessolov and M. V. Lebedev, Fiz. Tekh. Poluprovodn. (St. Petersburg) **32** (11), 1281 (1998) [Semiconductors **32**, 1141 (1998)].
4. V. G. Sredin, O. G. Lanskaya, and V. M. Popovnin, Fiz. Tekh. Poluprovodn. (St. Petersburg) **30** (3), 385 (1996) [Semiconductors **30**, 215 (1996)].
5. G. F. Wagner and D. R. Rhiger, J. Vac. Sci. Technol. A **3** (1), 212 (1985).
6. N. R. Aigina and N. N. Berchenko, Zarubezhn. Élektron. Tekh., No. 10 (305), 3 (1986).
7. M. A. Berding, K. Srinivasan, and A. Sher, J. Vac. Sci. Technol. B **9** (3), 1858 (1990).
8. *Physics and Chemistry of II–VI Compounds*, Ed. by M. Aven and J. S. Prener (North-Holland, Amsterdam, 1967; Mir, Moscow, 1970).
9. G. Ginader, A. Raizman, and A. Sher, J. Vac. Sci. Technol. B **9**, 1634 (1991).
10. R. Korenstein, P. Hallok, B. MacLeod, *et al.*, J. Vac. Sci. Technol. A **8** (2), 1039 (1990).
11. L. L. Chang, Solid-State Electron. **10**, 69 (1967).

Translated by A. Zalesskiĭ

Semiconductors, Vol. 35, No. 11, 2001, pp. 1282–1284. Translated from Fizika i Tekhnika Poluprovodnikov, Vol. 35, No. 11, 2001, pp. 1338–1340.

SEMICONDUCTOR STRUCTURES, INTERFACES, AND SURFACES

Photosensitivity of *a*-C:H/*c*-Si Heterojunctions

V. G. Baryshnikov*, Yu. A. Nikolaev, V. Yu. Rud'***, Yu. V. Rud'**, and E. I. Terukov****

** Institute of Physics, Dagestan Science Center, Russian Academy of Sciences, Makhachkala, 367030 Russia*

*** Ioffe Physicotechnical Institute, Russian Academy of Sciences, ul. Politekhnicheskaya 26, St. Petersburg, 194021 Russia*

e-mail: yu.nikolaev@pop.ioffe.rssi.ru

**** St. Petersburg State Technical University, ul. Politekhnicheskaya 29, St. Petersburg, 195251 Russia*

Submitted March 19, 2001; accepted for publication April 3, 2001

Abstract—Layers of *a*-C:H were grown on *c*-Si wafers by the glow discharge method in a CH_4 + Ar gaseous mixture. The electrical and photoelectric properties of *a*-C:H/c-Si heterojunctions were studied. It was found that the heterojunctions display rectification and broad-band photovoltaic effects. It is shown that the polarization sensitivity in these structures occurs at an oblique incidence of linearly polarized light under the illumination of the surface coated with *a*-C:H layers. The observed oscillations in the spectrum of the coefficient of induced photopleochroism are attributed to the interference of light in these layers. © *2001 MAIK "Nauka/Interperiodica".*

There is increasing interest in the possible use of carbon in the form of *a*-C:H amorphous layers in Si-based photoconverters [1–4]. The central problem for this promising system is the choice of technology that would ensure sufficiently effective doping of C layers [3, 5]. We present here the first results of studying the photoelectric properties of heterojunctions (HJs) exposed to natural and linearly polarized light and obtained by depositing thin layers of amorphous C on the surface of single-crystal Si at various technological parameters.

The (100)-oriented single-crystal Si wafers with *p*-type conductivity and resistivity of ~20 Ω cm at T = 300 K were used as substrates for the deposition of C. The C layers were deposited from a gaseous mixture of 12% CH_4 with argon by the glow-discharge method in a capacitance-type reaction chamber with a quasi-closed volume and electrodes 110 mm in diameter. The substrate temperature during the deposition was maintained around 20 or 100°C. The applied high-frequency power at 13.5 MHz for the deposition duration of about 1 h is given in the table. Homogeneous dark-lilac-colored layers exhibiting high adhesion to the substrate material were formed on the surface of the Si wafers. The films had a thickness of about 100 nm.

Measurements of the steady-state current–voltage (*I–V*) characteristics of HJ showed that the chosen method of deposition of *a*-C:H layers provided reproducibility in the obtaining of rectifying structures. As an example, a steady-state *I–V* characteristic for one of the HJs is shown in Fig. 1. As a rule, the conducting direction in all structures corresponded to the negative polarity of an external bias applied to the *a*-C:H layers. If the bias exceeded the cutoff voltage U_0, the forward portions of the steady-state *I–V* characteristic followed the relation

$$I = (U - U_0)/R_r,$$

with the residual resistance R_r and the voltage U_0 depending on the parameters of the technological process (see table). The range of variation of R_r and U_0

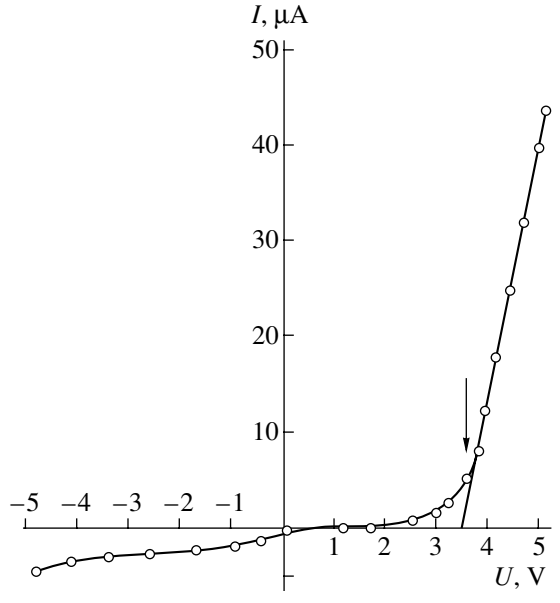

Fig. 1. Steady-state current–voltage characteristic of *a*-C:H/c-Si heterojunction for sample 1 at T = 300 K. The conducting direction corresponds to positive voltage on *c*-Si.

with applied power P and the substrate temperature T_S was quite wide, which made it possible to control the electrical properties of this type of HJ.

During illumination, the photovoltaic effect was observed. Its sign was independent of the position of the light spot (its diameter was about 0.5 mm) on the surface of a structure. The layers always became negatively charged with respect to a substrate which corresponded to the polarity of rectification. The photosensitivity of all HJ was highest under illumination of the surface coated with *a*-C:H layers. The data given in the table correspond to this geometry of experiment. It can be seen that the highest voltage photosensitivity S_U^{m} depends on the conditions of the deposition of C layers, and the highest current photosensitivity reaches the value $S_I^{\mathrm{m}} \approx 27$ μA/W and is controlled predominantly by the resistance of these layers.

The spectral variations of relative quantum efficiency η of HJ under exposure to unpolarized light are shown in Fig. 2. It can be seen that the position and the shape of the long-wavelength cutoff of η are determined by the interband absorption in crystalline Si irrespective from which side of the HJ was illuminated: from the side covered with *a*-C:H layers or from the side of thick single-crystal Si substrate. In the region of the fundamental absorption of *c*-Si, a pronounced dependence of $\eta(\hbar\omega)$ on the geometry of illumination was observed as the optical absorption coefficient increased. Under the illumination of the substrate side (Fig. 2, curve *1*'), a sharp drop in the photosensitivity of structures at $\hbar\omega > 1.2$ eV was observed; this drop is due to the increase in the distance of the absorption zone from the active area of the structures. In contrast, under the illumination of the side coated with *a*-C:H layers, broad-band spectra (Fig. 2, curves *1–4*) with a constant sign of photocurrent in the entire spectral range of photosensitivity were observed. Therefore, it may be assumed that the heterocontact between the amorphous C and crystalline Si gives rise to an effective energy barrier, and the observed interference features in $\eta(\hbar\omega)$ spectra for some of the HJs (Fig. 2, curves *1* and *3*) are indicative of high optical quality of the amorphous *a*-C:H layers.

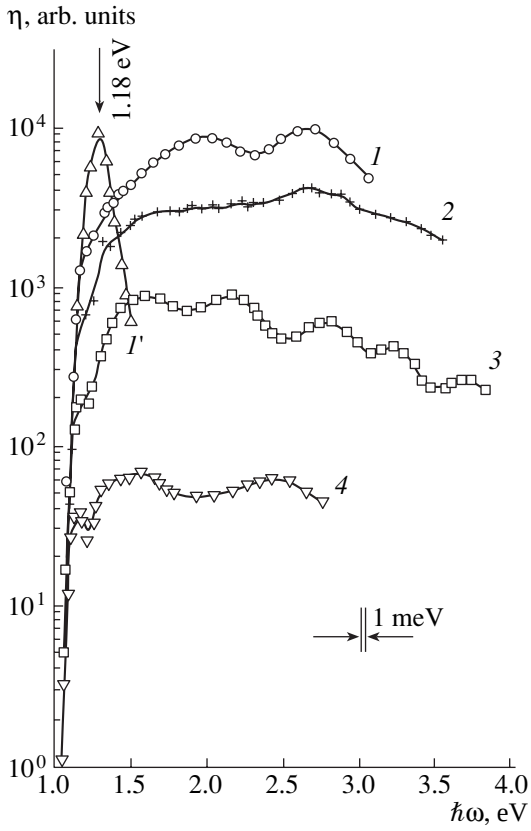

Fig. 2. Spectra of relative quantum efficiency of *a*-C:H/*c*-Si heterojunctions exposed to unpolarized light at $T = 300$ K: (*1–4*) illumination of *a*-C:H layer; (*1*') illumination of the *c*-Si substrate 0.3 mm in thickness. Numeration of curves corresponds to samples numbered in the table. Curve *1*' corresponds to sample 1.

It should be mentioned that, as the high-frequency power applied during the growth of the layers increases, well-defined peaks appear on the long-wavelength side of the spectra at an energy of $\hbar\omega^{\mathrm{m}} \approx 1.13$ eV (Fig. 2, curves *3* and *4*), whereas, at a lower applied power, the $\eta(\hbar\omega)$ spectra only show inflections near this energy (Fig. 2, curves *1* and *3*). It may be assumed that this feature is caused by the formation of sublayers or inclusions of the carbon phase with a band gap $E_g \approx$ 1 eV [4] in these *a*-C layers, while the major part of the

Photoelectric characteristics of *a*-C:H/*c*-Si heterojunctions

Sample no.	Conditions of *a*-C:H deposition		U_0, V	R_r, 10^5 Ω	S_U^{m}, V/W	S_I^{m}, μA/W
	P, W	T_s, K				
1	15	300	3.5	1.2	43	27
2	15	400	1.9	3.1	80	–
3	30	300	4.0	5.3	150	–
4	30	400	2.5	6.0	26	–

Note: The temperature of the measurement was $T = 300$ K; illumination was from the side of the surface coated with amorphous C.

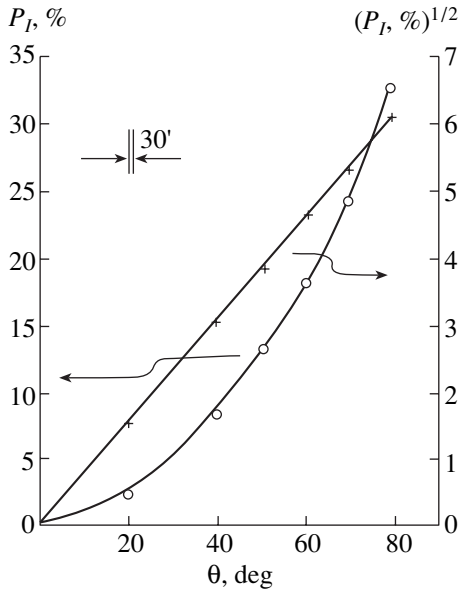

Fig. 3. Dependence of the coefficient of induced photopleochroism on the angle of incidence of linearly polarized light on the *a*-C:H surface of *a*-C:H/*c*-Si heterojunction at T = 300 K. Sample 3, $\hbar\omega$ = 2.2 eV.

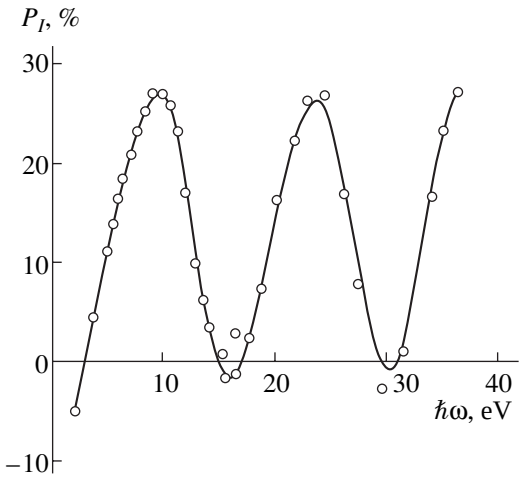

Fig. 4. Spectral dependence of the coefficient of induced photopleochroism for *a*-C:H/*c*-Si heterojunction at T = 300 K. Sample 3, θ = 70°.

a-C:H layers consists of a wide-gap phase responsible for the broad-band character of the photosensitivity of the HJ obtained by glow discharge method in the CH_4 + Ar gaseous mixture. The range of the highest photosensitivity of HJs coincides with the solar radiation spectrum, which is promising evidence for their use in the design of highly efficient solar cells.

The studies of the photosensitivity of *a*-C:H/*c*-Si HJ under exposure to linearly polarized light at the incidence normal to the plane of *a*-C:H do not reveal any dependence of photoresponse on the orientation of the electric-field vector **E** of a light wave with respect to the structures studied, which indicates that photoactive absorption in both heterocomponents is isotropic. The polarization sensitivity of the HJ exists only at an oblique incidence of linearly polarized light. The angular variations of short-circuit photocurrents for both polarizations i^p and i^s in such an HJ are similar. These variations are intensified and form peaks with increasing angle of incidence θ due to the interference (according to [6, 7]) of incident light, thus indicating a high quality of *a*-C:H layers.

The angular dependence of the coefficient of induced photopleochroism P_I typical of all *a*-C:H/*c*-Si HJs is shown in Fig. 3. Within the entire range of photosensitivity, this dependence follows the parabolic law $P_I^{1/2} \sim \theta$, which is consistent with the theoretical considerations [8]. Spectral variations of this coefficient in such HJs (Fig. 4) exhibit pronounced oscillations caused, according to [7–9], by the interference of incident light in the layers of amorphous C. The $P_I(\hbar\omega)$ spectra clearly show that the HJs studied can be used as selective photoanalyzers for linearly polarized light in the vicinity of $P_I(\hbar\omega)$ peaks, while the spectral range in the vicinity of the minima of $P_I(\hbar\omega)$ curves ensures the conditions for maximal transmission $P_I = 0$ [8].

Thus, the obtained heterostructures based on thin C layers and Si crystals display a broad-band photovoltaic effect and induced pleochroism. The oblique incidence of linearly polarized light gives rise to the induced pleochroism controlled by the conditions of the deposition of *a*-C:H layers and by the angle of incidence. The induced pleochroism can be used for diagnostics of such structures and for the development of polarimetric photosensors of linearly polarized light.

REFERENCES

1. H. N. Konofaos and C. B. Tomas, J. Appl. Phys. **81**, 6238 (1997).
2. S. Birkle, J. Kammermaier, and G. P. Rutmayer, US Patent 5206534 (1993).
3. K. M. Krishna, T. Soga, T. Jimbo, and M. Umeno, Carbon **37**, 531 (1999).
4. K. M. Krishna, Y. Nukaya, T. Soga, *et al.*, Sol. Energy Mater. Sol. Cells **65**, 163 (2001).
5. K. L. Narayanan and M. Yamaguchi, Appl. Phys. Lett. **75**, 2106 (1999).
6. V. Yu. Rud' and Yu. V. Rud', Fiz. Tekh. Poluprovodn. (St. Petersburg) **31**, 245 (1997) [Semiconductors **31**, 197 (1997)].
7. V. M. Botnaryuk, A. V. Koval', V. Yu. Rud', *et al.*, Fiz. Tekh. Poluprovodn. (St. Petersburg) **31**, 800 (1997) [Semiconductors **31**, 677 (1997)].
8. F. P. Kesamanly, V. Yu. Rud', and Yu. V. Rud', Fiz. Tekh. Poluprovodn. (St. Petersburg) **33**, 513 (1999) [Semiconductors **33**, 483 (1999)].
9. V. Yu. Rud', Yu. V. Rud', and H. W. Schock, Solid State Phenom. **67–68**, 421 (1999).

Translated by A. Zalesskiĭ

Semiconductors, Vol. 35, No. 11, 2001, pp. 1285–1290. Translated from Fizika i Tekhnika Poluprovodnikov, Vol. 35, No. 11, 2001, pp. 1341–1346.

SEMICONDUCTOR STRUCTURES, INTERFACES, AND SURFACES

Reverse Current in Graded-Gap *p–n* Structure with Nonmonotonic Coordinate Dependence of the Band Gap

B. S. Sokolovskiĭ

Franko State University, Lviv, 79602 Ukraine

Submitted February 6, 2001; accepted for publication April 5, 2001

Abstract—The specific features of the reverse current of a graded-gap *p–n* structure with the band gap linearly increasing with the distance from the interface plane are analyzed theoretically. It is shown that the graded gap makes it possible to substantially reduce the reverse current of the *p–n* junction associated with the thermal generation of carriers in the base regions of the structure and at ohmic contacts. The possible appearance of a region with negative differential resistance in the reverse current–voltage characteristic in the case of a large band-gap gradient is predicted. © *2001 MAIK "Nauka/Interperiodica".*

1. INTRODUCTION

One of the important problems to be tackled in developing threshold photodiode detectors of weak electromagnetic radiation for, in particular, the IR spectral range consists in the necessity of lowering the reverse current (RC), which determines the detectivity of photodetectors [1]. The conventional method of suppressing the diffusion component of the RC of a *p–n* junction, associated with thermal generation of carriers in the base and at contacts, is to raise the doping level of the entire base or its near-contact regions [2]. However, the decrease in the carrier lifetime with increasing doping level and the narrowing of the gap of a heavily doped semiconductor impose limitations on the maximum efficiency of RC suppression by this method. Therefore, the search for new methods for RC suppression is a topical problem of semiconductor photoelectronics. Quite promising in this connection is the application of "band diagram engineering" to develop not only high-sensitivity photoresistors [3–6], but also photodiode detectors with low dark RC. This is, in particular, indicated by the results of an analytical calculation of RC for a semiconductor diode with a wide band-gap layer in the base region [7] and by numerical calculation of the sensitivity of a photodiode with graded-gap layers at the contacts [8].

In this study, we substantiate theoretically the possibility of significantly suppressing the RC in *p–n* structures associated with thermal carrier generation in the base regions and at contacts. This suppression can be achieved by the gradual increase of the band gap with increasing distance from the *p–n* junction interface.

2. ENERGY DIAGRAM OF A GRADED-GAP *p–n* STRUCTURE

Let us consider a graded-gap structure uniformly doped with acceptor and donor impurities at concentrations N_a and N_d in, respectively, the regions $-d_p \le x < 0$ and $0 < x \le d_n$, where the band gap E_g and the electron affinity χ linearly vary with the coordinate and E_g has a minimum at the interface ($x = 0$) (Fig. 1a). To calculate the current transport through such a structure, it is necessary to know the coordinate dependences of the conduction and valence band edges E_c and E_v, defined at a given $E_g(x)$ and $\chi(x)$ by the spatial distribution of the electrostatic potential φ [9]

$$E_c = E_0 - \chi - e\varphi, \tag{1}$$

$$E_v = E_0 - \chi - E_g - e\varphi, \tag{2}$$

where E_0 is the vacuum level.

A space charge region (SCR) ($-x_p \le x \le x_n$) and quasi-neutral base regions ($-d_p < x \le -x_p$, $x_n \le x < d_n$) can be distinguished in the graded-gap *p–n* structure under consideration. On the assumption that nondegenerate statistics are observed and the minority carrier densities are small in comparison with N_a and N_d, the equilibrium majority carrier densities in the quasi-neutral regions are given by

$$p_p^{(0)} = N_v \exp\left(\frac{E_v - E_F}{kT}\right) \cong N_a, \tag{3}$$

$$n_n^{(0)} = N_c \exp\left(\frac{E_F - E_c}{kT}\right) \cong N_d, \tag{4}$$

where N_c and N_v are the effective densities of states in the conduction and valence bands (these densities are assumed to be coordinate-independent), and E_F is the Fermi level.

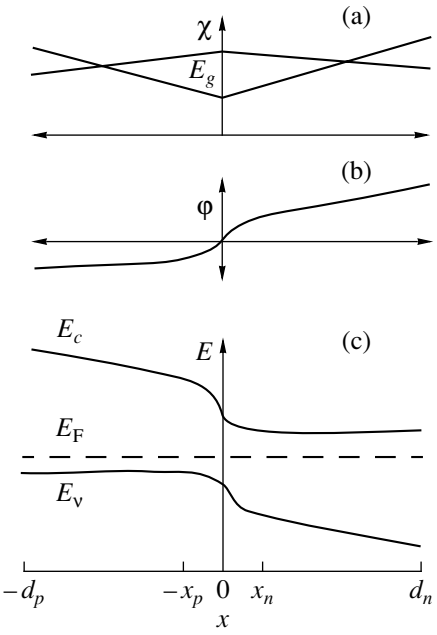

Fig. 1. Coordinate profiles of (a) band gap and electron affinity and (b) electrostatic potential; (c) equilibrium energy diagram for the graded-gap *p–n* structure under study.

From (1)–(4) it follows that there are uniform electric fields in the quasi-neutral base regions defined by the expressions

$$\frac{d\varphi}{dx} = -\frac{1}{e}\left(\frac{dE_g}{dx} + \frac{\chi}{dx}\right), \tag{5}$$

$$\frac{d\varphi}{dx} = -\frac{1}{e}\frac{d\chi}{dx}, \tag{6}$$

for, respectively, the *p* and *n* regions; i.e., the potential linearly depends on the coordinate in the base regions of the graded-gap structure (Fig. 1b).

The spatial distribution of the electrostatic potential in the SCR ($-x_p \le x \le x_n$) is described in the approximation of a totally depleted contact layer by the equation

$$\frac{d^2\varphi}{dx^2} = -\frac{e}{\varepsilon\varepsilon_0}[N_d\theta(x) - N_a\theta(-x)], \tag{7}$$

where ε is the dielectric constant of the graded-gap semiconductor, considered to be coordinate-independent; ε_0 the permittivity of free space; and θ(*z*) the step-function (θ(*z*) = 0 at *z* <0, θ(*z*) = 1 at $z \ge 0$).

Solving Eq. (7) with boundary conditions stemming from (5) and (6) and assuming that φ = 0 at *x* = 0, we obtain

$$\varphi(x) = \frac{eN_a}{2\varepsilon\varepsilon_0}x^2 + \left[\frac{eN_a x_p}{\varepsilon\varepsilon_0} + \frac{kT}{e}(\beta_p + \gamma_p)\right]x \quad \text{for} \quad -x_p \le x \le 0, \tag{8}$$

$$\varphi(x) = -\frac{eN_d}{2\varepsilon\varepsilon_0}x^2 + \left[\frac{N_d x_n}{\varepsilon\varepsilon_0} + \frac{kT}{e}\beta_n\right]x \quad \text{for} \quad 0 \le x \le x_n. \tag{9}$$

For any specific graded-gap semiconductor, the reduced (normalized to *kT*) electron affinity gradients

$$\beta_p = -\frac{1}{kT}\frac{d\chi}{dx}\bigg|_{x<0}, \quad \beta_n = \frac{1}{kT}\frac{d\chi}{dx}\bigg|_{x>0}, \tag{10}$$

appearing in (8) and (9) are related in a certain way to the reduced band gap gradients

$$\gamma_p = -\frac{1}{kT}\frac{dE_g}{dx}\bigg|_{x<0}, \quad \gamma_n = \frac{1}{kT}\frac{dE_g}{dx}\bigg|_{x>0}. \tag{11}$$

In particular, according to the experimental data [10], $\beta_{p,n} \cong -2/3\gamma_{p,n}$ for the graded-gap CdHgTe solid solution.

The total voltage drop $\varphi(x_n) - \varphi(-x_p)$ across the *p–n* junction is constituted by the source voltage *U* (*U* < 0 at reverse bias) and the contact potential U_c equal to the difference of the thermionic work functions for the SCR boundaries normalized to unit charge:

$$U_c = U_{c0} + \frac{kT}{e}[(\beta_p + \gamma_p)x_{p0} - \beta_n x_{n0}], \tag{12}$$

where $U_{c0} = (kT/e)\ln(N_a N_d/n_{i0}^2)$; n_{i0} is the intrinsic carrier density at *x* = 0; x_{p0}, x_{n0} are the values of x_p, x_n at U_0. We obtain from (8) and (9):

$$U_c - U = U_p + U_n = \frac{eN_a}{2\varepsilon\varepsilon_0}x_p^2 + \frac{eN_d}{2\varepsilon\varepsilon_0}x_n^2 + \frac{kT}{e}[(\beta_p + \gamma_p)x_p - \beta_n x_n], \tag{13}$$

where $U_p = -\varphi(-x_p)$, $U_n = \varphi(x_n)$ are the voltage drops across the SCR parts situated, respectively, in the *p* and *n* regions.

Using the relation

$$x_n N_d = x_p N_a + \frac{kT\varepsilon\varepsilon_0}{e^2}(\beta_p + \beta_n + \gamma_p), \tag{14}$$

which follows from the electric field continuity at *x* = 0, and taking (13) into account, we obtain expressions for the space charge layer thickness in the *p* and *n* regions of the graded-gap *p–n* structure, which are necessary for the subsequent calculation of the RC,

$$x_p = L_{Dp}^2\left[-\beta_p - \gamma_p + \sqrt{\frac{2e}{kT}\frac{U_c + U_\nabla - U}{L_{Dp}^2 + L_{Dn}^2}}\right], \tag{15}$$

$$x_n = L_{Dn}^2\left[\beta_n + \sqrt{\frac{2e}{kT}\frac{U_c + U_\nabla - U}{L_{Dp}^2 + L_{Dn}^2}}\right], \tag{16}$$

with the contact potential difference for the p–n junction given by

$$U_c = U_{c0} - 2U_\nabla + \frac{kT}{e}\delta\left[\delta + \sqrt{\frac{2e}{kT}(U_{c0} - U_\nabla) + \delta^2}\right] \quad (17)$$

in accordance with (12).

The following designations are introduced in (15)–(17):

$$L_{Dp,n} = \sqrt{\frac{\varepsilon\varepsilon_0 kT}{e^2 N_{a,d}}},$$

$$U_\nabla = \frac{kT}{2e}[L_{Dp}^2(\beta_p^2 + \gamma_p^2) + L_{Dp}^2\beta_n^2], \quad (18)$$

$$\delta = \frac{(\beta_p + \gamma_p)L_{Dp}^2 - \beta_n L_{Dn}^2}{\sqrt{L_{Dp}^2 + L_{Dn}^2}}.$$

An energy diagram of a graded-gap p–n structure is shown in Fig. 1c. Its characteristic feature is the presence of cusps at $x = 0$ in the spatial dependence of band edges, resulting from jump discontinuities in the band-gap and electron affinity gradient at this point.

3. SPECIFIC FEATURES OF THE DIFFUSION–DRIFT REVERSE CURRENT IN A GRADED-GAP p–n STRUCTURE

In the graded-gap p–n structure, the RC, associated with the thermal generation of carriers in the base regions of the p–n structure and at contacts, has a diffusion–drift nature because of the presence in the graded-gap semiconductor of quasi-electric fields proportional to the valence and conduction band edge gradients for, respectively, the p- and n-type semiconductors. The electron j_n and hole j_p current densities or, more precisely, their x components are defined in the p and n quasi-neutral regions by the expressions [11]

$$j_n = kT\mu_n\left[\frac{dn_p}{dx} - \gamma_p n_p\right], \quad (19)$$

$$j_p = -kT\mu_p\left[\frac{dp_n}{dx} - \gamma_n p_n\right], \quad (20)$$

where n_p and p_n are the densities of nonequilibrium electrons and holes in the p and n base regions; μ_n and μ_p are the electron and hole mobilities, assumed to be coordinate independent; γ_n and γ_p are defined by the equalities (11).

Taking (19) and (20) into account, the coordinate dependences of the nonequilibrium minority carrier densities in the base regions can be found from the following continuity equations:

$$\frac{d^2 n_p}{dx^2} - \gamma_p\frac{dn_p}{dx} - \frac{n_p}{L_n^2} = -\frac{n_{i0}^2}{L_n^2 N_a}\exp(\gamma_p x) \quad (21)$$

$$\text{for } -d_p \le x \le -x_p,$$

$$\frac{d^2 p_n}{dx^2} + \gamma_n\frac{dp_n}{dx} - \frac{p_n}{L_p^2} = -\frac{n_{i0}^2}{L_p^2 N_d}\exp(-\gamma_n x) \quad (22)$$

$$\text{for } x_n \le x \le d_n,$$

where L_n and L_p are the diffusion lengths for electrons and holes, assumed to be constant throughout the structure, and n_{i0} is the intrinsic carrier density at the p–n junction interface ($x = 0$).

We supplement Eqs. (21) and (22) with the boundary conditions

$$n_p(-d_p) = \frac{n_{i0}^2}{N_a}\exp(-\gamma_p d_p), \quad (23)$$

$$p_n(d_n) = \frac{n_{i0}^2}{N_d}\exp(-\gamma_n d_n), \quad (24)$$

corresponding to ohmic contacts, and

$$n_p(-x_p) = \frac{n_{i0}^2}{N_a}\exp(-\gamma_p x_p)\exp\frac{eU}{kT}, \quad (25)$$

$$p_n(x_n) = \frac{n_{i0}^2}{N_d}\exp(-\gamma_n x_n)\exp\frac{eU}{kT}, \quad (26)$$

which follow from the Boltzmann relation between the minority carrier densities at the SCR boundaries in equilibrium and on applying voltage U (as before, $U < 0$ for reverse bias).

With the carrier generation current in the SCR neglected, we can calculate the RC of the graded-gap p–n structure as the sum of the diffusion–drift currents of the minority carriers at the SCR boundaries, i.e.,

$$j_r = j_n(-x_p) + j_p(x_n). \quad (27)$$

Having determined the coordinate dependences of the minority carrier densities from (21)–(26), we obtain on the basis of (19), (20), and (27) the following expression for the diffusion–drift RC of the graded-gap p–n junction

$$j_r(U) = (j_r^p + j_r^n)\exp\left[\left(-\frac{e|U|}{kT}\right) - 1\right], \quad (28)$$

where

$$j_r^{p,n} = \frac{en_{i0}^2 L_{n,p}^2}{2\tau_{n,p}N_{a,d}}\left[\sqrt{\gamma_{p,n}^2 + 4L_{n,p}^{-2}}\right.$$

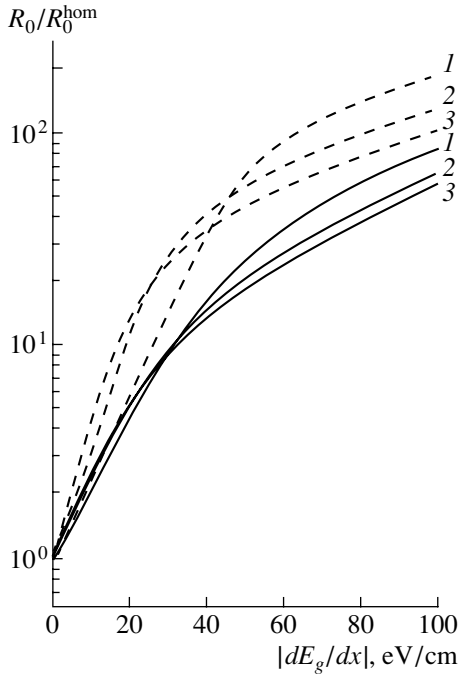

Fig. 2. Differential resistance at zero bias vs. band-gap gradient for graded-gap *p–n* structure based on a CdHgTe solid solution of variable composition with Cd content at the interface $x_{\text{Cd}} = 0.3$ at $T = 77$ K, $N_a = 5 \times 10^{15}$ cm^{-3}, $\gamma_p = \gamma_n$, $d_p = d_n$ and different base region thicknesses: (*1*) 10, (*2*) 15, and (*3*) 20 μm. Impurity concentration in the *n*-region N_a is (solid line) 5×10^{14} and (dashed line) 5×10^{16} cm^{-3}.

$$\times \coth\left(\frac{(d_{p,n} - x_{p,n})\sqrt{\gamma_{p,n}^2 + 4L_{n,p}^{-2}}}{2}\right) - \gamma_{p,n}\Bigg] \qquad (29)$$

$$\times \exp(-\gamma_{p,n} x_{p,n}).$$

In (29), we introduced, on the basis of the relations $L_{n,p}^2 = (kT/e)\mu_{n,p}\tau_{n,p}$, the electron τ_n and hole τ_p lifetimes in the *p* and *n* regions.

In the particular cases of $\gamma_p = \gamma_n = 0$, (29) yields the known formulas for the diffusion RC in the homo-band *p–n* junction [2].

It is noteworthy that, although the carrier transport in the quasi-neutral base regions is controlled only by the band-gap gradient, the electron affinity gradient also affects the RC by exerting influence on the thickness of the SCR layer.

From (29), it follows that a steady decrease in the RC components corresponding to the *p* and *n* base regions occurs with increasing E_g gradient. In the case of high quasi-electric fields ($\gamma_{n,p} \gg L_{p,n}^{-1}$) and widely separated ohmic contacts ($d_{n,p} \gg \gamma_{n,p}^{-1}$), the expressions for j_r^p and j_r^n are reduced to

$$j_r^{p,n} = \frac{en_{i0}^2}{\tau_{n,p}\gamma_{p,n}N_{a,d}}\exp(-\gamma_{p,n}x_{p,n}), \qquad (30)$$

i.e., the decrease in RC with increasing E_g gradients follows either the power law (for $\gamma_{n,p} \ll x_{n,p}^{-1}$) or the exponential law (for $\gamma_{n,p} \gtrsim x_{n,p}^{-1}$).

We can distinguish three factors leading to a decrease in the RC in the graded-gap *p–n* junction in comparison with its homoband analogue. First, with the band gap increasing with the distance from the interface, the rate of thermal carrier generation in the base regions becomes slower owing to a decrease in the carrier density. Second, in view of the fact that the characteristic lengths in the distribution of minority carriers in the base regions adjacent to the SCR are, following from the solutions of Eqs. (21) and (22), the "against-the-field" diffusion-drift lengths $L_{n,p}^* = 2/(\gamma_{p,n} + \sqrt{\gamma_{p,n}^2 + 4L_{n,p}^{-2}}) < L_{n,p}$, the sizes of the regions in the *p* and *n* parts of the structure, contributing to RC, decrease. Finally, the influence of carrier generation at the contacts decreases both through an increase in the effective distance between contacts (by the factor $L_{n,p}/L_{n,p}^*$) and as a result of the decrease in the emissivity of the contacts because of the increasing band gap in the adjoining regions.

Using (29), we can calculate the effect of the graded-gap type of the structure on such an important parameter of the threshold photodetectors as the differential resistance of the *p–n* structure at zero bias, $R_0 = [Adj_r/dU]^{-1}|_{U=0}$ (where *A* is the contact area), associated with the diffusion-drift current transport mechanism under consideration. In particular, at $L_{p,n}^{-1}, d_{n,p}^{-1} \ll \gamma_{n,p} \ll x_{n,p}^{-1}$, we have

$$\frac{R_0}{R_0^{\text{hom}}} = \frac{\gamma_n\gamma_p}{\zeta\gamma_n L_n^{-1} + \gamma_p L_p^{-1}} \times\left(\zeta\coth\frac{d_p - x_p^0}{L_n} + \coth\frac{d_n - x_n^0}{L_p}\right), \qquad (31)$$

where R_0^{hom} is the differential resistance at zero bias for a homoband *p–n* structure with band gap $E_g(0)$, and all other parameters are the same as those in the graded-gap *p–n* structure; $\zeta = \tau_p L_n N_d/\tau_n L_p N_a$ is the ratio of electron and hole RC components in the graded-gap *p–n* structure with thick base regions ($d_{n,p} \gg L_{p,n}$); x_p^0, x_n^0 are the SCR thicknesses in the *p* and *n* parts of the homoband *p–n* structure, given by (15) and (16) at $\gamma_{p,n} = \beta_{p,n} = 0$.

As follows from (31), under the conditions when the electron component of the RC both in the graded-gap and in the related homoband structures is predominant, i.e., in the case when the inequality $\zeta \gg \coth[(d_n - x_n^0)/L_p]/\coth[(d_p - x_p^0)/L_p]$, $\gamma_p L_n/\gamma_n L_p$ is valid, the relative increase in R_0 is proportional to $\gamma_p L_n \coth[(d_p - x_p^0)/L_n]$. If, by contrast, the hole current predominates, and the opposite inequality is valid, then $R_0/R_0^{\text{hom}} \gg \gamma_n L_p \coth[(d_n - x_n^0)/L_p]$. Since the quasi-electric field exerts a stronger influence on the transport of minority carriers characterized by a larger diffusion length [11], it is quite understandable why the effect of the graded-gap nature of the structure on R_0 is more pronounced in thin structures, in which the RC is determined by carriers with a higher mobility.

On passing to band-gap gradients at which the band-gap variation across the SCR in the *n* and *p* parts of the structure is approximately equal to or greater than *kT* ($\gamma_{n,p} \gtrsim x_{n,p}^{-1}$), the increase in R_0 is mainly determined by the decrease in the minority carrier density at the SCR boundary because of its increasing thickness. This results in the linear growth of R_0 changing for the exponential behavior with the index increasing as the impurity concentration in the base regions is lowered.

As an example, Fig. 2 shows the dependence of the differential resistance at zero bias on the E_g gradient for a photodiode for the mid IR spectral range, fabricated on the basis of an asymmetrically doped ($N_a \neq N_d$) graded-gap CdHgTe solid solution. This dependence is normalized to R_0^{hom} of a photodiode fabricated from the corresponding homoband material. In the calculations, the lifetimes of electrons and holes were assumed equal, and the diffusion lengths of the electrons and holes at $T = 77$ K were chosen as 30 and 10 μm [12, 13], respectively. In addition, we used the relation $\beta_{p,n} = -2/3\gamma_{p,n}$, which is valid, as mentioned above, for a graded-gap CdHgTe. As seen from Fig. 2, a significant increase in R_0 can be achieved even at relatively small E_g gradients, particularly in thin-layer structures with a heavily doped *n* region.

It is noteworthy that, in practice, to ensure effective light absorption, the thickness of the base regions of the photodiode must not be smaller than the inverse light absorption coefficient [14], which is taken into account in the calculations whose results are presented in Fig. 2. At the same time, there is no fundamental restriction on the difference between the band gaps of the base regions. In addition to the broadening of the photodiode's sensitivity spectral range, an increase in these differences at fixed thicknesses of the base regions favors the transport of minority carriers into the narrow bandgap region, where the SCR is located, because of the increasing quasi-electric fields [15, 16].

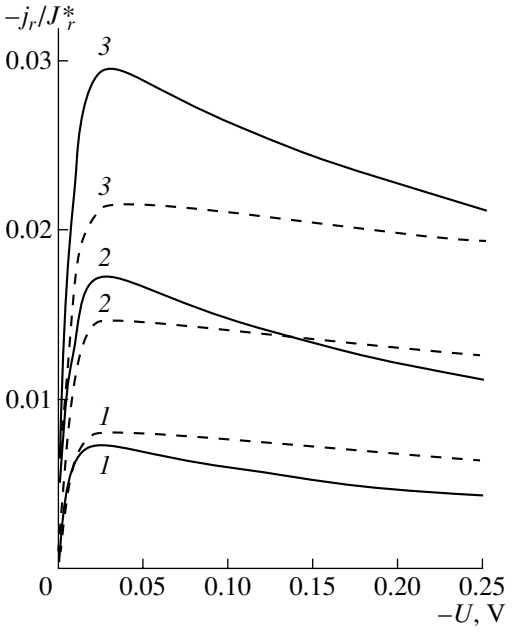

Fig. 3. Diffusion–drift reverse current vs voltage for a graded-gap *p–n* structure based on CdHgTe solid solution with composition changing from $x_{\text{Cd}} = 0.3$ to $x_{\text{Cd}} = 0.4$ at the same parameter values as in Fig. 2.

An important feature of graded-gap *p–n* structures with nonmonotonic coordinate dependence of the band gap is the possibility of the occurrence of nonmonotonic field dependences of RC, which is associated with the SCR expansion with increasing reverse bias and the resulting decrease in the minority carrier density at the SCR boundary. At E_g gradients determined by the inequality $\gamma_{n,p} \gg d_{n,p}^{-1}, L_{p,n}^{-1}$, the product of the differential resistance *R* and the *p–n* junction area *A* at $|eU| \gg kT$ is given, on the basis of (15), (16), and (29), by

$$(RA)^{-1} = en_{i0}^2 \eta(U) \times \left[\frac{L_{Dp}^2}{\tau_n N_a}\exp(-\gamma_p x_p) + \frac{L_{Dn}^2}{\tau_p N_d}\exp(-\gamma_n x_n)\right]. \quad (32)$$

Here, the reduced rate $\eta(U)$ of variation with the voltage of the SCR thicknesses in the *p* and *n* parts of the structure, can be expressed in terms of quantities defined by the equalities (17) and (18):

$$\eta(U) = \frac{1}{L_{Dp}^2}\frac{dx_p}{dU} = \frac{1}{L_{Dn}^2}\frac{dx_n}{dU} = -\sqrt{\frac{e}{2kT}\frac{1}{(L_{Dp}^2 + L_{Dn}^2)(U_c + U_\nabla - U)}}. \quad (33)$$

In order for the nonmonotonic voltage dependence of RC to be sufficiently pronounced, the condition $\gamma_{n,p} \gtrsim x_{n,p}^{-1}$ must be satisfied. In this case, the absolute value of the negative differential resistance (NDR)

grows exponentially, as does R_0, with increasing E_g in that region of the p–n structure, which mainly contributes to the RC. The initial part of the NDR region in the case of a symmetric graded-gap structure ($\gamma_p = \gamma_n$, $N_a = N_d$) corresponds, by the lowest approximation with respect to $U/(U_c + U_\nabla)$, to the voltage

$$U \cong -\frac{kT}{e}\ln\left[1 + \frac{2}{\gamma_p L_{Dp}}\sqrt{\frac{e}{kT}(U_c + U_\nabla)}\right], \qquad (34)$$

i.e., the larger the E_g gradient and the smaller the impurity concentration in the base regions, the earlier the NDR region appears.

The voltage dependences of the diffusion-drift RC for a graded-gap p–n CdHgTe structure with the fixed composition difference ($x_{\mathrm{Cd}}(0) = 0.3$, $x_{\mathrm{Cd}}(-d_p) = x_{\mathrm{Cd}}(d_n) = 0.4$) normalized to the RC $j_r^* = e n_{i0}^2 L_n/\tau_n N_a + e n_{i0}^2 L_p/\tau_p N_d$ of a homo-band p–n junction with thick base regions ($d_{n,p} \gg L_{p,n}$) are presented in Fig. 3. It can be seen that, for the chosen parameters of the graded-gap structure, the most pronounced NDR is observed in the case of a weakly doped n region and a maximum base thickness, i.e., at the smallest E_g. This can be accounted for by the increase, with decreasing base thickness, in the relative contribution to the RC from the electron component (because of the influence of the adjacent ohmic contact), which exhibits a weaker dependence on voltage (since $x_p < x_n$ at $N_a > N_d$). It is clear that the diffusion-drift component of the RC must predominate for the NDR to be observed experimentally in the reverse current–voltage (I–V) characteristic. Since the tunnel component of the RC can be neglected in the voltage range under consideration (0–0.25 V) [17], it is necessary to ensure that small values of the RC, associated with carrier generation in the SCR for the NDR, be manifested in the I–V characteristic. It is noteworthy that descending portions of similar shape but of different origin were observed in I–V characteristics of abrupt CdHgTe heterostructures under the conditions of carrier extraction [18].

4. CONCLUSION

This theoretical analysis of a model graded-gap p–n structure with the band gap linearly increasing with the distance from the interface plane demonstrated the possibility of a significant decrease in the RC associated with thermal generation of carriers in the base regions of the structure and at ohmic contacts. In the case of large band-gap gradients (with band-gap variation across the SCR in n- and p-type regions of the graded-gap structure comparable with or larger than kT), an NDR region appears in the reverse I–V characteristic formed under the conditions of predominant diffusion-drift current transport. The revealed RC features, combined with the fact that the internal quasi-electric field makes the carrier-collection coefficient larger [15], indicate that the graded-gap structures considered in this study hold promise for the development of high-sensitivity photodetectors.

REFERENCES

1. *Optical and Infrared Detectors*, Ed. by R. J. Keyes (Springer-Verlag, New York, 1977; Radio i Svyaz', Moscow, 1985).
2. S. Sze, *Physics of Semiconductor Devices* (Wiley, New York, 1981; Mir, Moscow, 1984).
3. V. G. Savitskiĭ and B. S. Sokolovskiĭ, Fiz. Tekh. Poluprovodn. (Leningrad) **13**, 1452 (1979) [Sov. Phys. Semicond. **13**, 851 (1979)].
4. V. G. Savitskiĭ and B. S. Sokolovskiĭ, Fiz. Tekh. Poluprovodn. (St. Petersburg) **31**, 3 (1997) [Semiconductors **31**, 1 (1997)].
5. V. M. Osadchiĭ, A. O. Suslyakov, V. V. Vasil'ev, and S. A. Dvoretskiĭ, Fiz. Tekh. Poluprovodn. (St. Petersburg) **33**, 293 (1999) [Semiconductors **33**, 297 (1999)].
6. V. A. Kholodnov and A. A. Drugova, Pis'ma Zh. Tekh. Fiz. **26** (5), 49 (2000) [Tech. Phys. Lett. **26**, 202 (2000)].
7. B. S. Sokolovskiĭ, Pis'ma Zh. Tekh. Fiz. **26** (7), 51 (2000) [Tech. Phys. Lett. **26**, 292 (2000)].
8. V. V. Vasil'ev, D. E. Esaev, F. A. Kravchenko, *et al.*, Fiz. Tekh. Poluprovodn. (St. Petersburg) **34**, 877 (2000) [Semiconductors **34**, 844 (2000)].
9. A. H. Marshak and K. M. Vliet, Solid-State Electron. **21**, 417 (1978).
10. D. Eich, K. Ortner, U. Groh, *et al.*, Phys. Status Solidi A **173**, 261 (1999).
11. O. V. Konstantinov and G. V. Tsarenkov, Fiz. Tekh. Poluprovodn. (Leningrad) **10**, 720 (1976) [Sov. Phys. Semicond. **10**, 427 (1976)].
12. *Properties of Narrow Gap Cadmium-Based Compounds*, Ed. by P. Capper (INSPEC, 1994).
13. J. Franc, E. Belas, R. Grill, *et al.*, Proc. SPIE **3182**, 207 (1997).
14. J. Piotrowski and W. Gawton, Infrared Phys. Technol. **38**, 63 (1997).
15. G. V. Tsarenkov, Fiz. Tekh. Poluprovodn. (Leningrad) **9**, 253 (1975) [Sov. Phys. Semicond. **9**, 166 (1975)].
16. *Heterojunction Band Discontinuities. Physics and Device Applications*, Ed. by F. Capasso and G. Margaritondo (Elsevier, Amsterdam, 1987).
17. A. Schenk, M. Stahl, and H.-J. Wünsche, J. Cryst. Growth **101**, 350 (1990).
18. I. M. Baker, M. P. Hastings, L. G. Hipwood, *et al.*, III–Vs Review **9** (2), 50 (1996).

Translated by S. Ktitorov

Semiconductors, Vol. 35, No. 11, 2001, pp. 1291–1299. Translated from Fizika i Tekhnika Poluprovodnikov, Vol. 35, No. 11, 2001, pp. 1347–1355.

SEMICONDUCTOR STRUCTURES, INTERFACES, AND SURFACES

Role of Sulfide Ion Solvation in the Modification of GaAs Surface Electronic Structure

M. V. Lebedev

Ioffe Physicotechnical Institute, Russian Academy of Sciences, Politekhnicheskaya ul. 26, St. Petersburg, 194021 Russia
e-mail: mleb@triat.ioffe.rssi.ru

Submitted April 18, 2001; accepted for publication April 24, 2001

Abstract—A model is proposed wherein the interaction of the adsorbate (sulfide ion) with the GaAs surface is considered with allowance made for the influence of the solvation shell. It is shown by quantum-chemical calculations that the solvation of the adsorbate by different solvent molecules results in the variation of the relationship between the adsorbate ability to accept and donate electrons in chemical reactions, which has a determining effect on the adsorbate interaction with the semiconductor surface states and, thus, on the modification of the electronic structure of the semiconductor surface. *© 2001 MAIK "Nauka/Interperiodica".*

1. INTRODUCTION

A GaAs(100) surface, even prepared in conditions of molecular beam epitaxy, has a high density of states located near the midgap, which cause a high rate of nonradiative surface recombination [1]. Since these states are of chemical origin, the chemical treatment of the surface can modify the electronic structure of a semiconductor surface. Among various chemical treatments suggested for the modification of III–V compound semiconductors, special attention by researchers has been given to the treatment with different sulfide-containing compounds [2–6], which results in the formation of the ordered layer of the adsorbed sulfur atoms at the semiconductor surface. Sulfur adsorption at the GaAs(100) surface causes the photoluminescence intensity to increase [7] and the surface band bending to vary [8], which enable this technique to be used to improve the performance of transistors [2] and lasers [9, 10] made on the basis of GaAs and other III–V compound semiconductors.

Theoretical studies of the electronic structure of GaAs surfaces have shown [11–13] that the sulfur adsorption could result in the substantial rearrangement of the surface states in the band gap, so that in a number of cases the states could be pulled out completely from the gap [11]. The energy-band structure of the semiconductor surface therewith is determined by the surface atomic arrangement [12], which depends on the adsorption technology.

Solvation, i.e., the surrounding of an atom or ion by solvent molecules, results in the modification of the electronic shell of the solute atoms or ions and, consequently, leads to a radical alteration in their chemical properties [14]. The most pronounced ionic solvation is observed in aqueous and alcoholic solutions, in which, apart from the pure electrostatic interaction of the polar solvent molecule with the ion, the formation of coordination hydrogen bonds is possible, which change appreciably the electron density distribution in the solvated atom.

It has been found experimentally that solvation by different solvents of the ions adsorbing at the surface of semiconductors can affect surface electronic structure. For instance, the adsorption of sulfur in the form of sulfide ions from alcohol solutions results in a more effective modification of the electronic properties of GaAs and other III–V semiconductors than the adsorption from aqueous solutions. Specifically, such a modification includes a greater increase in the photoluminescence yield of GaAs [15] and GaN [16], a significant decrease in the surface depletion layer width of GaAs and InP [15, 17], and a considerable (by 0.5–0.6 eV) shift of the GaAs surface Fermi level toward the conduction band [18]. Furthermore, depending on the solvent used, treatment with alcoholic sulfide solutions improves the performance of semiconductor lasers [19, 20]. These results show that ionic solvation opens ways for affecting the chemical processes at the surface and, thus, provides a possibility for the effective engineering of the electronic properties of semiconductor surfaces.

Despite substantial efforts undertaken to explain the mechanism of the modification of the electronic properties of the semiconductor surface by sulfur atom adsorption [11–13], a comprehensive model capable of describing the response from the electronic structure of the semiconductor surface to the chemical interactions is still lacking.

In this study, quantum-chemical calculations are used to gain insight into the effect of the solvation shell on the ability of the sulfide ion HS^- to capture charge from the surface of GaAs; a model is suggested to explain the influence of the solvation of the adsorbing ion on the modification of the electronic properties of the semiconductor surface.

1063-7826/01/3511-1291$21.00

2. METHODOLOGY FOR DESCRIBING THE MOLECULAR REACTIVITY

Electronic structure modification involves the variation of the energy distribution of the electronic state density on the semiconductor surface. Therefore, to consider the adsorption-stimulated modification of the surface electronic properties, it is first necessary to examine the ability of an atom or ion to donate and accept electrons in the course of chemisorption. Density functional theory [21] provides a very useful basis for understanding the chemical reactivity of atoms and molecules. According to this theory, all properties of the system are completely determined by the spatial distribution of the electron density in this system. As one molecule approaches another (it takes place in the course of the chemical reaction), the electron shells of reactants start to interact in such a way that the electrons are transported from the less electronegative reactant to the more electronegative one. In terms of the density functional theory, electronegativity is assumed to be equal to the negative chemical potential μ of electrons in the system and, after completion of the chemical reaction, this should be constant everywhere within the electron shell of the product. The reactivity of the molecule can be characterized by the global hardness η

$$\eta = \left(\frac{\partial \mu}{\partial N}\right)_v = \frac{1}{S}, \tag{1}$$

where N is the number of electrons in the system, v is the external potential, and S is the global softness, which is the reciprocal of global hardness. The global hardness (softness) value constitutes the basis for the hard and soft acids and bases principle [22], which implies that reactions will occur most readily between molecules matching in hardness (softness). The soft reactants tend to form covalent bonds while the hard reactants tend to form ionic bonds. The interaction energy then increases with a decrease in the hardness (the increase in the softness) of the reactants [21]. This means that the softer reactants are favored energetically to participate in chemical reactions; therefore, the lower the softness (greater hardness) of the reactant, the greater its reactivity.

One way to evaluate the global hardness of molecules is by using Koopmans' approximation

$$\eta = \frac{e_{\mathrm{LUMO}} - e_{\mathrm{HOMO}}}{2}, \tag{2}$$

where e_{LUMO} and e_{HOMO} are the energies of the lowest unoccupied (LUMO) and the highest occupied (HOMO) molecular orbitals, respectively.

In such an approximation, the global hardness of the semiconductor is equal to half of its band gap or, more strictly, to half of its surface gap (the gap between occupied and unoccupied surface states). In the absence of the surface gap, i.e., when the surface is "metallic", the global hardness of the semiconductor will be in inverse proportion to the surface state density at the Fermi level [21].

Considering the semiconductor surfaces (or any other large system), for which many nonequivalent adsorption sites are possible, of particular interest is the problem of local reactivity, i.e., at which sites of the surface the chemical interaction with the given adsorbate will proceed with the higher probability.

In parallel with the global reactivity indices defining the reactivity of the molecule as a whole, the local reactivity indices are introduced. This, first of all, is the Fukui function

$$f(\mathbf{r}) = \left(\frac{\partial \rho(\mathbf{r})}{\partial N}\right)_v, \tag{3}$$

which defines the response of the electron density $\rho(\mathbf{r})$ of the system to a change in the number of electrons for a constant external potential (constant arrangement of nuclei). The other index is the local softness

$$s(\mathbf{r}) = \left(\frac{\partial \rho(\mathbf{r})}{\partial \mu}\right)_v, \tag{4}$$

which determines the response of the electron density $\rho(\mathbf{r})$ of the system to a change in the chemical potential for a constant external potential (constant arrangement of nuclei). The local softness is related to the Fukui function by the formula

$$s(\mathbf{r}) = f(\mathbf{r})S. \tag{5}$$

The integral of the Fukui function over the entire volume of the molecule is equal to unity, and, accordingly, the integral of the local softness is equal to the global softness of the molecule.

The Fukui function indicates the tendency of the molecule's electron density to deform in a given region; i.e., the larger the Fukui function, the higher the reactivity in this region. The local softness contains more information than the Fukui function and makes possible a comparison of the reactivity of different molecules with respect to the semiconductor surface (or any other complex molecule) [23].

Depending on the electronegativity difference between reacting species, chemical interaction occurs either between HOMO of the semiconductor and LUMO of the adsorbate (nucleophilic attack) or between LUMO of the semiconductor and HOMO of the adsorbate (electrophilic attack). In the nucleophilic attack of the surface, the adsorbate is an electron acceptor while in the electrophilic attack it is a donor. Since, for systems with a finite number of particles, the left- and right-hand derivatives of (3) with respect to the number of particles are different, the Fukui function and the local softness are recognized for the nucleophilic $f^+(\mathbf{r})$ ($s^+(\mathbf{r})$), electrophilic $f^-(\mathbf{r})$ ($s^-(\mathbf{r})$), and radical (interaction between species with equal electronegativity) attacks $f^0(\mathbf{r}) = (1/2)[f^+(\mathbf{r}) + f^-(\mathbf{r})]$, ($s^0(\mathbf{r}) = (1/2)[s^+(\mathbf{r}) - s^-(\mathbf{r})]$).

The principle of hard and soft acids and bases is valid in local form as well [24]; specifically, the interaction between molecules is favored when it occurs via sites matching in local softness.

A simple and yet reliable method for assigning a value to the Fukui function [and, accordingly, the value of local softness using (5)] is the integrating of the electron density over all orbitals of *i*th atom to obtain the discrete value of the charge q_i of an atom in the molecule and then differentiating it with respect to the total number of electrons in the system. In a finite difference approximation, the condensed Fukui functions can be obtained [25]

$$\begin{aligned} f_i^+ &= q_i^{N+1} - q_i^N, \\ f_i^- &= q_i^N - q_i^{N-1}, \\ f_i^0 &= \frac{1}{2}(q_i^{N+1} - q_i^{N-1}). \end{aligned} \tag{6}$$

Equations (6) are then multiplied by the value of the global softness of the molecule, and the corresponding expressions for the condensed softnesses of individual atoms in the molecule are obtained according to Eq. (5). The charges q_i^{N+1}, q_i^N, and q_i^{N-1} can be determined by different quantum-chemical population analysis techniques for systems with the same arrangement of nuclei but with a different number of electrons ($N + 1$, N and $N - 1$, respectively).

The local softness distribution over the GaAs surface was considered by Piquini *et al.* [26] using geometry optimization on the basis of Hartree–Fock calculations of the planar Ga_2As_2 cluster that simulated the unit cell of an ideal surface. In spite of the simplicity of this approach, Piquini *et al.*, using the local hard and soft acids and bases principle, correctly predicted the most reactive sites at the surface, as well as the likely adsorption sites for a number of atoms. It was found that the softer areas correspond to the regions above the arsenic atoms, and the harder ones are the regions between atoms. At the ideal surface, HOMOs are represented by the saturated dangling bonds localized at arsenic surface atoms and LUMOs are represented by unsaturated dangling bonds localized at surface gallium atoms. At the actual semiconductor surface, however, different defects exist, which can induce states in the band gap. These states can be either LUMO (unoccupied states) or HOMO (occupied states) depending on their origin. The qualitative distribution of the local softness on the GaAs surface obtained in [26] was used in this study for analysis of the interaction of the solvated ions with the surface atoms of the semiconductor.

Quantum-chemical geometry optimization and calculations of the reactivity indices of the solvated HS^- sulfide ions were performed with the GAUSSIAN-94 software package [27]. The calculations were carried out in terms of the density functional theory using Becke's three-parameter functional [28] and the Lee–Yang–Parr correlation functional [29] (B3LYP-functional). The 6-31+G(d,p) basis-function set was used throughout the calculations. Charges for substitution into Eq. (6) were taken from the Mulliken population analysis. The ion was considered to be associated with several (n) solvent molecules. The solvent molecules were water (H_2O) (n = 1–4), methanol (CH_3OH) (n = 1, 2), ethanol (C_2H_5OH) (n = 1), isopropyl alcohol (i-C_3H_7OH) (n = 1) and *tert*-butyl alcohol (t-C_4H_9OH) (n = 1) used previously in experiments with sulfide modification of semiconductor surfaces [15, 17, 19, 30]. It should be mentioned that the more complex cases (H_2O, $n \geq 5$; CH_3OH, $n \geq 3$; other alcohols, $n \geq 2$), at a given computational level using the available computer technique, required too much computer time; therefore, no consideration was given to these cases in this study.

3. REACTIVITY OF A SOLVATED SULFIDE ION

In previous experimental studies of sulfur adsorption at the semiconductor surface from different solutions [15, 17, 19, 30], the solvent was classified by its static dielectric constant. In this study, however, the solvation of the sulfide ions by a limited number of solvent molecules is considered; therefore, the static dielectric constant can no longer be used for solvent classification. On the other hand, the static dielectric constant of the liquid is related, even if in a complex manner, to the static dipole polarizability of constituent molecules, which in turn is related to their global softness [31]. The global softness of the molecules of solvents used, calculated using Eqs. (1) and (2), are listed in the table wherein, in addition, the static dielectric constant values of liquid solvents are given for comparison. By and large, the solvent with softer polar molecules has the smaller dielectric constant. However, it should be noted that although the softness of methanol and ethanol are close, they contradict the above tendency. This points to the fact that, for exact evaluation of the dielectric constant of liquid, several other characteristics of the molecule, as well as its interaction with neighbors, should be taken into account in addition to softness (polarizability). Free space is considered to be infinitely hard (absolutely unpolarizable); therefore, its softness is taken to be zero.

3.1. Reactivity of the Monosolvated Sulfide Ion

At first, let us consider monosolvation, i.e., the interaction of an ion with a single solvent molecule. Ion–solvent complexes each have a different global hardness and, therefore, different reactivity depending on the solvent molecule (Fig. 1a). The hardness of the sulfide ion in a complex with the relatively hard water molecule is somewhat higher than the hardness of a free (nonsolvated) ion. Solvation by softer alcohol molecules causes a decrease in the global hardness of the complex. This decrease is more important when the

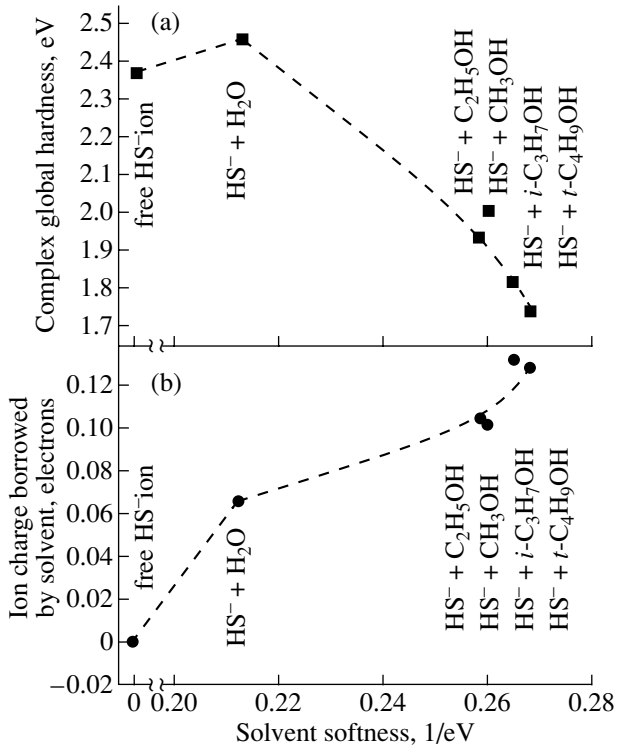

Fig. 1. The global hardness of (a) the monosolvated complex and (b) the charge involved in the hydrogen bond of the sulfide ion with the solvent molecule in relation to the global softness of free solvent molecule.

softer solvent solvates the ion. Accordingly, the reactivity of the hydrated sulfide ion (i.e., solvated by a water molecule) is below that of the ion solvated by alcohol molecules. Indeed, it was shown experimentally [15, 17, 30] that the rate of the sulfide coating formation (the rate constant of sulfur adsorption) on the surface of semiconductors was the lowest when the sulfur adsorption was carried out from aqueous solutions. On adsorption from alcohol solutions, the rate was higher and increased with decreasing dielectric constant of the solvent, i.e., exactly in the same order in which the hardness of the monosolvated sulfide ion decreases (Fig. 1a). Thus, the suggested approach describes adequately the influence of the solvation on the reactivity of the sulfide ion.

Global softness (S) of the free solvent molecules and static dielectric constant (ε) of the liquid solvent

Solvent molecule	S, eV^{-1}	ε
H_2O	0.212	80.1
CH_3OH	0.260	33.0
C_2H_5OH	0.258	25.3
i-C_3H_7OH	0.265	20.2
i-C_4H_9OH	0.268	12.5

The solvation causes the borrowing of the ion charge by the solvent molecule; i.e., a hydrogen bond is formed. This effect is more pronounced when the ion is solvated by an alcohol molecule (Fig. 1b).

In order to study the electronic processes during the interaction of an ion with a semiconductor surface, the distribution of the local reactivity indices in the solvated sulfide ions should be analyzed. To this end, the condensed softness of sulfur and hydrogen atoms in the sulfide ion, as well as of the solvent molecule solvating the ion, was calculated using Eqs. (5) and (6) (Fig. 2). Ionic solvation substantially modifies the condensed softness of the sulfur atom (Fig. 2a). Although the solvation by water molecules reduces the softness for electrophilic, nucleophilic, and radical attacks, the relationship between them remains practically the same as for the nonsolvated ion. The solvation by alcohol molecules results in an increase in the condensed softness for the electrophilic attack s_S^- (i.e., the ability of an atom to donate electrons) and in a decrease in the condensed softness for the nucleophilic attack s_S^+ (i.e., the ability of an atom to accept electrons). The softness ratio s_S^-/s_S^+, i.e., the ratio of donor and acceptor abilities of sulfur atoms, is higher, the softer the solvent solvating the ion (Fig. 3). The condensed softness for the radical attack s_S^0 (i.e., the reaction without charge transfer) for the ion solvated by the alcohol molecule is lower than that for the hydrated ion, but it increases slightly with the increase in the softness of the alcohol molecule solvating the ion.

The proton incorporated in the sulfide ion is very hard with respect to both donation and acceptance of electrons (its condensed softness is more than an order of magnitude lower than the appropriate condensed softness of the sulfur atom and, in certain cases, it is even negative (Fig. 2b)). The condensed softness of the solvent molecules involved in the complex is displayed in Fig. 2c. Evidently, water solvating the sulfide ion is very hard for any reaction, while the acceptor reactivity of alcohol molecules solvating the ion with respect to nucleophilic and radical attacks is fairly high.

3.2. Reactivity of Multisolvated Sulfide Ions

The real pattern of the ionic solvation is clearly much more complex than in the above monosolvation example; specifically, the ions are solvated by several solvent molecules rather than by one. In order to understand how the additional solvent molecules affect the reactivity of the solvated sulfide ion, let us consider two basically different cases of multisolvation by n solvent molecules. First, we have solvation by water molecules (n = 1–4), for which almost the same donor and acceptor abilities of sulfur atoms are characteristic of monosolvation (n = 1). Second, there is solvation by metha-

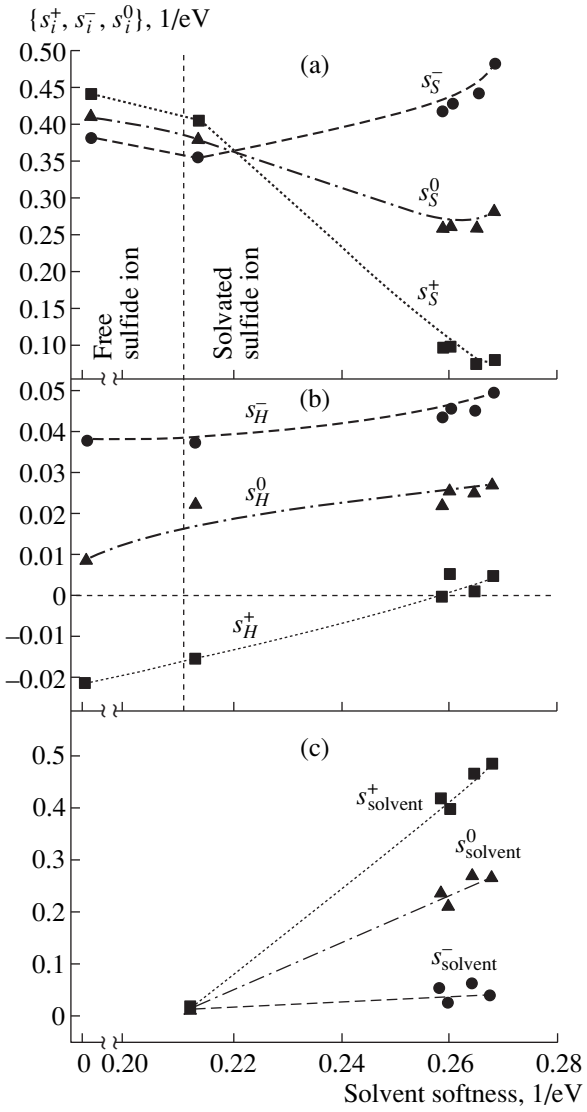

Fig. 2. Condensed softnesses for the nucleophilic s_i^+, electrophilic s_i^-, and radical s_i^0 reactions for the sulfur atom (a), hydrogen atom in the sulfide ion (b), and for the solvent molecule solvating the ion (c) as a function of the global softness of free solvent molecule.

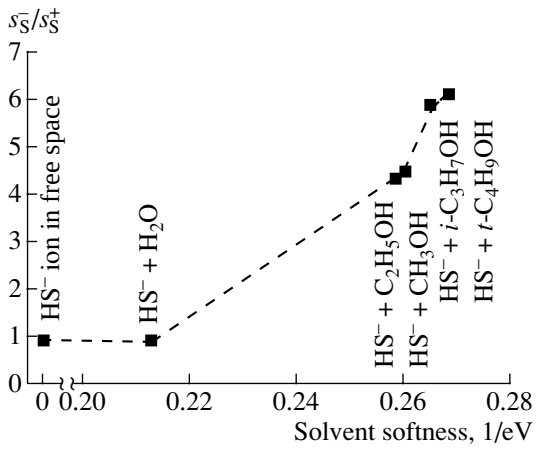

Fig. 3. The ratio of the softnesses s_S^-/s_S^+ (the ratio of abilities to donate and accept electrons) of the sulfur atom in the monosolvated sulfide ion as a function of the global softness of a free solvent molecule.

nol molecules (n = 1, 2), for which the ability to donate electrons is dominant in monosolvation (n = 1).

An increase in the number of solvent molecules results in an increase in the global hardness of the complex, i.e., in the decrease in its reactivity (Fig. 4). Nevertheless, the reactivity of an ion solvated by a methanol molecule remains higher than that of a hydrated ion.

The ratio of the softnesses s_S^-/s_S^+ (the ratio of the donor and acceptor abilities of a sulfur atom) for the hydrated ion is nearly independent of the number of water molecules solvating the ion and, as in the case of monohydration, remains close to unity (Fig. 5). For the ion solvated by methanol molecules, this ratio far exceeds unity and, for solvation by two methanol molecules, it is distinctly higher than for monosolvation.

Thus, the complication of the problem due to the increase of the number of molecules solvating the ion supports the conclusions made on consideration of monosolvation. On the one hand, solvation by polar amphiprotic solvents results in the variation of the global reactivity of the sulfide ion; in particular, the reactivity is higher, the softer the solvent solvating the ion. On the other hand, solvation by alcohol molecules results in the noticeable predominance of the donor ability of a sulfur atom over its ability to accept electrons, whereas in free and hydrated sulfide ions, the donor and acceptor abilities of a sulfur atom coincide closely.

4. INTERACTION OF SOLVATED SULFIDE ION WITH GaAs SURFACE

As an example, we consider the interaction of a solvated sulfide ion with the most extensively studied GaAs(100) surface. It was found experimentally that sulfide ions in solutions interact both with arsenic and with gallium atoms at the GaAs(100) surface [3, 4, 30]. Since the saturated dangling bonds occur at the surface arsenic atoms and the unsaturated dangling bonds occur at the surface gallium atoms, the reaction of the sulfide ions with the arsenic atoms is equivalent to nucleophilic attack; and the reaction with the gallium atoms, to electrophilic attack. Therefore, the reactivity of the sulfur atom with respect to the surface arsenic and gallium atoms can be determined by the condensed softnesses s_S^+ and s_S^-, respectively. Moreover, due to the

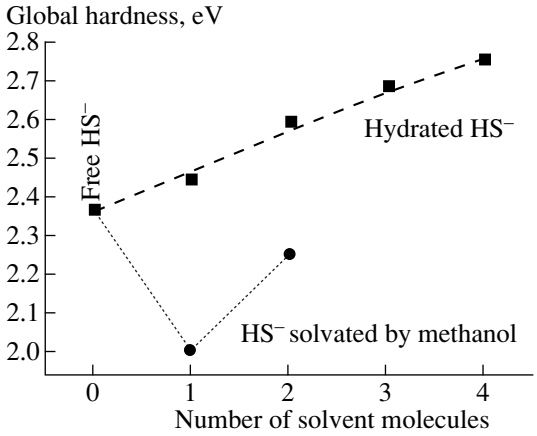

Fig. 4. Dependence of the global hardness of sulfide ions hydrated and solvated by methanol molecules on the number of solvent molecules solvating the ion.

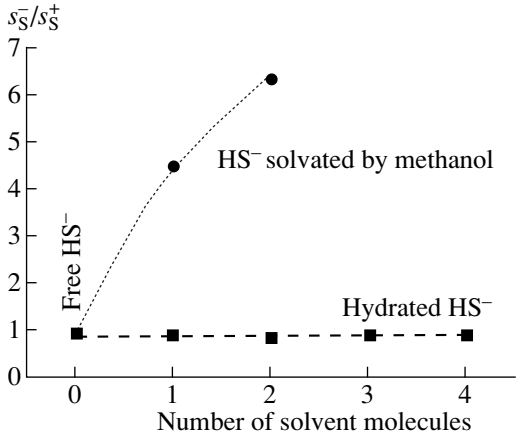

Fig. 5. The ratio of the softnesses s_S^-/s_S^+ (the ratio of abilities to donate and accept electrons) of the sulfur atoms in the sulfide ions hydrated and solvated by methanol molecules as a function of the number of solvent molecules solvating the ion.

high density of the surface states inherent to GaAs, the reaction of the adsorbate with the surface states represents an important channel of the chemical interaction modifying the surface electronic structure of GaAs.

4.1. Interaction with Surface Atoms

The softness s_S^+ of a sulfur atom in free and hydrated ions is rather high (Fig. 3a). Since the arsenic atom at the GaAs surface is the soft base center [26], the free and hydrated sulfide ions actively interact with the surface As atoms with the formation of a stable covalent bond. The sulfur atoms of ions solvated by alcohol molecules are considerably more hard with respect to nucleophilic attack; therefore, according to the principle of local hard and soft acids and bases [24], they cannot form covalent bonds with arsenic atoms. In this case, the alcohol molecules, which have high condensed softness for nucleophilic attack (Fig. 2c), react with arsenic. The alcohol molecules cannot be chemisorbed at the surface (at least at room temperature), but they can split off the alkyl group that can react with arsenic atoms. The products of such a reaction are soluble in an alcohol; therefore, the surface after sulfidizing in alcohol solutions should be depleted of arsenic, which was observed experimentally [30].

On the other hand, the sulfur atom in the ion solvated by an alcohol molecule is hard, with respect to electrophilic attack, and can be adsorbed at the hard region of the surface, which, according to [26], is the region between atoms. Such an interaction should result in insignificant shear of the electronic shells and, hence, the adsorption bond will be mostly ionic. In this case, the surface should possess a high dipole moment. The high dipole moment at the GaAs(100) surface treated with a solution of ammonium sulfide in isopropyl alcohol was observed experimentally [18, 32], and it was confirmed that this dipole moment stems from the interaction of arsenic with sulfur [32].

The surface gallium atoms are the soft acid centers [26]. The condensed softness s_S^- of sulfur atoms in all ions is rather high (Fig. 2a); therefore, sulfur atoms in all cases will actively interact with the surface gallium atoms. The interaction energy will be higher on adsorption of the softer sulfide ions solvated by the alcohol molecules.

4.2. Interaction with Surface States

The Fermi level at the free GaAs(100) surface grown by molecular beam epitaxy is pinned mainly by the acceptor-type surface states related to the occurrence of different surface defects [1]. These states capture electrons from the near-surface semiconductor bulk causing it to be depleted. Thus, band bending exists at the surface (upward at *n*-GaAs surface and downward at *p*-GaAs one). Since the density of states at the GaAs(100) surface is rather high, the chemical softness of the surface states is fairly high as well, according to [33]. The Fermi level at the GaAs(100) surface (both *n*- and *p*-type) is pinned near the midgap; therefore, the surface states enhance the rate of nonradiative surface recombination.

Since the acceptor states at the GaAs(100) surface are occupied by the electrons captured from the semiconductor bulk, on the one hand, these states are soft acid centers, while on the other hand, they represent the soft HOMO. As a result, the interaction of the surface state with the sulfur atom of the sulfide ion would be controlled by the condensed softness s_S^+. The softness s_S^+ of free and hydrated sulfide ions is rather high (Fig. 2a). Therefore, the sulfur atom in free and hydrated sulfide ions readily interacts with the semi-

conductor surface states (Fig. 6a). In this case, a stable covalent bond is formed, and the bonding energy shifts the surface state level toward the valence band (E_V) of the semiconductor. Since this state remains within the band gap, the charge localized at this state is not diminished; hence, the depletion layer width and the surface Fermi level position (E_{FS}) remain almost unchanged. On the other hand, since the state shifts from the midgap, its participation in nonradiative recombination will be less important; thus, the rate of nonradiative surface recombination should decrease. Such a mechanism accounts for the reduction in the surface recombination rate of GaAs(100) treated with the aqueous sulfide solution without a noticeable change in the surface Fermi level position and depletion layer width [7, 15, 17].

The mechanism of the interaction of the sulfide ion solvated by the alcohol molecule with the acceptor surface state is different (Fig. 6b). In this case, the softness s_S^+ is small; thus, it is difficult for the sulfur atom to interact with the occupied surface state. However, the solvent molecule that has high softness for nucleophilic attack (acceptor ability) s_{solvent}^+ (Fig. 2c) can readily interact with this state. As a result, the electron from the surface state is captured by the alkyl group of the alcohol molecule (the most reactive part, according to the distribution of the local softness s_i^+ over the alcohol molecule) and leaves the surface for the gas phase. The surface state can then either capture another electron from the semiconductor bulk or be subjected to electrophilic attack from the sulfur atom of the sulfide ion, whose softness s_S^- is rather high. The capture of electrons from the semiconductor will be hampered by the surface electron-depletion layer. Therefore, the adsorption of the sulfide ion at the vacant orbital of the surface state is more probable. As a result of its interaction, the acceptor level (LUMO) noticeably shifts toward the conduction band (E_C). This causes, first, the decrease in nonradiative recombination efficiency, as in the case of hydrated ion adsorption, and, second, the reduction of the charge localized at the surface state and, therefore, the decrease in the surface depletion-layer width. Simultaneously, the hard–hard interaction of sulfur atoms with the surface arsenic atoms results in the formation of a dipole layer on the surface, which, in the case of *n*-GaAs, causes a greater reduction of the band bending than that due to the decrease in the surface depletion-layer width. In the case of *p*-GaAs, on the contrary, the formation of a dipole layer causes a considerable increase in the band bending. All these effects were observed experimentally in the course of the sulfide ions adsorption from the alcohol solutions on the *n*-GaAs(100) surface [15, 17, 18, 30, 32].

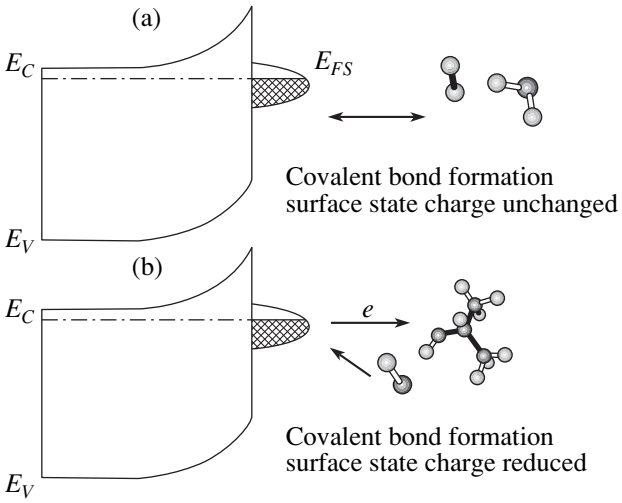

Fig. 6. Direction of the electron transfer in the course of interaction of the hydrated (a) and solvated by the alcohol molecule (b) sulfide ion with the acceptor surface states of a semiconductor.

5. POSSIBLE APPLICATIONS OF THE RESULTS

In the suggested model, the interaction of the solvated sulfide ion with the semiconductor surface is treated on the basis of the analysis of the local reactivity indices. The solvation therewith is introduced at the simplest level; namely, the sulfide ion is considered to be solvated by a limited number of solvent molecules. Nevertheless, even such a simplified approach makes possible the explanation of all experimental results previously obtained in studies of the adsorption of the sulfide ions from different solutions on the GaAs(100) surface. In particular, this approach explains the change in the position of the surface Fermi level with respect to the band edges of the semiconductor and the increase in the ionization energy as a result of sulfide treatment with alcohol solutions, and it also reasonably describes the observed dependence of the photoluminescence intensity and variation in the surface depletion layer width (i.e., the rate of nonradiative surface recombination) on the properties of the solvent wherein the sulfide ion adsorption occurs [15, 17, 18, 30, 32].

Although the suggested model was considered using a GaAs(100) surface as an example, it should also be valid for the examination of the adsorption of solvated ions on other GaAs surfaces, to which the occurrence of the acceptor surface states is inherent. It stands to reason that, when considering the adsorbate interaction with the surface atoms of the semiconductor, the special features of the stoichiometry of the particular surface should be taken into account. For instance, the upper layer of the GaAs(111)A surface consists mainly of gallium atoms; therefore, the adsorbate interaction with the surface arsenic atoms can be ignored on such a surface. On the other hand, there are no states in the

band gap at the GaAs(110) surface prepared by cleavaging the crystal in ultra-high vacuum and, thus, the formation of the electronic structure will be determined only by the interaction of the adsorbate with surface atoms. Moreover, the suggested approach could be valid for other III–V semiconductors as well.

In the last few years, considerable progress has been achieved in the study of the properties of microsolvated atomic, ionic, and molecular clusters [34–36]. These clusters are formed in vacuum by the ultrasonic expansion of the mixture of ions with the solvent vapor, and, in these conditions, the mass selection of clusters is possible using time-of-flight spectrometry. The obtained results and suggested model show that the adsorption at the GaAs(100) surface of the clusters consisting of the ion HS^- associated with one or several molecules of the amphiprotic solvent holds great promise for GaAs surface modification, which makes it possible to modify the surface electronic properties in a wide range. Such a technique combines the possibility of controlling the adsorbate properties by the solvate shell with such advantages of the gas-phase adsorption process as reproducibility, controllability, and avoidance of unwanted contaminations.

6. CONCLUSION

Density functional theory was used to examine the reactivity of complexes that consisted of sulfide ion HS^- solvated by one or more molecules of different amphiprotic solvents. The solvents consisted of water molecules and different monobasic alcohols (methanol, ethanol, isopropyl alcohol, and *tert*-butyl alcohol). It was found that the solvation of the sulfide ion by soft alcohol molecules causes an increase in the ion's reactivity, compared with the reactivity of nonsolvated and hydrated ions. The ability of the sulfur atom in the complex to donate electrons in the course of the reaction increases and its ability to accept electrons decreases with an increase in the softness of the solvent molecule. The model suggested describes the interaction of a solvated sulfide ion with a GaAs(100) surface, and it reasonably explains the experimentally observed solvent effect on the electronic structure of the semiconductor surface modified with the sulfide solutions. The present findings show great promise for using the adsorption of the microsolvated clusters for the modification of the electronic properties of the semiconductor surface.

ACKNOWLEDGMENTS

I am grateful to Professor B. Brutschy and my colleagues from the Institut für Physikalische und Theoretische Chemie, Johann Wolfgang Goethe-Universität (Frankfurt am Main, Germany) for their hospitality and the friendly atmosphere, which was a great help in carrying out this investigation.

This study was supported in part by the Russian Foundation for Basic Research, project no. 00-03-32230.

REFERENCES

1. Y. Ishikawa, T. Fujui, and H. Hasegawa, J. Vac. Sci. Technol. B **15**, 1163 (1997).
2. C. J. Sandroff, R. N. Nottenburg, J.-C. Bischoff, and R. Bhat, Appl. Phys. Lett. **51**, 33 (1987).
3. S. R. Lunt, G. N. Ryba, P. G. Santangelo, and N. S. Lewis, J. Appl. Phys. **70**, 7449 (1991).
4. Z. S. Li, W. Z. Cai, R. Z. Su, *et al.*, Appl. Phys. Lett. **64**, 3425 (1994).
5. M. G. Nooney, V. Liberman, and R. M. Martin, J. Vac. Sci. Technol. A **13**, 1837 (1995).
6. L. Koenders, M. Blomacher, and W. Mönch, J. Vac. Sci. Technol. B **6**, 1416 (1988).
7. B. J. Skromme, C. J. Sandroff, E. Yablonovich, and T. J. Gmitter, Appl. Phys. Lett. **51**, 2022 (1987).
8. P. Moriarty, B. Murphy, L. Roberts, *et al.*, Phys. Rev. B **50**, 14237 (1994).
9. A. J. Howard, C. I. H. Ashby, J. A. Lott, *et al.*, J. Vac. Sci. Technol. A **12**, 1063 (1994).
10. G. Beister, J. Maege, D. Grutsche, *et al.*, Appl. Phys. Lett. **68**, 2467 (1996).
11. T. Ohno and K. Shiraishi, Phys. Rev. B **42**, 11194 (1990).
12. K. N. Ow and X. W. Wang, Phys. Rev. B **54**, 17661 (1996).
13. G. Hirsch, P. Kruger, and J. Pollmann, Surf. Sci. **402–404**, 778 (1998).
14. J. Tomasi and M. Persico, Chem. Rev. **94**, 2027 (1994).
15. V. N. Bessolov, M. V. Lebedev, N.-M. Binh, *et al.*, Semicond. Sci. Technol. **13**, 611 (1998).
16. C. Huh, S.-W. Kim, H.-S. Kim, *et al.*, J. Appl. Phys. **87**, 4591 (2000).
17. V. N. Bessolov, E. V. Konenkova, M. V. Lebedev, and D. R. T. Zahn, Fiz. Tverd. Tela (St. Petersburg) **41**, 875 (1999) [Phys. Solid State **41**, 793 (1999)].
18. V. N. Bessolov, M. V. Lebedev, S. Hohenecker, and D. R. T. Zahn, Phys. Low-Dimens. Struct., Nos. 9/10, 105 (1998).
19. V. N. Bessolov, M. V. Lebedev, Yu. M. Shernyakov, and B. V. Tsarenkov, Mater. Sci. Eng. B **B44**, 380 (1997).
20. R. Hakimi and M.-C. Amann, Semicond. Sci. Technol. **12**, 778 (1997).
21. R. G. Parr and W. Yang, *Density Functional Theory of Atoms and Molecules* (Oxford Univ. Press, Oxford, 1989).
22. R. G. Pearson, J. Am. Chem. Soc. **85**, 3533 (1963).
23. P. W. Ayers and R. G. Parr, J. Am. Chem. Soc. **122**, 2010 (2000).
24. F. Méndez and J. L. Gázquez, J. Am. Chem. Soc. **116**, 9298 (1994).
25. W. Yang and W. Mortier, J. Am. Chem. Soc. **108**, 5708 (1986).
26. P. Piquini, A. Fazzio, and A. Dal Pino, Jr., Surf. Sci. **313**, 41 (1994).

27. M. J. Frisch, G. W. Trucks, H. B. Schlegel, P. M. W. Gill, B. G. Johnson, M. A. Robb, J. R. Cheeseman, T. Keith, G. A. Petersson, J. A. Montgomery, K. Raghavachari, M. A. Al-Laham, V. G. Zakrzewski, J. V. Ortiz, J. B. Foresman, J. Cioslowski, B. B. Stefanov, A. Nanayakkara, M. Challacombe, C. Y. Peng, P. Y. Ayala, W. Chen, M. W. Wong, J. L. Andres, E. S. Replogle, R. Gomperts, R. L. Martin, D. J. Fox, J. S. Binkley, D. J. Defrees, J. Baker, J. P. Stewart, M. Head-Gordon, C. Gonzalez, and J. A. Pople, *Gaussian 94, Revision D.4* (Gaussian Inc., Pittsburgh, 1995).
28. A. D. Becke, J. Chem. Phys. **98**, 5648 (1993).
29. C. Lee, W. Yang, and R. G. Parr, Phys. Rev. B **37**, 785 (1988).
30. V. N. Bessolov, E. V. Konenkova, and M. V. Lebedev, J. Vac. Sci. Technol. B **14**, 2761 (1996).
31. Y. Simon-Manso and P. Fuentealba, J. Phys. Chem. A **102**, 2029 (1998).
32. M. V. Lebedev and M. Aono, J. Appl. Phys. **87**, 289 (2000).
33. W. Yang and R. G. Parr, Proc. Natl. Acad. Sci. USA **83**, 8440 (1985).
34. H.-D. Barth, K. Buchhold, S. Djafari, *et al.*, Chem. Phys. **49**, 239 (1998).
35. O. M. Cabarcos, C. J. Weinheimer, T. J. Martinez, and J. M. Lisy, J. Chem. Phys. **110**, 9516 (1999).
36. S.-I. Koizumi, H. Yasumatsu, A. Terasaki, and T. Kondow, J. Chem. Phys. **111**, 6565 (1999).

Translated by the author

Semiconductors, Vol. 35, No. 11, 2001, pp. 1300–1304. Translated from Fizika i Tekhnika Poluprovodnikov, Vol. 35, No. 11, 2001, pp. 1356–1360.

LOW-DIMENSIONAL SYSTEMS

Analogue of Gunn Effect in Tunneling between Quantum Wells with Different Mobilities

P. I. Biryulin*, A. A. Gorbatsevich*, V. V. Kapaev, Yu. V. Kopaev**, and V. T. Trofimov****

** Moscow State Institute of Electronic Engineering, Moscow, 103498 Russia*
e-mail: pol@qdn.mill.ru
*** Lebedev Institute of Physics, Russian Academy of Sciences, Leninskiĭ pr. 53, Moscow, 117924 Russia*
Submitted February 26, 2001; accepted for publication March 10, 2001

Abstract—The electronic transport in a heterostructure with tunnel-coupled quantum wells (QWs) has been studied numerically under conditions of a strongly non-one-dimensional potential in the structure. Current–voltage (*I–V*) characteristics, potential distribution, and mobility and density of electrons in QWs have been calculated. The numerical technique is based on a two-dimensional consistent calculation of the quantum and classical regions of the heterostructure. The possibility of the occurrence in heterostructures of this kind of an effect similar to the Gunn effect in a homogeneous semiconductor is demonstrated for the first time. The effect is due to electron tunneling between QWs with different mobilities and is characterized by the formation of a high-electric-field domain and the presence of a region of negative differential resistance in the *I–V* characteristic.

INTRODUCTION

Heterostructures with tunnel-coupled quantum wells (TCQWs) have long attracted attention as an alternative to conventional semiconductor devices. Conductivity change occurs in such structures through tunnel coupling of quantum states at distances of about 10 nm, which is an order of magnitude better than that achieved with planar technology. Moreover, heterostructures with TCQWs are convenient objects for studying quantum effects in a macroscopic system by merely measuring changes in the system conductance.

Various devices based on structures of this kind (FETs, microwave generators, and logic elements) have been proposed [1–5]. For their operation, all these devices rely upon the tunnel coupling of states in QWs with different conductivities (mobilities). Effects in TCQWs have been studied experimentally [6–8]; in particular, a decrease in conductance due to anticrossing of size-quantization levels in TCQWs with different mobilities was confirmed.

A few models of the conductance of a system of TCQWs in external electric and magnetic fields were developed and numerical calculations were carried out in theoretical studies [9–14]. The one-dimensional (1D) nature of these models and calculations restricts their applicability to the calculation of real heterostructures with complex geometry. 2D or 3D calculations of real heterostructures with TCQWs have not been carried out so far, and it is this fact that initiated the present study. Since the properties of heterostructures with TCQWs are uniform in the QW plane, we can confine ourselves to 2D calculations.

HETEROSTRUCTURE UNDER STUDY

A schematic of the heterostructure being studied and its band diagram under the gate at zero source–drain voltage are presented in Fig. 1a. This structure was previously proposed and studied in a 1D approximation [14]. The conducting channel comprises two tunnel-coupled undoped GaAs QWs confined between $Al_{0.3}Ga_{0.7}As$ barriers. The main function of the impurity charge in the lower barrier is to keep the potential of the quantum well QW1 and carrier density constant when the gate voltage changes. The doping level is chosen so that only two lower size-quantization levels in the wells are occupied in a wide range of gate voltages. The topology of electrodes similar to that in FETs allows effective control over the electric field in the structure.

The mobility μ_2 in the narrow QW is much lower than that in the wide QW because of scattering on the interface irregularities. As shown in [15], μ_2 is temperature independent and proportional to a sixth power of the QW width; the irregularity size can be controlled by changing the growth temperature in fabricating a heterostructure [8]. At a gate voltage V_{gs} far from the anticrossing point, the wave function envelopes of different subbands are localized within their own QWs (Fig. 1b, cases *1* and *3*). In this case, only electrons of the first subband are scattered intensively on the irregularities of the narrow QW2, with mainly high-mobility carriers of the wide QW1 contributing to the conduction. At $V_{gs} = –0.7$ V, anticrossing of the first and second quantum levels occurs, wave functions of these states are present in both QWs, and electrons of both subbands in both QWs are scattered by QW2 irregularities (Fig. 1b,

case *2*). As a result, the effective mobility of carriers in the TCQWs falls and the heterostructure conductance decreases.

For an MBE-grown 35- to 50-Å-wide GaAs QW with a characteristic irregularity length and height of 100 and 3–5 Å, respectively, the mobility is within the range μ_2 = 100–1000 cm^2/(V s), and within this same range it was varied in calculations. For the wide QW1, the mobility μ_1 is determined only by scattering on phonons and a remote impurity. In calculations, μ_1 was assumed to be equal to the characteristic value of 7×10^4 cm^2/(V s) at 77 K for which all the calculations were done. For the given configuration of the structure, the mobilities μ_1 and μ_2 in separately taken QWs are the only free parameters of the problem.

CONDUCTION MODEL AND CALCULATION TECHNIQUE

Tunnel coupling between QWs can be essentially weakened by the 2D momentum scattering in the QW. At characteristic mobilities in the QWs, $\mu_{1,2} \approx 10^3$–10^4 cm^2/(V s), the maximum broadening of the level due to scattering is $\hbar/\tau_{1,2} \approx 10$–$1$ meV (with $\mu_{1,2} = e\tau_{1,2}/m^*$, where e, m^*, and $\hbar$ are the electron charge, effective electron mass, and Planck constant, respectively). This broadening is comparable to the interwell tunneling matrix element T in TCQWs for the system GaAs/$Al_{0.3}Ga_{0.7}$As with a barrier thickness of 5–10 nm (0.5–5 meV).

The expression for the longitudinal conductance of two TCQWs with two filled size-quantization subbands has been obtained by the Green function technique for nonequilibrium systems with the scattering-induced suppression of tunneling being taken into account [11]:

$$\sigma = en\mu_{\text{eff}},$$

where

$$\mu_{\text{eff}} = 2\mu\frac{1+\alpha^2 4\mu^2(\Delta\varepsilon^2+4T^2)}{(1-\mu_s^2)+\alpha^2 4\mu^2(\Delta\varepsilon^2(1-\mu_s^2))+4T^2}. \quad (1)$$

Here,

$$1/\mu = 1/\mu_1 + 1/\mu_2,$$

$$\mu_s = (\mu_1-\mu_2)/(\mu_1+\mu_2),$$

μ_1 and μ_2 are the mobilities of isolated uncoupled QWs; $\alpha = m^*/e\hbar$; n is the total carrier density in the TCQW; and $\Delta\varepsilon$ is the spacing between the energy levels in the first and second subbands without regard for tunnel-induced splitting; $\Delta\varepsilon$ is controlled by the external field and vanishes at the anticrossing point. At a finite asymmetry of scattering ($\mu_s \neq 0$), the conductance is at a minimum at $\Delta\varepsilon = 0$. The "classical" case, when the scattering processes do not suppress the tunnel superposition of states in the QW, can be obtained from (1) by passing to the limit $2T\alpha\mu \gg 1$.

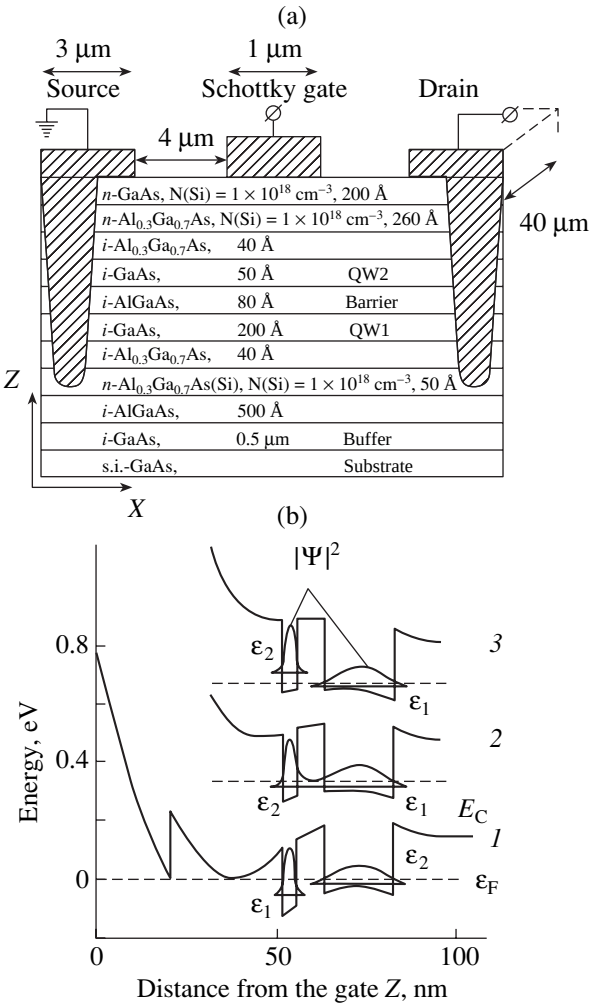

Fig. 1. Structure, topology, and band diagram of the heterostructure under the gate at different gate voltages V_{gs}: (*1*) 0, (*2*) –0.7, and (*3*) –0.9 V; V_{ds} = 0.

The relative change in the conductivity of the system of TCQWs,

$$\frac{\sigma(\Delta\varepsilon=\infty)-\sigma(\Delta\varepsilon=0)}{\sigma(\Delta\varepsilon=0)} = \frac{\mu_s^2 4T^2\alpha^2\mu^2}{(1-\mu_s^2)(1+4T^2\alpha^2\mu^2)} \quad (2)$$

is the greatest just in this case ($\mu_s^2/(1-\mu_s^2)$) and decreases noticeably when the scattering is suppressed by tunneling ($2T\alpha\mu \ll 1$).

As shown in [11], the broadening of size-quantization levels due to QW width fluctuations can be neglected if $2\pi\varepsilon_F\Lambda^4/d^4 \gg \hbar/\tau$, where ε_F is the Fermi level, Λ the longitudinal characteristic length of fluctuations, and d the QW width. At a QW width of 50–200 Å and a mobility of ~10^3 cm^2/(V s), this inequality is well satisfied in a wide concentration range.

In the heterostructure being studied, the potential varies only slightly along the QW over a distance of the

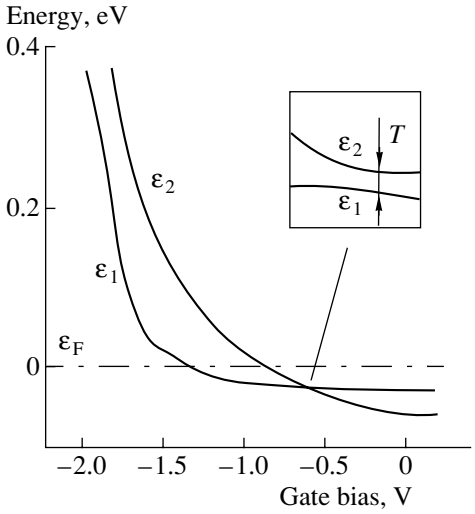

Fig. 2. Energy of the two lower states in TCQWs vs gate voltage; $V_{ds} = 0$.

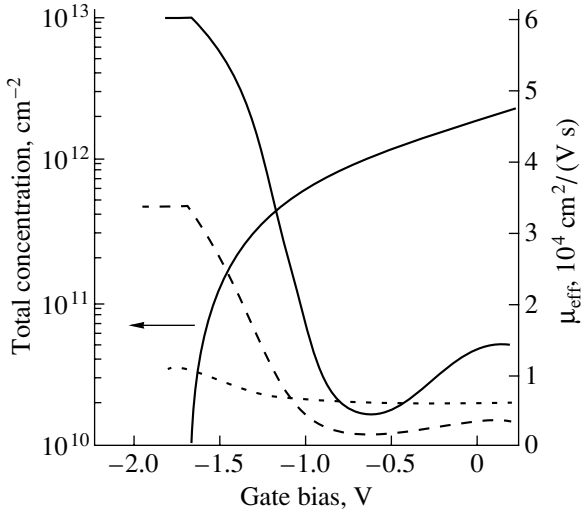

Fig. 3. Mobility μ_{eff} and total carrier density in TCQWs vs gate voltage at different mobilities μ_2 in the narrow QW. μ_2: solid line—700, dashed line—500, and dotted line—100 $cm^2/(V\ s)$; $V_{ds} = 0$.

electron wavelength. Therefore, to find $\Delta\varepsilon$ and T in the TCQWs, a 1D Schrödinger equation for the wave function envelope was solved numerically in various TCQW cross-sections along the entire heterostructure. The electron density in the QW was calculated in the Hartree approximation. 2D Poisson and continuity equations were solved numerically over the entire heterostructure. Expression (1) was used as a model of mobility in the TCQWs, with the calculated mobility assumed to be the same at all points of a given section of the TCQWs. Electron mobility models based on phonon and impurity scattering were used outside the TCQWs. In order to take into account the velocity saturation, two high-field mobility models were employed for comparison: monotonic

$$\mu = \frac{\mu_0}{1 + (\mu_0 |E_\parallel| / v_{sat})} \tag{3}$$

and nonmonotonic (describing the intervalley transfer in III–V semiconductors)

$$\mu = \frac{\mu_0 + v_{sat} |E_\parallel|^{\beta-1} / E_0^\beta}{1 + |E_\parallel|^\beta / E_0^\beta}. \tag{4}$$

Here, μ_0 is the weak-field mobility, $v_{sat} = 10^7$ cm/s is the saturation velocity, $E_\parallel$ is the field component parallel to the current density vector, $E_0 = 2.691 \times 10^3$ V/cm is the threshold field, and $\beta = 4$. For μ_0 in the TCQWs, we took the mobility calculated using (1). The diffusion coefficient was found from the mobility with the use of the Einstein relation. An iteration procedure was employed for the joint solution of the Poisson, continuity, and Schrödinger equations. The smallness of the difference in total current between successive iteration steps served as the condition for termination of iterations.

CALCULATION RESULTS

The calculated dependence of the lower two size-quantization energy levels of the TCQWs on the gate voltage at zero source–drain voltage is shown in Fig. 2. The energy levels are the same under the entire gate, since the potential distribution under the gate is almost 1D at small source–drain voltages V_{ds}. The anticrossing of the size-quantization levels occurs at a gate voltage $V_{gs} = -0.7$ V.

The dependence of the effective mobility μ_{eff} and total carrier density in the heterostructure channel on the gate voltage, calculated at varied μ_2, is presented in Fig. 3. The maximum change in the carrier mobility in the channel occurs not at a zero mobility $\mu_2 = 0$ in the narrow QW (which corresponds to an infinite broadening of its size-quantization level), but at some optimum value, which is about 700 $cm^2/(V\ s)$ for the given structure.

The gate-voltage dependence of the lateral current through the heterostructure, calculated at different μ_2 values and small source–drain voltage when the potential distribution under the gate is almost 1D, is shown in Fig. 4.

The initial decrease (beginning at $V_{gs} = 0$) in the drain current occurs since the levels in the TCQWs approach each other and the effective mobility decreases on the background of a weakly changing carrier density in the channel (cf. Fig. 2). The first minimum occurs in the anticrossing of the TCQW size-quantization levels (cf. Fig. 2). With the gate voltage changing further, the TCQWs go out of the anticrossing mode, and the mobility in the TCQWs and the current

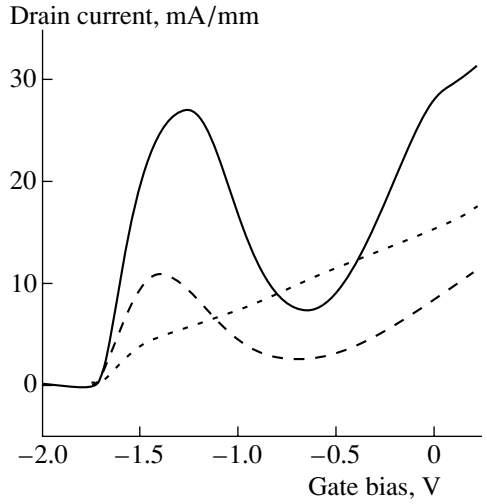

Fig. 4. Drain current vs. gate voltage at different mobilities μ_2 in the narrow QW. μ_2: solid line—700, dashed line—500, and dotted line—100 cm^2/(V s); V_{ds} = 0.001 V.

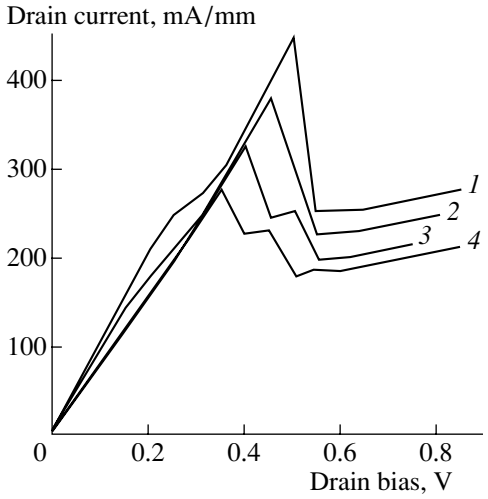

Fig. 5. Drain current vs. drain voltage at different gate voltages V_{gs}: (*1*) 0, (*2*) –0.1, (*3*) –0.3, and (*4*) –0.4 V.

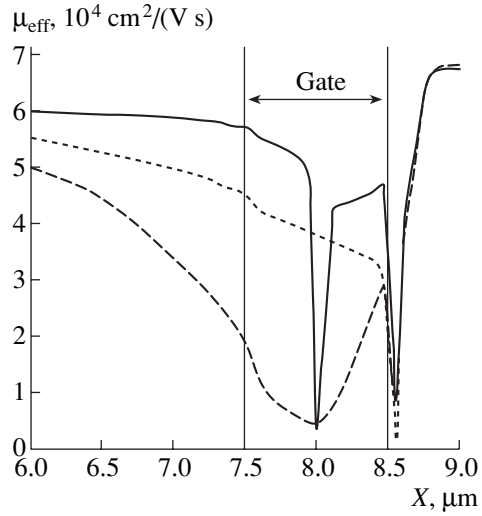

Fig. 6. Mobility in the TCQWs vs. longitudinal coordinate at different drain–source voltages V_{ds}. V_{ds}: solid line—0.56, dashed line—0.55, and dotted line—0.50 V; V_{gs} = 0.

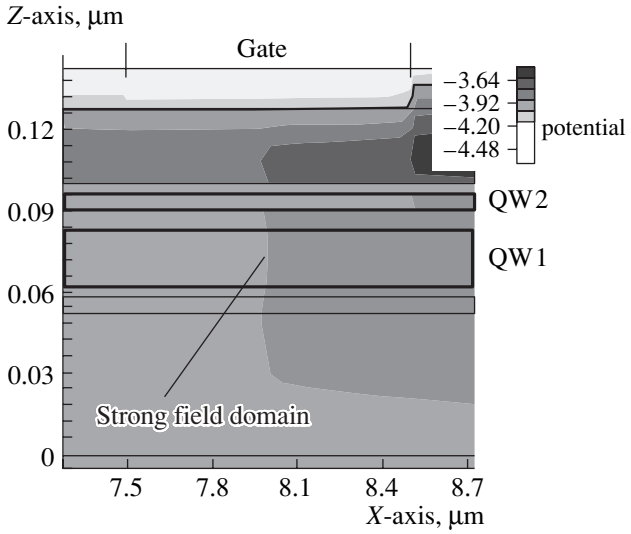

Fig. 7. 2D potential distribution in the heterostructure. Drain–source voltage V_{ds} = 0.56 V, V_{gs} = 0.

through the heterostructure increase. Simultaneously, the carrier density in the TCQWs falls owing to the field effect. At a certain voltage, the decrease in density compensates for the increase in mobility, and the *I–V* characteristic passes through a maximum. After that, the current falls because of the decrease in the electron density, as in the case of the conventional FET (cf. Fig. 3).

The potential distribution under the gate becomes essentially 2D at a source–drain voltage close to the Schottky barrier height when the longitudinal electric field is comparable with the transverse one. Figure 5 presents dependences of the lateral current on V_{gs}, which were calculated for various gate voltages at μ_2 = 700 cm^2/(V s). Their characteristic feature is the region with negative differential resistance (NDR), whose mechanism is as follows.

The source–drain voltage falls faster along the wide QW, since its potential is fixed to a lesser extent by the gate potential. As a result, the potential difference between the QWs (which determines $\Delta\varepsilon$) changes along the gate, and the anticrossing of states at $\Delta\varepsilon = 0$ does not occur under the entire gate, but at a single point only. This leads to a sharp drop in mobility (Fig. 6) and to charge accumulation in the vicinity of this point. The charge accumulation causes local enhancement of the longitudinal electric field and saturation of the carrier drift velocity in this region. The mobility falls even more, which leads to still stronger

charge accumulation and velocity saturation. A potential-controlled feedback emerges and the state of the device becomes unstable.

As a result, a high-field domain forms under the gate (Fig. 7), and the lateral current decreases. Since mobility is at a minimum in the anticrossing range, the domain is static and autolocalized in the middle of the gate. Another region of small mobility also forms, as usual, at the gate edge, but it does not lead to NDR. A large enough mobility drop in the anticrossing of states in the QW is a condition for the occurrence of NDR and domain formation. The characteristics calculated for $\mu_1 = 8000$ cm^2/(V s), when the mobility decreases in the anticrossing by less than a factor of 4, show no NDR region. The results of calculations are virtually the same for both mobility models (3) and (4), indicating the predominance of the interwell transfer over the inter-valley one. The effect is stable with respect to variations of geometry, mobility, dopant concentration, and other structure parameters.

In fact, this effect is similar to the Gunn effect. In contrast to the intervalley transfer in a bulk semiconductor, the effect in heterostructures with QWs is induced by the interwell transfer of carriers.

CONCLUSION

In this study, we analyzed numerically the electronic transport in a heterostructure with tunnel-coupled QWs with different mobilities under the conditions of an essentially 2D potential distribution in the structure. The numerical procedure of the joint solution of the Poisson and continuity equations in the whole structure and the 1D Schrödinger equation in the TCQWs allowed modeling of the electronic transport in TCQWs with the interaction between the quantum and classical regions of the heterostructure being taken into account.

The size-quantization energy levels, density and mobility of electrons in the TCQWs, and *I–V* characteristics were calculated. The tunnel coupling of states in the wells gives rise to nonmonotonic *I–V* characteristics exhibiting regions of negative differential resistance.

It was shown for the first time that an effect similar to the Gunn effect in a bulk semiconductor is possible in heterostructures with TCQWs. The effect is due to the tunnel transfer of electrons between QWs with different mobilities, similar to intervalley transfer in the Gunn effect, and it is characterized by the formation of a high-field domain and an NDR region in the *I–V* characteristic of the structure.

ACKNOWLEDGMENTS

We thank I.V. Tokatly for fruitful collaboration and helpful participation in discussions. This study was supported by the Russian Federal Programs “Integration” and “Physics of Solid-State Nanostructures.”

REFERENCES

1. H. Sakaki, Jpn. J. Appl. Phys. **21** (6), L381 (1982).
2. S. Kirchoefer, R. Magno, and J. Comas, Appl. Phys. Lett. **44**, 1054 (1984).
3. J. M. Pond, S. Kirchoefer, and E. J. Gukauskas, Appl. Phys. Lett. **47**, 1175 (1985).
4. B. Vinter and A. Tardela, Appl. Phys. Lett. **50**, 410 (1987).
5. A. A. Gorbatsevich, V. V. Kapaev, Yu. V. Kopaev, and V. Ya. Kremlev, Phys. Low-Dimens. Struct., Nos. 4/5, 57 (1994).
6. A. Palevski, F. Beltram, F. Capasso, *et al.*, Phys. Rev. Lett. **65**, 1929 (1990).
7. Y. Ohno, M. Tsuchiya, and H. Sakaki, Appl. Phys. Lett. **62**, 1952 (1993).
8. P. I. Biryulin, S. P. Grishechkina, A. S. Ignatiev, *et al.*, Semicond. Sci. Technol. **12** (4), 427 (1997).
9. V. L. Borblik, Z. S. Gribnikov, and B. P. Markevich, Fiz. Tekh. Poluprovodn. (Leningrad) **25**, 1302 (1991) [Sov. Phys. Semicond. **25**, 786 (1991)].
10. V. I. Belyavsky, Yu. V. Kopaev, and Yu. A. Pomerantsev, Phys. Low-Dimens. Struct., Nos. 1/2, 1 (1997).
11. F. T. Vas’ko and O. É. Raĭchev, Zh. Éksp. Teor. Fiz. **107**, 951 (1995) [JETP **80**, 539 (1995)].
12. P. Owen and M. Pepper, Semicond. Sci. Technol. **8** (1), 123 (1993).
13. P. Owen and M. Pepper, Appl. Phys. Lett. **62**, 1274 (1993).
14. P. I. Biryulin, Yu. V. Kopaev, V. T. Trofimov, and N. A. Volchkov, Semicond. Sci. Technol. **14** (8), 699 (1999).
15. H. Sakaki, T. Noda, K. Hirakawa, *et al.*, Appl. Phys. Lett. **51**, 1934 (1987).

Translated by S. Ktitorov

Semiconductors, Vol. 35, No. 11, 2001, pp. 1305–1308. From Fizika i Tekhnika Poluprovodnikov, Vol. 35, No. 11, 2001, pp. 1361–1364.

LOW-DIMENSIONAL SYSTEMS

Electron Nonelastic Scattering by Confined and Interface Polar Optical Phonons in a Modulation-Doped AlGaAs/GaAs/AlGaAs Quantum Well

K. Požela

Semiconductor Physics Institute, Vilnius, 2600 Lithuania

Submitted March 19, 2001; accepted for publication April 10, 2001

Abstract—The calculations of electron scattering rates by polar optical (PO) phonons in an AlGaAs/GaAs/AlGaAs quantum well (QW) with a different width and doping level are performed. The electron- and PO-phonon scattering mechanisms which are responsible for the alternate dependence of electron mobility on a QW width, as well as for the decrease of conductivity in the QW with increasing sheet electron concentration, are determined. It is shown that the enhancement of the scattering rate by PO-phonon absorption when the lower subband electron gas is degenerated is responsible for the decrease of QW conductivity with increasing sheet electron concentration. The competition between the decrease of the intrasubband scattering and the increase of the intersubband scattering by PO-phonon absorption is responsible for the alternate changes of the mobility with a QW width. © *2001 MAIK "Nauka/Interperiodica".*

INTRODUCTION

The alternate change (increase and decrease) of electron mobility as a function of quantum well (QW) width and doping level in modulation-doped AlGaAs/GaAs and AlGaAs/InGaAs QWs was recently observed [1–3]. The predominant mechanism which determines the electron mobility in modulation-doped GaAs QW at $T > 77$ K is electron scattering by confined and interface polar optical (PO) phonons.

In this paper, the separate contribution to electron mobility of definite-type intra- and intersubband electron transitions with absorption or emission of PO phonons is considered. The scattering mechanisms which are responsible for alternate mobility changes with a QW width and doping level are determined.

1. CONFINED ELECTRON- AND PO-PHONON SCATTERING RATE AND MOBILITY IN $Al_{0.25}Ga_{0.75}As/GaAs/Al_{0.25}Ga_{0.75}As$ QUANTUM WELLS

The transition frequency of electrons, confined in a quantum well (QW), from an initial state in the *i*th subband with momentum $\mathbf{k}_i$ and subband electron energy E_{si} to any final state, $\mathbf{k}_f$, E_{sf}, in subband f by emission (absorption) of a ν-mode PO-phonon can be written as [4–7]

$$\mathbf{w}_{if\nu}^{a,e}(k_i, E_{si}) = \sum_{\mathbf{k}_f} \frac{4\pi m e^2}{\hbar^3} |G_\nu|^2 F_{q\nu}^2 \left(N_{q\nu} + \frac{1}{2} \pm \frac{1}{2} \right) \times \delta(\mathbf{k}_f^2 - \mathbf{k}_i^2 + \beta_\pm), \quad (1)$$

where G_ν is the overlap integral of the normalized electron- and phonon wave functions, $N_{q\nu}$ is the occupation number of ν-mode phonons, and $\beta_\pm = \frac{2m}{\hbar^2}(E_{sf} - E_{si} \pm \hbar\omega_\nu)$. The upper sign (+) is for phonon emission and the lower sign (–) is for phonon absorption. The phonon potentials and their interaction intensity with electrons ($F_{q\nu}^2$) are calculated by using the dielectric continuum model [7, 8].

The electron- and PO-phonon scattering rates were calculated at $T = 100$ K for the symmetric rectangular $Al_{0.25}Ga_{0.75}As/GaAs/Al_{0.25}Ga_{0.75}As$ QW with sheet electron concentration in the range of $5 \times 10^{15} < n_s < 6 \times 10^{16}$ m^{-2} and QW widths 15 nm $< L <$ 35 nm. The parameters used in the calculations were the following: $m/m_0 = 0.67$, $\hbar\omega_0 = 36.2$ meV, $\chi_\infty = 10.9$, $\chi_s = 12.9$ for GaAs and $m/m_0 = 0.09$, $\hbar\omega_0 = 46.8$ meV, $\chi_\infty = 10.1$, $\chi_s = 13.0$ for AlGaAs. The $Al_{0.25}Ga_{0.75}As/GaAs$ barrier is assumed as $U_0 = 0.3$ eV.

The nonelastic electron- and PO-phonon scattering with a large change of scattered electron energy requires us to take into account the different occupation of electrons in the initial and final states. Taking into account the electron state occupation, the mean frequency of electron transitions (scattering rates) from the initial state in subband *i* to the final one in subband *f* can

1063-7826/01/3511-1305$21.00

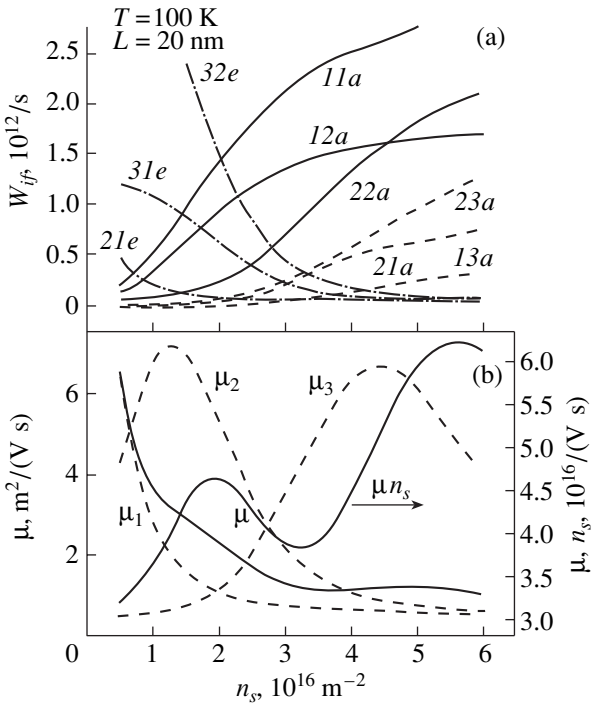

Fig. 1. The electron- and PO-photon scattering rates W_{if} with electron transitions from the initial state in subband i to the final one in subband f by photon emission and absorption (labeled by *ife* and *ifa*, respectively) (a) and the electron mobilities in subbands $i = 1, 2, 3$ (labeled by μ_1, μ_2, μ_3), the total mobility μ and conductivity (μn_s) (b) as functions of sheet electron concentration n_s in the QW of width L = 20 nm.

be written in the form

$$W_{if}^{a,e} = \sum_{\nu} \int_{E_{si}}^{\infty} w_{if\nu}^{a,e}(E) \times \frac{1 - f(E \pm \hbar\omega_\nu)}{1 - f(E)} dE / \int_{E_{si}}^{\infty} f(E) dE, \quad (2)$$

where $f(E)$ is the electron Fermi–Dirac distribution function, the sign "+" is for phonon absorption, and the sign "–" is for phonon emission.

The electron mobility in pure GaAs at $T > 77$ K is determined by electron- and PO-phonon scattering. In this paper, an estimation of the separate contribution to electron mobility of various types of electron- and PO-phonon scattering is made assuming the inverse mean frequency of electron transitions by PO-phonon absorption (emission) as a momentum relaxation time

$$\tau_{if} = 1/W_{if}. \quad (3)$$

This relaxation time approximation gives only a crude estimation of the mobility limited by PO-phonon scattering, but it is expected that this approximation is sufficient both for estimation of the relative difference between the mobilities in QWs with different widths and sheet electron concentrations and for estimation of the relative contribution to electron mobility of various electron scattering mechanisms by various phonon modes. Note that the values of mobility calculated within the used relaxation time approximation in the GaAs QW are close to the values observed experimentally.

In this approximation, the i-subband electron mobility is

$$\mu_i = \frac{e}{m} / \sum_f (W_{if}^e + W_{if}^a), \quad (4)$$

and the total electron mobility in the QW is

$$\mu = \frac{1}{n_s} \sum_i \mu_i n_i, \quad (5)$$

where n_s and

$$n_i = \frac{m}{\pi\hbar^2} \int_{E_{si}}^{\infty} f(E) dE \quad (6)$$

are the sheet electron concentrations in the QW and in subband i, respectively.

2. THE DEPENDENCE OF ELECTRON SUBBAND MOBILITY ON SHEET ELECTRON CONCENTRATION

The calculated intra- and intersubband electron- and PO-phonon scattering rates as functions of sheet electron concentration n_s in the $Al_{0.25}Ga_{0.75}As/GaAs/Al_{0.25}Ga_{0.75}As$ QW of the width L = 20 nm are presented in Fig. 1a.

The significant enhancement of the intra- and intersubband scattering rates by PO-phonon absorption with increasing n_s is observed in the lower subbands (W_{11}^a, W_{12}^a, W_{22}^a). The enhancement takes place in the subbands with degenerate electron gas. This is largest in the lowest (first) electron subband (W_{11}^a), where the electron gas is most degenerated (see Fig. 1a). On the other hand, the scattering rates by phonon emission from the upper subband to the lower one (W_{32}^e, W_{32}^e, W_{21}^e) decrease with electron gas degeneration in the lower subband. The scattering rate by phonon emission in the lower subband can be neglected.

The increase of scattering rates by PO-phonon absorption (W_{11}^a and W_{12}^a) is responsible for the strong decrease of electron mobility in the lowest (first) electron subband, μ_1, with increasing n_s, as is shown in Fig. 1b. The second subband mobility μ_2 increases due to decreasing the second subband electron scattering by phonon emission when n_s changes in the range of

$(5–15) \times 10^{15}$ m^{-2}. At $n_s > 15 \times 10^{15}$ m^{-2}, μ_2 decreases rapidly because of the strong increase of electron scattering rates W^a_{22}, W^a_{21}, W^a_{23} by phonon absorption. The contribution of the second subband electrons to the total QW mobility increases with increasing second-subband electron population.

This decrease of the mobilities in the first and second subbands exceeds the increase of n_s in the range of $(2–3) \times 10^{16}$ m^{-2}. As a result, the decrease of QW conductivity (μn_s) with increasing n_s takes place. This is shown in Fig. 1b. When $n_s > 3 \times 10^{16}$ cm^{-2}, the third subband electrons with increased mobility, due to the decrease in W^e_{31} and W^e_{32}, enhance the total QW conductivity, in spite of decreasing the first and second subband mobilities.

The increase of μ_3 is limited at $n_s > 4.5 \times 10^{16}$ m^{-2}, due to the increase of electron scattering by phonon absorption in the third subband, and the second decrease of the conductivity μn_s is observed (Fig. 1b).

It is worth noting that the electron mobility in the second subband twice exceeds the first subband mobility at $n_s = 1.5 \times 10^{16}$ m^{-2}. There are two types of electrons in the QW: low mobility electrons in the first subband and electrons in the second subband which are twice as fast. At $n_s > 3 \times 10^{16}$ m^{-2}, the faster electrons are in the third subband (see Fig. 1b).

Therefore, the increase in the intra- and intersubband scattering rates by PO-phonon absorption in degenerate electron gas is responsible for a decrease in mobility with increasing n_s in the $Al_{0.25}Ga_{0.75}As/GaAs/Al_{0.25}Ga_{0.75}As$ QW. The decrease in the intersubband scattering by PO-phonon emission in the upper subbands, W^e_{31}, W^e_{32}, W^e_{21}, is responsible for the alternate increase of conductivity (because of electron gas degeneracy in the lower subbands).

3. THE DEPENDENCE OF ELECTRON MOBILITY ON A QW WIDTH

Figure 2a shows the QW width dependencies of electron intra- and intersubband scattering rates in the $Al_{0.25}Ga_{0.75}As/GaAs/Al_{0.25}Ga_{0.75}As$ QW at sheet electron concentration $n_s = 5 \times 10^{15}$ m^{-2}. At all QW widths in the range of 15 nm $< L <$ 35 nm, the main electron scattering mechanism in the lowest subband remains W^a_{11} and W^a_{12}. At $L >$ 18 nm, the scattering rates W^a_{11} and W^a_{12} decrease slowly with increasing QW width. In the second and third subbands, the intersubband transitions by PO-phonon emission are permitted and the scattering rates W^e_{31}, W^e_{32}, W^e_{21} are very high and exceed 10^{12} s^{-1}.

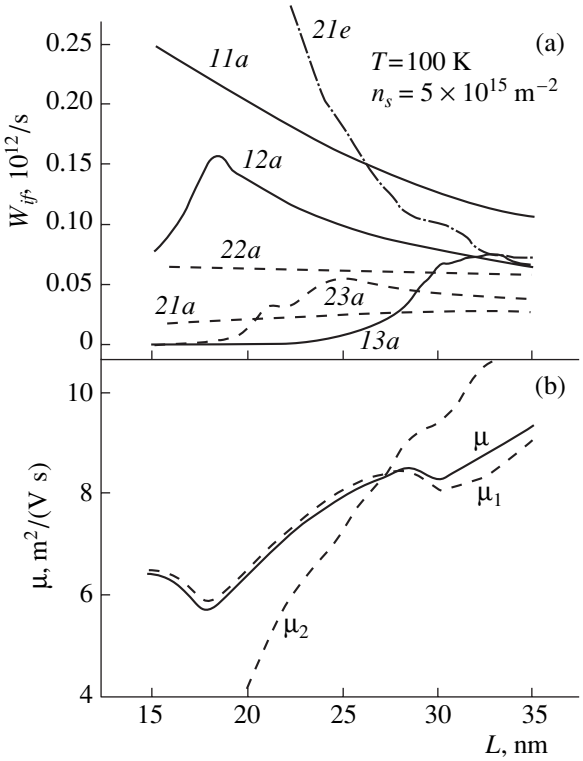

Fig. 2. The electron- and PO-phonon scattering rates W_{if} (a) and the subband and total electron mobilities (b) as functions of QW width at $n_s = 5 \times 10^{15}$ m^{-2}. Notations are as in Fig. 1.

Such behavior of electron- and PO-phonon scattering explains the alternate dependence of the mobility on GaAs QW width shown in Fig. 2b.

We see that the increase of the first subband electron mobility μ_1 with increasing QW width L due to the decrease of W^a_{11} is limited at two QW widths—at L = 15–18 and L = 25–30 nm—by the increase of the intersubband scattering rates W^a_{12} and W^a_{13}, respectively. Between these two limited scattering rates (in the interval of L = 18–25 nm) the mobility monotonically increases with a QW width L.

At QW widths L = 15–25 nm, the intersubband scattering rate with PO-phonon emission W^e_{21} decreases due to filling the electron states in the first subband. Therefore, the second subband electron mobility μ_2 increases. At $L >$ 27 nm, μ_2 becomes larger than μ_1 (see Fig. 2b).

When the sheet electron concentration in the QW increases until $n_s = 3 \times 10^{16}$ m^{-2}, the electron–phonon intersubband scattering rates change significantly due to the occupation of electron states in the lower subbands (see Fig. 1b). This gives a tenfold increase in the scattering rate by PO-phonon absorption in the lowest subband, and a decrease of the scattering rate by

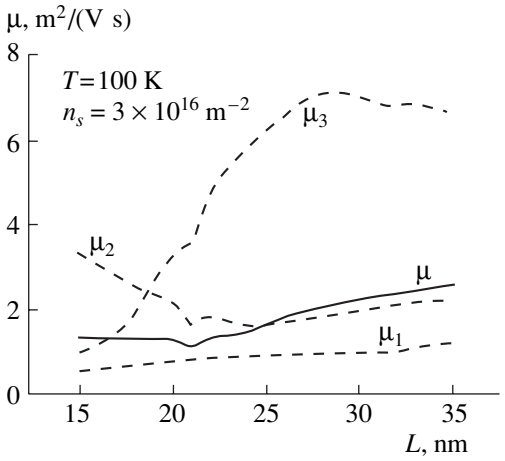

Fig. 3. The subband and total electron mobilities as functions of QW width at $n_s = 3 \times 10^{16}$ m^{-2}. Notations are as in Fig. 1.

PO-phonon emission in the upper subbands (see Fig. 1a).

As a result, the electron mobility strongly decreases in the lower QW subband and increases in the upper (third) subband. At $n_s = 3 \times 10^{16}$ m^{-2}, the population of electrons in the upper subbands is large, and their contribution to the total mobility is significant.

Figure 3 shows the QW width dependence of electron mobilities at $n_s = 3 \times 10^{16}$ m^{-2}.

We see that the second subband electrons provide the main contribution to the total mobility. The decrease of the mobility is observed only at $L = 22$ nm. It is explained by the increase of the scattering of second subband electrons to the third subband by phonon absorption (W^a_{23}). At $L > 22$ nm, the electron scattering rates in all subbands, both with phonon emission and absorption, decrease slowly with increasing QW width. This circumstance gives an increase of the total mobility with increasing QW width in the range of 22 nm < L < 35 nm. Note that at $L > 25$ nm the third subband mobility is seven times larger than the mobility in the first subband.

Therefore, the total electron mobility increases with QW width. This increase limits the electron intersubband scattering rates by phonon absorption: W^a_{12} and W^a_{13} in the QW with $n_s = 5 \times 10^{15}$ m^{-2} and W^a_{23} in the QW with $n_s = 6 \times 10^{16}$ m^{-2}.

CONCLUSIONS

The electron- and PO-phonon scattering mechanisms which are responsible for the dependencies of electron mobility on QW width and doping level are determined. It is shown that:

1. The degeneracy of subband electron gas decreases the electron scattering by PO-phonon emission and increases the scattering by phonon absorption. With the QW width L = 20 nm, the scattering by PO-phonon absorption exceeds the scattering by PO-phonon emission in the first subband at $n_s > 5 \times 10^{15}$ m^{-2}, in the second subband at $n_s \geq 1.5 \times 10^{15}$ m^{-2}, and in the third subband at $n_s \geq 4.5 \times 10^{15}$ m^{-2}. At these n_s, the mobility in the upper subbands exceeds the mobility in the lower ones. The increase of the scattering by PO-phonon absorption is responsible for the decrease of QW conductivity with increasing sheet electron concentration in the range of n_s = (2–3) $\times 10^{16}$ m^{-2} and $n_s > 5.5 \times 10^{16}$ m^{-2}.

2. The enhancement of the mobility with increasing QW width due to a reduction in the intrasubband scattering rates by PO-phonon absorption (W^a_{11}, W^a_{22}) at $n_s = 5 \times 10^{15}$ m^{-2} is limited by the increase in the intersubband scattering of the first subband electrons (W^a_{12} and W^a_{13}), and, at $n_s = 3 \times 10^{16}$ m^{-2}, by the increase of the scattering of the second subband electrons (W^a_{23}). The competition between these scattering mechanisms explains the alternate changes of the mobility with QW width.

REFERENCES

1. J. Požela, K. Požela, and V. Jucienė, Fiz. Tekh. Poluprovodn. (St. Petersburg) **34**, 1053 (2000) [Semiconductors **34**, 1011 (2000)].
2. J. Požela, K. Požela, A. Namajūnas, *et al.*, J. Appl. Phys. **88**, 1056 (2000).
3. T. Tsuchiya and T. Ando, Phys. Rev. B **48**, 4599 (1993).
4. N. Mori and T. Ando, Phys. Rev. B **40**, 6175 (1989).
5. H. Rücker, E. Molinary, and P. Lugli, Phys. Rev. B **45**, 6747 (1992).
6. B. K. Ridley, Phys. Rev. B **39**, 5282 (1989).
7. I. Lee, S. M. Goodnick, M. Gulia, *et al.*, Phys. Rev. B **51**, 7046 (1995).
8. J. Požela, V. Jucienė, A. Namajūnas, and K. Požela, Physica E (Amsterdam) **5**, 108 (1999).
9. J. Požela, V. Jucienė, and K. Požela, Semicond. Sci. Technol. **10**, 1555 (1995).

Semiconductors, Vol. 35, No. 11, 2001, pp. 1309–1313. Translated from Fizika i Tekhnika Poluprovodnikov, Vol. 35, No. 11, 2001, pp. 1365–1369.

LOW-DIMENSIONAL SYSTEMS

Electrical Characteristics of Single-Gate Interference Transistors Based on Various Semiconductor Materials

I. I. Abramov and A. I. Rahachou

Belarussian State University of Information Science and Radio Engineering, ul. Brovki 17, Minsk, 220027 Belarus

Submitted December 19, 2000; accepted for publication April 14, 2001

Abstract—The current–voltage and high-frequency characteristics of single-gate interference *T* transistors based on quantum wires made of various semiconductors, specifically, Si, Ge, GaAs, InAs, GaSb, InSb, GaP, and InP, were studied theoretically. Two scattering mechanisms were taken into account in the *T*-transistor model in order to assess their effect on the electrical characteristics of devices. The adequacy of the suggested model was verified by comparing the results of simulation with experimental data. The calculations were performed using the QW-NANODEV subsystem for simulating the devices based on quantum wires. © *2001 MAIK "Nauka/Interperiodica".*

INTRODUCTION

Radically new opportunities are opening up for designing superlarge-integration circuits of solid-state electronics in connection with the development of device structures based on quantum wires [1–3]. On the one hand, this is related to good compatibility of the methods for fabricating such structures with both the well-developed planar technology for conventional integrated circuits and the methods of modern nanotechnology. On the other hand, it is expected that the devices based on quantum wires will have acceptable and, in a number of cases, unique electrical characteristics. In particular, it has been shown recently that interference *T* transistors may feature saturation portions in their output current–voltage (*I*–*V*) characteristics for small-bias voltages at the drain [4]. As a result, these devices can be used in both analog and digital integrated circuits in nanoelectronics. Furthermore, these devices can operate at very high frequencies [4]. Based on the above reasoning, it should be expected that nanoelectronic integrated circuits, including the devices based on quantum wires, will be developed in the near future, as is also expected for resonance-tunneling [5] and one-electron [6, 7] structures. Experimental samples of the devices based on quantum wires have already been fabricated [8].

In this paper, we report the results of using the developed model to study theoretically the electrical characteristics of interference single-gate *T* transistors based on quantum wires and made of various semiconductors with the aim of selecting the most preferential of these materials.

MODEL

In this study, we analyze a single-gate structure of the interference *T* transistor [2]; this structure is shown in Fig. 1. The developed model was based on the scattering-matrix method [1, 2].

Let us consider the basic modification of the model compared to that adopted in [2]. First, the model accounts for the dependence of the effective electron mass on geometric dimensions of the quantum wire and on the impurity concentration in the wire according to [9]. Since the model adopted in [9] is transcendental, we used a self-consistent calculation of effective mass in contrast to [4]. We note that the iterative process converged after four–seven iteration steps.

Second, the model allows consideration of the scattering mechanisms characteristic of the structures under consideration. In this study, we used the models of scattering by a remote charged impurity (the effect of substrate) and by irregularities of the quantum-wire surface.

Thus, the intensity of scattering by a remote charged impurity is calculated using the formula [10]

$$\tau_r^{-1} = \frac{n_1 m^* q^4}{4\pi^2 \hbar^3 (\varepsilon\varepsilon_0)^2 k_x} K^2\left[2 d_0 k_x \sin\left(\frac{\theta}{2}\right)\right], \qquad (1)$$

where n_1 is the linear concentration of the impurity in the substrate; m^* is the effective electron mass in the quantum wire; q is the elementary charge; $\hbar$ is the reduced Planck constant; $\varepsilon\varepsilon_0$ is the absolute dielectric constant of a semiconductor; k_x is the wave vector; d_0 is the distance between the impurity center and the origin of coordinates, which is located at the center of the square cross section of the wire; θ is the scattering angle; and K is the modified Bessel function of the second kind. The intensity of scattering by irregularities of

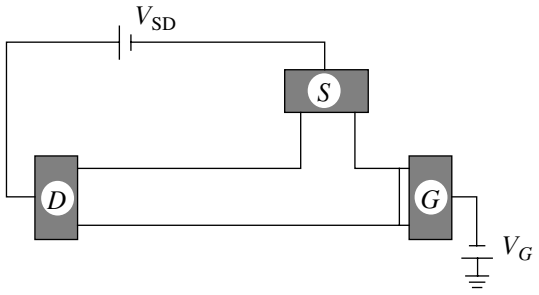

Fig. 1. Schematic representation of a single-gate interference *T* transistor based on a quantum wire. *S* stands for the source; *D*, for the drain; and *G*, for the gate.

the quantum-wire surface is given by [11]

$$\tau_{sr}^{-1} = \frac{2\pi^{\frac{9}{2}}\Lambda\Delta^2\hbar}{m^*Lk_x\exp[k_x^2\Lambda^2\sin^2(\theta/2)]}. \quad (2)$$

Here, Δ and Λ are the correlation length and the mean amplitude of the surface irregularities, respectively; and L is the quantum-wire length. The total scattering intensity is expressed as

$$\tau_\Sigma^{-1} = \tau_r^{-1} + \tau_{sr}^{-1}. \quad (3)$$

In considering the scattering processes, we used the following additional assumptions. Since a quantum wire is basically a one-dimensional structure, we assume that the scattering angle θ is equal to π, which corresponds to the "total" scattering; the value of d_0 was set equal to the wire thickness.

Third, in order to take into account the effect of the scattering mechanisms on the drain current, we used the following modified expression (rather than the Tsu–Esaki formula):

$$I_{SD} = \frac{2q}{h}\int_0^{E_F} |t(E, V_G)|^2 D(E) \times [f(E) - f(E + qV_{SD})]dE. \quad (4)$$

Here, I_{SD} is the drain current, $|t(E, V_G)|^2$ is the electron-wave transmission coefficient determined using the scattering matrix [2], V_G is the gate voltage, V_{SD} is the drain voltage, $f(E)$ is the Fermi–Dirac distribution function, h is the Planck constant, E_F is the Fermi energy, and $D(E)$ is a coefficient characterizing the electron-wave attenuation due to scattering. The latter coefficient is given by

$$D(E) = \exp(-\alpha t_T \tau_\Sigma^{-1}), \quad (5)$$

where t_T is the time of transit of charge carriers through the structure under the conditions of ballistic transport, τ_Σ^{-1} is the total intensity of scattering mechanisms, and α is a constant coefficient defined by the interconnection between different scattering mechanisms; in the strict sense, this coefficient should be determined from experimental data. The transit time is calculated on the basis of the Fermi velocity and is given by

$$t_T = L\frac{m^*}{\hbar k_F}, \quad (6)$$

where k_F is the Fermi wave vector.

For single-gate *T* transistors, the highest operating frequency is calculated using the formula [2]

$$f_{max} = \frac{I_{SD}^{max}}{4\pi q}. \quad (7)$$

Here, I_{SD}^{max} is the maximal drain current calculated using expression (4).

The above-described model was implemented in the QW-NANODEV subsystem for simulating the device structures based on quantum wires; this subsystem is incorporated in the NANODEV system of simulating nanoelectronics devices based on the effects of resonance and one-electron tunneling and on quantum interference [6].

RESULTS AND DISCUSSION

We studied theoretically the single-gate interference *T* transistors made of eight semiconductors. Their most important parameters used in simulation are listed in the table [12].

We analyzed the structures with small sizes. The device length L was chosen to equal 100 nm in order to ensure that the quantum-mechanical effects were pronounced and the scattering mechanisms were of lesser importance. The quantum-wire thickness d_0 was

Parameters of materials under consideration

Parameter	GaSb	GaP	InP	Ge	Si	GaAs	InAs	InSb
Dielectric constant ε	15.7	11.1	12.5	16.2	11.7	12.9	15.15	16.8
Band gap E_g, eV	0.726	2.26	1.344	0.661	1.12	1.424	0.354	0.17
Longitudinal effective electron mass m_l/m_0	0.041	1.12	0.08	1.6	0.98	0.063	0.023	0.014
Transverse effective electron mass m_t/m_0	0.041	0.22	0.08	0.08	0.19	0.063	0.023	0.014
Spin–orbit splitting Δ, eV	0.8	0.08	0.11	0.29	0.044	0.34	0.41	0.8

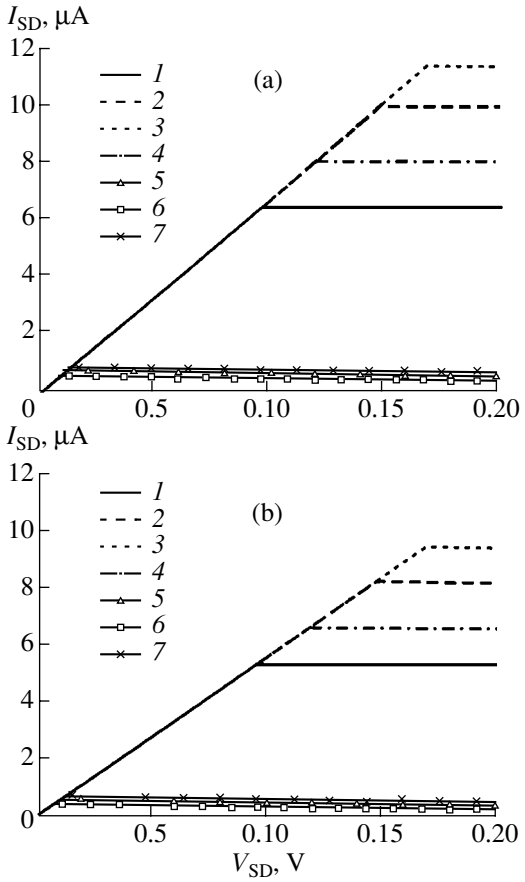

Fig. 2. The current–voltage characteristics of a single-gate interference *T* transistor calculated (a) without and (b) with taking into account the scattering mechanisms. The curves correspond to (*1*) InSb, (*2*) GaSb and InAs, (*3*) GaAs, (*4*) InP, (*5*) Si, (*6*) GaP, and (*7*) Ge.

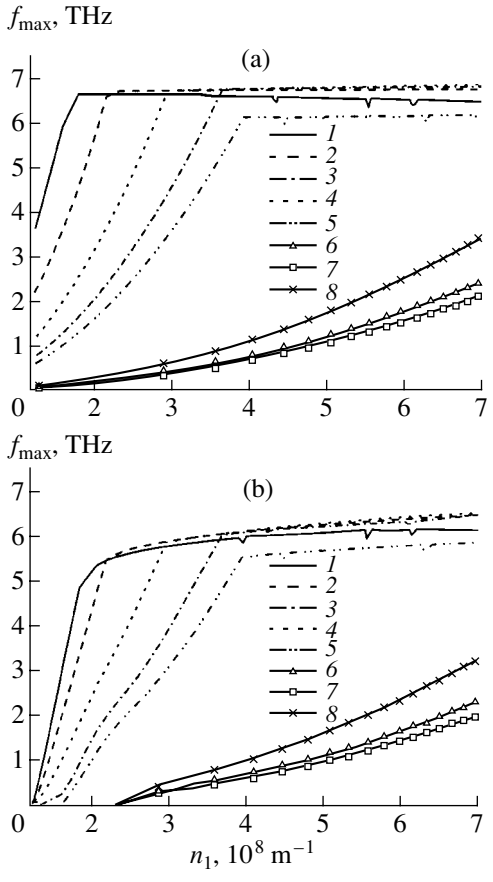

Fig. 3. The high-frequency characteristics of a single-gate interference *T* transistor (a) without and (b) with taking into account the scattering mechanisms. Curve (*1*) corresponds to InSb; (*2*), to InAs; (*3*), to GaAs; (*4*), to GaSb; (*5*), to InP; (*6*), to Si; (*7*), to GaP; and (*8*), to Ge.

assumed equal to 10 nm if the transistor operated in a single mode, in accordance with the capabilities of modern nanotechnology. In order to reduce the effects of the phonon-scattering processes, the simulation was performed at a low temperature (4.2 K). The temperature dependence of the effective mass was ignored. The correlation length Δ and the mean surface-roughness amplitude Λ were assumed to be equal to 0.3 nm and 0.15 nm, respectively; this is consistent with experimental data on nanoscale films [13]. The impurity concentration in the quantum wire was set at $N_c = 10^{25}$ m^{-3}. We chose a lightly doped substrate with an impurity concentration of $N_0 = 10^{23}$ m^{-3}. The coefficient α in formula (5) was assumed to be equal to unity in theoretical studies under consideration.

In Fig. 2, we show the calculated *I–V* characteristics of the interference *T* transistors made of various materials for the gate voltage $V_G = 0.2$ V; the calculations were performed either with (Fig. 2a) or without (Fig. 2b) considering the scattering. It can be seen that, for all materials, saturation regions appear in the drain-current characteristics of the transistors, irrespective of whether the scattering was taken into account; this is consistent with results reported recently [4]. Saturation sets in when the drain voltage corresponds to the Fermi energy. It follows from Fig. 2 that the drain currents differ for dissimilar materials. This is related to the combined effect of the material parameters; however, it is the effective electron mass in the quantum wire that exerts the most pronounced effect. On the one hand, for materials with a small effective mass of electrons ($m^* < 0.1m_0$, where m_0 is the free-electron mass), such as GaAs, InAs, GaSb, InSb, and InP, higher drain currents can be obtained than those in the case of using the materials with "heavy" electrons (Ge, Si, and GaP) in the quantum wire. On the other hand, the scattering processes more profoundly affect the device characteristics made of the former group of materials; in particular, a larger reduction of the drain current is observed in this case (Fig. 2b).

We used the suggested model to calculate the highest operating frequency in relation to the linear impurity concentration in a quantum wire made of the eight aforementioned materials. In contrast to [4], the gate

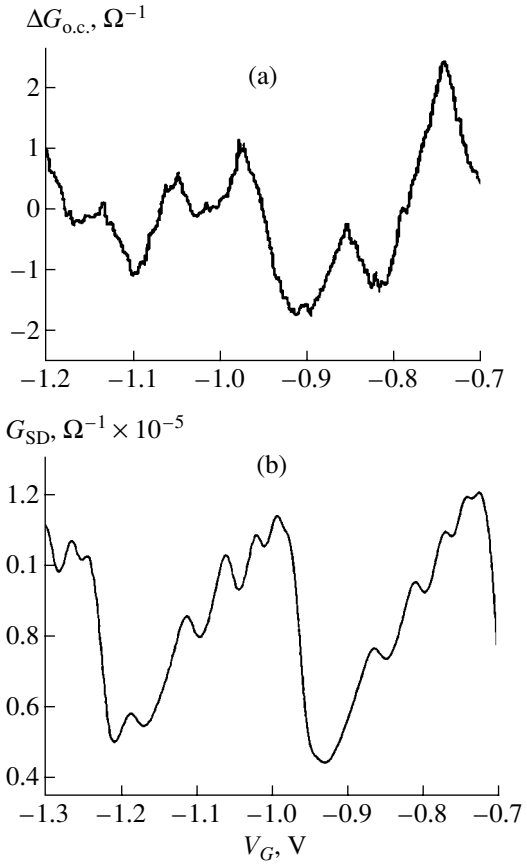

Fig. 4. (a) Experimental dependence [8] of the *T*-transistor conductance on the gate voltage and (b) the results of simulating the structure conductance.

voltage was assumed equal to 0.01 V in order to minimize its effect on the high-frequency characteristics. In addition, we assumed here that the quantum wire is thicker. In order to assess the effect of scattering, we simulated the high-frequency characteristics without considering this effect for $D(E) = 1$ (Fig. 3a) and with considering it (Fig. 3b). It follows from Fig. 3 that the scattering processes most profoundly impair the high-frequency characteristics of devices in the range of low impurity concentrations in a quantum wire for all materials under consideration. This is related to the fact that, for low impurity concentrations, the fraction of electrons experiencing the scattering becomes comparable to the total number of charge carriers involved in the charge transport. This causes the drain current to be reduced almost to zero, which, in turn, affects the high-frequency characteristics. However, the aforementioned tendency, according to which the transistors based on the materials with smaller effective electron mass in a quantum wire have superior characteristics, is retained in the reported frequency dependences.

In order to verify the adequacy of the model used, we compared the results of simulation not only with the results of previous calculations [4] but also with experimental data. Unfortunately, there is currently a lack of experimental data available on *T* transistors with the aforementioned small sizes; therefore, the transistor structure reported previously [8] was considered in this study. The length and thickness of quantum wire in the structure were chosen to be 8 μm and 280 nm, respectively. The device operates under multimode conditions (nine modes), and the quantum-wire material is GaAs. We calculated the source–drain channel conductivity in relation to the voltage applied to the gate using the well-known Landauer formula [2]. As a result, we obtained a good qualitative agreement with corresponding experimental characteristics. The data reported by Appenzeller *et al*. [8] and the results of simulation in this study are shown in Figs. 4a and 4b, respectively. Unfortunately, it is impossible to compare the above results in more detail because more comprehensive data on the structure used in [8] are lacking.

CONCLUSION

We suggested a model that adequately describes the characteristics of a single-gate interference *T* transistor based on quantum wire and that can account for different mechanisms of scattering. Using this model, we calculated the current–voltage and high-frequency characteristics of *T* transistors made of the eight materials (see above) with allowance made for scattering by a remote charged impurity and surface irregularities. The structure sizes were chosen in accordance with the capabilities of modern nanotechnology. It is shown that, when using a material with a small effective electron mass in a quantum wire, it is possible to obtain a larger drain current and higher ultimate operating frequency than those typical of materials with “heavier” electrons. At the same time, it is established that the considered scattering mechanisms more profoundly affect the transistor characteristics in materials with a small effective electron mass in the quantum wire. The results of simulation in this study are consistent with experimental data, which verifies the applicability of the suggested model to theoretical studies of the considered transistor types.

ACKNOWLEDGMENT

This study was supported in part by the Belarussian Scientific and Technological Programs in Information Science, Low-Dimensional Systems, and Nanoelectronics.

REFERENCES

1. S. Datta, Superlattices Microstruct. **6**, 83 (1989).
2. S. Subramaniam, S. Bandyopadhyay, and W. Porod, J. Appl. Phys. **68**, 4861 (1990).
3. Zh. I. Alferov, Fiz. Tekh. Poluprovodn. (St. Petersburg) **32**, 3 (1998) [Semiconductors **32**, 1 (1998)].

4. I. I. Abramov, Yu. A. Berashevich, and A. L. Danilyuk, Zh. Tekh. Fiz. **69** (11), 130 (1999) [Tech. Phys. **44**, 1384 (1999)].
5. J. I. Bergman, J. Chang, Y. Joo, *et al.*, IEEE Electron Device Lett. **20**, 119 (1999).
6. I. I. Abramov and E. G. Novik, *Numerical Simulation of Metallic One-Electron Transistors* (Bestprint, Minsk, 2000).
7. A. C. Irvine, Z. A. K. Durrani, and H. Ahmed, J. Appl. Phys. **87**, 8594 (2000).
8. J. Appenzeller, Ch. Schoer, Th. Schapers, *et al.*, Phys. Rev. B **53**, 9959 (1996).
9. A. Ghoshal, B. Mitra, and K. P. Ghatak, Nuovo Cimento **12**, 891 (1990).
10. C.-C. Wu and C.-J. Lin, J. Appl. Phys. **83**, 1390 (1998).
11. J. Motohisa and H. Sakaki, Appl. Phys. Lett. **60**, 1315 (1992).
12. M. E. Levinshtein and S. L. Rumyantsev, *Handbook Series on Semiconductor Parameters* (World Scientific, London, 1996).
13. V. M. Borzdov and F. F. Komarov, *Simulation of Electrical Properties of Solid-State Layered Structures of Integrated Electronics* (Beloruss. Univ., Minsk, 1999).

Translated by A. Spitsyn

Semiconductors, Vol. 35, No. 11, 2001, pp. 1314–1319. Translated from Fizika i Tekhnika Poluprovodnikov, Vol. 35, No. 11, 2001, pp. 1370–1375.

LOW-DIMENSIONAL SYSTEMS

Medium-Range Order and Optoelectronic Properties of a Tetrahedrally Coordinated Hydrogenated Amorphous Semiconductor

O. A. Golikova

Ioffe Physicotechnical Institute, Russian Academy of Sciences, Politekhnicheskaya ul. 26, St. Petersburg, 194021 Russia

Submitted April 3, 2001; accepted for publication April 5, 2001

Abstract—Correlations were determined between the medium-range-order characteristic in an *a*-Si:H structure and the density of defects, their charge state, the optical band gap, and its spatial fluctuations. It was shown that the modification of the structure at the medium-range-order level, owing to the formation of nanoinclusions, can lead to a radical increase in photoconductivity and to ordering of the structure of the amorphous matrix. *© 2001 MAIK "Nauka/Interperiodica".*

INTRODUCTION

The objective of this study was to determine the correlations between structure ordering at the medium-range level and certain optoelectronic properties of a tetrahedrally coordinated hydrogenated amorphous semiconductor. This objective is attained using hydrogenated amorphous silicon (*a*-Si:H) as an example.

As is well known, there is no long-range order in the structure of an amorphous semiconductor, but the short-range order is preserved. Its parameters are as follows: the number of the nearest neighboring atoms (coordination number), the spacing between them (bond length), and the angle between the neighboring bonds (valent-bond angle φ). The structure ordering at this level depends on the variance of the angle φ. The above parameters affect not only the first coordination sphere, but also the second one, at least partially [1]. However, there is a certain ordering in the structure of an amorphous semiconductor even beyond the second coordination sphere (the medium-range order). The ordering at this level depends on the variance of dihedral angles, which determines, on the one hand, the mutual arrangement of silicon tetrahedra and, on the other hand, the formation of clusters in the form of five-, six-, and seven-member silicon rings [2]. The *a*-Si:H structure can be modified at the level of the medium-range order when nanodimensional ordered inclusions are formed in the amorphous matrix [for example, nanocrystals or nanoclusters of silicon and also polymeric chains of the $(SiH_2)_n$ type]. In recent years, such a modification has attracted a significant amount of attention from researchers as a method for controlling the optoelectronic properties of material. In this paper, we report some results of our investigations of *a*-Si:H modified at the level of the medium-range order. In our opinion, these results hold significance for developing the physics of heterogeneous amorphous semiconductors.

EXPERIMENTAL RESULTS AND DISCUSSION

We begin with the results obtained for a "conventional" homogeneous *a*-Si:H. Films were deposited by the method of radio-frequency decomposition of silane (rf-PECVD) at T_s = 300°C. We investigated both undoped and boron-doped films. Boron was introduced into the films either by gas doping (by adding diborane to silane) or by ion implantation (at room temperature, with the average ion energy E = 60 keV, the average dose $D = 10^{11}$–10^{15} cm^{-2}, and with subsequent annealing in vacuum at 200°C for 1 h). From the infrared-spectroscopy data, the hydrogen content C_H in all the films amounted to 2–8 at. %.

The data on the medium-range order in the *a*-Si:H structure were obtained by Raman spectroscopy. As is known, the Raman spectra from *a*-Si:H exhibit bands of transverse acoustic, longitudinal acoustic, and transverse optical phonons. They are designated as TA-, LA-, and TO-bands and are peaked at frequencies $\omega \approx$ 160, 300, and 480 cm^{-1}, respectively.

The TA-band origin is associated with vibrations of silicon tetrahedra [3]. The LA-band is associated with vibrations of silicon rings, i.e., also with the medium-range order [4]. However, noticeable variations in this band intensity were not observed in the spectra of films we investigated. For this reason, as a characteristic of the medium-range order, the ratio I_{TA}/I_{TO} (I_{TA} and I_{TO} are the intensities at the peaks of the corresponding bands) was considered [3]. According to [3], an increase in I_{TA}/I_{TO} indicates that the degree of disordering in the arrangement of tetrahedra increases.

1063-7826/01/3511-1314$21.00

However, for determining the direct interrelation between the medium-range order and the properties of the material, it was necessary to know the correlation of its characteristics with those of the medium-range order, i.e., a $\Delta\omega_{TO}$ quantity equal to the half-width of the TO-band. An increase in $\Delta\omega_{TO}$, as is known, points to an increase in the variance of the valent-bond angle φ.

The quantities $\Delta\omega_{TO}$ and I_{TA}/I_{TO} were previously shown [5] to depend on the position of the Fermi level ε_F relative to the conduction-band edge ε_c, with these quantities being at their minimum in "native" *a*-Si:H for which $(\varepsilon_c - \varepsilon_F)_{T=0} \approx 0.85$ eV. For ε_F shifts in either direction from $E_g/2$, a simultaneous increase was observed for both $\Delta\omega_{TO}$ and I_{TA}/I_{TO}; i.e., the material became more disordered at both levels.

Based on data [5], we consider how $\Delta\omega_{TO}$ and I_{TA}/I_{TO} intercorrelate (Fig. 1). It can be seen that I_{TA}/I_{TO} varies more noticeably compared with $\Delta\omega_{TO}$ (by a factor of ≈3 and ≈1.4, respectively). Hence, it follows that the *a*-Si:H-structure ordering depends to a greater extent on its medium-range order. We consider the dependence of the density of defects (dangling bonds) N_D on an *a*-Si:H-structure characteristic at the medium-range-order level (Fig. 2). In this case, it is necessary to note the different origin and charge state of the defects.

First, these are the defects formed in the course of the growth of undoped films ("deposition-induced" or "native" defects). If ε_F is located at $E_g/2$, the defects are in the D^0 state. For ε_F shifts towards ε_c (conduction-band edge) or ε_v (valence-band edge), the defects in the D^- and D^+ states, respectively, begin to be dominant.

Second, there are the defects formed in the case of the long-term illumination of the film ("light-induced" defects), which are in the D^0 state.

Third, there are the defects formed during doping with boron ("doping-induced" defects); these are at the D+ state.

It follows from the data shown in Fig. 2 that I_{TA}/I_{TO} and N_D increase simultaneously when the defects are formed in the course of the film growth or doping. However, the rate of increase in I_{TA}/I_{TO} (i.e., an increase in disordering) depends on the charge state of the defects; D^+ leads to a greater disordering than D^-.

It should be noted that the interrelation between the I_{TA}/I_{TO} ratio and N_D is of an opposite character in the case of the light-induced defects. The concentration $N_D \geq 5 \times 10^{16}$ cm^{-3} is known to be the highest one for such defects when ε_F is shifted to $E_g/2$. Thus, as follows from Fig. 2, long-term intense illumination, during which the defects in the D^0 state are formed, leads to ordering of the *a*-Si:H structure at the medium-range-order level. Apparently, it is such an ordering of the *a*-Si:H structure that causes a decrease in its entropy after the illumination [6] in spite of a relatively weak increase in the disordering at the short-range-order level [5].

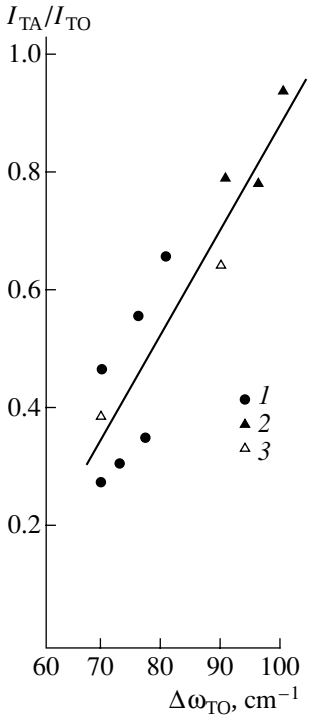

Fig. 1. Relation between characteristics of the short-range order and medium-range order. (*1*) Undoped *a*-Si:H; (*2*) *a*-Si:H doped with boron from gaseous phase; (*3*) *a*-Si:H doped with boron by ion implantation.

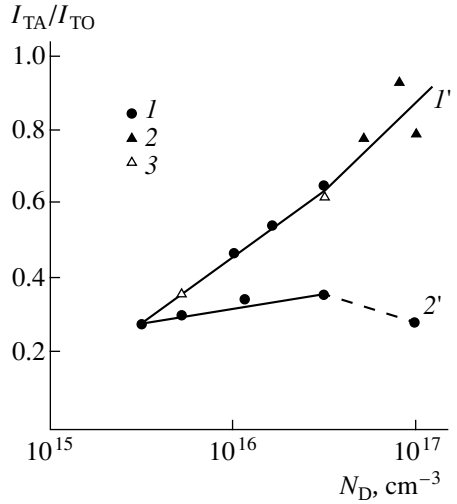

Fig. 2. Medium-range-order characteristic I_{TA}/I_{TO} as a function of the defect density N_D. Designations are the same as in Fig. 1. The charge states of D^0 defects for N_{Dmin}: predominantly D^+ (curve *1*'), predominantly D^- (curve *2*'), the dashed line shows the transition to the D^0 state after a long-term intense illumination.

Returning to the data shown in Fig. 2, we note a more abrupt increase in I_{TA}/I_{TO} with heavier doping

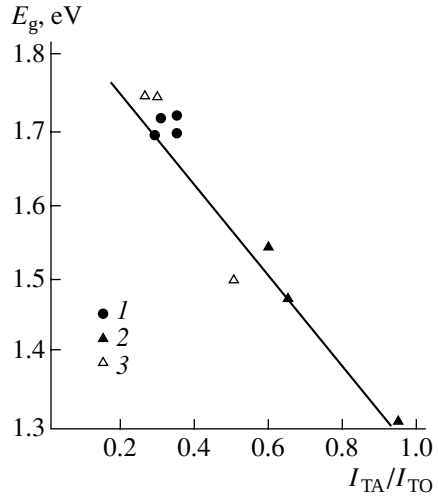

Fig. 3. Optical band gap E_g as a function of the medium-range-order characteristic I_{TA}/I_{TO}. The designations are the same as in Fig. 1.

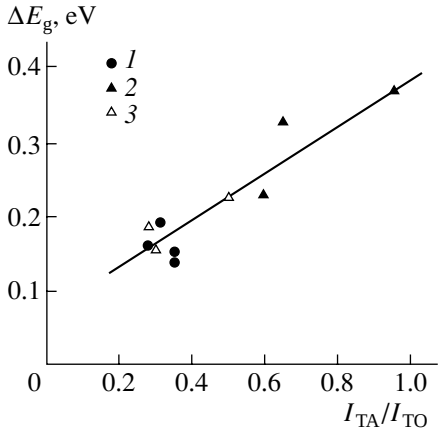

Fig. 4. Magnitude of fluctuations of the band gap ΔE_g as a function of the medium-range-order characteristic I_{TA}/I_{TO}. The designations are the same as in Fig. 1.

with boron (when $N_D \geq 5 \times 10^{16}$ cm^{-3}). This fact could imply that boron atoms replacing silicon atoms in tetrahedra introduce an additional disorder in the *a*-Si:H structure. One more cause of the structure disordering should not be excluded. This is the relatively low electrical activity of boron in *a*-Si:H [7]. A significant fraction of boron atoms do not enter into the silicon tetrahedra and, possibly, form clusters (the B_{12} icosahedra, more likely). In fact, the tendency of boron atoms to form icosahedral structure units is well known [8].

In concluding this section of the paper, we note once more the "sensitivity" of the medium-range order to the charge state of the defects and emphasize that the most ordered structure at this level is inherent in the films containing the neutral D^0 defects typical of "native" *a*-Si:H irrespective of whether it was produced directly in the course of deposition or as a result of ε_F shifts after long-term intense illumination and also in spite of a large distinction in N_D values for these two cases (Fig. 2).

Furthermore, it should be noted that no direct correlations between changes in the degree of ordering at the medium-range-order level and electron parameters of *a*-Si:H (such as the photoconductivity) were established.

In Fig. 3, we show the relation between the band gap E_g determined from the Tauc formula and the value of the I_{TA}/I_{TO} ratio. We can conclude from these data that E_g depends mainly on disordering in the *a*-Si:H structure at the medium-range-order level. In fact, as follows from Fig. 1, the short-range order contributes to structure disordering much less than the medium-range order. Second, although the content of hydrogen in the samples under investigation varies (2–8 at. %), these variations are apparently of little importance: according to [3], when C_H increases by 1 at. %, an increase in E_g amounts to only $(1.0–1.5) \times 10^{-2}$ eV.

Further, we consider the coefficient of interband absorption in *a*-Si:H. The spectral dependence of α is often analyzed using the quadratic approximation (the Tauc formula)

$$(\alpha\hbar\omega)^{1/2} = \beta(\hbar\omega - E_g), \quad (1)$$

where $\beta = 700 \pm 30$ (cm eV)$^{-1/2}$ when E_g varies from 1.32 to 1.76 eV. We denote E_g in this approximation as E_{g2}.

However, the spectral dependence of α can be approximated also as

$$(\alpha\hbar\omega)^{1/3} = \gamma(\hbar\omega - E_g). \quad (2)$$

We denote E_g in formula (2) as E_{g3}. This value varies from 0.95 to 1.6 eV, respectively, and the γ value ranges from 50 to 80 (cm eV)$^{-1/3}$.

In study [9], it was shown that formula (2) can be derived if one assumes that the band gap fluctuates spatially as a result of structural disordering. In this case, we use (1) and (2) to obtain $E_{g2} = E_{gmax}$ and $E_{g3} = E_{gmin}$, and their difference is considered as a measure of the fluctuation of the band gap (ΔE_g).

It follows from Fig. 4 that there is a direct correlation between I_{TA}/I_{TO} and E_g. If we assume that ΔE_g is mainly caused by the valence-band-edge fluctuations, $\Delta E_g = 0.15$ eV for undoped *a*-Si:H; this is consistent with data [10] on the width of the tail that has slowly varying density of states and is closer in energy to the valence-band edge than the Urbach exponential tail. However, it seems to be more realistic to assign the value of ΔE_g to the approximately equal fluctuations of the edges of both bands. In this case, $\Delta E_g/2$ coincides satisfactory with the quantity $\delta = 0.05$ eV, considered as a measure of the fluctuations of electrostatic potential

in undoped *a*-Si:H [1]. The value of δ can be determined from the experimental data on conductivity (σ) and thermoelectric power (*S*) when the charge transport is realized over the conduction-band states. In this case,

$$\sigma \propto \exp(-\Delta E_\sigma/kT), \quad (3)$$

$$S \propto (\text{const} + \Delta E_S/kT). \quad (4)$$

Typically, $\Delta E_\sigma > \Delta E_S$; i.e.,

$$\Delta E_\sigma = (\varepsilon_c - \varepsilon_F)_{T=0} + \delta. \quad (5)$$

We now consider the results of investigations of *a*-Si:H modified at the medium-range-order level, i.e., containing Si nanoinclusions in its amorphous matrix.

The *a*-Si:H films with nanoinclusions were deposited at T_s = (300–380)°C by the rf-PECVD with an elevated pressure of silane and an increased discharge power compared to those used for depositing the conventional *a*-Si:H films. In addition, the films were deposited by the magnetron-assisted silane decomposition (MASD) method, the special feature of which is the possibility of a wide variation in the microstructure of these films [12]. At first, we concentrate our attention on the properties of such films referring to them as MASD films. In spite of high deposition temperatures, T_s = (300–380)°C, the MASD films have microstructure parameters R = 0.65–1.0. The quantity R, determined by the conventional method, indicates a contribution of dihydride complexes SiH_2 to the total number of silicon–hydrogen complexes (SiH_2 + SiH).

Previously [12], it was noted that such large values of R were not characteristic of the *a*-Si:H films deposited at such high temperatures T_s. In fact, it was afterwards shown [13] that these films contained nanocrystalline Si inclusions and could be divided into two groups.

According to the Raman spectroscopy data, the films of the first group have $R \approx 1$ and contain nanocrystals (with a size $d_{\text{Raman}} \lesssim 5$ nm and a crystalline-phase contribution $X_C \lesssim 20\%$).

In the Raman spectra of the films of the second group with R = 0.65–0.75, no bands typical of Si nanocrystals (at ω = 515–517 cm^{-1}) were identified. It is possible to judge the presence of nanocrystals in this group of films from the results of studying these films after the Si^+ ion implantation [13]. Actually, the films start to crystallize under very "soft" conditions of implantation (with an ion energy of 70 keV, $D = 10^{13}$ cm^{-2}, implantation at room temperature and subsequent annealing at 200°C for 1 h). This fact shows that, in the course of the growth of such films, silicon nanocrystals are formed in the amorphous matrix; however, their sizes and bulk fraction are so small that it is impossible to identify them by Raman spectroscopy. However, under subsequent exposure to external effects—in particular, Si^+ implantation—such nanocrystals serve as the crystallization nuclei.

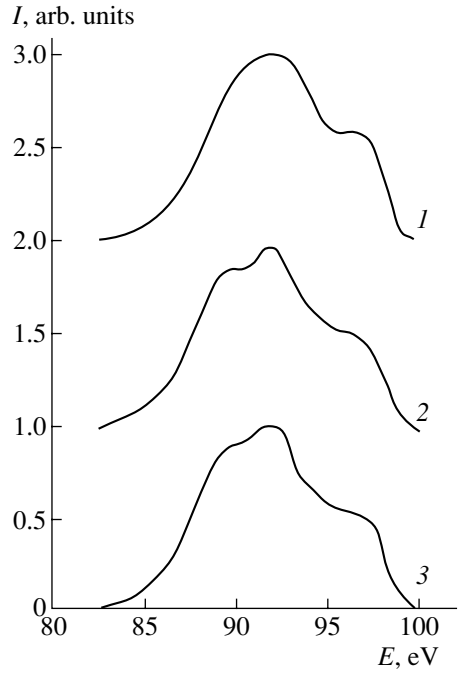

Fig. 5. Si L_{23} spectra for (*1*) conventional *a*-Si:H; (*2*) *a*-Si:H with Si nanocrystalline inclusions, and (*3*) *a*-Si:H with the $(SiH_2)_n$ inclusions.

Furthermore, the MASD can be used for obtaining *a*-Si:H films at T_s = 300°C with ordered inclusions of a different type: $(SiH_2)_n$ polymer chains.

Thus, the structure of *a*-Si:H MASD films is modified at the medium-range-order level in the case of forming both Si nanocrystals and polymer chains. We consider which material properties are the most "sensitive" to such modification.

At first, we will dwell on the results of investigations of ultrasoft L_{23} X-ray emission spectra of Si. As is known, their intensity reflects a partial density of all the occupied 3s states in Si, while the shape of spectra related to the interval of valence-band energies is sensitive to a change in the *a*-Si:H-structure ordering [14].

In Fig. 5, we show the ultrasoft X-ray emission spectra for a conventional *a*-Si:H with a broad principal peak at $E_v - E$ = 7–9 eV. The nanocrystalline silicon inclusions lead to a pronounced structure of this peak, which points to an increasing degree of ordering in the amorphous matrix of the film. It should be noted that almost the same result was obtained in the case of the formation of inclusions in the form of $(SiH_2)_n$ chains (Fig. 5).

Next, we focus on the results of investigating the conductivity σ and the photoconductivity σ_{ph} for the MASD-films, which we divided above into two groups.

The films assigned to the first group have temperature dependences of σ characteristic of a two-phase material. For these, two activation energies are

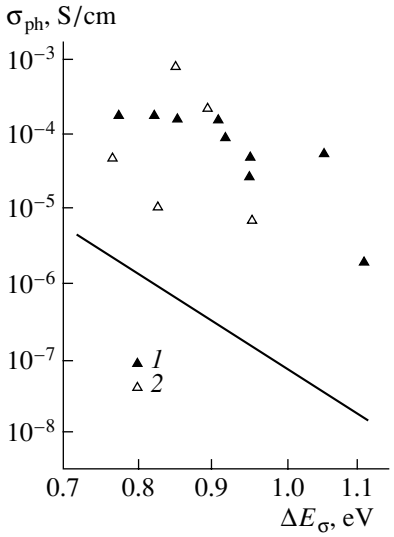

Fig. 6. Photoconductivity σ_{ph} as a function of the activation energy of the dark conductivity ΔE_σ; T = 300 K, $\hbar\omega$ = 2 eV, and the photocarrier-generation rate $G = 10^{19}$ cm^{-3} s^{-1}. The solid line is for conventional *a*-Si:H; (*1*) data of this study, and (*2*) data reported in [16].

observed for σ: $\Delta E_1 < \Delta E_2$ near room temperature and at higher temperatures, respectively. It is evident that the conductivity at higher temperatures is determined by the main amorphous phase, whereas the second phase with lower resistivity gives a certain contribution near room temperature. The photoconductivity of films from this group is much lower compared with σ_{ph} for *a*-Si:H.

The films of the second group are no different from *a*-Si:H in terms of their temperature dependences, but they have smaller values of σ_{ph}. The same conclusion can also be made from investigations of σ and σ_{ph} for the films containing the $(SiH_2)_n$ inclusions.

We now consider the results obtained for the PECVD *a*-Si:H films modified at the medium-range-order level.

According to the Raman spectroscopy data, some of these films contain the nanocrystals $d_{Raman} \approx 5$ nm, X_C = 10%. As to their properties, they are close to the MASD films and have a similar structure; specifically, they have a significantly lower photoconductivity σ_{ph} than conventional *a*-Si:H. However, the films with no bands at ω = 515–517 cm^{-1} in their Raman spectra have, on the contrary, a very high photoconductivity (Fig. 6). For these films, a correlation was established between the σ_{ph} quantity and the I_{TA}/I_{TO} ratio, which, according to [15], can be attributed to a modification of the *a*-Si:H structure at the medium-range-order level associated with the formation of silicon nanoclusters.

It should be noted that a number of other parameters of the film are close to those of conventional device-grade *a*-Si:H: E_g = 1.88 eV, ΔE_σ = 0.8–1.0 eV, $N_D \approx 10^{16}$ cm^{-3}, and C_H = 8–10 at. % (in the form of SiH).

We note also that σ_{ph} of the PECVD films, whose structure is modified at the medium-range-order level, is actually independent of the conditions of their deposition (Fig. 6). In fact, in this study they were deposited using undiluted silane at T_s = (300–380)°C, while, in study [16], they were deposited from silane, which was heavily diluted with hydrogen at T_s = 250°C. However, determining the reasons for such an abrupt increase in σ_{ph} of these films compared with that of conventional *a*-Si:H remains a subject for further investigations.

CONCLUSION

In summary, we list the principal results of the investigations carried out and the conclusions.

(i) A correlation is established between characteristics of the small-range and medium-range orders in the *a*-Si:H structure. Its ordering is shown to be determined to a greater extent by the medium-range order (by the ordering in arrangement of silicon tetrahedra).

(ii) An interrelation is determined between the degree of the medium-range order and the density of dangling bonds formed in the process of depositing the *a*-Si:H films, during their implantation with boron, and also as a result of long-term intense illumination of undoped films. The most ordered structure occurs in the films that contain neutral defects (D^0) irrespective of their origin and density. On the contrary, the formation of charged defects (especially, D^+) leads to a significant increase in the disorder of the structure.

(iii) The band gap and its fluctuations are shown to be determined mainly by a degree of ordering of the structure at the medium-range-order level. At the same time, no direct correlations between the degree of medium-range order and electron parameters are found.

(iv) On the contrary, the modification of the *a*-Si:H structures at the medium-range-order level, as a result of the formation of ordered nanocrystals in the amorphous matrix, is shown to lead to a change in electronic parameters. An example of this fact is the radical (at least hundred-fold) increase in the photoconductivity compared with that of conventional *a*-Si:H with the device quality.

However, as one might expect, changes in the electronic parameters depend on many factors: the nature of inclusions [Si nanocrystals, Si nanoclusters, and the chains of the $(Si:H_2)_n$ type], their dimensions, the volume fraction, the characteristics of distribution, and also their effect on the properties of the amorphous matrix. As an example of such an effect, we can cite the data on the ordering of the amorphous-matrix structure when the nanocrystalline silicon inclusions or the $(Si:H_2)_n$ chains mentioned in this study are formed.

Nevertheless, the modification of the structures of a tetrahedrally coordinated amorphous semiconductor at the medium-range-order level with the purpose of optimizing the optoelectronic properties of the material represents a rather complex and still unresolved problem.

REFERENCES

1. A. A. Aĭvazov, B. G. Budagyan, S. P. Vikhrov, and A. I. Popov, in *Unordered Semiconductors*, Ed. by A. A. Aĭvazov (Mosk. Énerg. Inst., Moscow, 1995), p. 67.
2. A. Madan and M. Shaw, *The Physics and Applications of Amorphous Semiconductors* (Academic, Boston, 1988; Mir, Moscow, 1991).
3. A. P. Sokolov, A. P. Shebanin, O. A. Sokolova, and M. M. Mezdrogina, J. Non-Cryst. Solids **137/139**, 99 (1991).
4. J. S. Lannin and M. Maley, Phys. Rev. B **36**, 1146 (1987).
5. O. A. Golikova and V. Kh. Kudoyarova, Fiz. Tekh. Poluprovodn. (St. Petersburg) **32**, 876 (1998) [Semiconductors **32**, 779 (1998)].
6. C. M. Formann, R. M. Dawson, H. Y. Lin, and C. R. Wronski, J. Appl. Phys. **76**, 768 (1994).
7. W. E. Spear and P. G. LeComber, in *The Physics of Hydrogenated Amorphous Silicon*, 1: *Structure, Preparation and Devices*, Ed. by J. D. Joannopoulos and G. Lucovsky (Springer-Verlag, Berlin, 1984), p. 63.
8. O. A. Golikova, Fiz. Tekh. Poluprovodn. (St. Petersburg) **34**, 369 (2000) [Semiconductors **34**, 363 (2000)].
9. V. N. Novikov, A. P. Sokolov, O. A. Golikova, *et al.*, Fiz. Tverd. Tela (Leningrad) **32**, 1515 (1990) [Sov. Phys. Solid State **32**, 884 (1990)].
10. M. Stutzman, Philos. Mag. B **60**, 531 (1989).
11. D. Ruff, H. Mell, L. Toft, *et al.*, in *Abstracts of the 17th International Conference on Amorphous Semiconductors, ICAMS17, Budapest, 1997*, Th-P 113/4.
12. O. A. Golikova, A. N. Kuznetsov, V. Kh. Kudoyarova, and M. M. Kazanin, Fiz. Tekh. Poluprovodn. (St. Petersburg) **31**, 816 (1997) [Semiconductors **31**, 691 (1997)].
13. O. A. Golikova, A. N. Kuznetsov, V. Kh. Kudoyarova, *et al.*, Fiz. Tekh. Poluprovodn. (St. Petersburg) **34**, 86 (2000) [Semiconductors **34**, 87 (2000)].
14. V. A. Terekhov, Author's Abstract of Doctoral Dissertation (Voronezhs. Gos. Univ., Voronezh, 1994).
15. O. A. Golikova and M. M. Kazanin, Fiz. Tekh. Poluprovodn. (St. Petersburg) **34**, 762 (2000) [Semiconductors **34**, 737 (2000)].
16. R. Butte, R. Meaudre, M. Meaudre, *et al.*, Philos. Mag. B **79**, 1079 (1999).

Translated by V. Bukhanov

Semiconductors, Vol. 35, No. 11, 2001, pp. 1320–1323. Translated from Fizika i Tekhnika Poluprovodnikov, Vol. 35, No. 11, 2001, pp. 1376–1379.

LOW-DIMENSIONAL SYSTEMS

Structural and Photonic Properties of Opal–GaN Nanocomposites

V. G. Golubev[1]*, D. A. Kurdyukov[1], A. V. Medvedev[1], A. B. Pevtsov[1], L. M. Sorokin[1], and J. L. Hutchison[2]

[1] *Ioffe Physicotechnical Institute, Russian Academy of Sciences, St. Petersburg, 194021 Russia*
* *e-mail: golubev@gvg.ioffe.rssi.ru*
[2] *Department of Materials, Oxford University, Oxford OXI 3PH, UK*
Submitted April 19, 2001; accepted for publication April 26, 2001

Abstract—Electron microscopic methods have been applied to demonstrate that gallium nitride synthesized in opal voids has perfect crystal structure. Studies of optical reflection spectra revealed that the obtained opal–⟨gallium nitride⟩ nanocomposites retain the photonic-crystal properties of the ordered host matrix at any (0–100%) degree of opal void filling with gallium nitride. © *2001 MAIK "Nauka/Interperiodica".*

Recently, it has been proposed [1] to use synthetic opals, widely employed as starting materials for creating photonic crystals [2, 3], as matrices for obtaining three-dimensional (3D) arrays of nanosize electronic devices. Recent results obtained for opal–Pt–Si nanocomposites indicate that 3D-ordered Schottky barriers can be formed on the inner surface of opal voids [4, 5]. The density of active nanoelements in such structures may be as high as 10^{14} cm^{-3}, which exceeds by approximately six orders of magnitude the values achieved by means of modern planar technology.

In this study, 3D-ordered synthetic opals were impregnated with GaN. The structural properties of GaN synthesized within interconnected opal voids were investigated by transmission electron microscopy (TEM). A study of optical reflection spectra confirmed that the obtained opal–GaN composites retain 3D-ordering. Use of opal matrices can, first, ensure a large specific surface area (on the order of 10 m^2/cm^3) of GaN-based light-emitting devices at a high density of elements. Second, the photonic-crystal properties of perfect opal–GaN composites, characterized by the presence of a photonic gap in the visible range, allow a substantial improvement and modification of the emitting properties of GaN-based nanodevices in this spectral region.

Synthetic opals were composed of monodisperse amorphous SiO_2 spheres forming a regular fcc lattice. Opal samples with spheres 235 or 250 nm in diameter were used in this study. The opals also contained an ordered sublattice of octahedral and tetrahedral voids accessible to filling with substances, with the volume of the sublattice constituting 26% of the total sample volume. Opal samples impregnated with precursor substances (Ga, Ga_2O_3) were annealed in an atmosphere of nitrogen hydrides at T = 1000–1100°C for 30–50 h [6, 7].

Electron-microscopic studies of the microstructure of opal–GaN nanocomposites were done using an FEG 3000 transmission electron microscope.

Figure 1a shows a section of a composite, in which its ordered "crystal" structure, close-packed in the (111) plane, is well seen. Nearly all voids and void-connecting channels (Figs. 1a–1d) are filled with a guest substance forming a cluster lattice. This conclusion is based on an analysis of the contrast between the SiO_2 sphere and the place that was an octahedral (tetrahedral) void prior to filling. The cluster is darker than the sphere. This means that the guest substance is enriched in an element heavier than Si. Figure 1b presents two regions [image plane coincides with the (100) plane] shifted by one half of the SiO_2 sphere diameter with respect to each other. As a result of such a shift, projections of filled octahedral and tetrahedral voids can be seen in the image. The figure shows truncated spheres with section planes not passing through the sphere diameter.

Electron microdiffraction patterns obtained from parts of clusters are point electron diffraction patterns characteristic of single-crystal objects. High-resolution images of these regions show a perfect single-crystal structure (Figs. 1e and 1f), with electron diffraction patterns obtained from neighboring clusters revealing one and the same crystallite orientation. This means that a single-crystal structure with one and the same azimuthal orientation is preserved within several micrometers. The substance in the channels connecting the clusters is also in the single-crystal state. Thus, the single-crystal structure extends continuously through a channel from one cluster into another, with the same orientation preserved. An analysis of point electron diffraction patterns identified the substance in clusters as hexagonal GaN with lattice constants a = 0.3095 and b = 0.500 nm, which is in rather good agreement with

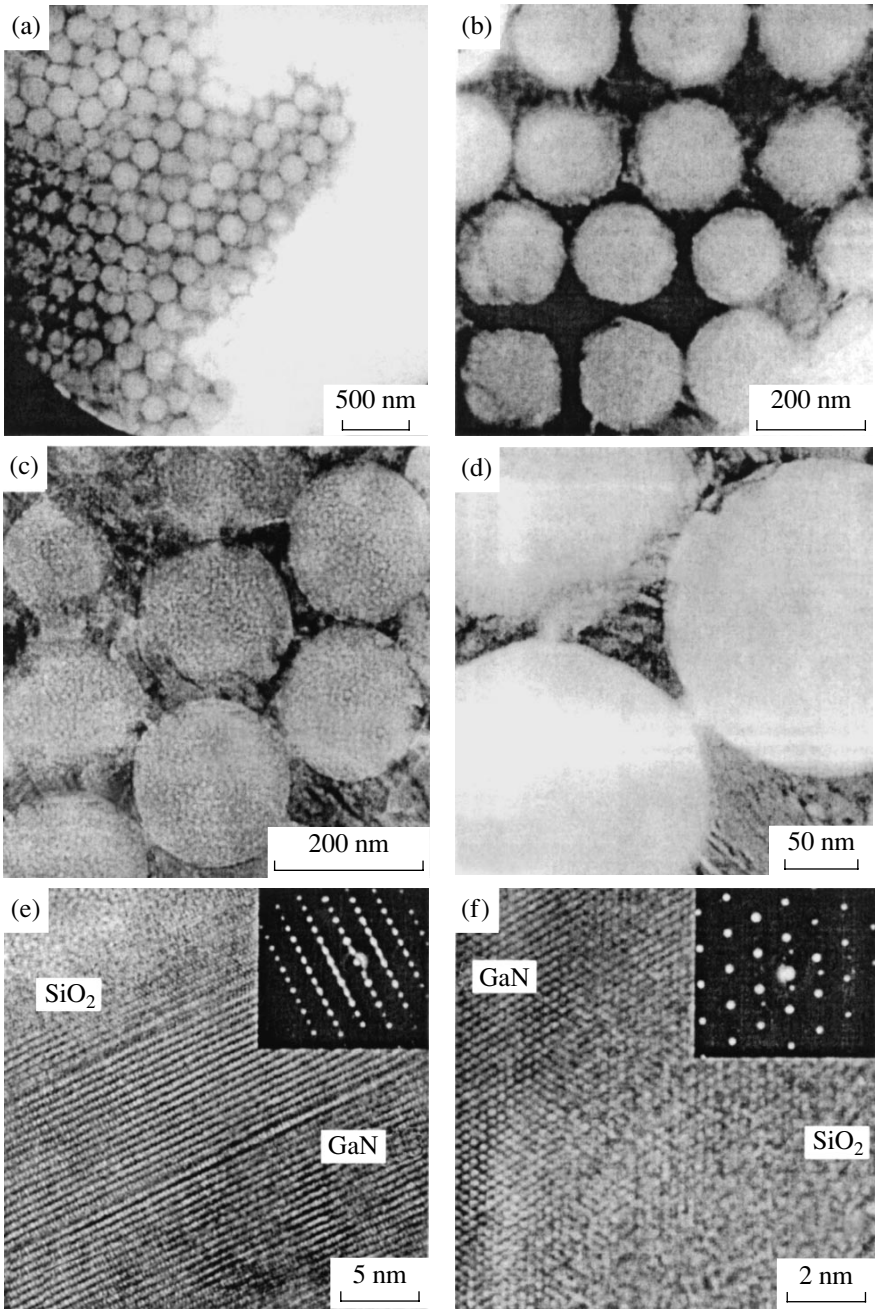

Fig. 1 TEM images of opal–GaN composite regions with complete void filling. Insets: electron microdiffraction patterns of fragments of GaN nanoclusters.

recent published data (a = 0.318 nm and b = 0.518 nm [8]) and the results of X-ray structural and Raman studies [6, 7].

Let us discuss in more detail the structure of GaN clusters. At medium magnifications, a striped pattern can be observed in cluster images. The electron diffraction patterns obtained from these regions exhibit a specific feature in the form of distinct streaks connecting reflections along directions perpendicular to the stripes in the cluster image. Such a structure of electron diffraction patterns is characteristic of 2D defects in an object, with the defect plane perpendicular to the plane of the image. A high-resolution image of such a region of a cluster is presented in Fig. 1e. The pertinent electron diffraction pattern (see the insert) corresponds to the $(10\bar{1}0)$ orientation of the image plane. In this image, interatomic distances d = 0.508 and 0.271 nm are resolved, which are interplanar spacings for, respectively, the crystallographic planes of the types (0001)

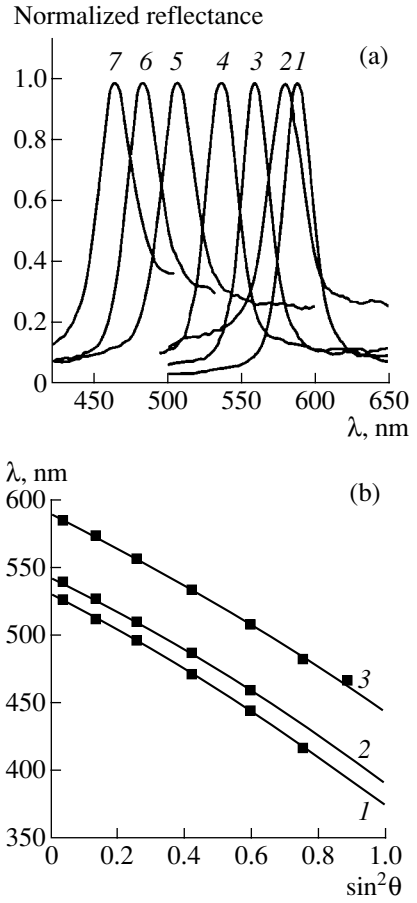

Fig. 2. (a) Normalized spectra of specular reflection of light from the (111) plane of opal–GaN–glycerol measured at different angles of incidence of light θ: (*1*) 10°, (*2*) 20°, (*3*) 30°, (*4*) 40°, (*5*) 50°, (*6*) 60°, and (*7*) 70°. (b) Experimental dependences of the reflectance peak position on the angle of incidence of light (points) and those calculated using the Bragg law (solid lines) for (*1*) opal–water, (*2*) opal–glycerol, and (*3*) opal–GaN–glycerol composites.

and $(01\bar{1}0)$ perpendicular to the image plane. Occasionally, (0002) planes are resolved in these images, with interplanar spacing equal to half the unit cell parameter *c*. The strictly periodic cluster structure in the image (Fig. 1e) is interrupted by wider stripes. One of these leads to a shift of atomic planes along this stripe by half the interatomic distance. The observed stripe is a 2D defect lying in the basal plane (0001) (stacking fault). Figure 1f shows part of a single-crystal cluster with $(01\bar{1}1)$ orientation. Here, crystallographic planes with interplanar spacings $d(10\bar{1}0) = 0.268$ nm and $d(0\bar{1}11) = 0.236$ nm are resolved.

The photonic-crystal properties of the synthesized nanocomposites with a varied extent of void filling are clearly manifested in optical reflection spectra. For example, spectra of specular reflection from the (111) plane of the opal–GaN composite with partially filled voids show a clearly pronounced reflectance peak whose position depends on the angle of incidence of light (Fig. 2a). The void volume remaining free in the given sample was filled with glycerol to suppress the strong scattering of light at the GaN–air interface. The observed peaks result from Bragg diffraction of electromagnetic waves on the periodic structure of the fcc lattice of the composite. The occurrence of clearly pronounced Bragg reflection peaks in a wide range of angles indicates a uniform distribution of the guest substance in the opal matrix voids and confirms the presence of a well-formed photonic-crystal structure in the composites under study.

An experimental dependence of the position of the Bragg reflection peak on the angle of incidence can be, to a first approximation, described by the expression

$$\lambda_m = 2d_{(111)}\sqrt{\langle\varepsilon\rangle - \sin^2\theta}, \qquad (1)$$

where $d_{(111)}$ is the interplanar spacing in the fcc lattice of a composite in the [111] direction, $\langle\varepsilon\rangle$ is the average dielectric constant of the composite, and θ is the angle of incidence of light. Expression (1) and relation $\langle\varepsilon\rangle = \sum\varepsilon_i f_i$, where ε_i and f_i are, respectively, the dielectric constant and the volume fraction of the *i*th component of the composite [9, 10], can be used to evaluate the size and dielectric constant of SiO_2 spheres and also the volume fractions and dielectric constants of the guest substances. For this purpose (to make the number of unknowns coincide with the number of equations), the angular dependence of the Bragg reflection peak was additionally measured for opals with voids completely filled with a substance with a known dielectric constant (water or glycerol), with identical plates of unimpregnated opal used as host matrices. The experimental dependences of the Bragg reflection peaks on the angle of incidence of light and their approximation by means of the least squares method in accordance with expression (1) are presented in Fig. 2b. Analysis of the data obtained for the sample, whose spectra are presented in Fig. 2a, gives an average SiO_2 sphere diameter of 233 ± 4 nm, which is in agreement with electron-microscopic data and an extent of opal void filling with gallium nitride equal to 27 ± 2%.

Thus, the developed technology enabled formation of an ordered 3D lattice of GaN nanoclusters in voids of a synthetic opal matrix. Electron-microscopic studies demonstrated that the single-crystal structure of one cluster extends through a void-connecting channel into another cluster, with the azimuthal orientation preserved. Optical studies revealed that the opal–GaN nanocomposites retain the photonic-crystal properties of the host opal matrix. It was found that the extent of GaN void filling can be varied over wide limits (0–100%), with the dielectric constant of the composite altered considerably. This allowed tuning the photonic gap in GaN-opal composites (at invariable sphere size) over virtually the entire visible spectral range.

ACKNOWLEDGMENTS

This study was supported by the Programs "Nanostructures" (project no. 97-2016) and INCO-Copernicus ("TIMOC" grant no. IC15 ST98 0819), and by the Royal Society of London.

REFERENCES

1. V. N. Bogomolov and T. M. Pavlova, Fiz. Tekh. Poluprovodn. (St. Petersburg) **29**, 826 (1995) [Semiconductors **29**, 428 (1995)].
2. V. N. Astratov, V. N. Bogomolov, A. A. Kaplyanskiĭ, *et al.*, Nuovo Cimento D **17**, 1349 (1995).
3. *Photonic Band Gap Materials*, Ed. by C. M. Soukoulis (Kluwer, Dordrecht, 1996), NATO ASI Ser., Ser. E **315**.
4. V. N. Bogomolov, N. A. Feoktistov, V. G. Golubev, *et al.*, J. Non-Cryst. Solids **266-269**, 1021 (2000).
5. C. Diaz-Guerra, J. Piqueras, V. G. Golubev, *et al.*, Appl. Phys. Lett. **77**, 3194 (2000).
6. V. Yu. Davydov, V. G. Golubev, N. F. Kartenko, *et al.*, Nanotechnology **11**, 291 (2000).
7. V. Yu. Davydov, R. E. Dunin-Borkovski, V. G. Golubev, *et al.*, Semicond. Sci. Technol. **16**, L5 (2001).
8. T. Kachi, K. Tomita, K. Itoh, and H. Tadano, Appl. Phys. Lett. **72**, 704 (1998).
9. H. Míguez, A. Blanco, F. Mesequer, *et al.*, Phys. Rev. B **59**, 1563 (1999).
10. V. G. Golubev, V. A. Kosobukin, D. A. Kurdyukov, *et al.*, Fiz. Tekh. Poluprovodn. (St. Petersburg) **35**, 710 (2001) [Semiconductors **35**, 680 (2001)].

Translated by M. Tagirdzhanov

Semiconductors, Vol. 35, No. 11, 2001, pp. 1324–1328. Translated from Fizika i Tekhnika Poluprovodnikov, Vol. 35, No. 11, 2001, pp. 1380–1384.

PHYSICS OF SEMICONDUCTOR DEVICES

MOCVD-Grown Broad Area InGaAs/GaAs/InGaP Laser Diodes

D. A. Vinokurov, V. A. Kapitonov, D. N. Nikolaev, A. L. Stankevich, A. V. Lyutetskiĭ, N. A. Pikhtin, S. O. Slipchenko, Z. N. Sokolova, N. V. Fetisova, I. N. Arsent'ev, and I. S. Tarasov

Ioffe Physicotechnical Institute, Russian Academy of Sciences, Politekhnicheskaya ul. 26, St. Petersburg, 194021 Russia

Submitted March 12, 2001; accepted for publication April 2, 2001

Abstract—A MOCVD technology for growth of InGaAs/GaAs/InGaP laser heterostructures on a modified Epiquip VP-50-RP installation was developed. Mesa stripe laser diodes with threshold current density J_{th} = 100–200 A/cm^2, internal optical loss α_i = 1.3–1.7 cm^{-1}, and internal quantum efficiency η_i = 60–70% have been fabricated. A CW output optical power of 5 W has been obtained for a single 100-μm-wide aperture mesa stripe laser diode emitting at 1.03 μm. It is shown that use of AlGaAs waveguide layers, which increase the conduction band barrier offset, lowers the temperature sensitivity of laser heterostructures within the temperature range 10–80°C. © *2001 MAIK "Nauka/Interperiodica".*

1. INTRODUCTION

High-power semiconductor lasers have multiple applications. Pumping of erbium fiber amplifiers, solid-state crystals and frequency doublers, design of laser guns, and material processing technology make up an incomplete list of the applications of high-power semiconductor light emitters.

Major advances in the design of high-power semiconductor light emitters have been achieved for laser diodes based on GaAs/AlGaAs/InGaAs solid solutions emitting at a wavelength λ = 0.98 μm [1–4]. The use of phosphorus-containing InGaAsP and InGaP compounds in fabrication of separate-confinement laser heterostructures opens up new ways in selecting optimal aluminum-free compositions for waveguide layers and quantum-size active regions [5].

In this paper, we report the results of studying the MOCVD-grown InGaP/GaAs/InGaAs epilayers, photoluminescent structures, and laser diodes with a broad stripe contact.

2. EXPERIMENTAL SETUP

The structures were fabricated on a modified MOCVD Epiquip VP-50-RP installation with a horizontal reactor and HF heating of the substrate holder. The standard high-precision gas supply system was replaced by a system designed by SIGM$^+$ Co. The epitaxial deposition of layers and heterostructures was performed under a low reactor pressure of 100 mbar at growth temperatures T_g = 600, 700 and 750°C. Trimethylgallium (TMGa), trimethylindium (TMIn), 20% arsine (AsH_3) in hydrogen, and 30% phosphine (PH_3) in hydrogen were used as precursors. Hydrogen served as the carrier gas.

3. EXPERIMENTAL EPILAYERS AND HETEROSTRUCTURES

The electrical and luminescent properties of InGaP/GaAs/InGaAs laser structures with a strained InGaAs active region largely depend on the morphology and crystal perfection of the wide-band $In_xGa_{1-x}P$ layer. In our experiment, the lattice mismatch between the $In_xGa_{1-x}P$ emitter layer and the GaAs substrate did not exceed $\Delta a/a = \pm 2 \times 10^{-4}$. The position and half-width of the emitter photoluminescence (PL) line were $h\nu \approx 1.88$ eV ($\lambda \approx 0.66$ μm) and $\Delta h\nu \approx 40$ meV at room temperature. The structures were grown at T_g = 600, 700, and 750°C. The ratio x/x_v of the parameters x and x_v = [In]/{[In]+[Ga]} (here [In] and [Ga] are the molar contents of indium and gallium in the gas phase) characterizing, respectively, the compositions of the $In_xGa_{1-x}P$ solid solution and the gas phase was 0.73 at 600°C and slightly decreased with increasing growth temperature. Epilayers grown at T_g = 600°C contained multiple defects (Fig. 1a), which did not affect the photoluminescent and electrical properties of epilayers and heterostructures but did strongly enhance the internal optical losses in laser diodes. With the growth temperature raised to 700°C, the density of defects decreased, and no defects could be observed in layers grown at

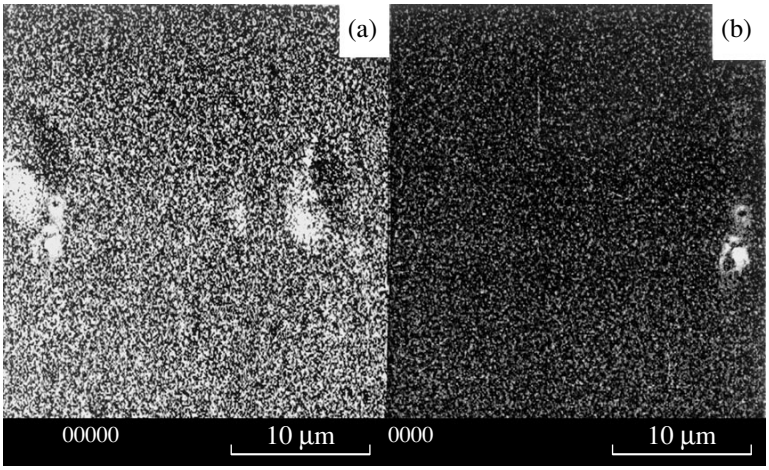

Fig. 1. Photomicrograph of the surface of $In_xGa_{1-x}P$ epilayers grown at (a) 600 and (b) 750°C.

T_g = 750°C (Fig. 1b). We attribute the defect formation to the low phosphorus content in the gas phase, resulting from the slow rate of PH_3 pyrolysis at low temperature of epitaxy (calculated ratio of the components V/III ≈ 200). Raising the growth temperature led to faster thermal decomposition of PH_3 and, correspondingly, to lower defect density.

Isotype and anisotype separate-confinement heterostructures were fabricated for the study. GaAs epilayers 0.20- to 0.25-μm-thick, served as waveguide layers. The active region of the laser heterostructure comprised a single strained $In_xGa_{1-x}As$ quantum well (QW), 70–160 Å thick, with x = 10–25%. The top wide-bandgap $In_xGa_{1-x}P$ emitter of the isotype structure was 0.3–0.5 μm thick. Figure 2 shows the band diagram of an anisotype separate-confinement heterostructure. Magnesium was used as the acceptor dopant, and silicon, as the donor. The estimated doping levels of the wide-bandgap emitters and the waveguide layers are shown in the diagram.

4. EXPERIMENTAL STUDY OF PHOTOLUMINESCENT STRUCTURES

Figure 3 presents experimental and calculated dependences of the peak energy ($h\nu_m$) of PL from a separate-confinement heterostructure on the In content in strained $In_xGa_{1-x}As$ QWs of thickness d_w = 90 and 115 Å. The internal quantum efficiency of PL was close to 100% over the entire range of compositions under study (x = 10–25%).

The energy of the PL peak increased with decreasing molar concentration of indium in the gas phase. The energies of quantum levels were calculated under the assumption of rectangular strained QWs in terms of the model [6], which relies upon the Luttinger–Kohn Hamiltonian. The deformation potential constants for the $In_xGa_{1-x}As$ solid solution were calculated by linear interpolation between the constants for GaAs and InAs [7]. Five sets of constants a^c, a^v, and b were considered (a^c, a^v are the hydrostatic potential constants for the conduction and valence bands; b is the shear potential constant). The best agreement with the experiment (Figs. 3 and 4) was obtained for the following values of the constants: GaAs: a^c = –7.17 eV, a^v = –1.16 eV, and b = –2.79 eV; InAs: a^c = –5.08 eV, a^v = –1 eV, and b = –2.33 eV.

Figure 4 shows experimental dependences of the PL peak energy on the $In_xGa_{1-x}As$ QW thickness for two solid solution compositions: x = 0.19 and x = 0.24. The lines show the energies of levels in a QW calculated as functions of its thickness for the same x (0.19 and 0.24) with due account for strain. In our opinion, the coincidence between the experimental and calculated depen-

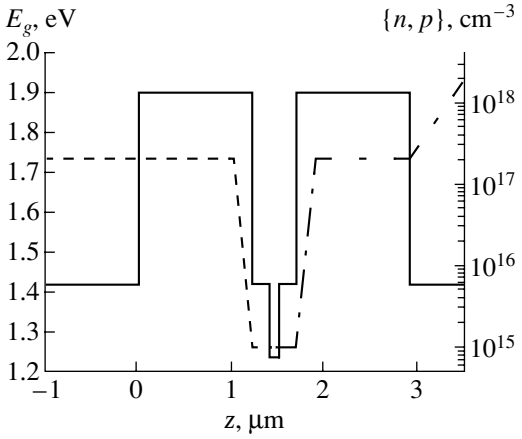

Fig. 2. Band diagram of InGaP/GaAs/InGaAs separate-confinement heterostructures (solid line). Calculated doping profiles for Si donor impurity (dashed line) and Mg acceptor impurity (dot-and-dash line). z is the coordinate in the growth direction.

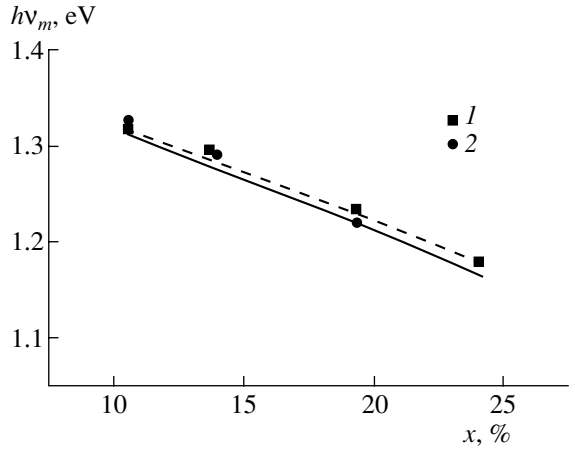

Fig. 3. Experimental dependences of the PL peak energies $h\nu_m$ (points) and calculated dependences of the energy level positions in a strained $In_xGa_{1-x}As$ QW on x (lines). Layer thickness: (*1*, dashed line) 90 and (*2*, solid line) 115 Å.

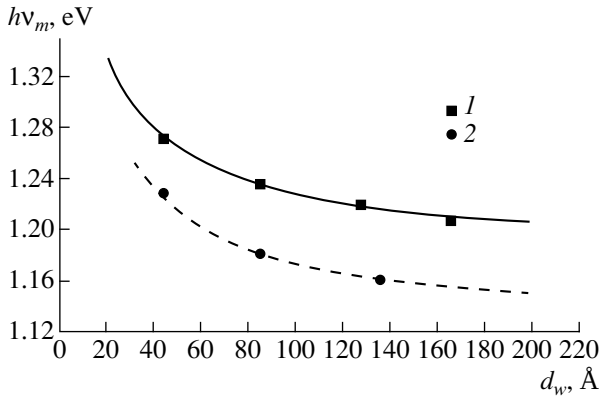

Fig. 4. Experimental dependences of the PL peak energies $h\nu_m$ (points) and calculated dependences of the energy level positions in a strained $In_xGa_{1-x}As$ QW on thickness for compositions with x = 0.19 (*1*, solid line) and x = 0.24 (*2*, dashed line).

dences supports the assumption that the $In_xGa_{1-x}As$ QW has an almost rectangular shape.

The existence of two experimental dependences allows us to control the positions of quantum levels in the potential well of the strained active region in a heterostructure by adjusting two parameters: the thickness of a $In_xGa_{1-x}As$ epilayer and its composition (x).

5. EXPERIMENTAL LASER DIODES

Laser diodes with a stripe width w = 100 μm and emitting at λ = 1.03 μm were fabricated by the conventional technology [3, 4] from InGaP/GaAs/InGaAs separate-confinement heterostructures. The diodes were mounted onto a copper heat sink with the stripe contact down. Reflecting and anti-reflection dielectric coatings were deposited onto the faces of the Fabry–Perot cavity [3, 4]. Light–current and current–voltage characteristics of the laser diodes were recorded in the range T = 10–80°C with the heat sink temperature kept constant. The table lists typical parameters of laser diodes fabricated from structures grown at different temperatures. In all the laser heterostructures, the threshold current densities were in the range J_{th} = 100–250 A/cm^2, depending on the diode length, and were independent of the epitaxial growth temperature. The internal optical losses were α_i = 1.3–4.3 cm^{-1}; these were higher in the lasers fabricated from heterostructures grown at T_g = 600°C. The lasers fabricated from these same structures demonstrated a lower threshold of optical degradation [8], compared with the diodes fabricated from structures grown at T_g = 700°C (see table). We attribute these effects to a decrease in the defect density in the InGaP layer on raising the epitaxial growth temperature to 700°C. The internal quantum efficiency was 60–70% for laser diodes fabricated from all the heterostructures, which is lower than that in the best published data [1–4]. The differential quantum efficiency did not exceed 65% in the lasers with a 1- to 2-mm-long cavity. As a result, the maximum CW emission power obtained from the laser with a 100-μm-wide stripe was 5 W.

Another factor lowering the maximum emission power of the laser diodes studied is the high temperature sensitivity of the threshold current density and differential quantum efficiency. The use of GaAs waveguide layers simplifies the technology, eliminating sophisticated switching of gas flows during epitaxy. However, this restricts the depth of the QW for electrons and holes. Even using InGaAs as the active zone of a strained epilayer with emission wavelength λ = 1.03 μm raises this value only slightly to ~75 meV. Figure 5 shows the temperature dependences of the threshold current density for the laser diodes studied (curves *1–3*). The temperature sensitivity of the threshold current density J_{th} is commonly characterized by the parameter T_0 appearing in the empirical relation $J_{th} = J_0\exp(T/T_0)$. However, the experimental $J_{th}(T)$ plot is strongly nonlinear on a semilogarithmic scale even in the range T = 10–80°C, although it can be approximated with a straight line to find T_0. The temperature sensitivity of the threshold current density depends on the diode length, becoming stronger with decreasing cavity length. This occurs because the free carrier density in the active region of the diodes is higher at shorter cavity lengths [9].

Figure 6 presents the threshold current density and the characteristic parameter T_0 in relation to the cavity length for a heat sink temperature of 20°C. A good correlation between the threshold current density and T_0 is seen. This led us to conclude that an additional mechanism raising the threshold current density comes into play in short laser diodes at higher temperatures. This mechanism is possibly associated with the emission of electrons from the active zone into waveguide layers.

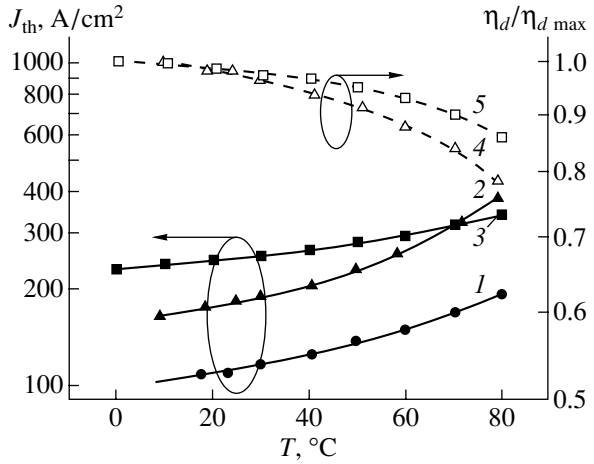

Fig. 5. (*1–3*) Threshold current density J_{th} and (*4*, *5*) normalized differential quantum efficiency $\eta_d/\eta_{d\max}$ vs. temperature T for laser diodes with different cavity lengths L and band gaps of waveguide layers, E_{gw}. (*1*, *4*) L = 1600 μm, E_{gw} = 1.42 eV; (*2*) L = 600 μm, E_{gw} = 1.42 eV; and (*3*, *5*) L = 1300 μm, E_{gw} = 1.7 eV.

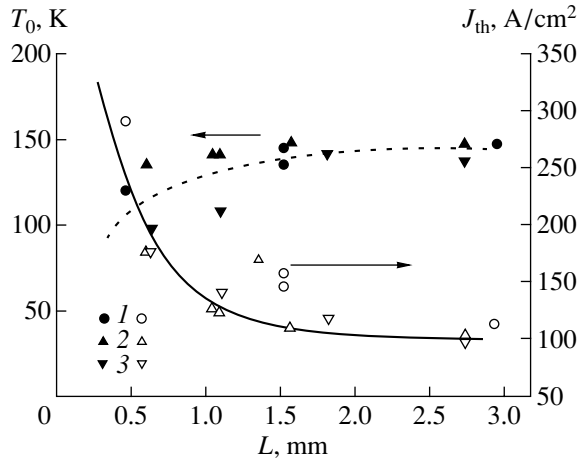

Fig. 6. Characteristic temperature T_0 and threshold current density J_{th} at T = 20°C vs. cavity length L for laser diodes fabricated from structures (*1*) X-2570, (*2*) X-2578, and (*3*) X-2582.

However, more significant is the decrease in the differential quantum efficiency with increasing temperature (Fig. 5, curve *4*). As shown in our previous study [10], the active region of a laser diode operating in the CW mode is overheated by 40–60°C relative to the copper heat sink. The increase in the threshold current has only a minor effect on the maximum optical power, whereas decreasing differential quantum efficiency may quench the lasing [10].

We also studied laser diodes fabricated from separate-confinement GaAs/AlGaAs/InGaAs heterostructures. The potential well for electrons in these structures is as deep as ~200 meV owing to a wider bandgap of the AlGaAs waveguide layer, E_{gw} = 1.6–1.7 eV. For diodes with a 200-meV potential well for electrons, the semilogarithmic plot of the threshold current density against temperature was essentially linear in the temperature range 10–80°C (Fig. 5, curve *3*). The characteristic parameter T_0 increased to 200–230°C, and the temperature sensitivity of the differential quantum efficiency (Fig. 5, curve *5*) simultaneously decreased.

The temperature dependences of the threshold current density and differential quantum efficiency are very important for designing high-power semiconductor lasers in view of the fact that the active region warms up by several tens of degrees on passing a continuous working current through it [10]. Therefore, suppressing the temperature sensitivity of heterostructures used in high-power semiconductor lasers is an urgent task, which can be accomplished by increasing the depth of the potential well for charge carriers.

6. CONCLUSION

The results obtained in this study are as follows.

MOCVD epitaxial technology for fabrication using a modified Epiquip VP-50-RP installation of laser heterostructures based on InGaP/GaAs/InGaAs solid solutions has been developed.

Mesa stripe laser diodes have been fabricated, and their light–current and current–voltage characteristics have been studied in the temperature range 10–80°C. Threshold current densities $J_{th} \approx 100$ A/cm^2, internal

Parameters of laser diodes

Structure no. (growth temperature)	Threshold current density (J_{th}, A/cm^2) (L = 1.5–2 mm)	Differential quantum efficiency (h_d, %) (L = 1.5–2 mm)	Internal quantum efficiency (h_i, %)	Internal optical loss (α_i, cm^{-1})
X-2570 (600°C)	110	53	65–70	3.2–4.3
X-2578 (700°C)	120	56	60–65	1.4–1.7
X-2582 (700°C)	130	53	60–65	1.3–1.8
X-2611 (700°C)	140	65	65–70	1.3–1.7

Note: L is the cavity length.

optical loss α_i = 1.3–1.7 cm^{-1}, and internal quantum efficiency η_i = 60–70% were obtained.

A CW optical power of 5 W at λ = 1.03 μm has been obtained from a laser diode with a 100-μm aperture.

The use of AlGaAs waveguide layers increases the depth of the electronic potential well to > 200 meV, thus suppressing the temperature sensitivity of laser heterostructures.

ACKNOWLEDGMENTS

We are grateful to I.D. Zalevskiĭ and A.A. Marmalyuk for providing us with the GaAs/AlGaAs/InGaAs laser heterostructures for the temperature studies; to T.N. Drokina, E.I. Kukhareva, T.A. Nalet, and E.A. Tret'yakova for assistance in the fabrication of laser diodes; and to D.A. Livshits for fruitful participation in discussions.

REFERENCES

1. A. Al-Muhanna, L. J. Mawst, D. Botez, *et al.*, Appl. Phys. Lett. **62**, 2402 (1993).
2. X. He, S. Srinivasan, S. Wilson, *et al.*, Electron. Lett. **34**, 2126 (1998).
3. D. A. Livshits, I. V. Kochnev, V. M. Lantratov, *et al.*, Electron. Lett. **36**, 1848 (2000).
4. D. A. Livshits, A. Yu. Egorov, I. V. Kochnev, *et al.*, Fiz. Tekh. Poluprovodn. (St. Petersburg) **35** (3), 380 (2001) [Semiconductors **35**, 365 (2001)].
5. J. K. Wade, L. J. Mawst, D. Botez, and J. A. Morris, Electron. Lett. **34**, 1100 (1998).
6. S. L. Chuang, Phys. Rev. B **43**, 9649 (1991).
7. S. Adachi, *Physical Properties of 3–5 Semiconductor Compounds* (Wiley, New York, 1992).
8. K. H. Park, J. K. Lee, D. H. Jang, *et al.*, Appl. Phys. Lett. **73**, 2567 (1998).
9. V. P. Evtikhiev, D. Z. Garbuzov, Z. N. Sokolova, *et al.*, Fiz. Tekh. Poluprovodn. (Leningrad) **19** (8), 1420 (1985) [Sov. Phys. Semicond. **19**, 873 (1985)].
10. E. G. Golikova, V. A. Kureshov, A. Yu. Leshko, *et al.*, Fiz. Tekh. Poluprovodn. (St. Petersburg) **34** (7), 886 (2000) [Semiconductors **34**, 853 (2000)].

Translated by D. Mashovets

Semiconductors, Vol. 35, No. 11, 2001, pp. 1329–1334. Translated from Fizika i Tekhnika Poluprovodnikov, Vol. 35, No. 11, 2001, pp. 1385–1390.

PHYSICS OF SEMICONDUCTOR DEVICES

Photoluminescence Properties of Polycrystalline ZnO/CdS/$CuInGaSe_2$ Solar Cells at a Low Temperature

G. A. Medvedkin[1,2], E. I. Terukov[1], K. Sato[2], Yu. Hasegava[2], and K. Hirose[2]

[1] *Ioffe Physicotechnical Institute, Russian Academy of Sciences, Politekhnicheskaya ul. 26, St. Petersburg, 194021 Russia*

[2] *Faculty of Technology, Tokyo University of A & T, 2-24-16 Nakacho, Koganei, Tokyo 184-8588, Japan*

Submitted March 26, 2001; accepted for publication April 2, 2001

Abstract—Emission properties of highly efficient polycrystalline solar cells based on ZnO/CdS/$CuInGaSe_2$ thin films were studied at $T = 20$ K. The edge photoluminescence band was observed for the reference device at a photon energy of 1.191 eV. This band vanishes after treating the unincapsulated device in a humid atmosphere (relative humidity of 85%) at an elevated temperature (85°C). Long-wavelength bands at 1.13 and 1.07 eV, which are associated with optical transitions via defect levels in the absorber film, preserve the intensity and spectral position. A decrease in the conversion efficiency of the solar cell after treatment is caused by the degradation of upper wide-gap films and a CdS–$CuInGaSe_2$ heterointerface. © *2001 MAIK "Nauka/Interperiodica".*

1. INTRODUCTION

Polycrystalline solar cells based on compound materials become more and more close to industrial fabrication, and pilot lines are already being put into operation in several countries [1]. The chalcopyrite semiconductor $CuInGaSe_2$ (CIGS) is accepted as one of the main solar-cell materials for terrestrial power engineering in this line. Recently, it was reported as having about 18.8% efficiency for small solar cells [2, 3] and higher than 10% efficiency for modules with verified stability [4, 5]. The purpose of fabricating cells with improved efficiency (higher than 14%) for minimodule cells from CIGS requires special attention to the stability. The reason is that the efficiency can drastically decrease (by as much as 30%) under the effect of moisture and elevated temperatures. We previously investigated the microdefect structure of the surface for similar device structures based on CIS ($CuInSe_2$) and CIGS films using laser scanning, and we established the relation of recombination processes with the surface structure [6–8]. In this study, we investigated the low-temperature photoluminescence (PL) of high-efficiency polycrystalline solar cells based on ZnO/CdS/CIGS thin films, which were not incapsulated and designed for CIGS minimodule cells.

2. EXPERIMENTAL

The CIGS-based photovoltaic devices were fabricated and tested at the Angström Solar Center, Uppsala University. In general, the structure of the reference solar cell comprised a multilayer sandwich made of thin polycrystalline ZnO:Al/ZnO/CdS/CIGS/Mo films. Fabrication was carried out on the basis of a continuous-production system using sodium-lime glass substrates. The polycrystalline layer of a CIGS absorber (2 μm thick) was deposited by the coevaporation technique using mass-spectrometry monitoring [5]. The barrier CdS layer was 0.05 μm thick, and the two-layer ZnO window was 0.55 μm thick. The three-layer Ni/Al/Ni grid current sink was chosen as the most corrosion-resistant one. Testing of the reference devices in a hot and humid atmosphere was carried out according to the international recommendations for IEC 1215 (1000 h, 85°C, and relative humidity of 85%).

The PL properties of CIGS solar cells were investigated using a JASCO CT-50C monochromator, quartz optics, and a Hamamatsu R1477 photomultiplier or cooled *p–i–n* Ge photodiode (North Coast EO-817L). The optical excitation was carried out using a YAG-SGH diode-pumped laser (532 nm, 65 mW) (Lazer-kompakt, Moscow), or a He-Cd gas laser (325 nm, 100 mW) (Kimmon Electric). A constant sample temperature of 20 K in a cryostat was maintained using a He refrigerator of the Cryo-Mini type. All spectra were corrected for the transmission of an optical channel and the sensitivity of photodetectors.

The estimation of the optical absorption depth in the multilayer ZnO/CdS/OVC/CIGS semiconductor struc-

1063-7826/01/3511-1329$21.00

Table 1. Electrical parameters of thin-film ZnO/CdS/CIGS solar cells at room temperature using an imitator of solar radiation

Sample	Area, cm^2	V_{oc}, mV	J_{sc}, mA/cm^2	*FF*, %	Efficiency, %
Calibrated cell	0.6	592	32.2	77.8	14.8
515C reference	0.5	668	28.8	75.0	14.1
513B tested cell	0.5	543	28.2	63.3	9.9

Note: Total illumination-power density is 1000 mW/cm^2 under the AM1.5 condition.

Table 2. Parameters of homogeneously broadened Gaussian bands obtained by decomposition of PL spectra

Band	Center, eV	FWHM, meV	Height, arb. units	Area, arb. units
Power 10 mW				
1	1.076	48.3	0.253	0.016
2	1.138	51.8	0.726	0.050
3	1.173	38.9	0.226	0.012
4	0.938	375.6	0.033	0.017
5	1.333	315.5	0.065	0.027
Power 65 mW				
1	1.075	50.0	0.278	0.019
2	1.131	42.2	0.715	0.040
3	1.173	46.7	0.266	0.016
4	0.957	685.9	0.040	0.031
5	1.467	522.1	0.037	0.038

Note: Excitation wavelength $\lambda = 532$ nm.

ture (OVC is the compound with ordered vacancies) yields the following result. For a green laser beam, the absorption occurs mainly in narrow-gap OVC/CIGS components ($1/\alpha \approx 100$ nm, α is the absorption coefficient), whereas for the ultraviolet laser beam, the absorption occurs mainly in the wide-gap ZnO:Al/ZnO structure. For this reason, we were able to probe the multilayer structures to various depths.

3. DEVICE CHARACTERISTICS

Let us describe briefly the load characteristics of solar cells measured at Uppsala University. The current–voltage ($J(V)$) characteristics of the standard reference device (curve *1*) and the device treated under the moisture–heat conditions (curve *2*) are shown in Fig. 2. The electrical parameters of the cells are given in Table 1. They are compared with the best quantity-produced minimodule cell with an efficiency of 14.8%.[1] The general deterioration of output parameters is observed as a result of treatment under the "moisture–heat" conditions. The photocurrent (J_{sc}) decreases by 0.6 mA/cm^2, whereas the open-circuit voltage (V_{oc}) and the filling factor (*FF*) decrease to a much greater extent, by 125 mV and 11.7%, respectively. For this reason, it is assumed that a decrease in the efficiency from 14.1 to 9.9% happens mainly due to the deterioration of the barrier properties of window layers. The energy-band diagram, which adequately describes the influence of moisture and heat, was suggested in [10, 11]. This diagram implies that the electrical conductivity of ZnO layers and an absorber decreases as a result of the moisture–heat effect. Inversion bending of the bands at the interface also decreases, whereas the barrier height for photogenerated electrons leaving the absorber increases. This consideration is consistent with the present and previous measurements of these solar cells [9, 12].

4. PHOTOLUMINESCENCE. MAIN PEAKS

It was experimentally found that the intensity of integrated PL decreases due to the treatment of the solar cells in a humid atmosphere by a factor ~1.5. This decrease approximately corresponds to a decrease in the device efficiency after treatment.

Two PL spectra, $I(\hbar\omega)$, which were measured in similar conditions for the reference and treated ZnO/CdS/CIGS solar cells, are shown in Fig. 2. The most intense short-wavelength peak at the photon energy $\hbar\omega = 1.191$ eV manifests itself in devices with a conversion efficiency >14%. After the device was kept in a hot humid atmosphere, this PL band vanished. According to measurements of spectral efficiency, the characteristic energy of 1.192 eV for the onset of photogeneration in reference devices corresponds to the band gap of the absorber film. This energy matches the peak of the PL spectrum with good accuracy. For this reason, this peak can be attributed to the band-to-band radiative transitions in the ternary $CuInGaSe_2$ semiconductor. Since the optical absorption coefficient of a ternary semiconductor for the high-energy region close to the band gap E_g is very large (~10^5 cm^{-1}), the absorption depth is about ~0.1 μm. Consequently, PL is emitted from the region adjacent to the CdS/CIGS heterointerface. Thus, it is possible to conclude that moisture and heat affects the optical properties of both the heterointerface and the region adjacent to the heterointerface in OVC.

In contrast with the band-to-band emission band, the effect of heating in a humid atmosphere causes no noticeable variations in other PL bands, specifically, at energies $\hbar\omega = 1.129$ and 1.07 eV. The spectral position and intensity of these bands actually undergo no varia-

[1] Recently, a Swedish team reported an unprecedently high efficiency of 16.6% for CIGS-based minimodules [9].

tions (Fig. 2). Corresponding recombination-related optical transitions are associated with the defect levels in CIGS (E_g = 1.2 eV) with the energy deficit relative to E_g Δ_1 = 60 meV and Δ_2 = 120 meV. Similar transitions were also observed in the PL spectra of single crystals of $CuInSe_2$ (E_g = 1.04 eV) and $CuGaSe_2$ (E_g = 1.7 eV) with close energy deficits Δ_1 and Δ_2. For stoichiometric $CuInSe_2$ crystals, the radiative transition from the donor V_{Se} to the valence band yields the energy of the donor level E_D = 57 meV, which is close to Δ_1. For nonstoichiometric crystals, a certain acceptor level with the activation energy equal to Δ_2 yields a weak PL band. For $CuGaSe_2$, it was found that the level with the energy Δ_1 is related to the charged vacancy V_{Se}^{+}, whereas the level with the energy Δ_2 is stable relative to thermal treatment of the crystal in various media [14]. Thus, the analogy between the PL properties of CIGS, $CuInSe_2$, and $CuGaSe_2$ is traced. The PL band at $\hbar\omega$ = 1.13 eV can be consistently attributed to the optical transition from V_{Se}^{+} to the valence band in the absorber film. The energy of stable PL bands at 1.13 and 1.07 eV in Fig. 2 corresponds to optical transitions below the CIGS absorption edge, i.e., the emission emerges from the absorber film bulk, specifically, from the depth $d \gtrsim 0.1$ μm. For this reason, we may assume that the moisture–heat treatment does not affect the bulk properties of the CIGS film (we consider the crystallites rather than the interfaces[2]), or this effect on CIGS films is considerably weaker compared to ZnO and CdS films.

The examination of PL spectra in relation to the laser radiation power (W = 5–65 mW) demonstrated the absence of the spectral shift of all three bands for the reference device. This indicates that the band-to-band and band-to-level transitions are responsible for the main emission of the reference device. The PL spectra for solar cells after testing in moisture–heat conditions are shown in Fig. 3 in relation to the laser radiation power. With increasing excitation power, the spectra are transformed, which demonstrates that the transfer of the emitted energy occurs between two high-energy PL bands. The apparent spectral shift is actually absent, as was proved by the decomposition of the complex spectrum (Fig. 3) into three elementary Gaussian lines. The parameters of spectral decomposition, specifically, the position of the band center, the full width at half-maximum (FWHM), the amplitude, and the area under the peak for two spectra (W = 10 and 65 mW) are given in Table 2. For low excitation levels W = 5–10 mW, the short-wavelength component at $\hbar\omega$ = 1.17 eV makes a major contribution. In contrast with this, for W = 20–65 mW, the main band at 1.13 eV becomes relatively more intense (cf. the heights and areas of spectral bands 2 and 3 in Table 2). It is clear that the recombination channel with the optical transition energy $\hbar\omega$ = 1.17 eV is saturated at a higher intensity of excitation. In this case, the generated charge carriers recombine via an alternative channel with the lower energy (energy deficit $\Delta \approx 40$ meV).

The onset of an increase in the PL emission, which is seen to shift with the excitation level, is indicated in Fig. 3 by arrows. For high-power laser radiation, the PL spectrum is broadened to higher energies by 15 meV, which could indicate the emergence of an additional channel of radiative recombination via the defect levels in the OVC interface layer.

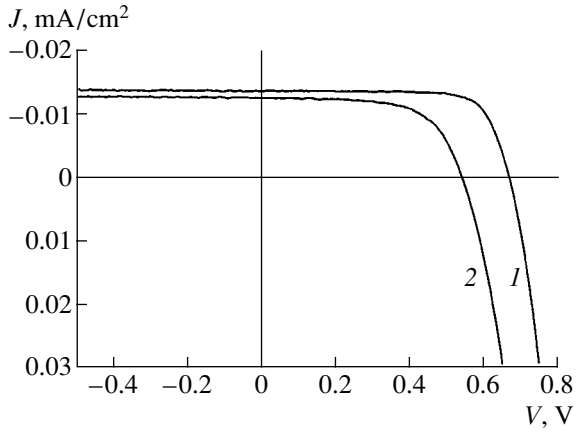

Fig. 1. Load characteristic of solar cells (*1*) prior to and (*2*) after treatment in a humid atmosphere at an elevated temperature. The measurement temperature T = 25°C.

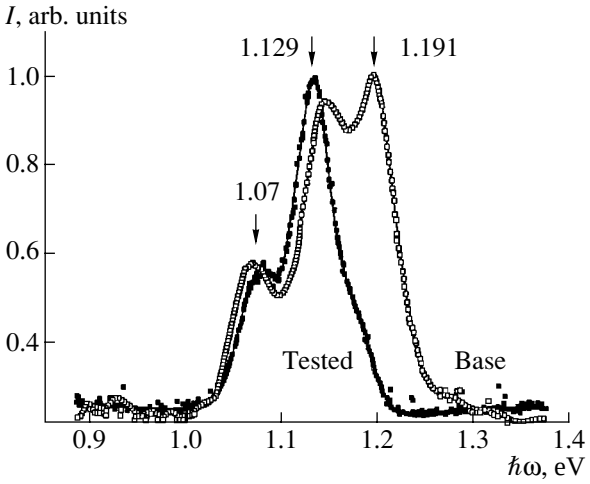

Fig. 2. PL spectra of CIGS solar cells prior to and after heating in humid atmosphere. The measurement temperature T = 20 K, the excitation wavelength λ = 532 nm, and the excitation power is 50 mW. Characteristic energies are given in eV.

[2] Interfaces play an important role in the diffusion of Na atoms from the glass substrate through the Mo layer in the bulk of the CIGS absorber [10] and may have properties differing from those of crystallites.

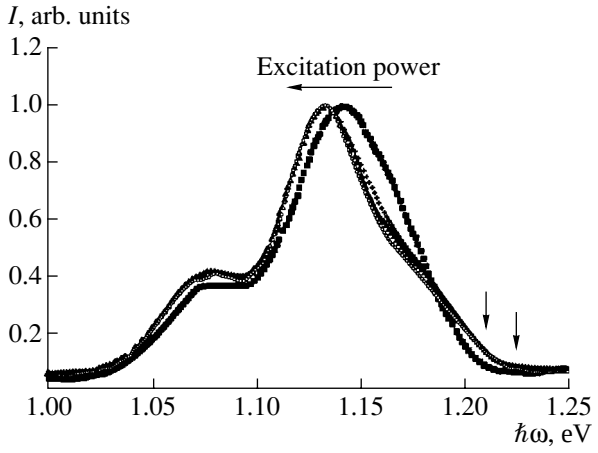

Fig. 3. Dependence of PL spectra of the tested sample on the excitation level in the range of 10–65 mW. The excitation wavelength λ = 532 nm, and the measurement temperature T = 20 K.

5. PHOTOLUMINESCENCE: THE SHORT- AND LONG-WAVELENGTH TAILS

We observed a considerable difference between the short-wavelength regions of the PL spectra for the two devices investigated. Although the slope of the PL fall at the high-energy wing has the similar value of 68 eV^{-1}, the edge is shifted to lower photon energies for the cells tested (Fig. 2). The shape of the short-wavelength PL wing in the vicinity of peaks at 1.13 and 1.19 eV is the same as the first approximation and can be described by the Gaussian contour. The high-energy part of the short-wavelength wing for the cell tested is distorted due to a slight contribution of recombination transitions with the energy close to E_g in the CIGS film.

The absolute PL intensity for the reference cell is higher relative to the PL intensity for the device treated in moisture–heat conditions. For this reason, we managed to record the emission in the shorter wavelength spectral region, for the energies as high as E_g (CdS) and E_g (ZnO), only for the CIGS reference solar cell. We used excitation by an ultraviolet beam of the He–Cd laser and obtained the distribution of spectral intensity shown in Fig. 4. The main PL spectral features are indicated by arrows. The inflection at 2.10 eV can be attributed to the optical transition via the defect levels in the wide-gap CdS (and/or ZnO) windows, rather than in the OVC layer. The latter has a narrower band gap, specifically, according to [11, 15], E_g = 1.3 eV. The lowest emissivity of the reference solar cell corresponds to the band gap for CdS (Fig. 4). The absence of the edge emission evidently points to the lower quality of the films from the standpoint of PL efficiency. Specifically, the quality of the CdS film, which was deposited by the chemical bath method, is lower compared to CIGS and ZnO films grown in a vacuum chamber. With increasing photon energy, the PL intensity for the solar cell increases and reaches a relatively high level at E_g(ZnO) = 3.45 eV. The PL spectrum in Fig. 4 has no distinct spectral features in the energy range of 2.8–3.5 eV, although a number of inflections can be attributed to certain local defect levels in the widest gap component in the thin-film device. Actually, wide-gap PL spectra are known for ZnO films obtained by various techniques [16, 17]. These films contain a diversity of emitting defects.

Using the data in Fig. 5, we can compare the PL spectrum with the emissivity spectrum for the Zn/CdS/CIGS heterojunction. The latter spectrum was obtained from the spectral distribution of quantum efficiency (QE) for the solar cell exposed to moisture and

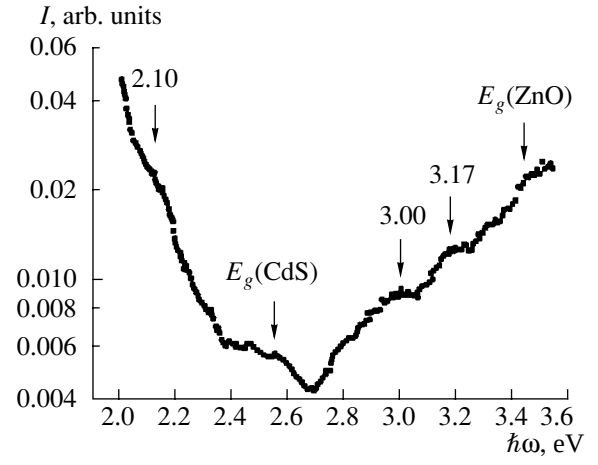

Fig. 4. Short-wavelength tail of the PL spectrum for the reference solar cell. The measurement temperature T = 20 K, the excitation wavelength λ = 325 nm, and the power is 100 mW. Characteristic energies are given in eV.

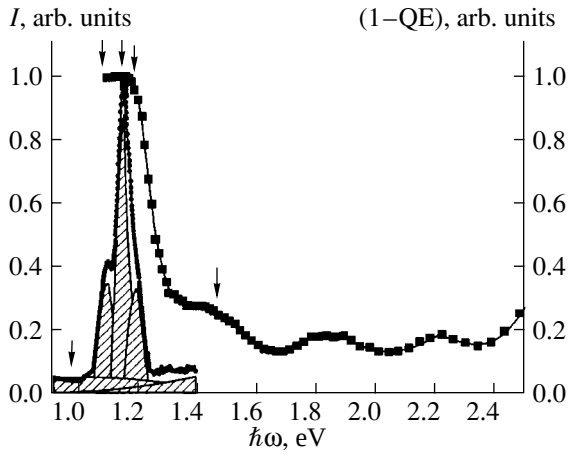

Fig. 5. Comparison of PL spectra and emissivity (1 – QE) for the solar cell heat-treated in the humid atmosphere. The measurement temperature T = 20 K. The spectral positions of peaks of Gaussian PL bands are indicated by arrows.

heat. The PL spectrum is decomposed into homogeneous Gaussian bands; three bands constitute the main radiation and two broad bands, which are shown only within the limits of experimental accuracy, constitute the radiation close to the background. The characteristic peaks of homogeneous PL bands are indicated in Fig. 5 by arrows. The short-wavelength PL wing is distinct at $\hbar\omega > 0.88$ eV and peaks at 0.94–0.96 eV. The edge emission reaches the largest value at the (1 – QE) spectrum cutoff. Subsequently, the PL falls with decreasing emissivity (increasing QE) in the same range. For energies $\hbar\omega > 1.25$ eV, the PL spectrum also correlates well with the spectral dependence of the solar cell efficiency. In this case, the interference in the antireflecting layer of the device begins to manifest itself. Despite a decrease in QE after device treatment in the hot and humid atmosphere, the long-wavelength edge of the QE spectrum hardly shifts at all. However, PL spectra make it possible to reveal the fine variations in the ensemble of optical transitions as well as to associate them with certain chemical and electrochemical reactions. One of the possible reactions proceeds in the ZnO:Al/ZnO window, where, presumably, humid air preferentially oxidizes Al atoms. Hydroxyl OH^- groups enter into the chemical reaction with ZnO and CdS films. As a result, hydroxyls $ZnOH^-$, $CdOH^-$, and $Cd(S,OH)_x$ are formed at various stages of heating in the humid atmosphere. These processes should lead to an increase in the resistivity of the ZnO film, and to the degradation of the CdS film and adjacent heterointerfaces including the heterointerface with OVC. The effect of Na in polycrystalline solar cells makes itself clearly evident by its diffusion, which leads to the inhibition of the shallow-lying acceptors V_{Cu} in the absorber film. For this reason, it is possible to consider the reverse process under the effect of moisture and heat. Sodium atoms at Cu sites interact with water and make the sites vacant. This increases the concentration of vacancies V_{Cu}, which are involved in the above-mentioned alternative channel of recombination. The detailed consideration of chemical interactions in the multilayer sandwich calls for further investigation of charge transport in the solar cell.

6. CONCLUSION

The effect of moisture and heat in standard testing conditions leads to a decrease in the emissivity of high-efficiency solar cells based on thin polycrystalline CIGS films. This correlates with a fall in the integral conversion efficiency of the device. The near-edge emission decreases abruptly, whereas long-wavelength emission bands at $\hbar\omega = 1.13$ and 1.07 eV are preserved. For the reference device, the minimum of emissivity in the short-wavelength region is observed at the energies corresponding to the CdS band gap. An increase in the PL intensity with the photon energy as high as E_g(ZnO) is probably associated with the emission via the defect levels in the wide-gap ZnO. Both films are susceptible to degradation, since no PL is observed in this spectral range after the device exposure to moisture and heat. Presumably, the presence of moisture at 85°C promotes certain chemical (or electrochemical) reactions in ZnO and CdS films and at the CdS/CIGS heterointerface. These reactions lead to a major degradation of the device emissivity in the blue–violet spectral region.

In general, the stability of CIGS-based solar cells remains high over a long period under conventional laboratory conditions. However, incapsulation becomes necessary for device operation out of doors, since it provides good protection from the effect of atmospheric moisture.

ACKNOWLEDGMENTS

We thank professor L. Stolt and J. Wennerberg (Ångström Solar Center, Uppsala University, Sweden) for providing us with samples, for measuring the reference characteristics of solar cells and for their fruitful participation in discussions.

This study was supported by a research grant of JSPS, Tokyo, Japan.

REFERENCES

1. H. W. Schock and R. Noufi, Prog. Photovoltaics **39**, 151 (2000).
2. T. Negami, Y. Hasimoto, and S. Nishiwakir, in *Proceedings of the 11th International Photovoltaic Science and Engineering Conference, Sapporo, PVSEC, 1999*, p. 993.
3. H. S. Ullal, K. Zweibel, and B. von Reodern, in *Proceedings of the 26th IEEE Photovoltaic Specialists Conference, PVSC, 1997*, p. 301.
4. K. Kushiya, I. Sugiyama, M. Tachiyuki, *et al.*, in *Proceedings of the 9th International Photovoltaic Science and Engineering Conference, PVSEC, 1996*, p. 143.
5. J. Kessler, M. Bodegård, J. Hedström, and L. Stolt, in *Technical Digest of the 11th International Photovoltaic Science and Engineering Conference, PVSEC, Sapporo, 1999*, p. 631.
6. G. A. Medvedkin, L. Stolt, and J. Wennerberg, Fiz. Tekh. Poluprovodn. (St. Petersburg) **33**, 1137 (1999) [Semiconductors **33**, 1037 (1999)].
7. G. A. Medvedkin and J. Wennerberg, *Polycrystalline Semiconductors V: Bulk Materials. Thin Films and Devices, Ser. Solid State Phenomena*, Ed. by J. H. Werner, H. P. Strunk, and H. W. Schock (Scitech Publ., Uettikon am See, 1999), p. 69.
8. G. A. Medvedkin and J. Wennerberg, in *Abstracts of the 12th International Conference on Ternary and Multinary Compounds, Taiwan, 2000*, Abstr. P2-36, Jpn. J. Appl. Phys., Suppl. **39-1** (2000).
9. J. Kessler, M. Bodegard, J. Hedström, and L. Stolt, in *Proceedings of the 16th European Photovoltaic Science and Engineering Conference, PVSEC, Glasgow, 2000.*
10. F. Karg, H. Calwer, J. Rimmasch, *et al.*, in *Proceedings of the 11th International Conference on Ternary and Multinary Compounds, Salford, 1997* (Inst. of Physics

Publ., Bristol, 1998), Inst. Phys. Conf. Ser. **152**, 909 (1998).

11. U. Rau, in *Abstracts of the 12th International Conference on Ternary and Multinary Compounds, Taiwan, 2000*, Abstr. Fr-A1-1, Jpn. J. Appl. Phys., Suppl. **39-1** (2000).
12. L. Stolt, M. Bodegård, J. Hedström, *et al.*, in *Proceedings of the 11th E.C. Photovoltaic Solar Energy Conference, Mountreux, 1992* (Harwood Academic Publ., Chur, 1993), p. 120.
13. G. A. Medvedkin and M. A. Magomedov, J. Appl. Phys. **82**, 4013 (1997).
14. T. Nishi, G. A. Medvedkin, Yu. Katsumata, *et al.*, Jpn. J. Appl. Phys. **40**, 59 (2001).
15. T. Dullweber, G. Hanna, U. Rau, and H. W. Schock, in *Proceedings of the 11th International Photovoltaic Science and Engineering Conference, Sapporo, PVSEC, 1999*, p. 85.
16. S. Choopun, R. D. Vispute, W. Noch, *et al.*, Appl. Phys. Lett. **75**, 3947 (1999).
17. S. Im, B. J. Jin, and S. Yi, J. Appl. Phys. **87**, 4558 (2000).

Translated by N. Korovin

Semiconductors, Vol. 35, No. 11, 2001, pp. 1335–1339. Translated from Fizika i Tekhnika Poluprovodnikov, Vol. 35, No. 11, 2001, pp. 1391–1395.

PHYSICS OF SEMICONDUCTOR DEVICES

Simulation of Current–Voltage Characteristics of a Ferroelectric Field-Effect Transistor

L. S. Berman

Ioffe Physicotechnical Institute, Russian Academy of Sciences, Politekhnicheskaya ul. 26, St. Petersburg, 194021 Russia

Submitted April 9, 2001; accepted for publication April 10, 2001

Abstract—Current–voltage (*I–V*) characteristics of an all-perovskite ferroelectric–semiconductor field-effect transistor (FET) were simulated. The modeling is based on an analysis of an experimental hysteresis loop of a metal–ferroelectric–metal structure. The charge in the semiconductor, electric fields in the semiconductor and ferroelectric (FE), and FE polarization at the FE–semiconductor interface are calculated at a given semiconductor surface potential. The Poisson equation is solved numerically across the FE thickness. The semiconductor surface potential, semiconductor charge, FE polarization, electric field and voltage drop in the FE are calculated as functions of the applied voltage. By using appropriate semiconductor thickness and built-in voltage between the FE and the gate, it is possible to provide a remanent polarization necessary for the opening and blocking of the FET channel in the ascending and descending portions of the hysteresis loop, respectively. The *I–V* characteristics and the voltage drop along the FET channel are calculated and analyzed for both polarities of the drain bias. The results make it possible to predict *I–V* characteristics of an all-perovskite ferroelectric FET. © *2001 MAIK "Nauka/Interperiodica".*

1. INTRODUCTION. FORMULATION OF THE PROBLEM

Recently, intensive research has been aimed at designing metal–ferroelectric–semiconductor (MFES) field-effect transistors (FETs) to be used as memory elements [1–9]. Mainly perovskite semiconductors, technologically compatible with ferroelectrics (FEs) [1, 2, 10, 11], are used in the development of such transistors (MFES FETs). The channel conductance of these FETs is modulated without the formation of an inversion layer. A topical task in designing MFES FETs is the simulation of their current–voltage (*I–V*) characteristics in order to predict the transistor parameters. *I–V* characteristics of MFES FET with $PbTiO_3$ FE and an *n*-Si channel were calculated in [8]. In [12], the MFES FET was simulated by analyzing its equivalent circuit.

In a previous study [13], we calculated the hysteresis loop of an MFES structure by analyzing an experimental hysteresis loop of a metal–ferroelectric–metal (MFEM) structure, $P(E_f)$, approximated by a hyperbolic tangent (here P is the FE polarization and E_f the electric field in the FE) [13]. In this investigation, the *I–V* characteristics of MFES FET are also calculated on the basis of experimental $P(E_f)$ dependences of MFEM structures; the polarization values are found to be stable if they lie on the saturated hysteresis loop or inside of it.

For an MFES structure, the $P(E_f)$ dependences for the ascending and descending portions of the hysteresis loop are the same as in the case of MFEM (all other factors being the same); however, the $P(V)$ dependences for two structures differ, since in the MFES structure part of the external bias V is applied to the semiconductor, thus giving rise to a depolarization effect of the semiconductor.

We assume that a Schottky barrier is formed at the contact to FE, the contact to the semiconductor is ohmic, and that the FE and the semiconductor are doped with shallow-level acceptors. We assume also that the current across the FE is small, not affecting the polarization, and that the charges at the FE–semiconductor interface are negligible.

2. POLARIZATION OF FERROELECTRIC

In an MFEM structure, the polarization $P(E_f)$ increasing from $-P_s$ to P_s (ascending portion of the saturated hysteresis loop, P_s is the spontaneous polarization) and its derivative are approximated by relations (20)–(22) from [14]. The decrease in polarization from P_s to $-P_s$ (descending portion of the saturated hysteresis loop) and its derivative are approximated by relations (19) and (23) from [14]. The $P(E_f)$ dependence inside the saturated hysteresis loop was calculated using relations (1) and (2) from [15].

A charge in a semiconductor Q_s is uniquely determined by the potential of the semiconductor surface, ψ_s [16–18], with the voltages reckoned from the contact to

1063-7826/01/3511-1335$21.00

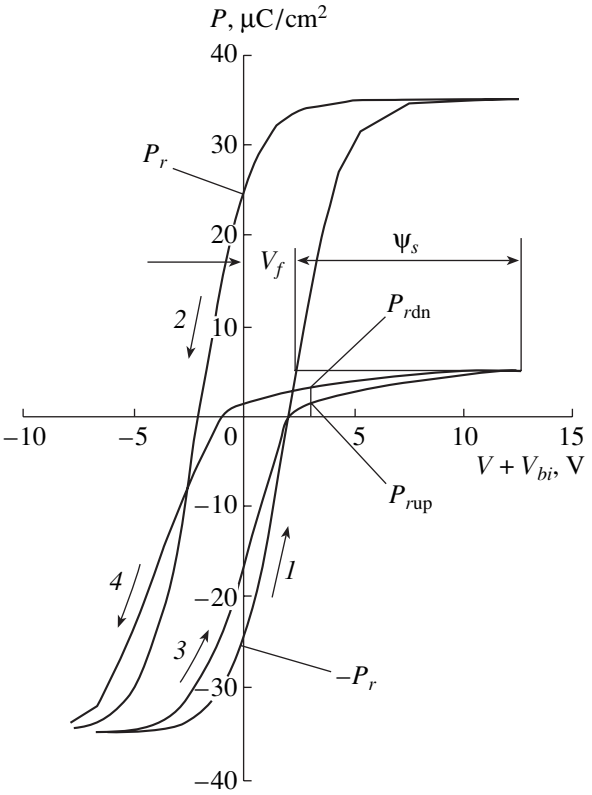

Fig. 1. Hysteresis loops of (*1*, *2*) MFEM and (*3*, *4*) MFES structures; for explanations, see text.

the semiconductor. At the semiconductor–ferroelectric interface, the relation

$$\varepsilon_0\varepsilon_s E_s = \varepsilon_0 E_f + P, \quad (1)$$

holds, where ε_0 is the permittivity of free space, ε_s the dielectric constant of the semiconductor, and E_s the electric field in the semiconductor.

Using the well-known relation

$$\varepsilon_0\varepsilon_s E_s = -Q_s, \quad (2)$$

we obtain

$$dE_f = -\frac{dQ_s}{\varepsilon_0 + dP/dE_f}, \quad (3)$$

Table

V_{bi}, V	Ascending portion		Descending portion	
	$P_{r\text{up}}$, μC/cm²	ψ_s, V	$P_{r\text{dn}}$, μC/cm²	ψ_s, V
1	−8.1	−0.5	1.8	1.1
2	−0.45	−0.01	2.4	2.0
3	1.4	0.85	2.8	2.8

where dQ_s and dE_f are changes in the charge Q_s and field E_f on varying the potential ψ_s. The E_f value can be determined from a transcendent equation (1), with $P(E_f)$ and dP/dE_f further calculated.

For an FE, the Poisson equation takes the following form (see, e.g., [19]):

$$\frac{d^2\psi}{dx^2} = -\frac{\rho}{\varepsilon_0 + dP/dE_f}, \quad (4)$$

where ρ is the space charge density in the FE.

The Poisson equation is numerically integrated across the FE thickness. At distance $dx_1 = w_f/n$ from the interface (here w_f is the FE thickness, and n is an integer), we have an electric field

$$E_1 = E_f + \frac{dE_f}{dx}dx_1 = E_f + \left(\frac{\rho}{\varepsilon_0 + dP/dE_f}\right)\frac{w_f}{n} \quad (5)$$

and a potential

$$\psi_1 = \psi_s - E_f\frac{w_f}{n}. \quad (6)$$

Further, we use a recurrence procedure: the field, potential, and polarization are calculated using their preceding values. By this method, we calculated the dependences of ψ_s, Q_s, V_f, P_{fs}, and P_{fm} on applied voltage V (here V_f is the voltage drop across the FE; and P_{fs} and P_{fm} are the FE polarizations at the interfaces with the semiconductor and metal, respectively; in what follows, we omit the *fs* subscript of P_{fs}).

In the case of polarization, the relation

$$\psi_s + V_f = V + V_{bi} \quad (7)$$

holds, where V_{bi} is the contact potential between FE and the electrode on it.

The principal parameters for an MFES FET are the two values of the remanent polarization:

(i) $P_{r\text{up}}$ for the ascending portion of the hysteresis loop, from $V < 0$ to $V = 0$;

(ii) $P_{r\text{dn}}$ for the descending portion, from $V > 0$ to $V = 0$.

Now we find $P_{r\text{up}}$ and $P_{r\text{dn}}$ for an MFES structure. The parameters are assumed to have the following values.

(I) For FE: spontaneous polarization $P_s = 35$ μC/cm², remanent polarization $P_r = 25$ μC/cm², coercive field $E_c = 2 \times 10^5$ V/cm, shallow-acceptor density $N_f = 10^{18}$ cm^{-3}, and thickness $w_f = 0.1$ μm.

(II) For the semiconductor: dielectric constant $\varepsilon_s = 10$, and shallow-acceptor density $N_s = 10^{19}$ cm^{-3}.

The calculated results are presented in Fig. 1 (curves *3* and *4*); for comparison, curves *1* and *2* show the saturated hysteresis loop of an MFEM structure with the same, but impurity-free, FE ($N_f = 0$). When the

semiconductor surface is enhanced ($\psi_s < 0$), its properties approach those of a metal, and, therefore, the ascending portions for the MFEM and MFES structures are similar (curves *1* and *3*). In the case of a depleted semiconductor surface ($\psi_s > 0$), the potential ψ_s grows with increasing bias V; therefore, the voltage drop across the FE (and, consequently, its polarization) change only slightly (see also [13]). The V_f and ψ_s values at $V = V_{bi} = 12.5$ V are shown in Fig. 1. The $P_{r\text{up}}$ and $P_{r\text{dn}}$, and also the corresponding ψ_s values, are presented in the table in relation to V_{bi}.

The calculations were carried out for the case when the thickness of the space charge region in the semiconductor, h, is less than the semiconductor thickness w_s even at the maximum ψ_s ($\psi_s = \psi_{s\max}$). A certain critical potential ψ_{scr} found from the relation (see [17]) corresponds to the case when $h = w_s$

$$\psi_{\text{scr}} = \frac{qN_s w_s^2}{2\varepsilon_0 \varepsilon_s}. \quad (8)$$

For the adopted $w_s = 0.01$ μm, formula (8) yields $\psi_{\text{scr}} = 0.9$ V. For the ascending portion, $\psi_{\text{scr}} = 0.9$ V corresponds to $V + V_{bi} = 3.2$ V. Therefore, the dependence $P(V + V_{bi})$ is calculated correctly for the ascending portion at $V + V_{bi} < 3.2$ V, whereas for $V + V_{bi} > 3.2$ V, and also for the entire descending portion, the $P(V + V_{bi})$ dependences presented in Fig. 1 should be regarded as a first approximation.

Let us specify $V_{bi} = 3$ V, which is close to the channel blocking voltage. We increase the voltage to 8–10 V in the ascending portion and then reduce it to zero. The descending portion goes above the ascending one, which means that $P_{r\text{dn}} > P_{r\text{up}}$ at $V = 0$. Therefore, at $V = 0$, the charge in the semiconductor $|Q_s|$ and the corresponding potential ψ_s are larger for the descending portion than for the ascending portion, i.e. the space charge region expands throughout the semiconductor (the channel is blocked).

3. *I–V* CHARACTERISTICS

Figure 2 shows schematically the design of a FET with an FE insulator. In the working mode, the gate voltage $V_G = 0$, with either $P = P_{r\text{up}}$ or $P = P_{r\text{dn}}$.

When the current flows in the channel, the relation

$$\psi_s + V_f = V_{bi} - V_{\text{ch}} \quad (9)$$

holds, where V_{ch} is the voltage drop along the channel [compare formulas (7) and (9)]. The current I in the channel is given by

$$I = u_p b Q_c E, \quad (10)$$

where u_p is the hole mobility, b is the channel width, Q_c is the charge of holes in the semiconductor (per unit gate area), and E is the field along the channel. The FE

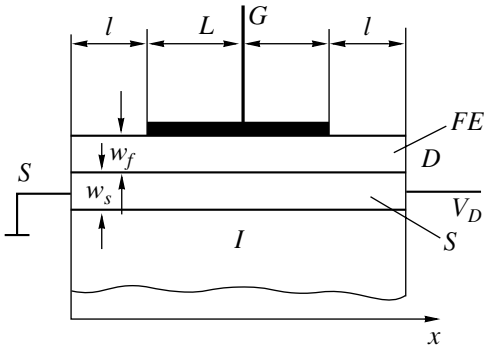

Fig. 2. Design of an MFES FET: *S*, source; *G*, gate; *D*, drain; *I*, insulator; *FE*, ferroelectric; *S*, semiconductor; and w_f, w_s, thicknesses of the FE and semiconductor, respectively. $b = 230$ μm, channel width; $w_f = 0.1$ μm, $w_s = 0.01$ μm, $l = 40$ μm, and $L = 320$ μm.

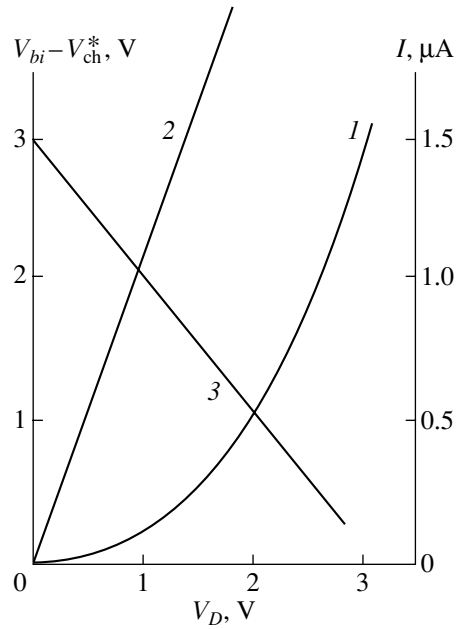

Fig. 3. *I–V* characteristics at (*1*) $V_{bi} = 3$ V and (*2*) 2 V; (*3*) $V_{bi} - V^*_{\text{ch}}$ vs. V_D for $V_{bi} = 3$ V.

is polarized prior to the application of the reading voltage V_D to the drain. This allows for the calculation of the dependences $Q_c(\psi_s)$ and $Q_c(V_{bi} - V_{\text{ch}})$, similarly to the case of $Q_s(\psi_s)$ and $Q_s(V + V_{bi})$ (see above).

The voltage drop between the source and the left-hand edge of the gate (at $x = l$, see Fig. 2) is found from the expression

$$V_l = \frac{Il}{u_p b Q_{\text{eq}}}, \quad (11)$$

where $Q_{\text{eq}} = qp_{\text{eq}}w_s$ is the equilibrium value of Q_c, and p_{eq} is the equilibrium density of holes in the semiconductor.

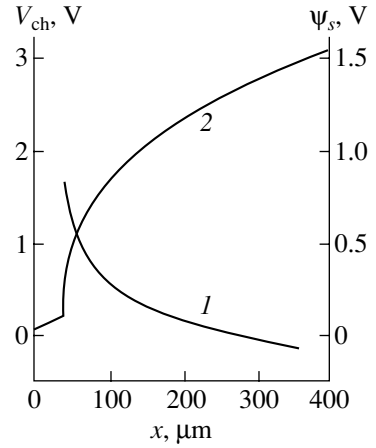

Fig. 4. Distribution of (*1*) potential ψ_s and (*2*) voltage V_{ch} along the channel length at $I = 1.6$ μA and $V_{bi} = 3$ V.

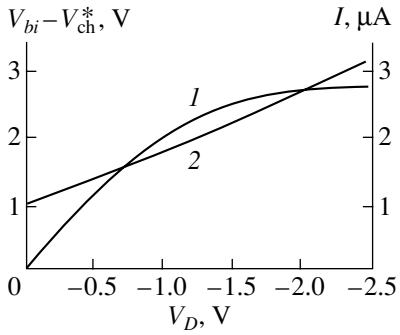

Fig. 5. (*1*) *I–V* characteristic and (*2*) $(V_{bi} - V_{ch}^*)$ vs. V_D at $V_{bi} = 1$ V.

In the working part of the channel, i.e., under the gate, we have

$$dV_{ch} = \frac{I}{u_p b Q_c} dx. \quad (12)$$

At $x = x_1 = L/n + l$

$$V_{ch(1)} = V_l + \frac{IL}{u_p b Q_{c0} n}, \quad (13)$$

where Q_{c0} is the Q_c value at $V_{ch} = V_l$, and $n \gg 1$ is an integer. At $x = x_i = Li/n + l$ $(0 < i < n)$, the relation

$$V_{ch(i+1)} = V_{ch(i)} + \frac{IL}{u_p b n Q_{ci}} \quad (14)$$

holds, where Q_{ci} is a known function of $(V_{bi} - V_{chi})$ (see above).

The dependence of Q_c on $V_{bi} - V_{ch}$ can be approximated, e.g., by an n-th order polynomial. Further, the I value is specified, and the voltage drop along the channel is calculated from (14). In this way, the entire *I–V* curve is calculated.

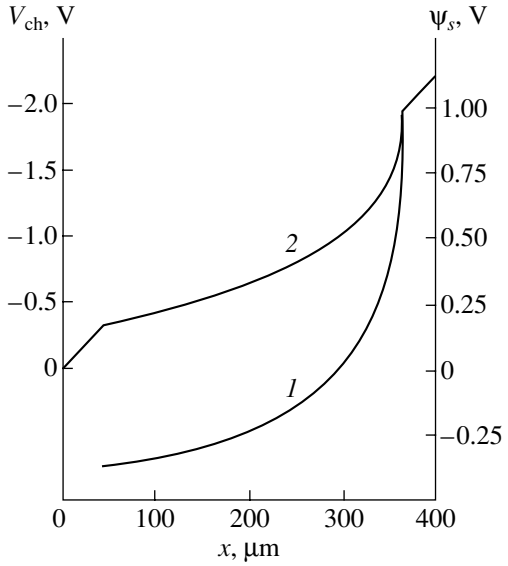

Fig. 6. Distribution of (*1*) potential ψ_s and (*2*) voltage V_{ch} along the channel length at $I = 2.75$ μA and $V_{bi} = 1$ V.

If the conduction types of the FE and the semiconductor are the same (e.g., *p*-type), an MFES FET can operate at either polarity of the drain bias. Below, we present the *I–V* characteristics calculated for the above parameters of the FE, semiconductor, and FET. The optimal operation mode for an MFES FET is that with complete blocking of the channel in the descending portion. As shown above, this can be achieved at $V_{bi} = 3$ V.

Figure 3 shows the *I–V* characteristics and the dependence of $V_{bi} - V_{ch}^*$ on V_D for operation in the ascending portion at $V_D > 0$ and $V_{bi} = 3$ V (curves *1* and *3*, respectively), where V_{ch}^* is the V_{ch} value for $x = L + l$. At $V_D \ll V_{bi}$, the channel current grows slowly, because the channel is nearly blocked. Then, with decreasing potential barrier height $V_{bi} - V_{ch}$, the conducting part of the channel expands and the current rises steeply. Figure 3 also presents a *I–V* characteristic for the same structure, but at $V_{bi} = 2$ V (curve *2*). At $V_D = 0$, we have $\psi_s \approx 0$, i.e., $Q_c \approx Q_{eq}$. With increasing V_D, the current first grows more quickly than at $V_{bi} = 3$ V, but then the current rise slows down. This is accounted for by the high equilibrium density of holes in the semiconductor, resulting in only a slight effect of the enhancement on the channel conductance.

Figure 4 shows the distributions of potential ψ_s and voltage V_{ch} along the channel at the maximum current $I = 1.6$ μA and $V_{bi} = 3$ V. At the given current, the voltage V_{ch} under the gate first grows quickly, and then slowly. This is accounted for by the fact that the left part of the channel is nearly blocked, but the increase in V_{ch} along the channel leads to expansion of its conducting part, slowing down the rise in V_{ch}. Along nearly the

entire active part of the channel, $\psi_s > 0$, i.e., the channel is depleted.

We also present the calculated results for the ascending portion at $V_D < 0$. In this case, $V_{ch} < 0$. With increasing V_D, the potential barrier $V_{bi} - V_{ch}$ and the potential ψ_s grow, making the conducting part of the channel narrower. Evidently, we have to specify $V_{bi} <$ 3 V, i.e., $\psi_s < \psi_{scr}$. In this case, the $P(V)$ dependence is an extension of the ascending portion from $V = 0$. Let us set $V_{bi} = 1$ V. Figure 5 presents a $I(V_D)$ dependence, which is typical of a conventional MOSFET. $V_{bi} - V_{ch}^*$ grows almost linearly from 1 V. Figure 6 shows the distributions of the potential ψ_s and voltage V_{ch} along the channel for the maximum current $I = 2.75$ μA. V_{ch} grows steeply at the end of the working part of the channel (at $x = L + l$), which is accounted for by the narrowing of the conducting part of the channel. The ψ_s value grows from –0.4 to 0.9 V ($\psi_s \approx \psi_{scr}$).

It will be recalled that the above results have been obtained under the following assumptions: (i) the FE and the semiconductor are doped with shallow impurities only, (ii) no charges are present at the FE–semiconductor interface, and (iii) the current through the FE is small and has no effect on the polarization. Therefore, our results represent the upper achievable limit for an MFES FET within the given parameters. The best experimental result for an all-perovskite FET is 70% modulation of the channel conductance [20].

4. CONCLUSION

The *I–V* characteristics of MFES FETs were simulated, which allow one to predict the behavior of FETs of this kind.

The cutoff mode for the MFES FET channel can be achieved by the proper choice of the contact difference of potentials at the FE–gate interface and the semiconductor thickness.

An MFES FET can operate with either polarity of the drain bias if the FE and the semiconductor have the same type of conduction.

ACKNOWLEDGMENT

I am grateful to I.V. Grekhov for the formulation of the problem and his helpful participation in discussions.

REFERENCES

1. Y. Watanabe, Jpn. J. Appl. Phys., Part 1 **35**, 1564 (1996).
2. Y. Watanabe, Y. Matsumoto, and M. Tanamura, Jpn. J. Appl. Phys., Part 1 **34**, 5254 (1995).
3. Y. Watanabe, Phys. Rev. B **59**, 11257 (1999).
4. Y. T. Kim and D. S. Shin, Appl. Phys. Lett. **71**, 3507 (1997).
5. W. Wu, K. H. Wong, C. L. Mak, *et al.*, J. Appl. Phys. **88**, 2068 (2000).
6. M. W. Prins, K. O. Grosse-Holz, G. Muller, *et al.*, Appl. Phys. Lett. **68**, 3650 (1996).
7. M. W. Prins, S. E. Zinemers, J. F. Cilessen, and J. B. Giesbers, Appl. Phys. Lett. **70**, 458 (1997).
8. F. Y. Chen, Y. K. Fang, M. J. Sun, and J.-R. Chen, Appl. Phys. Lett. **69**, 812 (1996).
9. F. Y. Chen, Y. K. Fang, M. J. Sun, and J.-R. Chen, Appl. Phys. Lett. **69**, 3275 (1996).
10. Y. Watanabe, Appl. Phys. Lett. **66**, 1770 (1995).
11. Y. Watanabe, Appl. Phys. Lett. **66**, 28 (1995).
12. D. B. A. Rep and M. W. Prins, J. Appl. Phys. **85**, 7923 (1999).
13. L. S. Berman, Fiz. Tekh. Poluprovodn. (St. Petersburg) **35**, 200 (2001) [Semiconductors **35**, 193 (2001)].
14. S. L. Miller, R. D. Nasby, J. R. Schwank, *et al.*, J. Appl. Phys. **68**, 6463 (1990).
15. S. L. Miller, J. R. Schwank, R. D. Nasby, and M. S. Rodgers, J. Appl. Phys. **70**, 2849 (1991).
16. I. E. Tamm, *The Principles of Electricity Theory* (Nauka, Moscow, 1989).
17. S. Sze, *Physics of Semiconductor Devices* (Wiley, New York, 1981; Mir, Moscow, 1984), Vol. 1.
18. J. S. Blakemore, *Semiconductor Statistics* (Pergamon, Oxford, 1962; Mir, Moscow, 1964).
19. P. W. M. Bloom, R. M. Wolf, J. F. M. Cilessen, and M. P. C. Krijk, Phys. Rev. Lett. **73**, 2107 (1994).
20. I. A. Veselovskiĭ, I. V. Grekhov, L. A. Delimova, and I. A. Liniĭchuk, Pis'ma Zh. Tekh. Fiz. **27** (1), 39 (2001) [Tech. Phys. Lett. **27**, 17 (2001)].

Translated by D. Mashovets

Semiconductors, Vol. 35, No. 11, 2001, pp. 1340–1344. Translated from Fizika i Tekhnika Poluprovodnikov, Vol. 35, No. 11, 2001, pp. 1396–1400.

PHYSICS OF SEMICONDUCTOR DEVICES

Improved Degradation Stability of Blue–Green II–VI Light-Emitting Diodes with Excluded Nitrogen-Doped ZnSe-Based Layers

N. Yu. Gordeev*, S. V. Ivanov*, V. I. Kopchatov*, I. I. Novikov*, T. V. Shubina*, N. D. Il'inskaya*, P. S. Kop'ev*, G. Reuscher, A. Waag***, and G. Landwehr****

** Ioffe Physicotechnical Institute, Russian Academy of Sciences, Politekhnicheskaya ul. 26, St. Petersburg, 194021 Russia*
e-mail: ivan@beam.ioffe.rssi.ru

*** Physikalisches Institut der Universität Würzburg, Am Hubland, D-97074 Würzburg, Germany*

**** Abteilung Halbleiterphysik, Universität Ulm, 89081 Ulm, Germany*

Submitted April 25, 2001; accepted for publication April 26, 2001

Abstract—Degradation characteristics of *p–i–n* BeZnSe/Zn(Be)CdSe light-emitting diodes were investigated. Undoped short-period superlattices, which provide efficient hole transport from the p^+-BeTe:N near-contact region (hole injector) into the active region, were used instead of the *p*-doped BeZnSe:N emitter. It is demonstrated that this makes it possible to considerably lengthen the operating life of the light-emitting diodes at highest direct current densities (~4.5 kA/cm^2) at room temperature. © *2001 MAIK "Nauka/Interperiodica".*

INTRODUCTION

Considerable progress in the development of optoelectronic devices, i.e., lasers and light-emitting diodes (LEDs), based on Group III nitrides has been achieved [1]. Despite this, studies of II–VI heterostructures (HSs) are still topical for the development of semiconductor lasers for the blue–green spectral range, since this range is inaccessible for Group III nitrides. In this case, the main effort was directed towards increasing the service life for these injection HSs.

An important problem, the solution of which should improve luminescence parameters and increase the service life of II–VI HSs, is the protection of the active region from the penetration and development of extended and point defects. First of all, it is important to eliminate the sources of these defects. Low activation energies of defect formation, which are comparable to the energy of the operating radiation quantum, are characteristic of most of the wide-gap II–VI compounds. In addition, relatively high cutoff voltages of the *p–n* junction and, as a consequence, the large operating power additionally stimulate the development and multiplication of defects during diode operation.

The problem of suppressing the rapid degradation of separate-confinement II–VI laser diodes due to extended structural defects (mainly stacking faults developed from the (II–VI)/GaAs heterointerface) is important. This problem was solved by significantly lowering the initial density of stacking faults and optimizing the *p*-contact region by introducing the ZnSe/ZnTe superlattice (SL), which increased the continuous operation lifetime to 400 h [4]. However, the design of the active region of the laser structure did not undergo any substantial variations.

The nonradiative recombination at point defects, which enhances their generation, is believed to be the prevailing mechanism of slow degradation [5]. It is assumed that the point defects enter into the active region mainly due to their diffusion from the *p*-doped compensated regions of the ZnSSe:N waveguide and a ZnMgSSe:N upper emitter [6]. Most likely, these defects are associated with compensating donor centers, specifically, interstitial N atoms, which are responsible for the instability of the electrical characteristics of ZnSe:N [7]. In addition, it was recently demonstrated by Gundel *et al.* [8] that, under certain conditions, the shallow-level N acceptor may apparently manifest a metastable nature itself via transforming into the charged interstitial.

In order to verify this concept, a new approach to the design of II–VI diodes is suggested in this publication by the example of BeZnSe/ZnCdSe LEDs. This approach consists in substituting the undoped BeZnSe/ZnSe SLs with constant and variable periods for the *p*-BeZnSe:N emitter. These SLs provide effective hole transport from the p^+-BeTe:N injector into the active region, specifically, into the ZnCdSe quantum well (QW). In addition, it has been found that the use of short-period SLs for fabricating the waveguide layers prevents the penetration of extended defects into the active region. As a result, these defects are effectively stopped at the emitter–waveguide interface, which provides simultaneous improvement of the optical and electron confinement [9].

1063-7826/01/3511-1340$21.00

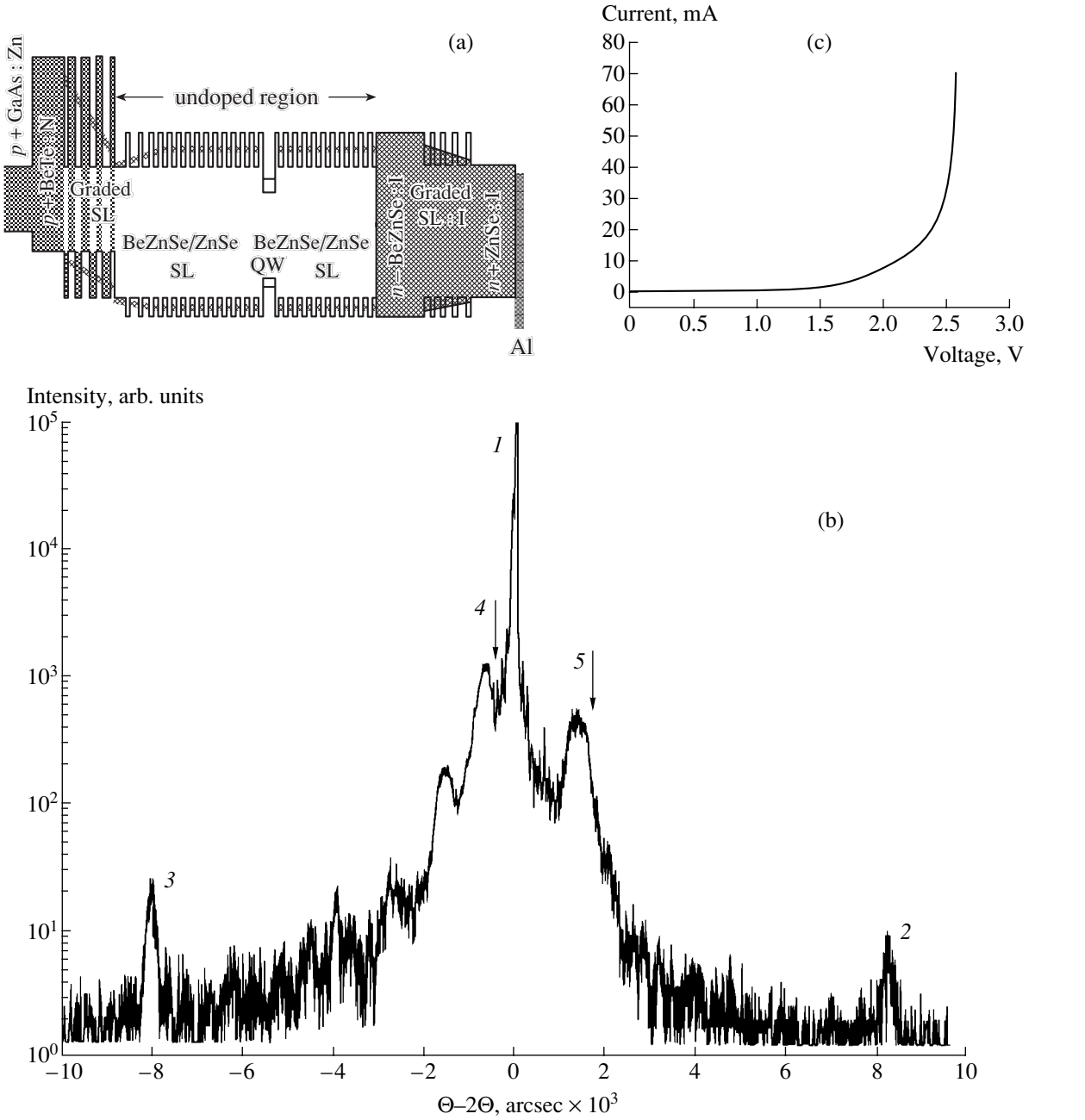

Fig. 1. (a) Schematic energy-band diagram. (b) Typical Θ–2Θ X-ray rocking curve for the structure with ZnCdSe QWs. Peaks: (*1*–*3*) GaAs + SL: (*1*) zero order, (*2*) first order, and (*3*) negative first order; (*4*) ZnSe:I; and (*5*) $Be_{0.08}Zn_{0.92}Se$. (c) Typical current–voltage characteristic for the LED heterostructures investigated.

EXPERIMENTAL

The LED HSs were grown by molecular-beam epitaxy (MBE) on p^+-GaAs substrates. The schematic energy-band diagram of the structures is shown in Fig. 1a. For the hole injector, the structures contain a p^+-BeTe:N buffer layer 2 nm thick doped to $p = 10^{19}$ cm^{-3}; and a modulation-doped alternately strained ZnSe/p^+-BeTe:N SL with a gradually varied step, which provides a gradual barrierless transition from BeTe to ZnSe. The heavy *p*-doping of BeTe is possible, and lattice parameters for BeTe and GaAs are close to each other. This makes it possible to obtain the defect-free low-resistance nonrectifying contact of the *p*-type to ZnSe and simultaneously suppress the formation of stacking faults at the heterointerface with GaAs [10]. The broadened waveguide region comprises the undoped SL (0.8 nm-$Be_{0.08}Zn_{0.92}Se$/1.5 nm-ZnSe)$_{130}$ 0.3 μm thick, in which the calculated energy position of minibands of light and heavy holes satisfies the condi-

tions for effective transport of holes across the SL by their thermal activation into a wide miniband of light holes [11]. A wide electron miniband, in turn, provides rapid electron transport from the relatively wide-gap upper emitter *n*-$Be_{0.08}Zn_{0.92}Se$:I 50 nm thick, which is heavily I-doped (5×10^{17} cm^{-3}), to the active region of the QW. The active region is located in the midplane of the waveguide. In order to form the nonrectifying *n*-type contact, the variation of the band gap from ZnSe to the waveguide SL and from the *n*-BeZnSe:I emitter to the upper heavily doped ($n > 10^{18}$ cm^{-3}) n^+-ZnSe:I layer (50 nm) should be gradual. This was accomplished using the $Be_{0.09}Zn_{0.91}Se$/ZnSe SL, in which the period and ratio of well-to-barrier width were variable. In the former case, this graded-gap SL is undoped, and, in the latter case, it is heavily I-doped. It was noted above that a characteristic feature of these structures is the absence of *p*-doping of ZnSe and BeZnSe layers. These layers are excluded with the purpose of suppressing the source of point defects associated with the metastable nature of N atoms in ZnSe. We grew several HSs with various active regions: QW ZnSe (10 nm), QW $Zn_{0.3}Cd_{0.7}Se$ (3 nm), and QW $Be_{0.45}Cd_{0.55}Se$ (4 nm). The latter is a new II–VI material, which is more stable compared to ZnCdSe. This material is lattice-matched to GaAs for this Be content and simultaneously makes it possible to obtain radiation in the blue–green spectral range [12]. The thicknesses of corresponding layers and SLs were chosen so that each single element and the structure as a whole were pseudomorphic.

The crystalline quality of structures was analyzed based on Θ–2Θ X-ray diffraction rocking curves, which were measured for the reflection (004) using a Philips X-ray diffractometer provided with a four-crystal Ge(220) monochromator.

During epitaxy, GaAs substrates were mounted on the Mo holder with an In solder. The final stage consisted of the deposition of the 0.1 μm thick Al layer on the structure surface in a metallization chamber, which was connected to an MBE growth chamber by a vacuum line. Thus, just prior to the post-growth treatment, the grown HSs had metallized *p*- and *n*-contacts, which allowed for electroluminescence (EL) measurements without additional metallization *ex situ*.

However, the substrate thickness (about 500 μm) gave no way of cleaving a sufficiently small sample with the radiation output through the side faces, whereas large linear sizes, in turn, brought about a significant increase in the absolute value of the current across the sample. As a result, the degradation of and damage to the sample were rapid. For this reason, in order to measure the EL characteristics, samples in the form of surface-emitting diodes with a deep mesa were fabricated. The diameter of the emission region was 300–500 μm, and the diameter of the metal contact in its center was 100–150 μm. The EL studies were carried out at room temperature. The samples were investigated using two pumping modes, specifically, by direct and pulsed currents. In the latter case, the pulse width was 1.5 μs, and the repetition frequency was 150 kHz.

RESULTS AND DISCUSSION

The high structural quality of the grown LED HSs is illustrated by Fig. 1b, in which the Θ–2Θ X-ray diffraction rocking curve of the structure with the ZnCdSe QWs is shown. The two nearest peaks (to the right and to the left of the peak for the GaAs substrate), which dominate in the spectrum, are related to the completely pseudomorphic ZnSe:I and BeZnSe:I ($x = 0.08$) layers, each 50 nm thick. The peaks, which correspond to satellites of the order ±1 for the BeZnSe/ZnSe SL with the period 2.3 nm, are clearly distinguishable in the curve. They are positioned symmetrically relative to the substrate peak, which suggests that the average lattice parameters for the SL and the substrate are fully matched. No noticeable broadening of the peak of the GaAs substrate, due to superposition of the zero-order SL peak on the former peak, is observed, whereas the equal-thickness fringes around the latter peak are present. This points to both the extreme low concentration of extended defects in the structure and a high degree of planarity of the SL layers.

A typical current–voltage characteristic of LEDs investigated is shown in Fig. 1c. The cutoff voltage for all HSs investigated was in the range of 2.2–3.0 V, whereas the differential resistance was 1.6–2.4 Ω. This resistance is fairly low for structures of this type. We attribute this fact primarily to the use of the low-resistance defect-free buffer structure, i.e., the graded-gap p^+-BeTe:N–ZnSe/BeTa:N SL, and to the effective transport of both types of carriers in undoped and modulation-doped SLs with the aligned structure of energy bands.

On passing the electric current across the samples, we observed the emission emerging from a narrow region immediately adjacent to the boundary of the metal contact only. No luminescence of a wide ring around the contact was observed. This specific feature imposed restrictions on EL investigations, specifically, it gave no way of investigating the quantum yield of a spontaneous emission. We assume that this effect can be caused by two factors. First, we have insufficient transverse conduction of the upper contact layer and the emitter and, as a consequence, small current spreading in the *p–n* junction plane. Second, there is insufficient transparency of the upper contact layer, which is heavily I-doped, at the wavelength of emission from the active region.

The structures manifested relatively high stability against degradation. The degradation investigations were carried out for dc pumping at room temperature. For each HS, the critical pumping current I_{cr} was determined. At this current, the mesa samples degraded instantaneously or, in fact, were damaged due to very

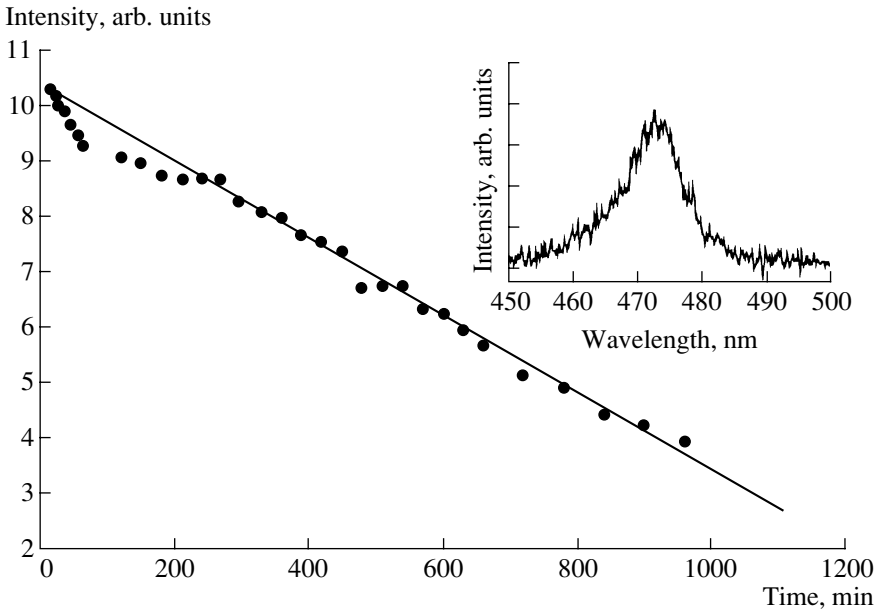

Fig. 2. Observation-time dependence of LED radiation intensity for a constant pumping current. Mesa-diameter is 140 μm, I_{cr} = 430 mA (8780 A/cm^2), $I_{op}(50\%)$ = 210 mA (4320 A/cm^2). The EL spectrum is shown in the inset. I_{pump} = 1.5 A (680 A/cm^2).

strong electrothermal heating. The critical-current density was quite high (7.5–8.5 kA/cm^2). Further, the time dependence of emission intensity for dc pumping (0.5–0.6 I_{cr}) was investigated. It should be noted that the samples for these investigations were not soldered to a heat sink, but were pressed against the Cu plate by a special spring contact. In this case, the effective heat sink during the device operation was absent. Taking into account the significant operating densities of the pumping current, this made these operating conditions very severe. The observation-time dependence of emission radiation intensity for the constant pumping current is shown in Fig. 2. The EL spectrum of the structure with ZnCdSe QWs for 1.5 A (680 A/cm^2) dc pumping at room temperature is shown in the inset. The time needed for the intensity decrease by a factor of e was compared for various samples; the average time was about 10 h. The longest time (16 h) was measured for the structure with an active region based on the $Zn_{0.3}Cd_{0.7}Se$ QW 3 nm thick. It is remarkable that the emission intensity for this structure was highest compared to other structures investigated, which is apparently associated with the larger depth of the ZnCdSe QW. This result indicates that the local elastic stress generated by the QW material in the active region, which is largest for the ZnCdSe QW and smallest for the BeCdSe QW, is not by itself the determining factor affecting the degradation of injection structures. In contrast to this, the presence of ZnSe:N-based layers adjacent to the active region apparently exerts a prevailing effect on the degradation process. In addition, it has been demonstrated previously [13] that the waveguide based on a alternately strained SL effectively redistributes the QW strain over the entire waveguide region, thus, additionally minimizing the strain effect for these structures.

It is our opinion that introduction of the Be-containing compounds into the waveguide SL regions of HSs should also enhance the functions of alternately strained SLs as barriers for the propagation and development of extended and point defects in the active region. We assume that the short-period SLs in the structures investigated, which are present as the waveguide, a buffer layer, and a confining layer, affect also the thermal operating conditions of LEDs fabricated on their basis. The largest heat release occurs in the active region of the device, and the thermal resistance of waveguide layers and emitters is a significant factor. It is experimentally found for III–V SLs that an increase in the number of layers of binary compounds along with their simultaneous thinning leads to a considerable decrease in thermal resistance compared to the ternary compound layer of the same thickness. It has been possible that a similar situation also takes place in II–VI materials, and an increase in the operating life of LEDs may also be associated with this effect.

Laser diodes, which include similar waveguide and active regions, and wide-gap *p*-BeMgZnSe:N emitters, which are 0.1 μm away from the QW, were tested under considerably milder conditions [9]. It is possible that an increase in the operating life of investigated LEDs, compared to laser diodes, is caused primarily by excluding the ZnSe:N-based layers from the structure of the LEDs. These layers are the source of the

increased concentration of mobile point defects apparently associated with the interstitial nitrogen atoms.

CONCLUSION

A number of light-emitting BeZnSe/(Zn,Be,Cd)Se heterostructures with the QW as the active region were grown by MBE. The specific features of the HSs design are as follows: (1) the use of short-period SLs for hole transport into the active region; and (2) the absence of the *p*-doping of ZnSe-based layers with the purpose of suppressing the development of point defects. These defects are associated with compensating N complexes—most probably, interstitial N atoms. The LEDs fabricated on the basis of these heterostructures demonstrated appropriate current–voltage characteristics with a low cutoff voltage (2.2–3.0 V) and an improved stability against degradation at room temperature during pumping with high-density direct current (J = 4.5 kA/cm^2). The results obtained indicate that the method used by us to suppress the development of defects and increase the operating life of the device is promising for the growth of long-life LED and laser II–VI heterostructures.

ACKNOWLEDGMENTS

This study was supported by the Volkswagen Foundation; INTAS, grant no. 97-31907; the Russian Foundation for Basic Research, project nos. 99-02-17907 and 00-02-17022; and the 6th Competition–Appraisal of Projects of Young Researchers of the Russian Academy of Sciences.

REFERENCES

1. S. Nagahama, N. Iwasa, M. Senoh, *et al.*, in *Proceedings of the International Workshop on Nitride Semiconductors*, IPAP Conf. Ser. 1, 899 (2000).
2. S. Guha, J. M. DePuydt, M. A. Haase, *et al.*, Appl. Phys. Lett. **63**, 3107 (1993).
3. S. Tomiya, E. Morita, M. Ukita, *et al.*, Appl. Phys. Lett. **66**, 1208 (1995).
4. E. Kato, H. Noguchi, M. Nagai, *et al.*, Electron. Lett. **34**, 282 (1998).
5. K. Nakano, K. Onabe, K. Hiramatsu, *et al.*, in *Proceedings of the 2nd International Symposium on Blue Laser and Light Emitting Diodes, Chiba, Japan, 1998*, p. 395.
6. D. Albert, J. Nürnberger, V. Hock, *et al.*, Appl. Phys. Lett. **74**, 1957 (1999).
7. V. N. Jmerik, S. V. Sorokin, T. V. Shubina, *et al.*, J. Cryst. Growth **214/215**, 502 (2000).
8. S. Gundel, D. Albert, J. Nurberger, and W. Faschinger, Phys. Rev. B **60**, R16271 (1999).
9. S. V. Ivanov, A. A. Toropov, S. V. Sorokin, *et al.*, Appl. Phys. Lett. **73**, 2104 (1998).
10. H.-J. Lugauer, Th. Litz, F. Fischer, *et al.*, J. Cryst. Growth **175/176**, 619 (1997).
11. A. A. Toporov, T. V. Shubina, A. V. Lebedev, *et al.*, in *Proceedings of the 2nd International Symposium on Blue Laser and Light Emitting Diodes, Chiba, Japan, 1998*, p. 254.
12. S. V. Ivanov, O. V. Nekrutkina, S. V. Sorokin, *et al.*, Appl. Phys. Lett. **78**, 404 (2001).
13. A. V. Ankudinov, A. N. Titkov, T. V. Shubina, *et al.*, Appl. Phys. Lett. **75**, 2626 (1999).
14. W. S. Capinski, M. Cardona, D. S. Katzer, *et al.*, Physica B (Amsterdam) **263–264**, 530 (1999).

Translated by N. Korovin

Semiconductors, Vol. 35, No. 11, 2001, pp. 1345–1346. Translated from Fizika i Tekhnika Poluprovodnikov, Vol. 35, No. 11, 2001, p. 1401.

PERSONALIA

In Memory of Aleksei Petrovich Shotov (1927–2001)

Aleksei Petrovich Shotov met with an untimely death on July 6, 2001; he was a prominent physicist, professor, Doctor of Science (Physics–Mathematics), full member of the Russian Academy of Natural Sciences, winner of the Lenin and State Prizes of the USSR, and a senior member of the staff of the Solid-State Physics Department at the Lebedev Physical Institute of the Russian Academy of Sciences.

A.P. Shotov was a person who had a deep knowledge of and scientific intuition in his field of research and he made a great contribution to the physics of semiconductors by enriching it with a number of achievements, which were of first-rate scientific and practical importance.

A. Shotov was born on March 7, 1927 in the village of Mavrino in the Korobov region of the Moscow oblast. From 1942 to 1946, he was a student at the Moscow Mechanical-Engineering College and worked nights at a mechanical engineering plant. In 1952, after having defended his graduate project at the Moscow Mechanical Institute (now, the Moscow Institute of Engineering Physics), he graduated with distinction from the Bauman Higher Technical School. Later, he was assigned to the laboratory headed by Professor B.M. Vul at the Lebedev Physical Institute of the USSR Academy of Sciences. At this institute, Shotov worked for almost 50 years, first as a junior researcher, then as a senior researcher, the head of a department, the head of the laboratory, and a chief researcher. Shotov defended his Candidate thesis in 1958 (physics–mathematics) and his Doctoral thesis (physics–mathematics) in 1968.

Shotov was extremely knowledgeable scientifically; the results of his studies belong to diverse fields of semiconductor physics. The range of his personal interests (and, at the same time, the range of his achievements at the Lebedev Physical Institute) included diffused transistors, impact ionization and avalanche breakdown, semiconductor lasers, infrared injection lasers and their applications, and narrow-gap semiconductors. He was the author and co-author of more than 200 scientific publications and the holder of 22 inventor's certificates.

He substantiated and developed methods for the diffusion of impurities into semiconductors for forming *p–n* junctions and he developed the first diffused diodes and transistors (1952–1953) and the first (in the USSR) semiconductor lasers (1962). Fundamental studies that led to the development of semiconductor lasers were honored with the Lenin prize (1964). Shotov made a notable contribution to the physics of impact ionization and avalanche breakdown in semiconductors, which became the scientific basis for the development of devices that operate in the avalanche mode.

From the 1970s, Shotov supervised a large number of studies in the physics and technology of narrow-gap semiconductors and the quantum-confinement structures based on these semiconductors. Development of tunable diode lasers emitting in a wide range of the infrared region of the spectrum has been an important result of these studies. These lasers have found application in high-resolution molecular spectroscopy and in high-sensitivity spectral analysis of gases; the latter use is important for solving problems in ecology, in particular, for the analysis of exhalated gases in medicine and for a number of special applications. A number of the designs have been implemented in the framework of international cooperation. This series of studies was honored with the USSR State Award (1985). One of the developed devices (a laser-based system for measuring the content of contaminations in the atmosphere) was awarded the gold medal at the International Exhibition in Leipzig (1986).

Shotov was deeply engaged in pedagogical activity. He was a professor at the special department (a higher school of Physics formed in collaboration between the Moscow Institute of Engineering Physics and the Lebedev Physical Institute) of the Moscow Institute of Engineering Physics. In 2001, Shotov was nominated (in a team of scientists of the Moscow Institute of Engineering Physics) as a candidate for receiving the Award of the President of the Russian Federation. Shotov supervised the dissertation studies of 20 Candidates of Science and 7 Doctors of Science. Shotov was a member of Degree granting academic councils and a permanent member of the editorial board of the journal "Krat-

1063-7826/01/3511-1345$21.00 © 2001 MAIK "Nauka/Interperiodica"

kie Soobshcheniya po Fizike" (Bulletin of the Lebedev Physics Institute").

For his scientific activity, Shotov was awarded the Order of the Red Banner of Labor, the Honor Sign Order and the Order of Honor of the Russian Federation, medals on the occasion of the 800- and 850-year anniversary of the foundation of Moscow, and he was honored with the Kapitsa Silver Medal of the Russian Academy of Sciences.

The bright memory of A.V. Shotov will always remain in our hearts.

Zh. I. Alferov, V. S. Bagaev,
B. A. Volkov, A. A. Gippius,
A. I. Golovashkin, S. P. Grishechkina,
A. I. Demeshina, I. I. Zasavitskiĭ,
A. I. Isakov, L. V. Keldysh,
Yu. V. Kopaev, B. D. Kopylovskiĭ,
O. N. Krokhin, A. I. Nadezhdinskiĭ,
I. G. Neizvestnyĭ, N. A. Penin, Yu. M. Popov,
N. N. Sibel'din, V. I. Stafeev,
V. A. Chuenkov, V. V. Shestakov,
and A. É. Yunovich

Translated by A. Spitsyn